

1

2

3

4

5

# Simultaneous Measurement of Oscillation Parameters in Beam and Atmospheric Neutrino Data from Tokai-to-Kamioka and Super-Kamiokande Experiments

6

Daniel Robert Clement Barrow

7

8

Magdalen College,  
Oxford University

9

Version 1.1

10

A Dissertation Submitted to Oxford University  
11 for the Degree of Doctor of Philosophy

13                   **Simultaneous Measurement of**

14                   **Oscillation Parameters in Beam and**

15                   **Atmospheric Neutrino Data from**

16                   **Tokai-to-Kamioka and**

17                   **Super-Kamiokande Experiments**

18                   *Abstract*

19                   Lorem ipsum dolor sit amet, consectetur adipiscing elit, sed do eiusmod tempor incididunt ut labore et dolore magna aliqua. Nulla aliquet porttitor lacus luctus accumsan tortor posuere. Pulvinar neque laoreet suspendisse interdum. Sem viverra aliquet eget sit. Nunc sed velit dignissim sodales ut eu sem integer vitae. At erat pellentesque adipiscing commodo elit at imperdiet dui accumsan. Fames ac turpis egestas integer eget aliquet nibh. Scelerisque eu ultrices vitae auctor eu augue. Purus non enim praesent elementum facilisis leo vel. Sollicitudin nibh sit amet commodo. Vitae auctor eu augue ut. Vel quam elementum pulvinar etiam. A condimentum vitae sapien pellentesque habitant morbi tristique senectus. Viverra accumsan in nisl nisi scelerisque eu ultrices. Sed viverra ipsum nunc aliquet bibendum enim.

## 32 Declaration

33 This dissertation is the result of my own work, except where ex-  
34 plicit reference is made to the work of others, and has not been sub-  
35 mitted for another qualification to this or any other university. This  
36 dissertation does not exceed the word limit for the respective Degree  
37 Committee.

38 Daniel Robert Clement Barrow

39 ©The copyright of this thesis rests with the author and is made available under a Creative  
40 Commons Attribution Non-Commercial No Derivatives licence. Researchers are free to copy,  
41 distribute or transmit the thesis on the condition that they attribute it, that they do not use  
42 it for commercial purposes and that they do not alter, transform or build upon it. For any  
43 reuse or redistribution, researchers must make clear to others the licence terms of this work.

44

## Acknowledgements

45 at pretium nibh ipsum. Eget nunc scelerisque viverra mauris in aliquam. Arcu vitae  
46 elementum curabitur vitae nunc sed velit dignissim. Sed arcu non odio euismod lacinia  
47 at quis risus sed. Vitae tempus quam pellentesque nec nam aliquam sem et tortor.  
48 Viverra aliquet eget sit amet tellus cras adipiscing. Purus sit amet luctus venenatis  
49 lectus magna. In aliquam sem fringilla ut morbi tincidunt augue. Fermentum dui  
50 faucibus in ornare. Aliquam malesuada bibendum arcu vitae elementum curabitur  
51 vitae nunc sed.

52 Ultricies leo integer malesuada nunc vel risus commodo. Tellus cras adipiscing  
53 enim eu turpis egestas pretium. Dictumst quisque sagittis purus sit amet volutpat  
54 consequat mauris nunc. Vitae congue mauris rhoncus aenean vel elit scelerisque  
55 mauris pellentesque. Vel facilisis volutpat est velit egestas dui id ornare. Suscipit  
56 adipiscing bibendum est ultricies. At in tellus integer feugiat scelerisque varius  
57 morbi enim. Cras semper auctor neque vitae tempus. Commodo sed egestas egestas  
58 fringilla phasellus faucibus. Cras pulvinar mattis nunc sed blandit. Pretium viverra  
59 suspendisse potenti nullam ac tortor vitae. Purus sit amet volutpat consequat. Orci  
60 sagittis eu volutpat odio facilisis mauris. Sit amet massa vitae tortor condimentum  
61 lacinia quis. Commodo sed egestas egestas fringilla phasellus. Sed libero enim sed  
62 faucibus turpis. Vitae tempus quam pellentesque nec.

63 Blandit massa enim nec dui. Viverra tellus in hac habitasse platea dictumst vestibulu-  
64 lum. Bibendum enim facilisis gravida neque convallis. Sagittis nisl rhoncus mattis  
65 rhoncus urna neque. Nisl rhoncus mattis rhoncus urna neque. Ac tortor vitae purus  
66 faucibus ornare. Aenean sed adipiscing diam donec adipiscing tristique risus. Sapien  
67 nec sagittis aliquam malesuada bibendum. Et leo duis ut diam quam nulla. Tellus  
68 rutrum tellus pellentesque eu tincidunt tortor aliquam nulla facilisi.

# **Contents**

<b>1</b>	<b>Introduction</b>	<b>1</b>
<b>2</b>	<b>Neutrino Oscillation Physics</b>	<b>2</b>
2.1	Discovery of Neutrinos . . . . .	2
2.2	Theory of Neutrino Oscillation . . . . .	4
2.2.1	Three Flavour Oscillations . . . . .	4
2.2.2	The MSW Effect . . . . .	8
2.3	Neutrino Oscillation Measurements . . . . .	9
2.3.1	Solar Neutrinos . . . . .	11
2.3.2	Atmospheric Neutrinos . . . . .	13
2.3.3	Accelerator Neutrinos . . . . .	16
2.3.4	Reactor Neutrinos . . . . .	18
2.4	Summary . . . . .	20
<b>3</b>	<b>T2K and SK Experiment Overview</b>	<b>23</b>
3.1	The Super-Kamiokande Experiment . . . . .	23
3.1.1	The SK Detector . . . . .	24
3.1.2	Calibration . . . . .	28
3.1.3	Data Acquisition and Triggering . . . . .	31
3.1.4	Cherenkov Radiation . . . . .	33
3.2	The Tokai to Kamioka Experiment . . . . .	35
3.2.1	The Neutrino Beam . . . . .	37
3.2.2	The Near Detector at 280m . . . . .	40
3.2.2.1	Fine Grained Detectors . . . . .	43
3.2.2.2	Time Projection Chambers . . . . .	44

93	3.2.2.3	$\pi^0$ Detector . . . . .	46
94	3.2.2.4	Electromagnetic Calorimeter . . . . .	46
95	3.2.2.5	Side Muon Range Detector . . . . .	48
96	3.2.3	The Interactive Neutrino GRID . . . . .	48
97	<b>4</b>	<b>Bayesian Statistics and Markov Chain Monte Carlo Techniques</b>	50
98	4.1	Bayesian Statistics . . . . .	51
99	4.2	Monte Carlo Simulation . . . . .	52
100	4.2.1	Markov Chain Monte Carlo . . . . .	53
101	4.2.2	Metropolis-Hastings Algorithm . . . . .	56
102	4.2.3	MCMC Optimisation . . . . .	58
103	4.3	Understanding the MCMC Results . . . . .	61
104	4.3.1	Marginalisation . . . . .	62
105	4.3.2	Parameter Estimation and Credible Intervals . . . . .	63
106	4.3.3	Bayesian Model Comparisons . . . . .	65
107	4.3.4	Comparison of MCMC Output to Expectation . . . . .	66
108	<b>5</b>	<b>Simulation, Reconstruction, and Event Reduction</b>	68
109	5.1	Simulation . . . . .	68
110	5.2	Event Reconstruction at SK . . . . .	73
111	5.3	Event Reduction at SK . . . . .	85
112	<b>6</b>	<b>Sample Selections and Systematics</b>	90
113	6.1	Atmospheric Samples . . . . .	92
114	6.2	Near Detector Beam Samples . . . . .	99
115	6.3	Far Detector Beam Samples . . . . .	102
116	6.4	Systematic Uncertainties . . . . .	107
117	6.4.1	Beam Flux . . . . .	107
118	6.4.2	Atmospheric Flux . . . . .	109

---

119	6.4.3	Neutrino Interaction . . . . .	110
120	6.4.4	Near Detector . . . . .	116
121	6.4.5	Far Detector . . . . .	118
122	6.4.5.1	Beam Samples . . . . .	118
123	6.4.5.2	Atmospheric Samples . . . . .	121
124	6.4.5.3	Correlated Detector Model . . . . .	122
125	<b>7</b>	<b>Oscillation Probability Calculation</b>	<b>130</b>
126	7.1	Overview . . . . .	131
127	7.2	Treatment of Fast Oscillations . . . . .	139
128	7.3	Calculation Engine . . . . .	145
129	7.4	Matter Density Profile . . . . .	148
130	7.5	Production Height Averaging . . . . .	154
131	<b>Bibliography</b>		<b>158</b>
132	<b>List of Figures</b>		<b>170</b>
133	<b>List of Tables</b>		<b>181</b>



<sup>135</sup> **Chapter 1**

<sup>136</sup> **Introduction**

<sup>137</sup> **Chapter 2**

<sup>138</sup> **Neutrino Oscillation Physics**

<sup>139</sup> When first proposed, neutrinos were expected to be massless fermions that only in-  
<sup>140</sup> teract through weak and gravitational forces. This meant they were very difficult to  
<sup>141</sup> detect as they can pass through significant amounts of matter without interacting. De-  
<sup>142</sup> spite this, experimental neutrino physics has developed with many different detection  
<sup>143</sup> techniques and neutrino sources being used today. In direct tension with standard  
<sup>144</sup> model physics, neutrinos have been determined to oscillate between different lepton  
<sup>145</sup> flavours, requiring them to have mass.

<sup>146</sup> The observation techniques which lead to the discovery of the neutrino are doc-  
<sup>147</sup> umented in section 2.1. The theory underpinning neutrino oscillation is described  
<sup>148</sup> in section 2.2 and includes the approximations which can be made to simplify the  
<sup>149</sup> understanding of neutrino oscillation in the two-flavour approximation. Past, current,  
<sup>150</sup> and future neutrino experiments are detailed in section 2.3, including the reactor,  
<sup>151</sup> atmospheric, and long-baseline accelerator neutrino sources that have been used to  
<sup>152</sup> successfully constrain oscillation parameters. Finally, the current state of oscillation  
<sup>153</sup> parameter measurements are summarised in section 2.4.

<sup>154</sup> **2.1 Discovery of Neutrinos**

<sup>155</sup> At the start of the 20<sup>th</sup> century, the electrons emitted from the  $\beta$ -decay of the nucleus  
<sup>156</sup> were found to have a continuous energy spectrum [1,2]. This observation seemingly  
<sup>157</sup> broke the energy conservation invoked within that period's nuclear models. Postulated

158 in 1930 by Pauli as the solution to this problem, the neutrino (originally termed  
159 “neutron”) was theorized to be an electrically neutral spin-1/2 fermion with a mass of  
160 the same order of magnitude as the electron [3]. This neutrino was to be emitted with  
161 the electron in  $\beta$ -decay to alleviate the apparent breaking of energy conservation. As a  
162 predecessor of today’s weak interaction model, Fermi’s theory of  $\beta$ -decay developed  
163 the understanding by coupling the four constituent particles; electron, proton, neutron,  
164 and neutrino, into a consistent model [4].

165 Whilst Pauli was not convinced of the ability to detect neutrinos, the first observa-  
166 tions of the particle were made in the mid-1950s when neutrinos from a reactor were  
167 observed via the inverse  $\beta$ -decay (IBD) process,  $\bar{\nu}_e + p \rightarrow n + e^+$  [5, 6]. The detector  
168 consisted of two parts: a neutrino interaction medium and a liquid scintillator. The  
169 interaction medium was built from two water tanks. These were loaded with cadmium  
170 chloride to allow increased efficiency of neutron capture. The positron emitted from  
171 IBD annihilates,  $e^+ + e^- \rightarrow 2\gamma$ , generating a prompt signal and the neutron is captured  
172 on the cadmium via  $n + {}^{108}Cd \rightarrow {}^{109*}Cd \rightarrow {}^{109}Cd + \gamma$ , producing a delayed signal. An  
173 increase in the coincidence rate was observed when the reactor was operating which  
174 was interpreted as interactions from neutrinos generated in the reactor.

175 After the discovery of the  $\nu_e$ , the natural question of how many flavours of neutrino  
176 exist was asked. In 1962, a measurement of the  $\nu_\mu$  was conducted at the Brookhaven  
177 National Laboratory [7]. A proton beam was directed at a beryllium target, generating  
178 a  $\pi$ -dominated beam which then decayed via  $\pi^\pm \rightarrow \mu^\pm + (\nu_\mu, \bar{\nu}_\mu)$ , and the subsequent  
179 interactions of the  $\nu_\mu$  were observed. As the subsequent interaction of the neutrino  
180 generates muons rather than electrons, it was determined the  $\nu_\mu$  was fundamentally  
181 different from  $\nu_e$ . The final observation to be made was that of the  $\nu_\tau$  from the DONUT  
182 experiment [8]. Three neutrinos seem the obvious solution as it mirrors the known  
183 number of charged lepton (as they form weak isospin doublets) but there could be

<sup>184</sup> evidence of more. Several neutrino experiments have found anomalous results [9, 10]  
<sup>185</sup> which could be attributed to sterile neutrinos. However, cosmological observations  
<sup>186</sup> indicate the number of neutrino species  $N_{eff} = 2.99 \pm 0.17$  [11], as measured from  
<sup>187</sup> the cosmic microwave background power spectrum, and LEP measured the number  
<sup>188</sup> of active neutrino flavours to be  $N_\nu 2.9840 \pm 0.0082$  [12] from measurements of the  
<sup>189</sup>  $Z$ -decay width.

## <sup>190</sup> 2.2 Theory of Neutrino Oscillation

<sup>191</sup> As direct evidence of beyond Standard Model physics, a neutrino generated with  
<sup>192</sup> lepton flavour  $\alpha$  can change into a different lepton flavour  $\beta$  after propagating some  
<sup>193</sup> distance. This phenomenon is called neutrino oscillation and requires that neutrinos  
<sup>194</sup> must have a non-zero mass (as seen in subsection 2.2.1). This observation is direct  
<sup>195</sup> evidence of beyond standard model physics. This behaviour has been characterised  
<sup>196</sup> by the Pontecorvo-Maki-Nakagawa-Sakata (PMNS) [13–15] mixing matrix which  
<sup>197</sup> describes how the flavour and mass of neutrinos are associated. This is analogous to  
<sup>198</sup> the Cabibbo-Kobayashi-Maskawa (CKM) [16] matrix measured in quark physics.

### <sup>199</sup> 2.2.1 Three Flavour Oscillations

<sup>200</sup> The PMNS parameterisation defines three flavour eigenstates,  $\nu_e$ ,  $\nu_\mu$  and  $\nu_\tau$  (indexed  
<sup>201</sup>  $\nu_\alpha$ ), which are eigenstates of the weak interaction and three mass eigenstates,  $\nu_1$ ,  $\nu_2$  and  
<sup>202</sup>  $\nu_3$  (indexed  $\nu_i$ ). Each mass eigenstate is the superposition of all three flavour states,

$$|\nu_i\rangle = \sum_\alpha U_{\alpha i} |\nu_\alpha\rangle. \quad (2.1)$$

203 Where  $U$  is the PMNS matrix which is unitary and connects the mass and flavour

204 eigenstates.

205 The weak interaction couples to flavour eigenstates so neutrinos interact with

206 leptons of the same flavour. The propagation of a neutrino flavour eigenstate, in a

207 vacuum, can be re-written as a plane-wave solution to the time-dependent Schrödinger

208 equation,

$$|\nu_\alpha(t)\rangle = \sum_i U_{\alpha i}^* |\nu_i\rangle e^{-i\phi_i}. \quad (2.2)$$

209 The probability of observing a neutrino of flavour eigenstate  $\beta$  from one which

210 originated as flavour  $\alpha$  can be calculated as,

$$P(\nu_\alpha \rightarrow \nu_\beta) = |\langle \nu_\beta | \nu_\alpha(t) \rangle|^2 = \sum_{i,j} U_{\alpha i}^* U_{\beta i} U_{\alpha j} U_{\beta j}^* e^{-i(\phi_j - \phi_i)} \quad (2.3)$$

211 The  $\phi_i$  term can be expressed in terms of the energy,  $E_i$ , and magnitude of the

212 three momenta,  $p_i$ , of the neutrino,  $\phi_i = E_i t - p_i x$  ( $t$  and  $x$  being time and position

213 coordinates). Therefore,

$$\phi_j - \phi_i = E_j t - E_i t - p_j x + p_i x. \quad (2.4)$$

214 For a relativistic particle,  $E_i \gg m_i$ ,

$$p_i = \sqrt{E_i^2 - m_i^2} \approx E_i - \frac{m_i^2}{2E_i}. \quad (2.5)$$

215 Making the approximations that neutrinos are relativistic, the mass eigenstates  
216 were created with the same energy and that  $x = L$ , where  $L$  is the distance traveled by  
217 the neutrino, Equation 2.4 then becomes

$$\phi_j - \phi_i = \frac{\Delta m_{ij}^2 L}{2E}, \quad (2.6)$$

218 where  $\Delta m_{ij}^2 = m_j^2 - m_i^2$ . This, combined with further use of unitarity relations  
219 results in Equation 2.3 becoming

$$P(\nu_\alpha \rightarrow \nu_\beta) = \delta_{\alpha\beta} - 4 \sum_{i>j} \Re \left( U_{\alpha i}^* U_{\beta i} U_{\alpha j} U_{\beta j}^* \right) \sin^2 \left( \frac{\Delta m_{ij}^2 L}{4E} \right) + (-) 2 \sum_{i>j} \Im \left( U_{\alpha i}^* U_{\beta i} U_{\alpha j} U_{\beta j}^* \right) \sin \left( \frac{\Delta m_{ij}^2 L}{2E} \right). \quad (2.7)$$

220 Where  $\delta_{\alpha\beta}$  is the Kronecker delta function and the negative sign on the last term is  
221 included for the oscillation probability of antineutrinos.

222 Typically, the PMNS matrix is parameterised into three mixing angles, a charge  
223 parity (CP) violating phase  $\delta_{CP}$ , and two Majorana phases  $\alpha_{1,2}$ ,

$$U = \underbrace{\begin{pmatrix} 1 & 0 & 0 \\ 0 & c_{23} & s_{23} \\ 0 & -s_{23} & c_{23} \end{pmatrix}}_{\text{Atmospheric, Accelerator}} \underbrace{\begin{pmatrix} c_{13} & 0 & s_{13}e^{-i\delta_{CP}} \\ 0 & 1 & 0 \\ -s_{13}e^{-i\delta_{CP}} & 0 & c_{13} \end{pmatrix}}_{\text{Reactor, Accelerator}} \underbrace{\begin{pmatrix} c_{12} & s_{12} & 0 \\ -s_{12} & c_{12} & 0 \\ 0 & 0 & 1 \end{pmatrix}}_{\text{Reactor, Solar}} \underbrace{\begin{pmatrix} e^{i\alpha_1/2} & 0 & 0 \\ 0 & e^{i\alpha_2/2} & 0 \\ 0 & 0 & 1 \end{pmatrix}}_{\text{Majorana}}. \quad (2.8)$$

<sup>224</sup> Where  $s_{ij} = \sin(\theta_{ij})$  and  $c_{ij} = \cos(\theta_{ij})$ . The oscillation parameters are often  
<sup>225</sup> grouped; (1,2) as “solar”, (2,3) as “atmospheric” and (1,3) as “reactor”. Many  
<sup>226</sup> neutrino experiments aim to measure the PMNS parameters from a wide array of  
<sup>227</sup> origins, as is the purpose of this thesis.

<sup>228</sup> The Majorana phase,  $\alpha_{1,2}$ , included within the fourth matrix in Equation 2.8 is only  
<sup>229</sup> included for completeness. For an oscillation analysis experiment, any terms contain-  
<sup>230</sup> ing this phase disappear due to taking the expectation value of the PMNS matrix.  
<sup>231</sup> Measurements of these phases are typically performed by experiments searching for  
<sup>232</sup> neutrino-less double  $\beta$ -decay [17].

<sup>233</sup> A two flavour approximation can be obtained when one assumes the third mass  
<sup>234</sup> eigenstate is degenerate with another. As discussed in section 2.3, it is found that  
<sup>235</sup>  $\Delta m_{21}^2 \ll |\Delta m_{31}^2|$ . This results in the two flavour approximation being reasonable for  
<sup>236</sup> understanding the features of the oscillation. In this two flavour case, the mixing  
<sup>237</sup> matrix becomes,

$$U_{2 \text{ Flav.}} = \begin{pmatrix} \cos(\theta) & \sin(\theta) \\ -\sin(\theta) & \cos(\theta) \end{pmatrix}. \quad (2.9)$$

<sup>238</sup> This culminates in the oscillation probability,

$$\begin{aligned} P(\nu_\alpha \rightarrow \nu_\alpha) &= 1 - \sin^2(2\theta) \sin^2\left(\frac{\Delta m^2 L}{4E}\right), \\ P(\nu_\alpha \rightarrow \nu_\beta) &= \sin^2(2\theta) \sin^2\left(\frac{\Delta m^2 L}{4E}\right). \end{aligned} \quad (2.10)$$

<sup>239</sup> Where  $\alpha \neq \beta$ . For a fixed neutrino energy, the oscillation probability is a sinusoidal  
<sup>240</sup> function depending upon the distance over which the neutrino propagates. The  
<sup>241</sup> frequency and amplitude of oscillation are dependent upon  $\Delta m^2/4E$  and  $\sin^2 2\theta$ ,  
<sup>242</sup> respectively. The oscillation probabilities presented thus far assume  $c = 1$ , where  
<sup>243</sup>  $c$  is the speed of light in vacuum. In more familiar units, the maximum oscillation  
<sup>244</sup> probability for a fixed value of  $\theta$  is given at  $L[km]/E[GeV] \sim 1.27/\Delta m^2$ . It is this  
<sup>245</sup> calculation that determines the best  $L/E$  value for a given experiment to be designed  
<sup>246</sup> around for measurements of a specific value of  $\Delta m^2$ .

## <sup>247</sup> 2.2.2 The MSW Effect

<sup>248</sup> The theory of neutrino oscillation in a vacuum has been described in subsection 2.2.1.  
<sup>249</sup> However, the beam neutrinos and atmospheric neutrinos originating from below the  
<sup>250</sup> horizon propagate through matter in the Earth. The coherent scattering of neutrinos  
<sup>251</sup> from a material target modifies the Hamiltonian of the system. This results in a change  
<sup>252</sup> in the oscillation probability. Notably, charged current scattering ( $\nu_e + e^- \rightarrow \nu_e + e^-$ ,  
<sup>253</sup> propagated by a  $W$  boson) only affects electron neutrinos whereas the neutral current  
<sup>254</sup> scattering ( $\nu_l + l^- \rightarrow \nu_l + l^-$ , propagated by a  $Z^0$  boson) interacts through all neutrino  
<sup>255</sup> flavours equally. In the two-flavour approximation, the effective mixing parameter  
<sup>256</sup> becomes

$$\sin^2(2\theta) \rightarrow \sin^2(2\theta_m) = \frac{\sin^2(2\theta)}{(A/\Delta m^2 - \cos(2\theta))^2 + \sin^2(2\theta)}, \quad (2.11)$$

where  $A = 2\sqrt{2}G_F N_e E$ ,  $N_e$  is the electron density of the medium and  $G_F$  is Fermi's constant. It is clear to see that there exists a value of  $A = \Delta m^2 \cos(2\theta)$  for  $\Delta m^2 > 0$  which results in a divergent mixing parameter. This resonance is termed the Mikheyev-Smirnov-Wolfenstein (MSW) effect (or more colloquially, the matter resonance) which regenerates the electron neutrino component of the neutrino flux [18–20]. The density at which the resonance occurs is given by

$$N_e = \frac{\Delta m^2 \cos(2\theta)}{2\sqrt{2}G_F E}. \quad (2.12)$$

At densities lower than this critical value, the oscillation probability will be much closer to that of vacuum oscillation. For antineutrinos,  $N_e \rightarrow -N_e$  [21]. The resonance occurring from the MSW effect depends on the sign of  $\Delta m^2$ . Therefore, any neutrino oscillation experiment which observes neutrinos and antineutrinos which have propagated through matter can have some sensitivity to the ordering of the neutrino mass eigenstates.

## 2.3 Neutrino Oscillation Measurements

As evidence of beyond standard model physics, the 2015 Nobel Prize in Physics was awarded to the Super-Kamiokande (SK) [22] and Sudbury Neutrino Observatory (SNO) [23] collaborations for the first definitive observation of solar and atmospheric

<sup>273</sup> neutrino oscillation [24]. Since then, the field has seen a wide array of oscillation  
<sup>274</sup> measurements from a variety of neutrino sources. As seen in subsection 2.2.1, the  
<sup>275</sup> neutrino oscillation probability is dependent on the ratio of the propagation baseline,  $L$ ,  
<sup>276</sup> to the neutrino energy,  $E$ . It is this ratio that determines the type of neutrino oscillation  
<sup>277</sup> a particular experiment is sensitive to.

<sup>278</sup> As illustrated in Figure 2.1, there are many neutrino sources that span a wide  
<sup>279</sup> range of energies. The least energetic neutrinos are from diffuse supernovae and  
<sup>280</sup> terrestrial neutrinos at  $O(1)$  MeV whereas the most energetic neutrinos originate from  
<sup>281</sup> atmospheric and galactic neutrinos of  $> O(1)$  TeV.

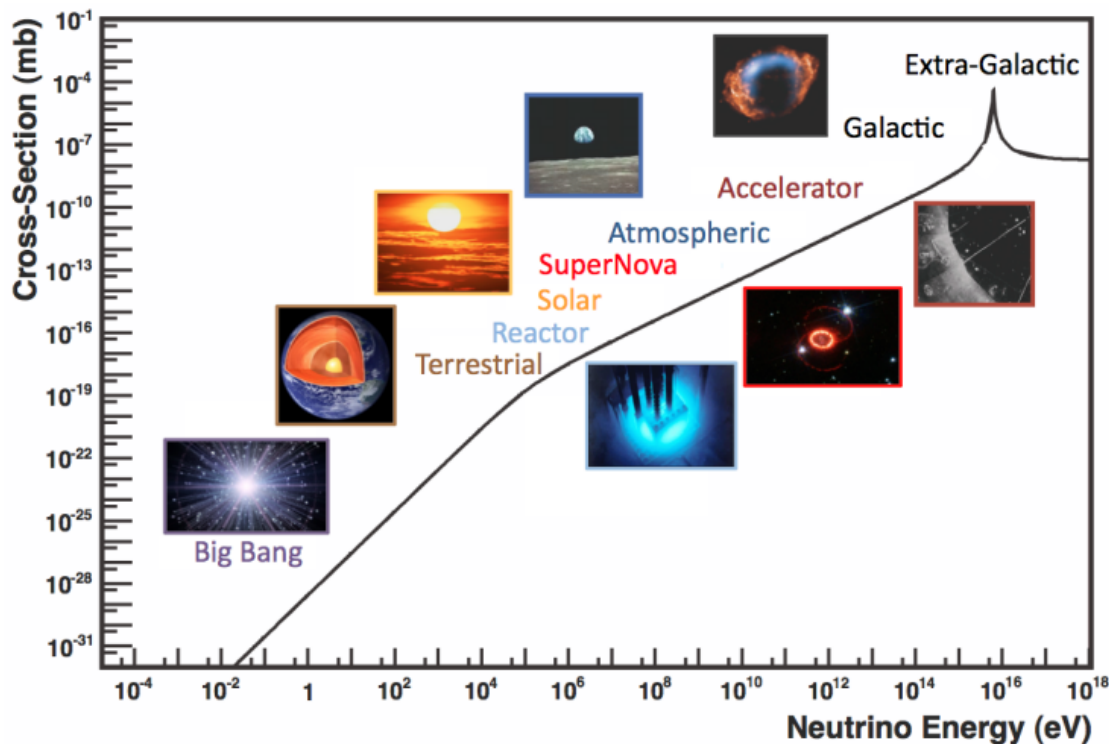


**Figure 2.1:** The cross-section of neutrinos from various natural and man-made sources as a function of neutrino energy. Taken from [25]

### <sup>282</sup> 2.3.1 Solar Neutrinos

<sup>283</sup> Solar neutrinos are emitted from fusion reaction chains at the center of the Sun. The  
<sup>284</sup> solar neutrino flux, given as a function of neutrino energy for different fusion and  
<sup>285</sup> decay chains, is illustrated in Figure 2.2. Whilst proton-proton fusion generates the  
<sup>286</sup> largest flux of neutrinos, the neutrinos are of low energy and are difficult to reconstruct  
<sup>287</sup> due to the IBD interaction threshold of 1.8MeV. Consequently, most experiments focus  
<sup>288</sup> on the neutrinos from the decay of  $^8B$  (via  $^8B \rightarrow ^8Be^* + e^+ + \nu_e$ ), which are higher  
<sup>289</sup> energy.

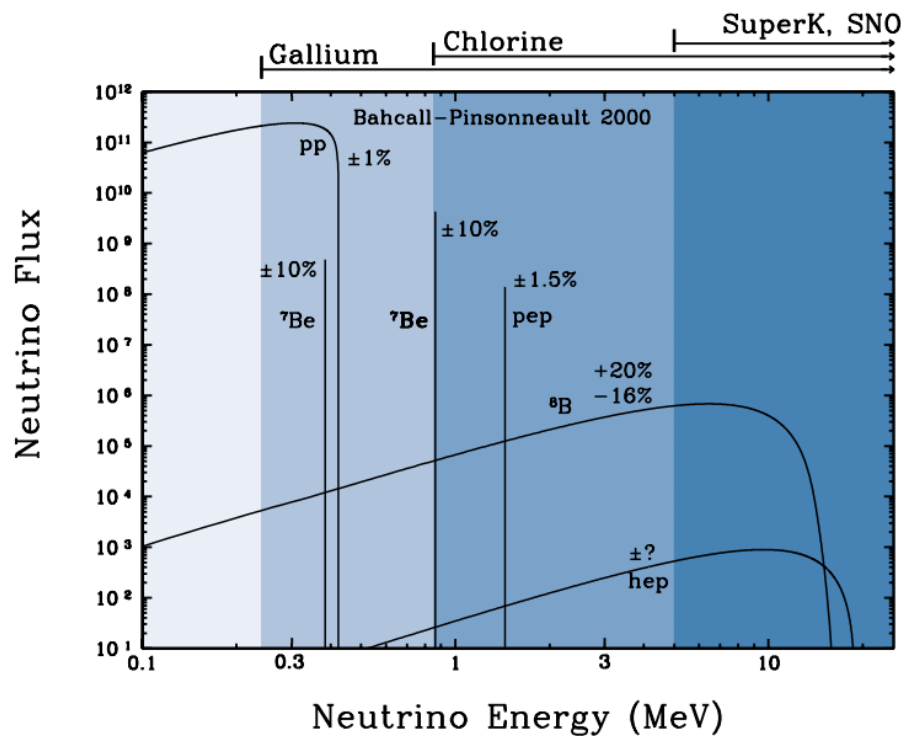
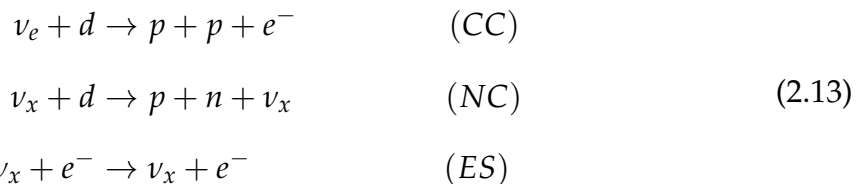


**Figure 2.2:** The solar neutrino flux as a function of neutrino energy for various fusion reactions and decay chains as predicted by the Standard Solar Model. Taken from [26].

<sup>290</sup> The first measurements of solar neutrinos observed a significant reduction in the  
<sup>291</sup> event rate compared to predictions from the Standard Solar Model [27, 28]. The  
<sup>292</sup> proposed solution to this “solar neutrino problem” was  $\nu_e \leftrightarrow \nu_\mu$  oscillations in a

<sup>293</sup> precursory version of the PMNS model [29]. The Kamiokande [30], Gallex [31] and  
<sup>294</sup> Sage [32] experiments confirmed the  $\sim 0.5$  factor deficit of solar neutrinos.

<sup>295</sup> The conclusive solution to this problem was determined by the SNO collaboration  
<sup>296</sup> [33]. Using a deuterium water target to observe  ${}^8B$  neutrinos, the event rate of charged  
<sup>297</sup> current (CC), neutral current (NC), and elastic scattering (ES) interactions (Given in  
<sup>298</sup> Equation 2.13) was simultaneously measured. CC events can only occur for electron  
<sup>299</sup> neutrinos, whereas the NC channel is agnostic to neutrino flavour, and the ES reaction  
<sup>300</sup> has a slight excess sensitivity to electron neutrino interactions. This meant that there  
<sup>301</sup> were direct measurements of the  $\nu_e$  and  $\nu_x$  neutrino flux. It was concluded that the  
<sup>302</sup> CC and ES interaction rates were consistent with the deficit previously observed.  
<sup>303</sup> Most importantly, the NC reaction rate was only consistent with the others under the  
<sup>304</sup> hypothesis of flavour transformation.



<sup>305</sup> Many experiments have since measured the neutrino flux of different interaction  
<sup>306</sup> chains within the sun [34–36]. The most recent measurement was that of CNO neutrinos  
<sup>307</sup> which were recently observed with  $5\sigma$  significance by the Borexino collaboration.  
<sup>308</sup> Future neutrino experiments aim to further these spectroscopic measurements of  
<sup>309</sup> different fusion chains within the Sun [37–39]. Solar neutrinos act as an irreducible  
<sup>310</sup> background for dark matter experiments like DARWIN but oscillation parameter  
<sup>311</sup> measurements can be made [40].

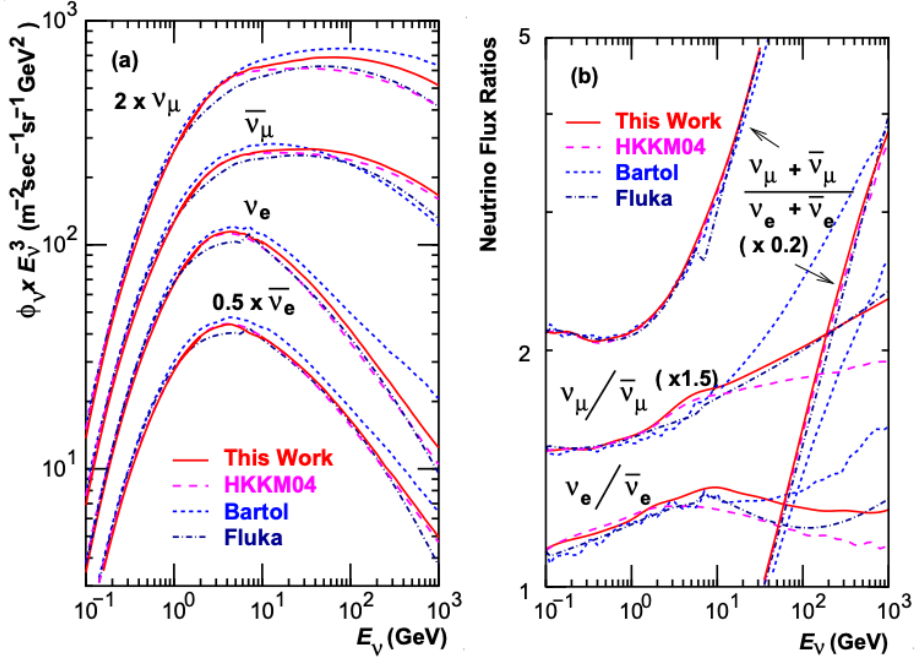
### <sup>312</sup> 2.3.2 Atmospheric Neutrinos

- <sup>313</sup> The interactions of primary cosmic ray protons in Earth's upper atmosphere generate  
<sup>314</sup> showers of energetic hadrons. These are mostly pions and kaons which when they  
<sup>315</sup> decay produce a natural source of neutrinos spanning energies of MeV to TeV [41].  
<sup>316</sup> The main decay is via

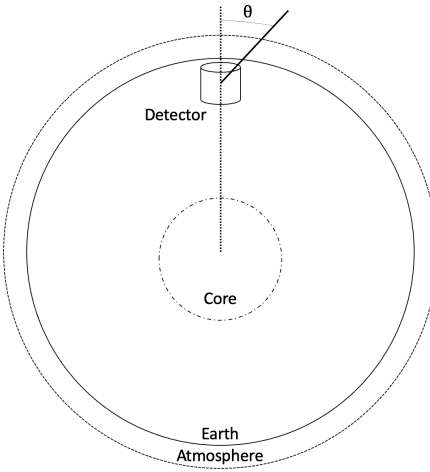
$$\begin{aligned} \pi^\pm &\rightarrow \mu^\pm + (\nu_\mu, \bar{\nu}_\mu) \\ \mu^\pm &\rightarrow e^\pm + (\nu_e, \bar{\nu}_e) + (\nu_\mu, \bar{\nu}_\mu) \end{aligned} \tag{2.14}$$

<sup>317</sup> such that for a single pion decay, three neutrinos are typically produced. The  
<sup>318</sup> atmospheric neutrino flux energy spectra as predicted by the Bartol [42], Honda  
<sup>319</sup> [43–45], and FLUKA [46] models are illustrated in Figure 2.3. The flux distribution  
<sup>320</sup> peaks at an energy of  $O(10)\text{GeV}$ . The uncertainties associated with these models  
<sup>321</sup> are dominated by the hadronic production of kaon and pions as well as the primary  
<sup>322</sup> cosmic flux.

<sup>323</sup> Unlike long-baseline experiments which have a fixed baseline, the distance at-  
<sup>324</sup> mospheric neutrinos propagate is dependent upon the zenith angle at which they  
<sup>325</sup> interact. This is illustrated in Figure 2.4. Neutrinos that are generated directly above  
<sup>326</sup> the detector ( $\cos(\theta) = 1.0$ ) have a baseline equivalent to the height of the atmosphere  
<sup>327</sup> whereas neutrinos that interact directly below the detector ( $\cos(\theta) = -1.0$ ) have to  
<sup>328</sup> travel a length equal to the diameter of the Earth. This means atmospheric neutrinos  
<sup>329</sup> have a baseline that varies from  $O(20)\text{km}$  to  $O(6 \times 10^3)\text{km}$ . Any neutrino generated  
<sup>330</sup> at or below the horizon will be subject to matter effects as they propagate through the  
<sup>331</sup> Earth.



**Figure 2.3:** Left panel: The atmospheric neutrino flux for different neutrino flavours as a function of neutrino energy as predicted by the 2007 Honda model (“This work”) [43], the 2004 Honda model (“HKKM04”) [44], the Bartol model [42] and the FLUKA model [46]. Right panel: The ratio of the muon to electron neutrino flux as predicted by all the quoted models. Both figures taken from [43].



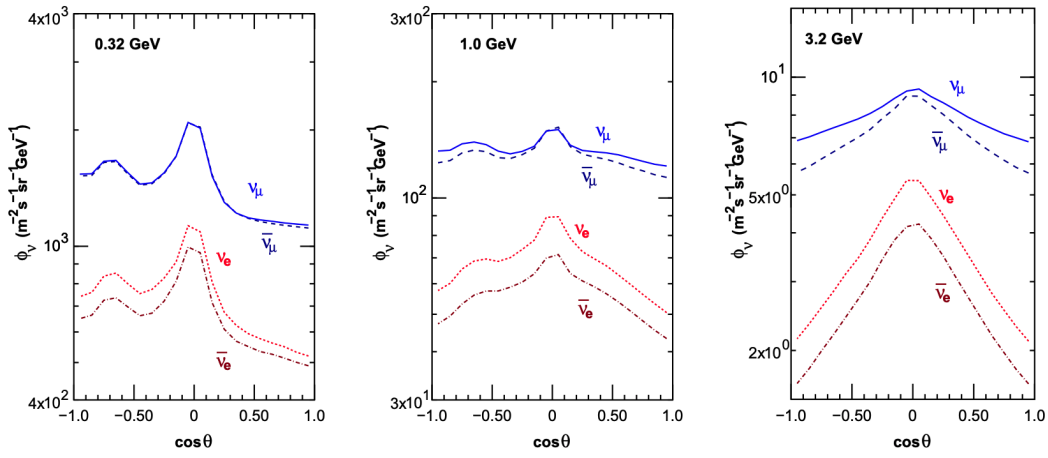
**Figure 2.4:** A diagram illustrating the definition of zenith angle as used in the Super Kamiokande experiment [47].

Figure 2.5 highlights the neutrino flux as a function of the zenith angle for different

slices of neutrino energy. For medium to high-energy neutrinos (and to a lesser degree

for low-energy neutrinos), the flux is approximately symmetric around  $\cos(\theta) = 0$ .

To the accuracy of this approximation, the systematic uncertainties associated with atmospheric flux for comparing upward-going and down-going neutrino cancels. This allows the down-going events, which are mostly insensitive to oscillation probabilities, to act as an unoscillated prediction (similar to a near detector in an accelerator neutrino experiment).



**Figure 2.5:** Prediction of  $\nu_e, \bar{\nu}_e, \nu_\mu, \bar{\nu}_\mu$  fluxes as a function of zenith angle as calculated by the HKKM model [45]. The left, middle and right panels represent three values of neutrino energy, 0.32GeV, 1.0GeV and 3.2GeV respectively. Predictions for other models including Bartol [42], Honda [43] and FLUKA [46] are given in [47].

Precursory hints of atmospheric neutrinos were observed in the mid-1960s searching for  $\nu_\mu + X \xrightarrow{(-)} X^* + \mu^\pm$  [48], although it was called an anomaly at the time of measurement. This was succeeded with the IMB-3 [49] and Kamiokande [50] experiments which measured the ratio of muon neutrinos compared to electron neutrinos  $R(\nu_\mu/\nu_e)$ . Both experiments were found to have a consistent deficit of muon neutrinos, with  $R(\nu_\mu/\nu_e) = 0.67 \pm 0.17$  and  $R(\nu_\mu/\nu_e) = 0.60^{+0.07}_{-0.06} \pm 0.05$ . Super-Kamiokande (SK) [47] extended this analysis by fitting oscillation parameters in  $P(\nu_\mu \rightarrow \nu_\tau)$  which found best fit parameters  $\sin^2(2\theta) > 0.92$  and  $1.5 \times 10^{-3} < \Delta m^2 < 3.4 \times 10^{-3}$ eV $^2$ .

Since then, atmospheric neutrino experiments have been making precision measurements of the  $\sin^2(\theta_{23})$  and  $\Delta m^2_{32}$  oscillation parameters. Atmospheric neutrino oscillation is dominated by  $P(\nu_\mu \rightarrow \nu_\tau)$ , where SK observed a  $4.6\sigma$  discovery of  $\nu_\tau$

<sup>351</sup> appearance [51]. Figure 2.6 illustrates the current estimates on the atmospheric mixing  
<sup>352</sup> parameters from a wide range of atmospheric and accelerator neutrino observatories.

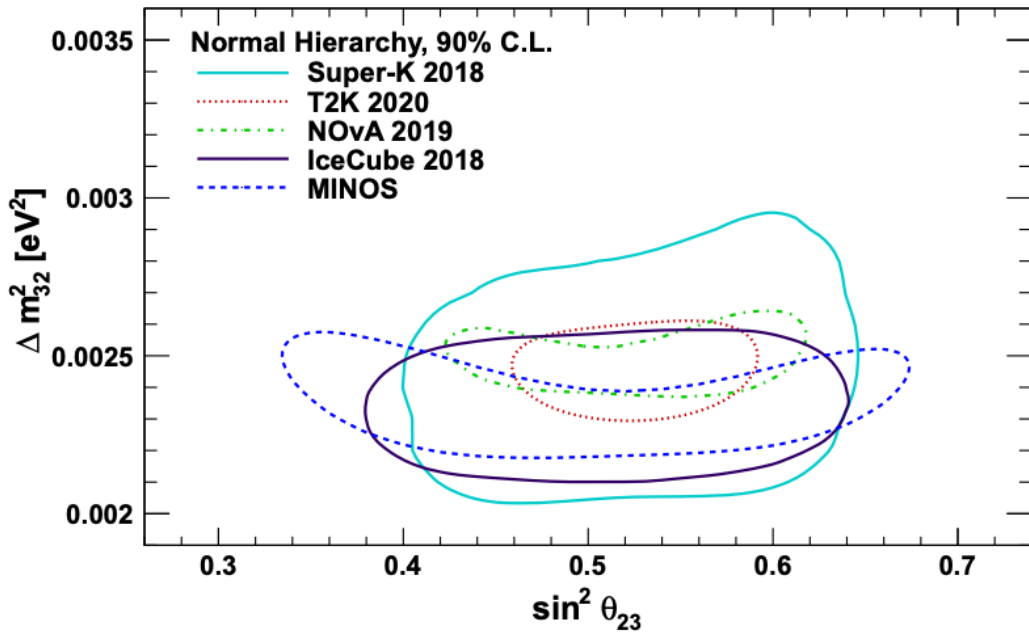


**Figure 2.6:** Constraints on the atmospheric oscillation parameters,  $\sin^2(\theta_{23})$  and  $\Delta m_{32}^2$ , from atmospheric and long baseline experiments: SK [52], T2K [53], NOvA [54], IceCube [55] and MINOS [56]. Figure taken from [57].

### <sup>353</sup> 2.3.3 Accelerator Neutrinos

<sup>354</sup> The concept of using a man-made “neutrino beam” was first realised in 1962 [58].  
<sup>355</sup> Since then, many experiments have followed which all use the same fundamental  
<sup>356</sup> concepts. Typically, a proton beam is aimed at a target producing charged mesons that  
<sup>357</sup> decay to neutrinos. The mesons can be sign-selected by the use of magnetic focusing  
<sup>358</sup> horns to generate a neutrino or antineutrino beam. Pions are the primary meson that  
<sup>359</sup> decay and depending on the orientation of the magnetic field, a muon (anti-)neutrino  
<sup>360</sup> beam is generated via  $\pi^+ \rightarrow \mu^+ + \nu_\mu$  or  $\pi^- \rightarrow \mu^- + \bar{\nu}_\mu$ . The decay of muons and  
<sup>361</sup> kaons does result in an irreducible intrinsic electron neutrino background. In T2K,  
<sup>362</sup> this background contamination is  $O(< 1\%)$  [59]. There is also an approximately  $\sim 5\%$

<sup>363</sup> “wrong-sign” neutrino background of  $\bar{\nu}_\mu$  generated via the same decays. As the beam is  
<sup>364</sup> generated by proton interactions (rather than anti-proton interactions), the wrong-sign  
<sup>365</sup> component in the antineutrino beam is larger when operating in neutrino mode.

<sup>366</sup> Tuning the proton energy in the beam and using beam focusing techniques allows  
<sup>367</sup> the neutrino energy to be set to a value that maximises the disappearance oscillation  
<sup>368</sup> probability in the  $L/E$  term in Equation 2.10. This means that accelerator experiments  
<sup>369</sup> are typically more sensitive to the mixing parameters as compared to a natural neutrino  
<sup>370</sup> source. However, the disadvantage compared to atmospheric neutrino experiments is  
<sup>371</sup> that the baseline has to be shorter due to the lower flux. Consequently, there is typically  
<sup>372</sup> less sensitivity to matter effects and the ordering of the neutrino mass eigenstates.

<sup>373</sup> A neutrino experiment measures

$$R(\vec{x}) = \Phi(E_\nu) \times \sigma(E_\nu) \times \epsilon(\vec{x}) \times P(\nu_\alpha \rightarrow \nu_\beta), \quad (2.15)$$

<sup>374</sup> where  $R(\vec{x})$  is the event rate of neutrinos at position  $\vec{x}$ ,  $\Phi(E_\nu)$  is the flux of neutrinos  
<sup>375</sup> with energy  $E_\nu$ ,  $\sigma(E_\nu)$  is the cross-section of the neutrino interaction and  $\epsilon(\vec{x})$  is the  
<sup>376</sup> efficiency and resolution of the detector. In order to leverage the most out of an  
<sup>377</sup> accelerator neutrino experiment, the flux and cross-section systematics need to be  
<sup>378</sup> constrained. This is typically done via the use of a “near detector”, situated at a baseline  
<sup>379</sup> of  $O(1)$ km. This detector observes the unoscillated neutrino flux and constrains the  
<sup>380</sup> parameters used within the flux and cross-section model.

<sup>381</sup> The first accelerator experiments to precisely measure oscillation parameters were  
<sup>382</sup> MINOS [60] and K2K [61]. These experiments confirmed the  $\nu_\mu$  disappearance seen in  
<sup>383</sup> atmospheric neutrino experiments by finding consistent parameter values for  $\sin^2(\theta_{23})$   
<sup>384</sup> and  $\Delta m_{23}^2$ . The current generation of accelerator neutrino experiments, T2K and NO $\nu$ A

385 extended this field by observing  $\bar{\nu}_\mu \rightarrow \bar{\nu}_e$  and lead the sensitivity to atmospheric mix-  
 386 ing parameters as seen in Figure 2.6 [62]. The two experiments differ in their peak  
 387 neutrino energy, baseline, and detection technique. The NO $\nu$ A experiment is situated  
 388 at a baseline of 810km from the NuMI beamline which delivers 2GeV neutrinos. The  
 389 T2K neutrino beam is peaked around 0.6GeV and propagates 295km. The NO $\nu$ A  
 390 experiment also uses functionally identical detectors (near and far) which allow the  
 391 approximate cancellation of detector systematics whereas T2K uses a plastic scintil-  
 392 lator technique at the near detector and a water Cherenkov far detector. The future  
 393 generation experiments DUNE [63] and Hyper-Kamiokande [64] will succeed these  
 394 experiments as the high-precision era of neutrino oscillation parameter measurements  
 395 develops.

396 Several anomalous results have been observed in the LSND [9] and MiniBooNE [10]  
 397 detectors which were designed with purposefully short baselines. Parts of the neu-  
 398 trino community attributed these results to oscillations induced by a fourth “sterile”  
 399 neutrino [65] but several searches in other experiments, MicroBooNE [66] and KAR-  
 400 MEN [67], found no hints of additional neutrino species. The solution to the anomalous  
 401 results is still being determined.

#### 402 2.3.4 Reactor Neutrinos

403 As illustrated in the first discovery of neutrinos (section 2.1), nuclear reactors are a very  
 404 useful man-made source of electron antineutrinos. For reactors that use low-enriched  
 405 uranium  $^{235}\text{U}$  as fuel, the antineutrino flux is dominated by the  $\beta$ -decay fission of  $^{235}\text{U}$ ,  
 406  $^{238}\text{U}$ ,  $^{239}\text{Pu}$  and  $^{241}\text{Pu}$  [68] as illustrated in Figure 2.7.

407 Due to their low energy, reactor electron antineutrinos predominantly interact  
 408 via the inverse  $\beta$ -decay (IBD) interaction. The typical signature contains two signals

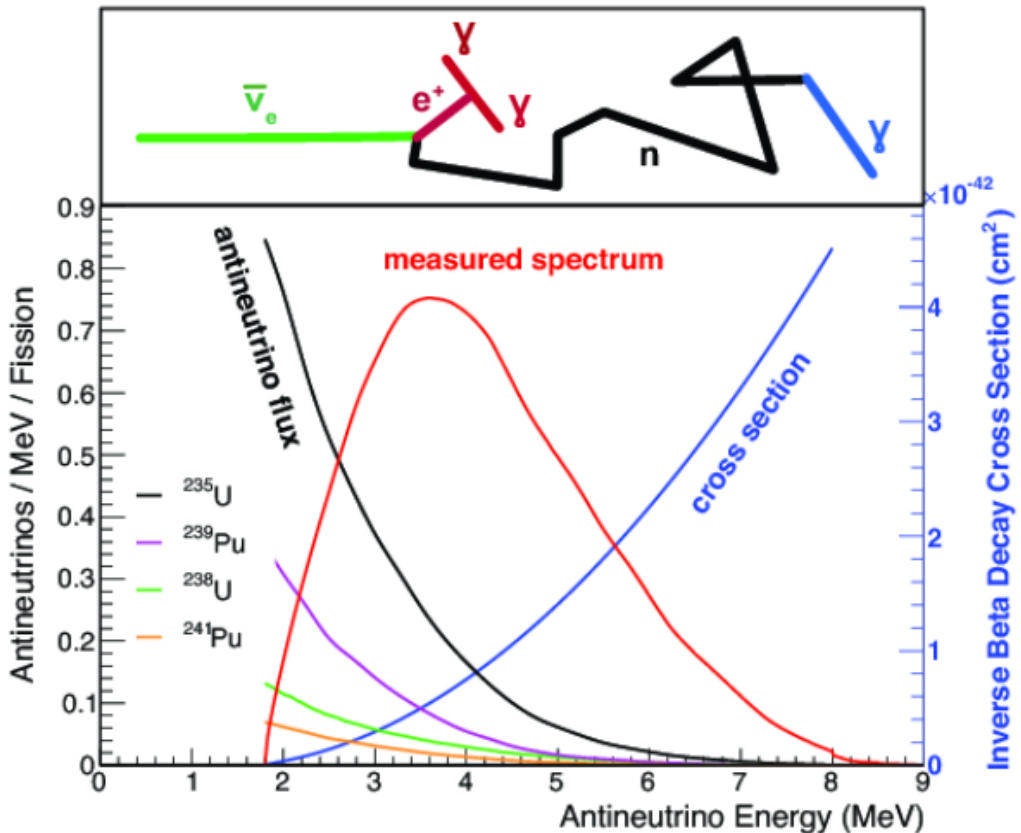


**Figure 2.7:** Reactor electron antineutrino fluxes for  $^{235}\text{U}$  (Black),  $^{238}\text{U}$  (Green),  $^{239}\text{Pu}$  (Purple), and  $^{241}\text{Pu}$  (Orange) isotopes. The inverse  $\beta$ -decay cross-section (Blue) and corresponding measurable neutrino spectrum (Red) are also given. Top panel: Schematic of Inverse  $\beta$ -decay interaction including the eventual capture of the emitted neutron. This capture emits a  $\gamma$ -ray which provides a second signal of the event. Taken from [69].

delayed by  $O(200)\mu\text{s}$ ; firstly the prompt photons from positron annihilation, and secondly the photons emitted ( $E_{tot}^\gamma = 2.2\text{MeV}$ ) from de-excitation after neutron capture on hydrogen. Searching for both signals improves the detector's ability to distinguish between background and signal events [70]. Recently, SK included gadolinium dopants into the ultra-pure water to increase the energy released from the photon cascade to  $\sim 8\text{MeV}$  and reduce the time of the delayed signal to  $\sim 28\mu\text{s}$ .

There are many short baseline experiments ( $L \sim O(1)\text{km}$ ) that have measured the  $\sin^2(\theta_{13})$  and  $\Delta m_{23}^2$  oscillation parameters. Daya Bay [71], RENO [72] and Double Chooz [73] have all provided precise measurements, with the first discovery of a

418 non-zero  $\theta_{13}$  made by Daya Bay and RENO (and complemented by T2K [73]). The  
419 constraints on  $\sin^2(\theta_{13})$  by the reactor experiments lead the field and are often used as  
420 external inputs to accelerator neutrino experiments to improve their sensitivity to  $\delta_{CP}$   
421 and mass hierarchy determination. JUNO-TAO [74], a small collaboration within the  
422 larger JUNO experiment, is a next-generation reactor experiment that aims to precisely  
423 measure the isotopic antineutrino yields from the different fission chains. Alongside  
424 this, it aims to explain the ‘5MeV excess’ [75–77] by conducting a search for sterile  
425 neutrinos with a mass scale of around 1eV.

426 Kamland [78] is the only experiment to have observed reactor neutrinos using a  
427 long baseline (flux weighted averaged baseline of  $L \sim 180\text{km}$ ) which allows it to have  
428 sensitivity to  $\Delta m_{12}^2$ . Combined with the SK solar neutrino experiment, the combined  
429 analysis puts the most stringent constraint on  $\Delta m_{12}^2$  [79].

## 430 2.4 Summary

431 Since observing the first evidence of neutrino oscillations in the late 1990’s, numerous  
432 measurements of the mixing parameters have been made. Many experiments use  
433 neutrinos as a tool for discovery of new physics (diffuse supernova background,  
434 neutrinoless double beta decay and others) so the PMNS parameters are summarised  
435 in the Particle Data Group (PDG) review tables. The analysis presented in this thesis  
436 focuses on the 2020 T2K oscillation analysis presented in [80] where the 2018 PDG  
437 constraints [81] were used. These constraints are outlined in Table 2.1.

438 The  $\sin^2(\theta_{13})$  measurement stems from the electron antineutrino disappearance,  
439  $P(\bar{\nu}_e \rightarrow \bar{\nu}_e)$ , and is take as the average best-fit from the combination of Daya Bay,  
440 Reno and Double Chooz. It is often used as a prior uncertainty within other neu-  
441 trino oscillation experiments, typically termed the reactor constraint. The  $\sin^2(\theta_{12})$

Parameter	2018 Constraint
$\sin^2(\theta_{12})$	$0.307 \pm 0.013$
$\Delta m_{21}^2$	$(7.53 \pm 0.18) \times 10^{-5} \text{ eV}^2$
$\sin^2(\theta_{13})$	$(2.12 \pm 0.08) \times 10^{-2}$
$\sin^2(\theta_{23})$ (I.H., Q1)	$0.421^{+0.033}_{-0.025}$
$\sin^2(\theta_{23})$ (I.H., Q2)	$0.592^{+0.023}_{-0.030}$
$\sin^2(\theta_{23})$ (N.H., Q1)	$0.417^{+0.025}_{-0.028}$
$\sin^2(\theta_{23})$ (N.H., Q2)	$0.597^{+0.024}_{-0.030}$
$\Delta m_{32}^2$ (I.H.)	$(-2.56 \pm 0.04) \times 10^{-3} \text{ eV}^2$
$\Delta m_{32}^2$ (N.H.)	$(2.51 \pm 0.05) \times 10^{-3} \text{ eV}^2$

**Table 2.1:** The 2018 Particle Data Group constraints of the oscillation parameters taken from [81]. The value of  $\Delta m_{23}^2$  is given for both normal hierarchy (N.H.) and inverted hierarchy (I.H.) and  $\sin^2(\theta_{23})$  is broken down by whether its value is below (Q1) or above (Q2) 0.5.

parameter is predominantly measured through electron neutrino disappearance,  $P(\nu_e \rightarrow \nu_{\mu,\tau})$ , in solar neutrino experiments. The long-baseline reactor neutrino experiment Kamland also has sensitivity to this parameter and is used in a joint fit to solar data from SNO and SK, using the reactor constraint. Measurements of  $\sin^2(\theta_{23})$  are made by long-baseline and atmospheric neutrino experiments. The PDG value is a joint fit of T2K, NOvA, MINOS and IceCube DeepCore experiments. The latest T2K-only measurement, provided at Neutrino2020 and is the basis of this thesis, is given as  $\sin^2(\theta_{23}) = 0.546^{+0.024}_{-0.046}$  [80]. The PDG constraint on  $\Delta m_{12}^2$  is provided by the KamLAND experiment using solar and geoneutrino data. This measurement utilised a  $\sin^2(\theta_{13})$  constraint from accelerator (T2K, MINOS) and reactor neutrino (Daya Bay, RENO, Double Chooz) experiments. Accelerator measurements make some of the most stringent constraints on  $\Delta m_{23}^2$  although atmospheric experiments have more sensitivity to the mass hierarchy determination. The PDG performs a joint fit of accelerator and atmospheric data, in both normal and inverted hierarchy separately. The latest T2K-only result is  $\Delta m_{32}^2 = 2.49^{+0.058}_{-0.082} \times 10^{-3} \text{ eV}^2$  favouring normal hierarchy [80]. The value of  $\delta_{CP}$  is largely undetermined. CP-conserving values of 0 and  $\pi$  were

458 rejected with  $\sim 2\sigma$  intervals, as published in Nature, although more recent analysis  
459 have reduced the rejection intervals to 90%. Since the 2018 PDG publication, there has  
460 been a new measurement of  $\sin^2(\theta_{13}) = (2.20 \pm 0.07) \times 10^{-2}$  [82], alongside updated  
461  $\Delta m_{23}^2$  and  $\sin^2(\theta_{23})$  measurements.

462 Throughout this thesis, several sample spectra predictions and contours are pre-  
463 sented which require oscillation parameters to be assumed. Table 2.2 defines two sets  
464 of oscillation parameters, with “Asimov A” set being close to the preferred values  
465 from a previous T2K-only fit [83] and “Asimov B” being CP-conserving and further  
466 from maximal  $\theta_{23}$  mixing.

Parameter	Asimov A	Asimov B
$\Delta m_{12}^2$	$7.53 \times 10^{-5} \text{ eV}^2$	
$\Delta m_{32}^2$	$2.509 \times 10^{-3} \text{ eV}^2$	
$\sin^2(\theta_{12})$	0.304	
$\sin^2(\theta_{13})$	0.0219	
$\sin^2(\theta_{23})$	0.528	0.45
$\delta_{CP}$	-1.601	0.0

**Table 2.2:** Reference values of the neutrino oscillation parameters for two different oscillation parameter sets.

467 **Chapter 3**

468 **T2K and SK Experiment Overview**

469 As the successor of the Kamiokande experiment, the Super-Kamiokande (SK) collabora-  
470 ration has been leading atmospheric neutrino oscillation analyses for over two decades.  
471 The detector has provided some of the strongest constraints on proton decay and the  
472 first precise measurements of the  $\Delta m_{23}^2$  and  $\sin^2(\theta_{23})$  neutrino oscillation parameters.  
473 The ability of the detector to low-energy neutrino events has been significantly im-  
474 proved with the recent gadolinium doping of the ultra-pure water target. The history,  
475 detection technique, and operation of the SK detector is described in section 3.1.

476 The Tokai-to-Kamioka (T2K) experiment was one of the first long-baseline ex-  
477 periments to use both neutrino and antineutrino beams to precisely measure the  
478 charge parity violation within the neutrino sector. With the SK detector observing  
479 the oscillated neutrino flux, the T2K experiment observed the first hints of a non-zero  
480  $\sin^2(\theta_{13})$  measurement and continues to lead the field with the constraints it provides  
481 on  $\sin^2(\theta_{13})$ ,  $\sin^2(\theta_{23})$ ,  $\Delta m_{23}^2$  and  $\delta_{CP}$ . The techniques which T2K uses in gener-  
482 ating its neutrino beam as well as the near-detector used to constrain the flux and  
483 cross-section parameters used in this analysis are documented in section 3.2.

484 **3.1 The Super-Kamiokande Experiment**

485 The SK experiment began taking data in 1996 [84] and has had many modifications  
486 throughout its lifespan. There have been seven defined periods of data taking as  
487 noted in Table 3.1. Data taking began in SK-I which ran for five years. Between the

488 SK-I and SK-II periods, a significant proportion of the PMTs were damaged during  
 489 maintenance. Those that survived were equally distributed throughout the detector  
 490 in the SK-II era, which resulted in a reduced photo-coverage. From SK-III onwards,  
 491 repairs to the detector meant the full suite of PMTs was operational. Before the  
 492 start of SK-IV, the data acquisition and electronic systems were upgraded. Between  
 493 SK-IV and SK-V, a significant effort was placed into tank open maintenance and  
 494 repair/replacement of defective PMTs, a task for which the author of this thesis was  
 495 required. Consequently, the detector conditions were significantly different between  
 496 the two operational periods. SK-VI saw the start of the 0.01% gadolinium doped water.  
 497 SK-VII, which started during the writing of this thesis, has increased the gadolinium  
 498 concentration to 0.03% for continued operation [85].

Period	Start Date	End Date	Live-time (days)
I	April 1996	July 2001	1489.19
II	October 2002	October 2005	798.59
III	July 2006	September 2008	518.08
IV	September 2008	May 2018	3244.4
V	January 2019	July 2020	461.02
VI	July 2020	May 2022	583.3
VII	May 2022	Ongoing	N/A

**Table 3.1:** The various SK periods and respective live-time. The SK-VI live-time is calculated until 1<sup>st</sup> April 2022. SK-VII started during the writing of this thesis.

### 499 3.1.1 The SK Detector

500 The basic structure of the Super-Kamiokande (SK) detector is a cylindrical tank with a  
 501 diameter 39.3m and height 41.1m filled with ultrapure water [86]. A diagram of the  
 502 significant components of the SK detector is given in Figure 3.1. The SK detector is  
 503 situated in the Kamioka mine in Gifu, Japan. The mine is underground with roughly  
 504 1km rock overburden (2.7km water equivalent overburden) [87]. At this depth, the

505 rate of cosmic ray muons is significantly decreased to a value of  $\sim 2\text{Hz}$ . The top of  
 506 the tank is covered with stainless steel which is designed as a working platform for  
 507 maintenance, calibration, and location for high voltage and data acquisition electronics.

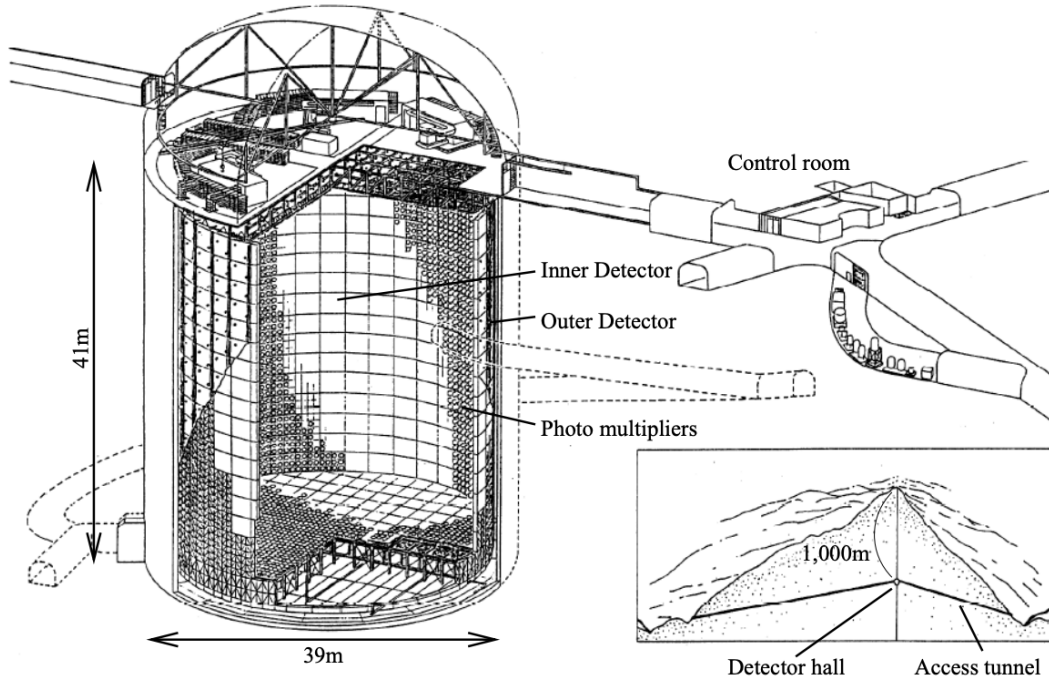


**Figure 3.1:** A schematic diagram of the Super-Kamiokande Detector. Taken from [88].

508 A smaller cylindrical structure (36.2m diameter, 33.8m height) is situated inside the  
 509 tank, with an approximate 2m gap between this structure and the outer tank wall. The  
 510 purpose of this structure is to support the photomultiplier tubes (PMTs). The volume  
 511 inside and outside the support structure is referred to as the inner detector (ID) and  
 512 outer detector (OD), respectively. In the SK-IV era, the ID and OD are instrumented  
 513 by 11,129 50cm and 1,885 20cm PMTs respectively [86]. The ID contains a 32kton  
 514 mass of water. Many analyses performed at SK use a “fiducial volume” defined by the  
 515 volume of water inside the ID excluding some distance to the ID wall. This reduces the  
 516 volume of the detector which is sensitive to neutrino events but reduces radioactive  
 517 backgrounds and allows for better reconstruction performance. The nominal fiducial

518 volume is defined as the area contained inside 2m from the ID wall for a total of  
519 22.5kton water [89].

520 The two regions of the detector (ID and OD) are optically separated with opaque  
521 black plastic. The purpose of this is to determine whether a track entered or exited  
522 the ID. This allows cosmic ray muons and partially contained events to be tagged and  
523 separated from neutrino events entirely contained within the ID. This black plastic is  
524 also used to cover the area between the ID PMTs to reduce photon reflection from the  
525 ID walls. Opposite to this, the OD is lined with a reflective material to allow photons to  
526 reflect around inside the OD until collected by one of the PMTs. Furthermore, each OD  
527 PMT is backed with  $50 \times 50\text{cm}$  plates of wavelength shifting acrylic which increases  
528 the efficiency of light collection [87].

529 In the SK-IV data-taking period, the photocathode coverage of the detector, or the  
530 fraction of the ID wall instrumented with PMTs, is  $\sim 40\%$  [87]. The PMTs have a  
531 quantum efficiency (the ratio of detected electrons to incident photons) of  $\sim 21\%$  for  
532 photons with wavelengths of  $360\text{nm} < \lambda < 390\text{nm}$ . The proportion of photoelectrons  
533 that produce a signal in the dynode of a PMT, termed the collection efficiency, is  
534  $> 70\%$  [87]. The PMTs used within SK are most sensitive to photons with wavelength  
535  $300\text{nm} \leq \lambda \leq 600\text{nm}$  [87]. One disadvantage of using PMTs as the detection media  
536 is that the Earth's geomagnetic field can modify its response. Therefore, a set of  
537 compensation coils is built around the inner surface of the detector to mitigate this  
538 effect [90].

539 As mentioned, the SK detector is filled with ultrapure water, which in a perfect  
540 world would contain no impurities. However, bacteria and organic compounds can  
541 significantly degrade the water quality. This decreases the attenuation length, which  
542 reduces the total number of photons that hit a PMT. To combat this, a sophisticated  
543 water treatment system has been developed [87, 91]. UV lights, mechanical filters,

544 and membrane degasifiers are used to reduce the bacteria, suspended particulates,  
545 and radioactive materials from the water. The flow of water within the tank is also  
546 critical as it can remove stagnant bacterial growth or build-up of dust on the surfaces  
547 within the tank. Gravity drifts impurities in the water towards the bottom of the  
548 tank which, if left uncontrolled, can create asymmetric water conditions between  
549 the top and bottom of the tank. Typically, the water entering the tank is cooled  
550 below the ambient temperature of the tank to control convection and inhibit bacteria  
551 growth. Furthermore, the rate of dark noise hits within PMTs is sensitive to the PMT  
552 temperature [92] so controlling the temperature gradients within the tank is beneficial  
553 for stable measurements.

554 SK-VI is the first phase of the SK experiment to use gadolinium dopants within  
555 the ultrapure water [85]. As such, the SK water system had to be replaced to avoid  
556 removing the gadolinium concentrate from the ultrapure water [93]. For an inverse  
557  $\beta$ -decay (IBD) interaction in a water target, the emitted neutron is thermally captured  
558 on hydrogen. This process releases 2.2MeV  $\gamma$  rays which are difficult to detect as  
559 the resulting Compton scattered electrons are very close to the Cherenkov threshold,  
560 limiting the number of photons produced. Thermal capture of neutrons on gadolin-  
561 ium generates  $\gamma$  rays with higher energy (8MeV [70]) meaning they are more easily  
562 detected. SK-VI has 0.01% Gd loading (0.02% gadolinium sulphate by mass) which  
563 causes  $\approx$  50% of neutrons emitted by IBD to be captured on gadolinium [94, 95].  
564 Whilst predominantly useful for low energy analyses, Gd loading allows better  $\nu/\bar{\nu}$   
565 separation for atmospheric neutrino event selections [96]. Efforts are currently in place  
566 to increase the gadolinium concentrate to 0.03% for  $\approx$  75% neutron capture efficiency  
567 on gadolinium [97]. The final stage of loading targets 0.1% concentrate.

### **568 3.1.2 Calibration**

569 The calibration of the SK detector is documented in [86] and summarised below. The  
570 analysis presented within this thesis is dependent upon ‘high energy events’ (Charged  
571 particles with  $O(> 100)\text{MeV}$  momenta). These are events that are expected to generate  
572 a larger number of photons such that each PMT will be hit with multiple photons.  
573 The reconstruction of these events depends upon the charge deposited within each  
574 PMT and the timing response of each individual PMT. Therefore, the most relevant  
575 calibration techniques to this thesis are outlined.

576 Before installation, 420 PMTs were calibrated to have identical charge responses  
577 and then distributed throughout the tank in a cross-shape pattern (As illustrated by  
578 Figure 3.2). These are used as a standardised measure for the rest of the PMTs installed  
579 at similar geometric positions within SK to be calibrated against. To perform this  
580 calibration, a xenon lamp is located at the center of the SK tank which flashes uniform  
581 light at 1Hz. This allows for geometrical effects, water quality variation, and timing  
582 effects to be measured in-situ throughout normal data-taking periods.

583 When specifically performing calibration of the detector (in out-of-data taking  
584 mode), the water in the tank was circulated to avoid top/bottom asymmetric water  
585 quality. Any non-uniformity within the tank significantly affects the PMT hit proba-  
586 bility through scattering or absorption. This becomes a dominant effect for the very  
587 low-intensity light sources discussed later which are designed such that only one  
588 photon is incident upon a given PMT.

589 The “gain” of a PMT is defined as the ratio of the total charge of the signal produced  
590 compared to the charge of photoelectrons emitted by the photocathodes within the  
591 PMT. To calibrate the signal of each PMT, the “relative” and “absolute” gain values are

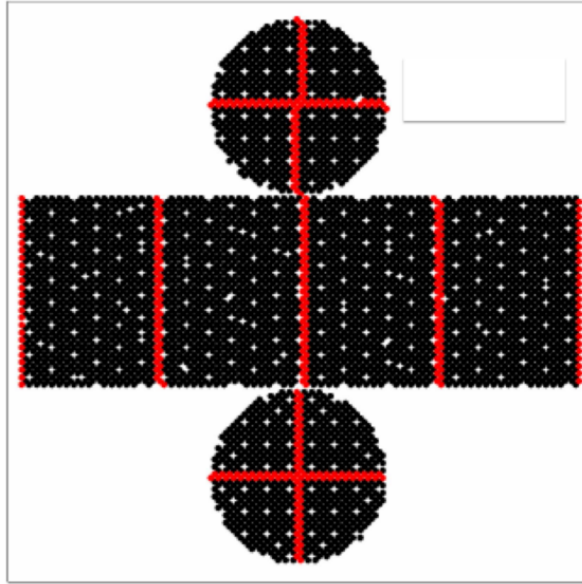


**Figure 3.2:** The location of “standard PMTs” (red) inside the SK detector. Taken from [86].

592 measured. The relative gain is the variation of gain among each of the PMTs whereas  
 593 the absolute gain is the average gain of all PMTs.

594 The relative gain is calibrated as follows. A laser is used to generate two measure-  
 595 ments: a high-intensity flash that illuminates every PMT with a sufficient number of  
 596 photons, and a low-intensity flash in which only a small number of PMTs collect light.  
 597 The first measurement creates an average charge,  $Q_{obs}(i)$  on PMT  $i$ , whereas the second  
 598 measurement ensures that each hit PMT only generates a single photoelectron. For the  
 599 low-intensity measurement, the number of times each PMT records a charge larger  
 600 than 1/4 photoelectrons,  $N_{obs}(i)$ , is counted. The values measured can be expressed as

$$\begin{aligned} Q_{obs}(i) &\propto I_H \times f(i) \times \epsilon(i) \times G(i), \\ N_{obs}(i) &\propto I_L \times f(i) \times \epsilon(i), \end{aligned} \tag{3.1}$$

601 Where  $I_H$  and  $I_L$  is the intensity of the high and low flashes,  $f(i)$  is the acceptance  
 602 efficiency of the  $i^{\text{th}}$  PMT,  $\epsilon(i)$  is the product of the quantum and collection efficiency

of the  $i^{\text{th}}$  PMT and  $G(i)$  is the gain of the  $i^{\text{th}}$  PMT. The relative gain for each PMT can be determined by taking the ratio of these quantities.

The absolute gain calibration is performed by observing fixed energy  $\gamma$ -rays of  $E_{\gamma} \sim 9\text{MeV}$  emitted isotropically from neutron capture on a NiCf source situated at the center of the detector. This generates a photon yield of about 0.004 photoelectrons/PMT/event, meaning that  $> 99\%$  of PMT signals are generated from single photoelectrons. A charge distribution is generated by performing this calibration over all PMTs, and the average value of this distribution is taken to be the absolute gain value.

As mentioned in subsection 3.1.1, the average quantum and collection efficiency for the SK detector is  $\sim 21\%$  and  $> 70\%$  respectively. However, these values do differ between each PMT and need to be calibrated accordingly. Consequently, the NiCf source is also used to calibrate the “quantum  $\times$  collection” efficiency (denoted “QE”) value of each PMT. The NiCf low-intensity source is used as the PMT hit probability is proportional to the QE ( $N_{\text{obs}}(i) \propto \epsilon(i)$  in Equation 3.1). A Monte Carlo prediction which includes photon absorption, scattering, and reflection is made to estimate the number of photons incident on each PMT and the ratio of the number of predicted to observed hits is calculated. The difference is attributed to the QE efficiency of that PMT. This technique is extended to calculate the relative QE efficiency by normalizing the average of all PMTs which removes the dependence on the light intensity.

Due to differing cable lengths and readout electronics, the timing response between a photon hitting the PMT and the signal being captured by the data acquisition can be different between each PMT. Due to threshold triggers (Described in subsection 3.1.3), the time at which a pulse reaches a threshold is dependent upon the size of the pulse. This is known as the ‘time-walk’ effect and also needs to be accounted for in each PMT. To calibrate the timing response, a pulse of light with width 0.2ns is emitted into the

629 detector through a diffuser. Two-dimensional distributions of time and pulse height  
630 (or charge) are made for each PMT and are used to calibrate the timing response. This  
631 is performed in-situ during data taking with the light source pulsing at 0.03Hz.

632 The top/bottom water quality asymmetry is measured using the NiCf calibration  
633 data and cross-referencing these results to the “standard PMTs”. The water attenuation  
634 length is continuously measured by the rate of vertically-downgoing cosmic-ray  
635 muons which enter via the top of the tank.

636 Dark noise is the phenomenon where a PMT registers a pulse that is consistent  
637 with a single photoelectron emitted from photon detection despite the PMT being in  
638 complete darkness. This is predominately caused by two processes. Firstly there is  
639 intrinsic dark noise which is where photoelectrons gain enough thermal energy to be  
640 emitted from the photocathode, and secondly, the radioactive decay of contaminants  
641 inside the structure of the PMT. Typical dark noise rate for PMTs used within SK are  
642  $O(3)$ kHz [87]. This is lower than the expected number of photons generated for a ‘high  
643 energy event’ (As described in subsection 3.1.4) but instability in this value can cause  
644 biases in reconstruction. Dark noise is related to the gain of a PMT and is calibrated  
645 using hits inside a time window recorded before an event trigger [98].

### 646 3.1.3 Data Acquisition and Triggering

647 The analysis presented in this thesis only uses the SK-IV period of the SK experiment  
648 so this subsection focuses on the relevant points of the data acquisition and triggering  
649 systems to that SK period. The earlier data acquisition and triggering systems are  
650 documented in [99, 100].

651 Before the SK-IV period started, the existing front-end electronics were replaced  
652 with “QTC-Based Electrons with Ethernet, QBEE” systems [101]. When the QBEE

observes a signal above a 1/4 photoelectron threshold, the charge-to-time (QTC) converter generates a rectangular pulse. The start of the rectangular pulse indicates the time at which the analog photoelectron signal was received and the width of the pulse indicates the total charge integrated throughout the signal. This is then digitized by time-to-digital converters and sent to the “front-end” PCs. The digitized signal from every QBEE is then chronologically ordered and sent to the “merger” PCs. It is the merger PCs that apply the software trigger. Any triggered events are passed to the “organizer” PC. This sorts the data stream of multiple merger PCs into chronologically ordered events which are then saved to disk. The schematic of data flow from PMTs to disk is illustrated in Figure 3.3.

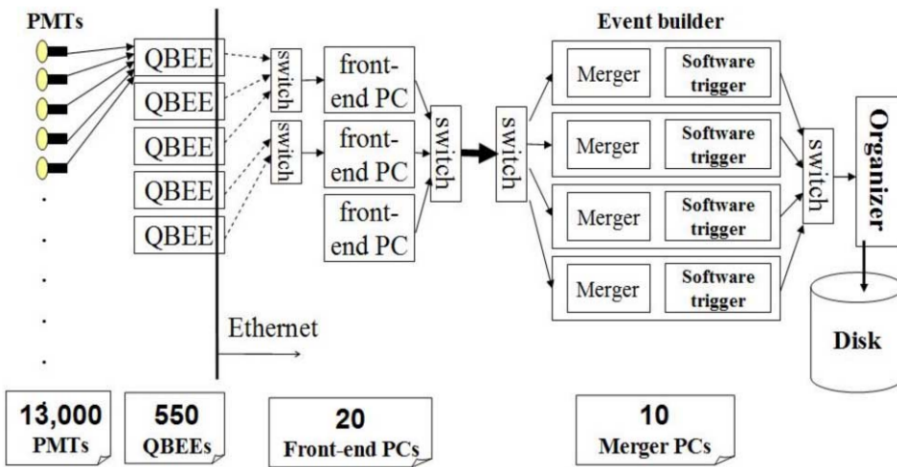


**Figure 3.3:** Schematic view of the data flow through the data acquisition and online system. Taken from [102].

The software trigger (described in [103]) operates by determining the number of PMT hits within a 200ns sliding window,  $N_{200}$ . This window coincides with the maximum time that a Cherenkov photon would take to traverse the length of the SK tank [100]. For lower energy events that generate fewer photons, this technique is useful for eliminating background processes like dark noise and radioactive decay which would be expected to separate in time. When the value of  $N_{200}$  exceeds some threshold, a software trigger is issued. There are several trigger thresholds used within

the SK-IV period which are detailed in Table 3.2. If one of these thresholds is met, the PMT hits within an extended time window are also read out and saved to disk. In the special case of an event that exceeds the SHE trigger but does not exceed the OD trigger, the AFT trigger looks for delayed coincidences of 2.2MeV gamma rays emitted from neutron capture in a  $535\mu\text{s}$  window after the SHE trigger. A similar but more complex “Wideband Intelligent Trigger (WIT)” has been deployed and is described in [104].

Trigger	Acronym	Condition	Extended time window ( $\mu\text{s}$ )
Super Low Energy	SLE	>34/31 hits	1.3
Low Energy	LE	>47 hits	40
High Energy	HE	>50 hits	40
Super High Energy	SHE	>70/58 hits	40
Outer Detector	OD	>22 hits in OD	N/A

**Table 3.2:** The trigger thresholds and extended time windows saved around an event which were utilised throughout the SK-IV period. The exact thresholds can change and the values listed here represent the thresholds at the start and end of the SK-IV period.

### 3.1.4 Cherenkov Radiation

Cherenkov light is emitted from any highly energetic charged particle traveling with relativistic velocity,  $\beta$ , greater than the local speed of light in a medium [105]. Cherenkov light is formed at the surface of a cone with characteristic pitch angle,

$$\cos(\theta) = \frac{1}{\beta n}. \quad (3.2)$$

where  $n$  is the refractive index of the medium. Consequently, the Cherenkov momentum threshold,  $P_{thres}$ , is dependent upon the mass,  $m$ , of the charged particle moving through the medium,

$$P_{thres} = \frac{m}{\sqrt{n^2 - 1}} \quad (3.3)$$

For water, where  $n = 1.33$ , the Cherenkov threshold momentum and energy for various particles are given in Table 3.3. In contrast,  $\gamma$ -rays are detected indirectly via the combination of photons generated by Compton scattering and pair production. The threshold for detection in the SK detector is typically higher than the threshold for photon production. This is due to the fact that the attenuation of photons in the water means that typically  $\sim 75\%$  of Cherenkov photons reach the ID PMTs. Then the collection and quantum efficiencies described in subsection 3.1.1 result in the number of detected photons being lower than the number of photons which reach the PMTs.

Particle	Threshold Momentum (MeV)	Threshold Energy (MeV)
Electron	0.5828	0.7751
Muon	120.5	160.3
Pion	159.2	211.7
Proton	1070.0	1423.1

**Table 3.3:** The threshold momentum and energy for a particle to generate Cherenkov light in ultrapure water, as calculated in Equation 3.2 in ultrapure water which has refractive index  $n = 1.33$ .

The Frank-Tamm equation [106] describes the relationship between the number of Cherenkov photons generated per unit length,  $dN/dx$ , the wavelength of the photons generated,  $\lambda$ , and the relativistic velocity of the charged particle,

$$\frac{d^2N}{dxd\lambda} = 2\pi\alpha \left(1 - \frac{1}{n^2\beta^2}\right) \frac{1}{\lambda^2}. \quad (3.4)$$

where  $\alpha$  is the fine structure constant. For a 100MeV momentum electron, approximately 330 photons will be produced per centimeter in the  $300\text{nm} \leq \lambda \leq 700\text{nm}$  region which the ID PMTs are most sensitive to [87].

## 3.2 The Tokai to Kamioka Experiment

The Tokai to Kamioka (T2K) experiment is a long-baseline neutrino oscillation experiment located in Japan. Proposed in the early 2000s [107, 108] to replace K2K [109], T2K was designed to observe electron neutrino appearance whilst precisely measuring the oscillation parameters associated with muon neutrino disappearance [110]. The experiment consists of a neutrino beam generated at the Japan Proton Accelerator Research Complex (J-PARC), a suite of near detectors situated 280m from the beam target, and the Super Kamiokande far detector positioned at a 295km baseline. The cross-section view of the T2K experiment is drawn in Figure 3.4.

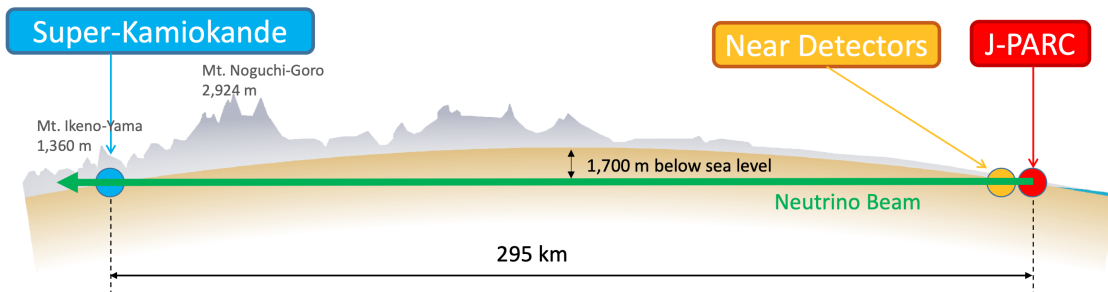


**Figure 3.4:** The cross-section view of the Tokai to Kamioka experiment illustrating the beam generation facility at J-PARC, the near detector situated at a baseline of 280m and the Super Kamiokande far detector situated 295km from the beam target.

The T2K collaboration makes world-leading measurements of the  $\sin^2(\theta_{23})$ ,  $\Delta m_{23}^2$ , and  $\delta_{CP}$  oscillation parameters. Improvements in the precision and accuracy of parameter estimates are still being made by including new data samples and developing the models which describe the neutrino interactions and detector responses [111]. Electron neutrino appearance was first observed at T2K in 2014 [112] with  $7.3\sigma$  significance.

The near detectors provide constraints on the beam flux and cross-section model parameters used within the oscillation analysis by observing the unoscillated neutrino beam. There are a host of detectors situated in the near detector hall (As illustrated in Figure 3.5): ND280 (subsection 3.2.2), INGRID (subsection 3.2.3), NINJA [113], WAGASCI [114], and Baby-MIND [115]. The latter three are not currently used within the oscillation analysis presented within this thesis.

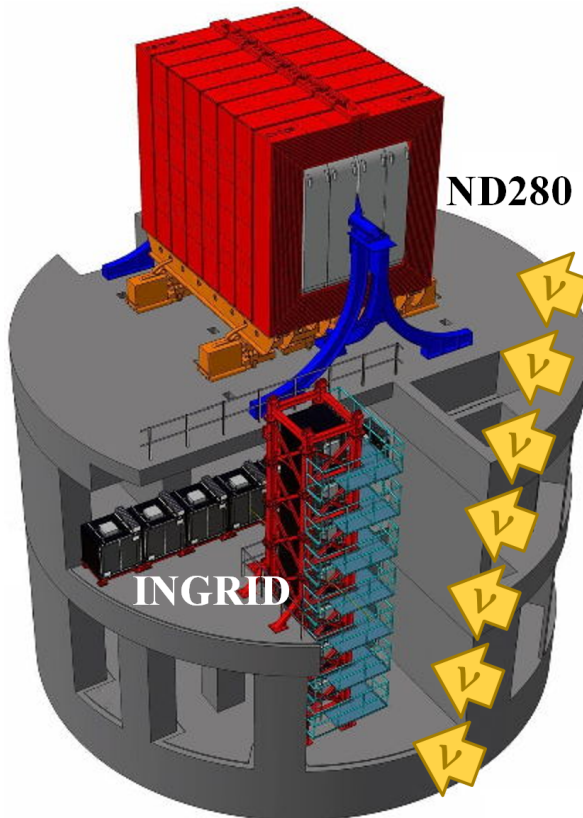


**Figure 3.5:** The near detector suite for the T2K experiment showing the ND280 and INGRID detectors. The distance between the detectors and the beam target is 280m.

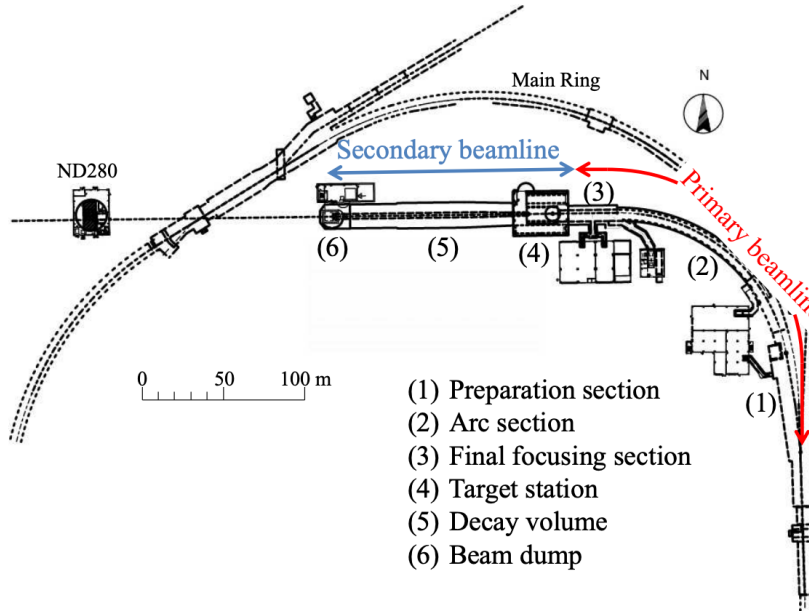
Whilst this thesis presents the ND280 in terms of its purpose for the oscillation analysis, the detector can also make many cross-section measurements at neutrino energies of  $O(1)$ GeV for the different targets within the detector [116, 117]. These measurements are of equal importance as they can lead the way in determining the model parameters used in the interaction models for the future high-precision era of neutrino physics.

DB: Discuss BANFF, PTheta, MaCh3 and covariance

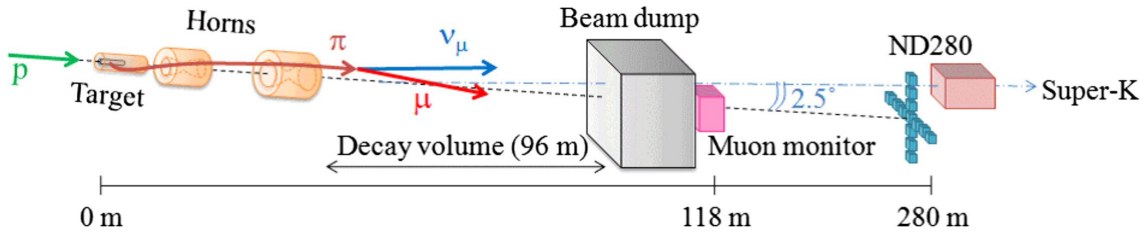
### 3.2.1 The Neutrino Beam

The neutrino beam used within the T2K experiment is described in [59, 118] and summarised below. The accelerating facility at J-PARC is composed of two sections; the primary and secondary beamlines. Figure 3.6 illustrates a schematic of the beamline, focusing mostly on the components of the secondary beamline. The primary beamline has three accelerators that progressively accelerate protons; a linear accelerator, a rapid-cycling synchrotron, and the main-ring (MR) synchrotron. Once fully accelerated by the MR, the protons have a kinetic energy of 30GeV. Eight bunches of these protons, separated by 500ns, are extracted per “spill” from the MR and directed towards a graphite target (a rod of length 91.4cm and diameter 2.6cm). Spills are extracted at 0.5Hz with  $\sim 3 \times 10^{14}$  protons contained per spill.

The secondary beamline consists of three main components: the target station, the decay volume, and the beam dump. The target station is comprised of the target, beam monitors, and three magnetic focusing horns. The proton beam interacts with the graphite target to form a secondary beam of mostly pions and kaons. The secondary beam travels through a 96m long decay volume, generating neutrinos through the following decays [59],



(a) Primary and secondary beamline



(b) Secondary beamline

**Figure 3.6:** Top panel: Bird's eye view of the most relevant part of primary and secondary beamline used within the T2K experiment. The primary beamline is the main-ring proton synchrotron, kicker magnet, and graphite target. The secondary beamline consists of the three focusing horns, decay volume, and beam dump. Figure taken from [118]. Bottom panel: The side-view of the secondary beamline including the focusing horns, beam dump and neutrino detectors. Figure taken from [119].

$$\begin{array}{ll}
 \pi^+ \rightarrow \mu^+ + \nu_\mu & \pi^- \rightarrow \mu^- + \bar{\nu}_\mu \\
 K^+ \rightarrow \mu^+ + \nu_\mu & K^- \rightarrow \mu^- + \bar{\nu}_\mu \\
 \rightarrow \pi^0 + e^+ + \nu_e & \rightarrow \pi^0 + e^- + \bar{\nu}_e \\
 \rightarrow \pi^0 + \mu^+ + \nu_\mu & \rightarrow \pi^0 + \mu^- + \bar{\nu}_\mu \\
 K_L^0 \rightarrow \pi^- + e^+ + \nu_e & K_L^0 \rightarrow \pi^+ + e^- + \bar{\nu}_e \\
 \rightarrow \pi^- + \mu^+ + \nu_\mu & \rightarrow \pi^+ + \mu^- + \bar{\nu}_\mu \\
 \mu^+ \rightarrow e^+ + \bar{\nu}_\mu + \nu_e & \mu^- \rightarrow e^- + \nu_\mu + \bar{\nu}_e
 \end{array}$$

The electrically charged component of the secondary beam is focused towards the far detector by the three magnetic horns. These horns direct charged particles of a particular polarity towards SK whilst defocusing the oppositely charged particles. This allows a mostly neutrino or mostly antineutrino beam to be used within the experiment, denoted as “forward horn current (FHC)” or “reverse horn current (RHC)” respectively.

Figure 3.7 illustrates the different contributions to the FHC and RHC neutrino flux.

The low energy flux is dominated by the decay of pions whereas kaon decay becomes the dominant source of neutrinos for  $E_\nu > 3\text{GeV}$ . The “wrong-sign” component, which is the  $\bar{\nu}_\mu$  background in a  $\nu_\mu$  beam, and the intrinsic irreducible  $\nu_e$  background, are predominantly due to muon decay for  $E_\nu < 2\text{GeV}$ . As the antineutrino production cross-section is smaller than the neutrino cross-section, the wrong-sign component is more dominant in the RHC beam as compared to that in the FHC beam.

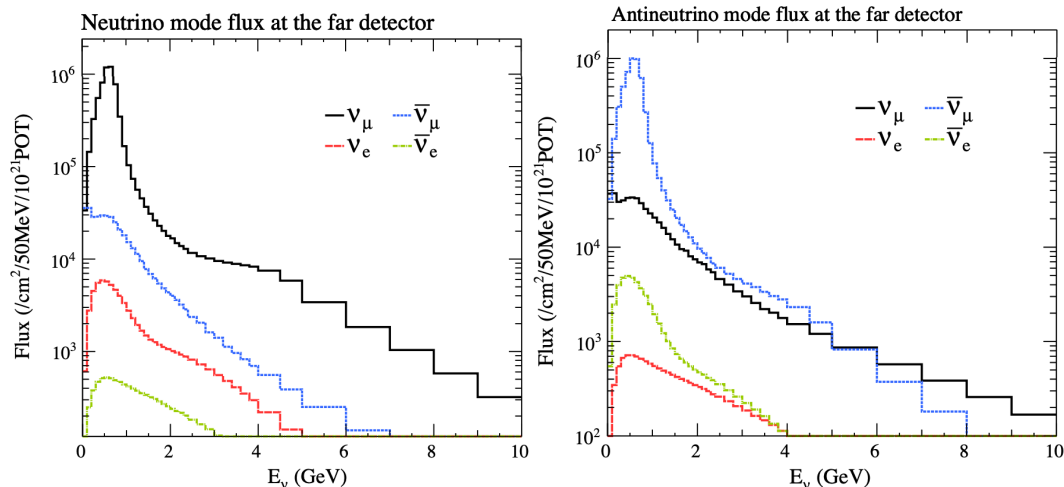


**Figure 3.7:** The Monte Carlo prediction of the energy spectrum for each flavour of neutrino ( $\nu_e$ ,  $\bar{\nu}_e$ ,  $\nu_\mu$  and  $\bar{\nu}_\mu$ ) in the neutrino dominated beam FHC mode (Left) and antineutrino dominated beam RHC mode (Right) expected at SK. Taken from [120].

The beam dump, situated at the end of the decay volume, stops all charged particles other than highly energetic muons ( $p_\mu > 5\text{GeV}$ ). The MuMon detector monitors the

<sup>758</sup> penetrating muons to determine the beam direction and intensity which is used to  
<sup>759</sup> constrain some of the beam flux systematics within the analysis [119, 121].

<sup>760</sup> The T2K experiment uses an off-axis beam to narrow the neutrino energy distribution.  
<sup>761</sup> This was the first implementation of this technique in a long-baseline neutrino  
<sup>762</sup> oscillation experiment after its original proposal [122]. Pion decay,  $\pi \rightarrow \mu + \nu_\mu$ , is a  
<sup>763</sup> two-body decay. Consequently, the neutrino energy,  $E_\nu$ , can be determined based on  
<sup>764</sup> the pion energy,  $E_\pi$ , and the angle at which the neutrino is emitted,  $\theta$ ,

$$E_\nu = \frac{m_\pi^2 - m_\mu^2}{2(E_\pi - p_\pi \cos(\theta))}, \quad (3.5)$$

<sup>765</sup> where  $m_\pi$  and  $m_\mu$  are the mass of the pion and muon respectively. For a fixed  
<sup>766</sup> energy pion, the neutrino energy distribution is dependent upon the angle at which the  
<sup>767</sup> neutrinos are observed from the initial pion beam direction. For the 295km baseline at  
<sup>768</sup> T2K,  $E_\nu = 0.6\text{GeV}$  maximises the electron neutrino appearance probability,  $P(\nu_\mu \rightarrow \nu_e)$ ,  
<sup>769</sup> whilst minimising the muon disappearance probability,  $P(\nu_\mu \rightarrow \nu_\mu)$ . Figure 3.8  
<sup>770</sup> illustrates the neutrino energy distribution for a range of off-axis angles, as well as the  
<sup>771</sup> oscillation probabilities most relevant to T2K.

### <sup>772</sup> 3.2.2 The Near Detector at 280m

<sup>773</sup> Whilst all the near detectors are situated in the same “pit” located at 280m from the  
<sup>774</sup> beamline, the “ND280” detector is the off-axis detector which is situated at the same  
<sup>775</sup> off-axis angle as the Super-Kamiokande far detector. It has two primary functions;  
<sup>776</sup> firstly it measures the neutrino flux and secondly it counts the event rates of different  
<sup>777</sup> types of neutrino interactions. Both of these constrain the flux and cross-section

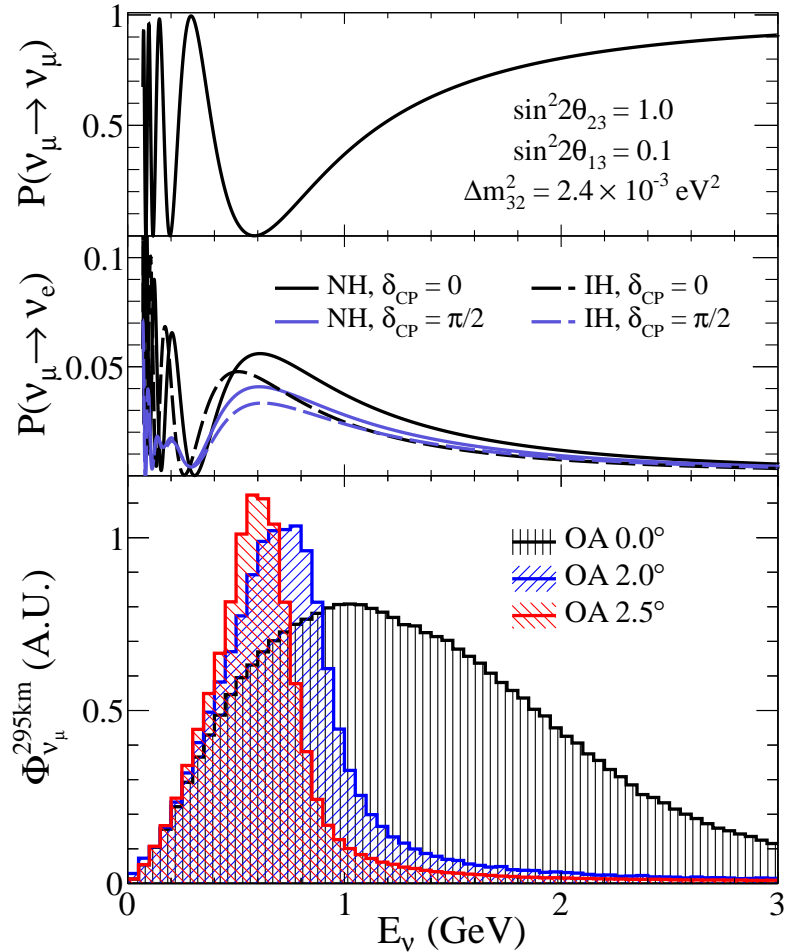


**Figure 3.8:** Top panel: T2K muon neutrino disappearance probability as a function of neutrino energy. Middle panel: T2K electron neutrino appearance probability as a function of neutrino energy. Bottom panel: The neutrino flux distribution for three different off-axis angles (Arbitrary units) as a function of neutrino energy.

systematics invoked within the model for a more accurate prediction of the expected event rate at the far detector.

As illustrated in Figure 3.9, the ND280 detector consists of several sub-detectors. The most important part of the detector for this analysis is the tracker region. This is comprised of two time projection chambers (TPCs) sandwiched between three fine grain detectors (FGDs). The FGDs contain both hydrocarbon plastics and water targets for neutrino interactions and provide track reconstruction near the interaction vertex. The emitted charged particles can then propagate into the TPCs which provide particle identification and momentum reconstruction. The FGDs and TPCs are

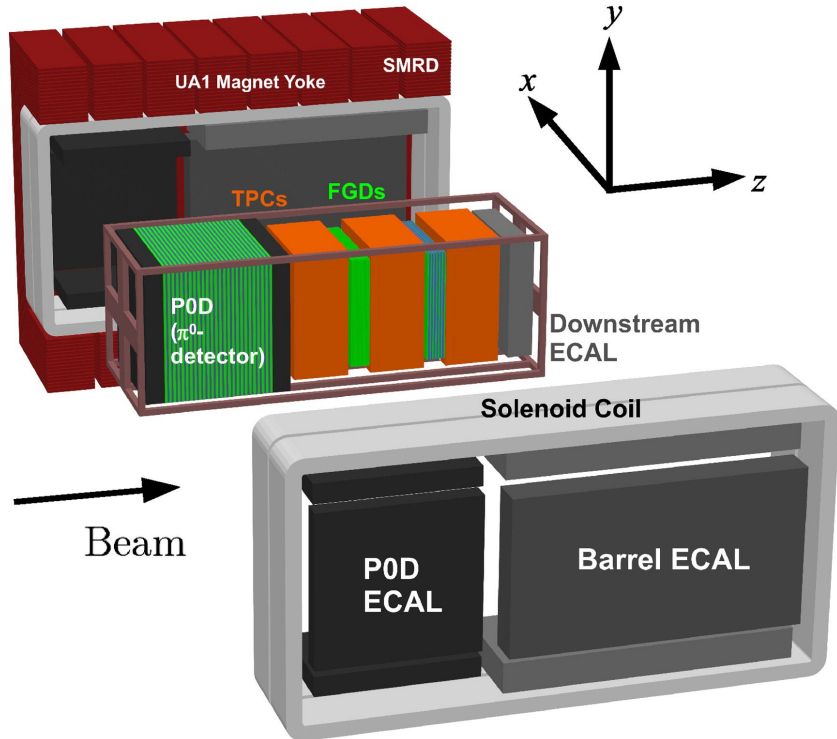


**Figure 3.9:** The components of the ND280 detector. The neutrino beam travels from left to right. Taken from [118].

787 further described in subsubsection 3.2.2.1 and subsubsection 3.2.2.2 respectively. The  
 788 electromagnetic calorimeter (ECAL) encapsulates the tracker region alongside the  $\pi^0$   
 789 detector (P0D). The ECAL measures the deposited energy from photons emitted from  
 790 interactions within the FGD. The P0D constrains the cross-section of neutral current  
 791 interactions which generate neutral pions, which is one of the largest backgrounds in  
 792 the electron neutrino appearance oscillation channel. The P0D and ECAL detectors  
 793 are detailed in subsubsection 3.2.2.3 and subsubsection 3.2.2.4 respectively. The entire  
 794 detector is located within a large yoke magnet which produces a 0.2T magnetic field.  
 795 This design of the magnet also includes a scintillating detector called the side muon  
 796 range detector (SMRD) which is used to track high-angle muons as well as acting as a  
 797 cosmic veto. The SMRD is described in subsubsection 3.2.2.5.

**798 3.2.2.1 Fine Grained Detectors**

799 The T2K tracker region is comprised of two fine grained detectors (FGD) and three  
800 Time Projection Chambers (TPC). A detailed description of the FGD design, construc-  
801 tion, and assembly is found in [123] and summarised below. The FGDs are the primary  
802 target for neutrino interactions with a mass of 1.1 tonnes per FGD. Alongside this,  
803 the FGDs are designed to be able to track short-range particles which do not exit the  
804 FGD. Typically, short-range particles are low momentum and are observed as tracks  
805 that deposit a large amount of energy per unit length. This means the FGD needs  
806 good granularity to resolve these particles. The FGDs have the best timing resolution  
807 ( $\sim 3\text{ns}$ ) of any of the sub-detectors of the ND280 detector. As such, the FGDs are  
808 used for time of flight measurements to distinguish forward going positively charged  
809 particles from backward going negatively charged particles. Finally, any tracks which  
810 pass through multiple sub-detectors are required to be track matched to the FGD.

811 Both FGDs are made from square scintillator planes of side length 186cm and  
812 width 2.02cm. Each plane consists of two layers of 192 scintillator bars in an X or Y  
813 orientation. A wavelength shifting fiber is threaded through the center of each bar and  
814 is read out by a multi-pixel photon counter (MPPC). FGD1 is the most upstream of  
815 the two FGDs and contains 15 planes of carbon plastic scintillator which is a common  
816 target in external neutrino scattering data. As the far detector is a pure water target, 7  
817 of the 15 scintillator planes in FGD2 have been replaced with a hybrid water-scintillator  
818 target. Due to the complexity of the nucleus, nuclear effects can not be extrapolated  
819 between different nuclei. Therefore having the ability to take data on one target which  
820 is the same as external data and another target which is the same as the far detector  
821 target is beneficial for reliable model parameter estimates.

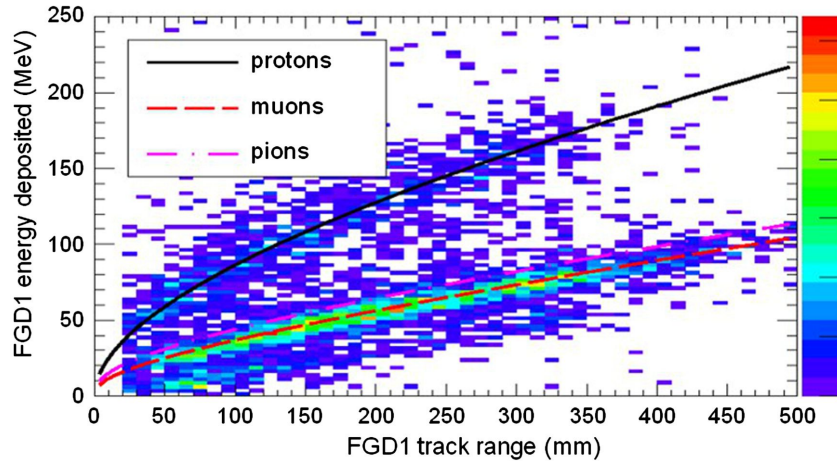


**Figure 3.10:** Comparison of data to Monte Carlo prediction of integrated deposited energy as a function of track length for particles that stopped in FGD1. Taken from [123].

The integrated deposited energy is used for particle identification. The FGD can distinguish protons from other charged particles by comparing the integrated deposited energy from data to Monte Carlo prediction as seen in Figure 3.10.

### 3.2.2.2 Time Projection Chambers

The majority of particle identification and momentum measurements within ND280 are provided by three Time Projection Chambers (TPCs) [124]. The TPCs are located on either side of the FGDs. They are located inside of the magnetic field meaning the momentum of a charged particle can be determined from the bending of the track.

Each TPC module consists of two gas-tight boxes, as shown in Figure 3.11, which are made of non-magnetic material. The outer box is filled with CO<sub>2</sub> which acts as an electrical insulator between the inner box and the ground. The inner box forms the field cage which produces a uniform electric drift field of  $\sim 275\text{V}/\text{cm}$  and is filled with an argon gas mixture. Charged particles moving through this gas mixture ionize the gas and the ionised charge is drifted towards micromegas detectors which measure the ionization charge. The time and position information in the readout allows a three-dimensional image of the neutrino interaction.

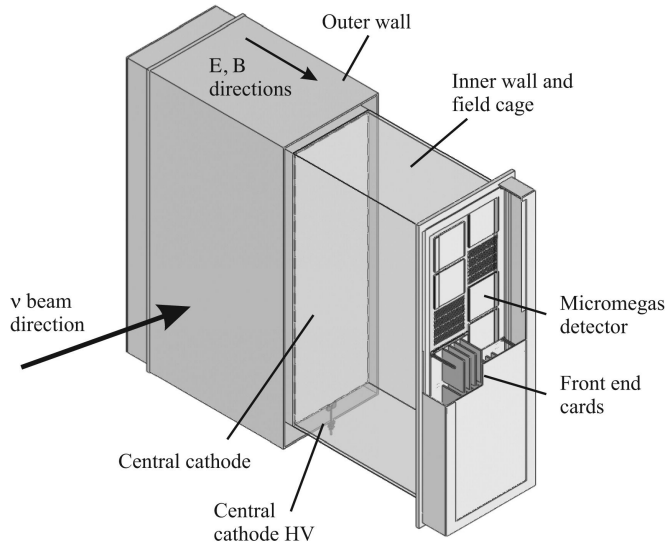


**Figure 3.11:** Schematic design of a Time Projection Chamber detector. Taken from [124].

The particle identification of tracks that pass through the TPCs is performed using

dE/dx measurements. Figure 3.12 illustrates the data to Monte Carlo distributions of the energy lost by a charged particle passing through the TPC as a function of the reconstructed particle momentum. The resolution is  $7.8 \pm 0.2\%$  meaning that electrons and muons can be distinguished. This allows reliable measurements of the intrinsic  $\nu_e$  component of the beam.

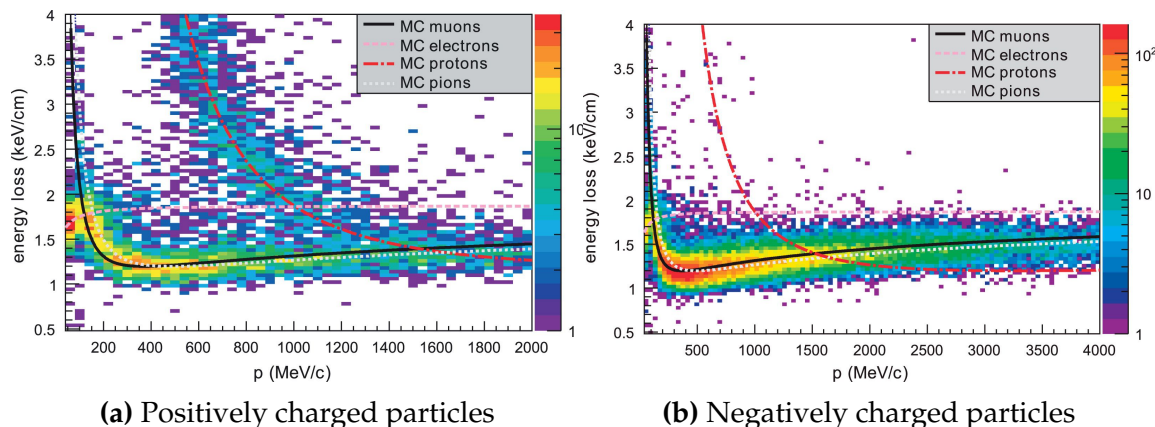


**Figure 3.12:** The distribution of energy loss as a function of reconstructed momentum for charged particles passing through the TPC, comparing data to Monte Carlo prediction. Taken from [124].

**<sup>844</sup> 3.2.2.3  $\pi^0$  Detector**

<sup>845</sup> If one of the  $\gamma$ -rays from a  $\pi^0 \rightarrow 2\gamma$  decay is missed at the far detector, the recon-  
<sup>846</sup> struction will determine that event to be a charge current  $\nu_e$ -like event. This is one of  
<sup>847</sup> the main backgrounds hindering the electron neutrino appearance searches. The  $\pi^0$   
<sup>848</sup> detector (P0D) measures the cross-section of the neutral current induced neutral pion  
<sup>849</sup> production on a water target to constrain this background.

<sup>850</sup> The P0D is a cube of approximately 2.5m length consisting of layers of scintillating  
<sup>851</sup> bars, brass and lead sheets, and water bags as illustrated in Figure 3.13. Two electro-  
<sup>852</sup> magnetic calorimeters are positioned at the most upstream and most downstream  
<sup>853</sup> position in the sub-detector and the water target is situated in between them. The  
<sup>854</sup> scintillator layers are built from two triangular bars orientated in opposite directions  
<sup>855</sup> to form a rectangular layer. Each triangular scintillator bar is threaded with optical  
<sup>856</sup> fiber which is read out by MPPCs. The high-Z brass and lead regions produce electron  
<sup>857</sup> showers from the photons emitted in  $\pi^0$  decay.

<sup>858</sup> The sub-detector can generate measurements of NC1 $\pi^0$  cross-sections on a water  
<sup>859</sup> target by measuring the event rate both with and without the water target, with the  
<sup>860</sup> cross-section on a water target being determined as the difference. The total active  
<sup>861</sup> mass is 16.1 tonnes when filled with water and 13.3 tonnes when empty.

**<sup>862</sup> 3.2.2.4 Electromagnetic Calorimeter**

<sup>863</sup> The electromagnetic calorimeter [126] (ECal) encapsulates the P0D and tracking sub-  
<sup>864</sup> detectors. Its primary purpose is to aid  $\pi^0$  reconstruction from any interaction in  
<sup>865</sup> the tracker. To do this, it measures the energy and direction of photon showers from  
<sup>866</sup>  $\pi^0 \rightarrow 2\gamma$  decay. It can also distinguish pion and muon tracks depending on the shape  
<sup>867</sup> of the photon shower deposited.

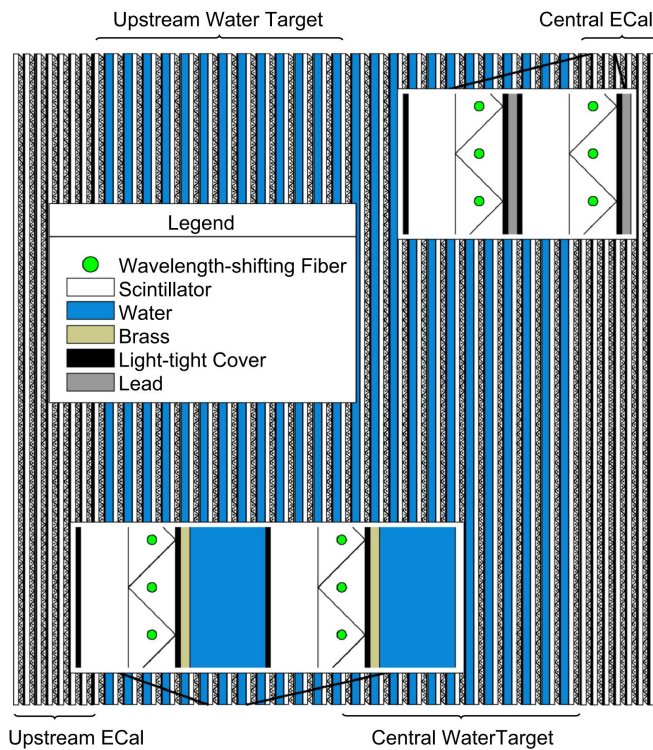


**Figure 3.13:** A schematic of the P0D side-view. Taken from [125].

The ECal is comprised of three sections; the P0D ECal which surrounds the P0D, the barrel ECal which encompasses the tracking region, and the downstream ECal which is situated downstream of the tracker region. The barrel and downstream ECals are tracking calorimeters that focus on electromagnetic showers from high-angle particles emitted from the tracking sub-detectors. Particularly in the TPC, high-angle tracks (those which travel perpendicularly to the beam-axis) can travel along a single scintillator bar resulting in very few hits. The width of the barrel and downstream ECal corresponds to  $\sim 11$  electron radiation lengths to ensure a significant amount of the  $\pi^0$  energy is contained. As the P0D has its own calorimetry which reconstructs showers, the P0D ECal determines the energy which escapes the P0D.

Each ECal is constructed of multiple layers of scintillating bars sandwiched between lead sheets. The scintillating bars are threaded with optical fiber and read out by MPPCs. Each sequential layer of the scintillator is orientated perpendicular to the previous which allows a three dimensional event reconstruction. The target mass

882 of the P0D ECal, barrel ECal, and downstream ECal are 1.50, 4.80 and 6.62 tonnes  
883 respectively.

884 **3.2.2.5 Side Muon Range Detector**

885 As illustrated in Figure 3.9, the ECal, FGDs, P0D, and TPCs are enclosed within the  
886 UA1 magnet. Originally designed for the NOMAD [127] experiment and reconditioned  
887 for use in the T2K experiment [128], the UA1 magnet provides a uniform horizontal  
888 magnetic field of 0.2T with an uncertainty of  $2 \times 10^{-4}$ T.

889 Built into the UA1 magnet, the side muon range detector (SMRD) [129] monitors  
890 high-energy muons which leave the tracking region and permeate through the ECal.  
891 It additionally acts as a cosmic muon veto and trigger.

892 **3.2.3 The Interactive Neutrino GRID**

893 The Interactive Neutrino GRID (INGRID) detector is situated within the same “pit” as  
894 the other near detectors. It is aligned with the beam in the “on-axis” position and mea-  
895 sures the beam direction, spread, and intensity. The detector was originally designed  
896 with 16 identical modules [118] (two modules have since been decommissioned) and a  
897 “proton” module. The design of the detector is cross-shaped with length and height  
898 10m × 10m as illustrated in Figure 3.14.

899 Each module is composed of iron sheets interlaced with eleven tracking scintillator  
900 planes for a total target mass of 7.1 tonnes per module. The scintillator design is an X-Y  
901 pattern of 24 bars in both orientations, where each bar contains wave-length shifting  
902 fibers which are connected to multi-pixel photon counters (MPPCs). Each module is  
903 encapsulated inside veto planes to aid the rejection of charged particles entering the  
904 module.

905     The proton module is different from the other modules in that it consists of entirely  
 906   scintillator planes with no iron target. The scintillator bars are also smaller than those  
 907   used in the other modules to increase the granularity of the detector and improve  
 908   tracking capabilities. The module sits in the center of the beamline and is designed to  
 909   give precise measurements of quasi-elastic charged current interactions to evaluate  
 910   the performance of the Monte Carlo simulation of the beamline.

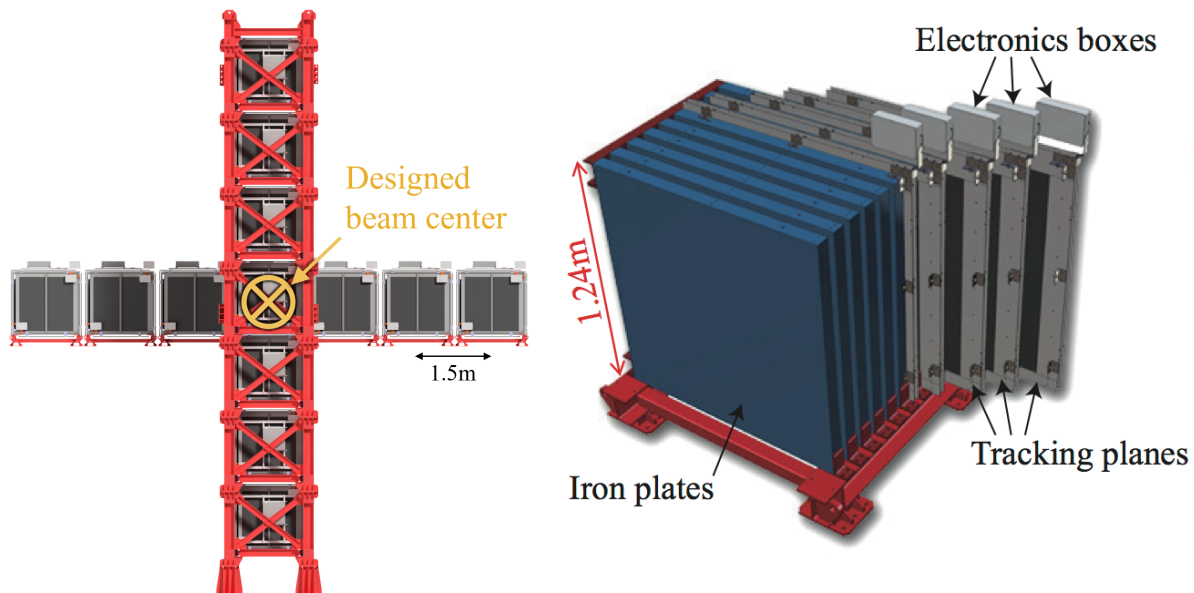


**Figure 3.14:** Left panel: The Interactive Neutrino GRID on-axis Detector. 14 modules are arranged in a cross-shape configuration, with the center modules being directly aligned with the on-axis beam. Right panel: The layout of a single module of the INGRID detector. Both figures are recreated from [118].

911     The INGRID detector can measure the beam direction to an uncertainty of 0.4mrad  
 912   and the beam center within a resolution of 10cm [118]. The beam direction in both the  
 913   vertical and horizontal directions is discussed in [130] and it is found to be in good  
 914   agreement with the MUMON monitor described in subsection 3.2.1.

915 **Chapter 4**

916 **Bayesian Statistics and Markov Chain**  
917 **Monte Carlo Techniques**

918 This thesis presents a Bayesian oscillation analysis. To extract the oscillation parameters,  
919 a Markov Chain Monte Carlo (MCMC) method is used. This chapter explains  
920 the theory of how parameter estimates can be determined using this technique and  
921 condenses the material found in the literature [131–134].

922 The oscillation parameter determination presented within this thesis is built upon  
923 a simultaneous fit to neutrino beam data in the near detector, beam data at SK and  
924 atmospheric data at SK. In total, there are four oscillation parameters of interest  
925 ( $\sin^2(\theta_{23})$ ,  $\sin^2(\theta_{13})$ ,  $\Delta m_{23}^2$ , and  $\delta_{CP}$ ), two oscillation parameters to which this study  
926 will not be sensitive ( $\sin^2(\theta_{12})$ ,  $\Delta m_{12}^2$ ) and many nuisance parameters that control the  
927 systematic uncertainty models invoked within this study.

928 The MCMC technique generates a multi-dimensional probability distribution across  
929 all of the model parameters used in the fit. To determine the parameter estimate of a  
930 single parameter, this multi-dimensional object is integrated over all other parameters.  
931 This process is called Marginalisation and is further described in subsection 4.3.1.  
932 Monte Carlo techniques approximate the probability distribution of each parameter  
933 within the limit of generating infinite samples. As ever, generating a large number of  
934 samples is time and resource-dependent. Therefore, an MCMC technique is utilised  
935 within this analysis to reduce the required number of steps to sufficiently sample the  
936 parameter space. This technique is described in further detail in subsection 4.2.1.

---

## 937 4.1 Bayesian Statistics

938 Bayesian inference treats observable data,  $D$ , and model parameters,  $\vec{\theta}$ , on equal  
 939 footing such that a probability model of both data and parameters is required. This is  
 940 the joint probability distribution  $P(D, \vec{\theta})$  and can be described by the prior distribution  
 941 for model parameters  $P(\vec{\theta})$  and the likelihood of the data given the model parameters  
 942  $P(D|\vec{\theta})$ ,

$$P(D, \vec{\theta}) = P(D|\vec{\theta})P(\vec{\theta}). \quad (4.1)$$

943 The prior distribution,  $P(\vec{\theta})$ , describes all previous knowledge about the parameters  
 944 within the model. For example, if the risk of developing health problems is known  
 945 to increase with age, the prior distribution would describe the increase. For the  
 946 purpose of this analysis, the prior distribution is typically the best-fit values taken  
 947 from external data measurements with a Gaussian uncertainty. The prior distribution  
 948 can also contain correlations between model parameters. In an analysis using Monte  
 949 Carlo techniques, the likelihood of measuring some data assuming some set of model  
 950 parameters is calculated by comparing the Monte Carlo prediction generated at that  
 951 particular set of model parameters to the data.

952 It is parameter estimation that is important for this analysis and as such, we apply  
 953 Bayes' theorem [135] to calculate the probability for each parameter to have a certain  
 954 value given the observed data,  $P(\vec{\theta}|D)$ , which is known as the posterior distribution  
 955 (often termed the posterior). This can be expressed as

$$P(\vec{\theta}|D) = \frac{P(D|\vec{\theta})P(\vec{\theta})}{\int P(D|\vec{\theta})P(\vec{\theta})d\vec{\theta}}. \quad (4.2)$$

956 The denominator in Equation 4.2 is the integral of the joint probability distribution

957 over all values of all parameters used within the fit. For brevity, we say that the  
958 posterior distribution is

$$P(\vec{\theta}|D) \propto P(D|\vec{\theta})P(\vec{\theta}). \quad (4.3)$$

959 In subsection 4.3.1, we see that for the cases used within this analysis, it is reason-  
960 able to know the posterior to some normalisation constant.

## 961 4.2 Monte Carlo Simulation

962 Monte Carlo techniques are used to numerically solve a complex problem that does  
963 not necessarily have an analytical solution. These techniques rely on building a large  
964 ensemble of samples from an unknown distribution and then using the ensemble to  
965 approximate the properties of the distribution.

966 An example that uses Monte Carlo techniques is to calculate the area underneath  
967 a curve. For example, take the problem of calculating the area under a straight line  
968 with gradient  $M = 0.4$  and intercept  $C = 1.0$ . Analytically, one can calculate the area  
969 under the line is equal to 30 units for  $0 \leq x \leq 10$ . Using Monte Carlo techniques,  
970 one can calculate the area under this line by throwing many random values for the  $x$   
971 and  $y$  components of each sample and then calculating whether that point falls below

the line. The area can then be calculated by the ratio of points below the line to the total number of samples thrown multiplied by the total area in which samples were scattered. The study is shown in Figure 4.1 highlights this technique and finds the area under the curve to be 29.9 compared to an analytical solution of 30.0. The deviation of the numerical to analytical solution can be attributed to the number of samples used in the study. The accuracy of the approximation in which the properties of the Monte Carlo samples replicate those of the desired distribution is dependent on the number of samples used. Replicating this study with a differing number of Monte Carlo samples used in each study (As shown in Figure 4.2) highlights how the Monte Carlo techniques are only accurate within the limit of a high number of samples.

Whilst the above example has an analytical solution, these techniques are just as applicable to complex solutions. Clearly, any numerical solution is only as useful as its efficiency. As discussed, the accuracy of the Monte Carlo technique is dependent upon the number of samples generated to approximate the properties of the distribution. Furthermore, if the positions at which the samples are evaluated are not ‘cleverly’ picked, the efficiency of the Monte Carlo technique significantly drops. Given the example in Figure 4.1, if the region in which the samples are scattered significantly extends passed the region of interest, many calculations will be calculated but do not add to the ability of the Monte Carlo technique to achieve the correct result. For instance, any sample evaluated at a  $y \geq 5$  could be removed without affecting the final result. This does bring in an aspect of the ‘chicken and egg’ problem in that to achieve efficient sampling, one needs to know the distribution beforehand.

#### 4.2.1 Markov Chain Monte Carlo

This analysis utilises a multi-dimensional probability distribution, with some dimensions being significantly more constrained than others. This could be from prior

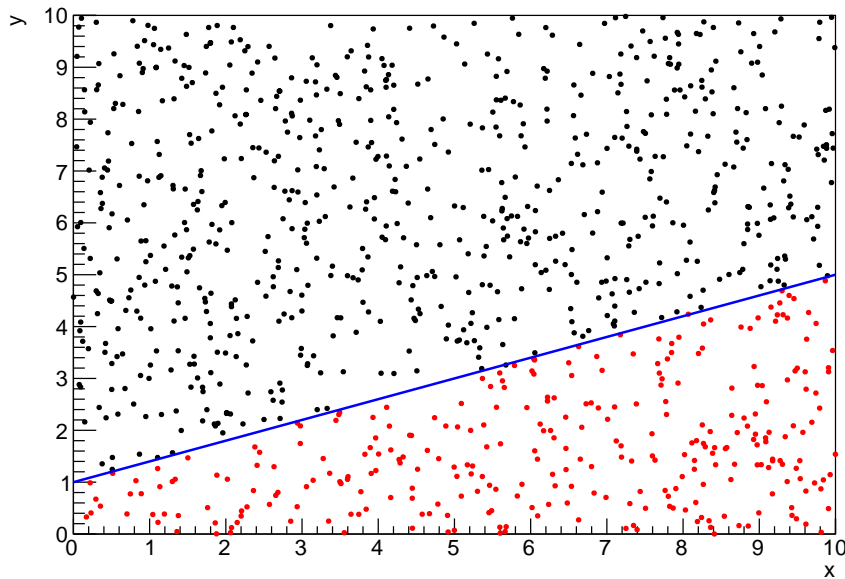


**Figure 4.1:** Example of using Monte Carlo techniques to find the area under the blue line. The gradient and intercept of the line are 0.4 and 1.0 respectively. The area found to be under the curve using one thousand samples is 29.9 units.

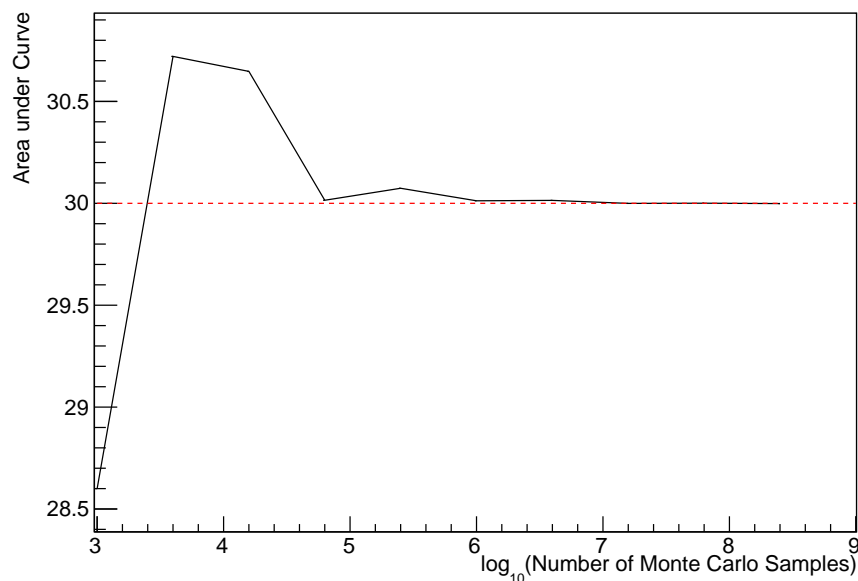


**Figure 4.2:** The area under a line of gradient 0.4 and intercept 1.0 for the range  $0 \leq x \leq 10$  as calculated using Monte Carlo techniques as a function of the number of samples used in each repetition. The analytical solution to the area is 30 units as given by the red line.

knowledge of parameter distributions from external data or un-physical regions in which parameters can not exist. Consequently, the Monte Carlo techniques used need to be as efficient as possible. For this analysis, the Markov Chain Monte Carlo (MCMC) technique is chosen. An MCMC technique is a Monte Carlo technique that uses a Markov chain to select which points at which to sample the parameter distribution. This technique performs a semi-random stochastic walk through the allowable parameter space. This builds a posterior distribution which has the property that the density of sampled points is proportional to the probability density of that parameter. This does mean that the samples produced by this technique are not statistically independent but they will cover the space of the distribution.

A Markov chain functions by selecting the position of step  $\vec{x}_{i+1}$  based on the position of  $\vec{x}_i$ . The space in which the Markov chain selects samples is dependent upon the total number of parameters utilised within the fit, where a discrete point in this space is described by the N-dimensional space  $\vec{x}$ . In a perfectly operating Markov chain, the position of the next step depends solely on the previous step and not on the further history of the chain ( $\vec{x}_0, \vec{x}_1$ , etc.). However, in solving the multi-dimensionality of the fit used within this analysis, each step becomes correlated with several of the steps preceding itself. This behaviour is further explained in subsection 4.2.3. Providing the MCMC chain is well optimised, it will begin to converge towards a unique stationary distribution. The period between the chain's initial starting point and the convergence to the unique stationary distribution is colloquially known as the burn-in period. This is discussed further in subsection 4.2.3. Once the chain reaches the stationary distribution, all points sampled after that point will look like samples from that distribution.

1021      Further details of the theories underpinning MCMC techniques are discussed  
1022    in [132] but can be summarised by the requirement that the chain satisfies the three  
1023    ‘regularity conditions’:

- 1024    • Irreducibility: From every position in the parameter space  $\vec{x}$ , there must exist a  
1025    non-zero probability for every other position in the parameter space to be reached.
- 1026    • Recurrence: Once the chain arrives at the stationary distribution, every step fol-  
1027    lowing from that position must be samples from the same stationary distribution.
- 1028    • Aperiodicity: The chain must not repeat the same sequence of steps at any point  
1029    throughout the sampling period.

1030      The output of the chain after burn-in (ie. the sampled points after the chain  
1031    has reached the stationary distribution) can be used to approximate the posterior  
1032    distribution and model parameters  $\vec{\theta}$ . To achieve the requirement that the unique  
1033    stationary distribution found by the chain be the posterior distribution, one can use  
1034    the Metropolis-Hastings algorithm. This guides the stochastic process depending on  
1035    the likelihood of the current proposed step compared to that of the previous step.  
1036    Implementation and other details of this technique are discussed in subsection 4.2.2.

### 1037 4.2.2 Metropolis-Hastings Algorithm

1038   As a requirement for MCMCs, the Markov chain implemented in this technique must  
1039   have a unique stationary distribution that is equivalent to the posterior distribution.  
1040   To ensure this requirement and that the regularity conditions are met, this analysis  
1041   utilises the Metropolis-Hastings (MH) algorithm [136,137]. For the  $i^{th}$  step in the chain,  
1042   the MH algorithm determines the position in the parameter space to which the chain  
1043   moves to based on the current step,  $\vec{x}_i$ , and the proposed step,  $\vec{y}_{i+1}$ . The proposed step  
1044   is randomly selected from some proposal function  $f(\vec{x}_{i+1} | \vec{x}_i)$ , which depends solely

1045 on the current step (ie. not the further history of the chain). The next step in the chain  
 1046  $\vec{x}_{i+1}$  can be either the current step or the proposed step determined by whether the  
 1047 proposed step is accepted or rejected. To decide if the proposed step is selected, the  
 1048 acceptance probability,  $\alpha(\vec{x}_i, \vec{y}_i)$ , is calculated as

$$\alpha(\vec{x}_i, \vec{y}_{i+1}) = \min \left( 1, \frac{P(\vec{y}_{i+1}|D)f(\vec{x}_i|\vec{y}_{i+1})}{P(\vec{x}_i|D)f(\vec{y}_{i+1}|\vec{x}_i)} \right). \quad (4.4)$$

1049 Where  $P(\vec{y}_{i+1}|D)$  is the posterior distribution as introduced in section 4.1. To  
 1050 simplify this calculation, the proposal function is required to be symmetric such that  
 1051  $f(\vec{x}_i|\vec{y}_{i+1}) = f(\vec{y}_{i+1}|\vec{x}_i)$ . In practice, a multi-variate Gaussian distribution is used to  
 1052 throw parameter proposals from. This reduces Equation 4.4 to

$$\alpha(\vec{x}_i, \vec{y}_{i+1}) = \min \left( 1, \frac{P(\vec{y}_{i+1}|D)}{P(\vec{x}_i|D)} \right). \quad (4.5)$$

1053 After calculating this quantity, a random number,  $\beta$ , is generated uniformly be-  
 1054 tween 0 and 1. If  $\beta \leq \alpha(\vec{x}_i, \vec{y}_{i+1})$ , the proposed step is accepted. Otherwise, the chain  
 1055 sets the next step equal to the current step and this procedure is repeated. This can be  
 1056 interpreted as if the posterior probability of the proposed step is greater than that of  
 1057 the current step, ( $P(\vec{y}_{i+1}|D) \geq P(\vec{x}_i|D)$ ), the proposed step will always be accepted.  
 1058 If the opposite is true, ( $P(\vec{y}_{i+1}|D) \leq P(\vec{x}_i|D)$ ), the proposed step will be accepted  
 1059 with probability  $P(\vec{x}_i|D)/P(\vec{y}_{i+1}|D)$ . This ensures that the Markov chain does not get  
 1060 trapped in any local minima in the potentially non-Gaussian posterior distribution.  
 1061 The outcome of this technique is that the density of steps taken in a discrete region is  
 1062 directly proportional to the probability density in that region.

### <sup>1063</sup> 4.2.3 MCMC Optimisation

<sup>1064</sup> As discussed in subsection 4.2.2, the proposal function invoked within the MH algo-  
<sup>1065</sup> rithm can take any form and the chain will still converge to the stationary distribution.  
<sup>1066</sup> At each set of proposed parameter values, a prediction of the same spectra has to be  
<sup>1067</sup> generated which requires significant computational resources. Therefore, the number  
<sup>1068</sup> of steps taken before the unique stationary distribution is found should be minimised  
<sup>1069</sup> as only steps after convergence add information to the oscillation analysis. Further-  
<sup>1070</sup> more, the chain should entirely cover the allowable parameter space to ensure that all  
<sup>1071</sup> values have been considered. Tuning the distance that the proposal function jumps  
<sup>1072</sup> between steps on a parameter-by-parameter basis can both minimise the length of the  
<sup>1073</sup> burn-in period and ensure that the correlation between step  $\vec{x}_i$  and  $\vec{x}_j$  is sufficiently  
<sup>1074</sup> small.

<sup>1075</sup> The effect of changing the width of the proposal function is highlighted in Figure 4.3.  
<sup>1076</sup> Three scenarios, each with the same underlying stationary distribution (A Gaussian of  
<sup>1077</sup> width 1.0 and mean 0.), are presented. The only difference between the three scenarios  
<sup>1078</sup> is the width of the proposal function, colloquially known as the ‘step size  $\sigma$ ’. Each  
<sup>1079</sup> scenario starts at an initial parameter value of 10.0 which would be considered an  
<sup>1080</sup> extreme variation. For the case where  $\sigma = 0.1$ , it is clear to see that the chain takes  
<sup>1081</sup> a long time to reach the expected region of the parameter. This indicates that this  
<sup>1082</sup> chain would have a large burn-in period and does not converge to the stationary  
<sup>1083</sup> distribution until step  $\sim 500$ . Furthermore, whilst the chain does move towards the  
<sup>1084</sup> expected region, each step is significantly correlated with the previous. Considering  
<sup>1085</sup> the case where  $\sigma = 5.0$ , the chain approaches the expected parameter region almost  
<sup>1086</sup> instantly meaning that the burn-in period is not significant. However, there are clearly  
<sup>1087</sup> large regions of steps where the chain does not move. This is likely due to the chain  
<sup>1088</sup> proposing steps in the tails of the distribution which have a low probability of being

1089 accepted. Consequently, this chain would take a significant number of steps to fully  
 1090 span the allowable parameter region. For the final scenario, where  $\sigma = 0.5$ , you can see  
 1091 a relatively small burn-in period of approximately 100 steps. Once the chain reaches  
 1092 the stationary distribution, it moves throughout the expected region of parameter  
 1093 values many times, sufficiently sampling the full parameter region. This example is a  
 1094 single parameter varying across a continuous distribution and does not fully reflect  
 1095 the difficulties in the many-hundred multi-variate parameter distribution used within  
 1096 this analysis. However, it does give a conceptual idea of the importance of selecting  
 1097 the proposal function and associated step size.

1098 As discussed, step size tuning directly correlates to the average step acceptance  
 1099 rate. If the step size is too small, many steps will be accepted but the chain moves  
 1100 slowly. If the opposite is true, many steps will be rejected as the chain proposes steps  
 1101 in the tails of the distribution. Discussion in [138] suggests that the ‘ideal’ acceptance  
 1102 rate of a high dimension MCMC chain should be approximately  $\sim 25\%$ . An “ideal”  
 1103 step size [138] of

$$\sigma = \frac{2.4}{N_p}, \quad (4.6)$$

1104 where  $N_p$  is the number of parameters included in the MCMC fit. However, the  
 1105 complex correlations between systematics mean that some parameters have to be hand  
 1106 tuned and many efforts have been taken to select a set of parameter-by-parameter step  
 1107 sizes to approximately reach the ideal acceptance rate.

1108 Figure 4.3 highlights the likelihood as calculated by the fit in [DB: Link to AsimovA](#)  
 1109 **Sensitivity Section** as a function of the number of steps in each chain. In practice,  
 1110 many independent MCMC chains are run simultaneously to parallelise the task of

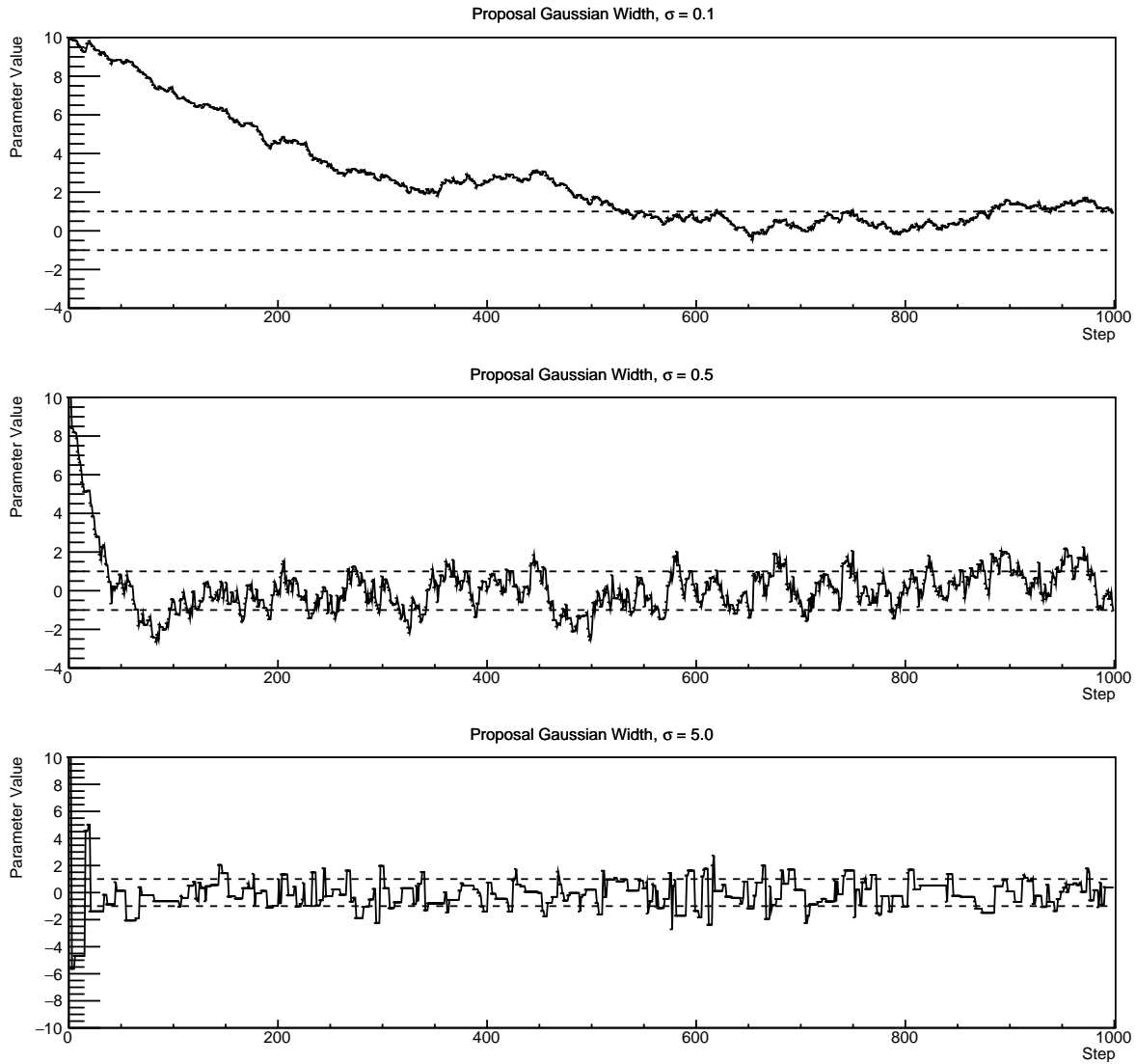


**Figure 4.3:** Three MCMC chains, each with a stationary distribution equal to a Gaussian centered at 0 and width 1 (As indicated by the black dotted lines). All of the chains use a Gaussian proposal function but have different widths (or ‘step size  $\sigma$ ’). The top panel has  $\sigma = 0.1$ , middle panel has  $\sigma = 0.5$  and the bottom panel has  $\sigma = 5.0$ .

1111 performing the fit. This figure overlays the distribution found in each chain. As seen,  
 1112 the likelihood decreases from its initial value and converges towards a stationary  
 1113 distribution after  $\sim 1 \times 10^5$  steps.

1114 Multiple configurations of this analysis have been performed throughout this thesis  
 1115 where different samples or systematics have been used. For all of these configurations,  
 1116 it was found that a burnin period of  $1 \times 10^5$  was sufficient in all cases.

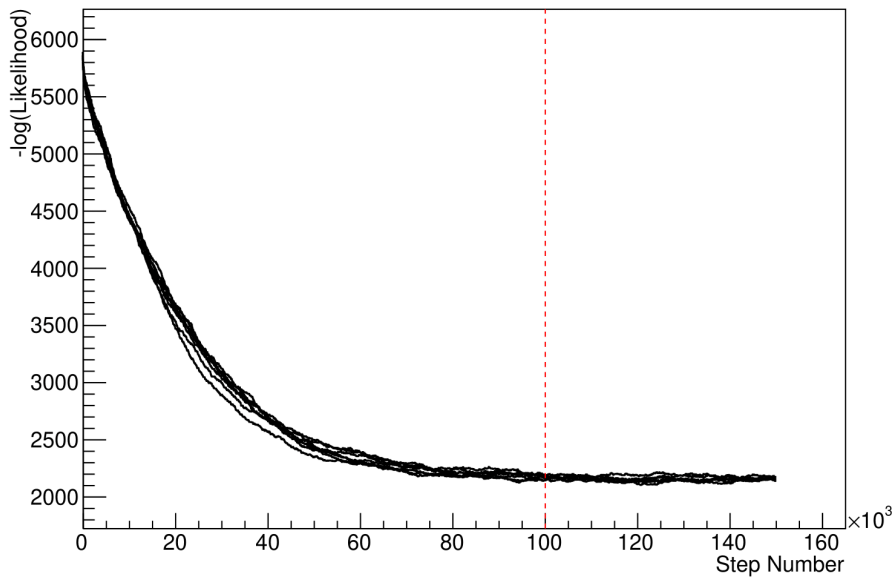


**Figure 4.4:** The log-likelihood from the fit detailed in DB: [Link to AsimovA Sensitivity Section](#) as a function of the number of steps accumulated in each fit. Many independent MCMC chains were run in parallel and overlaid on this plot. The red line indicates the  $1 \times 10^5$  step burn-in period after which the log-likelihood becomes stable.

## 1117 4.3 Understanding the MCMC Results

1118 The previous sections have described how to generate the posterior probability distri-  
1119 bution using Bayesian MCMC techniques. However, this analysis focuses on oscillation  
1120 parameter determination. The posterior distribution output from the chain is a high  
1121 dimension object, with as many dimensions as there are parameters included in the os-  
1122 cillation analysis. However, this multi-dimensional object is difficult to conceptualize  
1123 so parameter estimations are often presented in one or two-dimensional projections  
1124 of this probability distribution. To do this, we invoke the marginalisation technique  
1125 highlighted in subsection 4.3.1.

### <sup>1126</sup> 4.3.1 Marginalisation

<sup>1127</sup> The output of the MCMC chain is a highly dimensional probability distribution  
<sup>1128</sup> which is very difficult to interpret. From the standpoint of an oscillation analysis  
<sup>1129</sup> experiment, the one or two-dimensional ‘projections’ of the oscillation parameters of  
<sup>1130</sup> interest are most relevant. Despite this, the best fit values and uncertainties on the  
<sup>1131</sup> oscillation parameters of interest should correctly encapsulate the correlations to the  
<sup>1132</sup> other systematic uncertainties (colloquially called ‘nuisance’ parameters). For this joint  
<sup>1133</sup> beam and atmospheric analysis, the oscillation parameters of interest are  $\sin^2(\theta_{23})$ ,  
<sup>1134</sup>  $\sin^2(\theta_{13})$ ,  $\Delta m_{23}^2$ , and  $\delta_{CP}$ . All other parameters (Including the oscillation parameter  
<sup>1135</sup> this fit is insensitive to) are deemed nuisance parameters. To generate these projections,  
<sup>1136</sup> we rely upon integrating the posterior distribution over all nuisance parameters. This  
<sup>1137</sup> is called marginalisation. A simple example of this technique is to imagine the scenario  
<sup>1138</sup> where two coins are flipped. To determine the probability that the first coin returned  
<sup>1139</sup> a ‘head’, the exact result of the second coin flip is disregarded and simply integrated  
<sup>1140</sup> over. For the parameters of interest,  $\vec{\theta}_i$ , we can calculate the marginalised posterior by  
<sup>1141</sup> integrating over the nuisance parameters,  $\vec{\theta}_n$ . In this case, Equation 4.2 becomes

$$P(\vec{\theta}_i|D) = \frac{\int P(D|\vec{\theta}_i, \vec{\theta}_n)P(\vec{\theta}_i, \vec{\theta}_n)d\vec{\theta}_n}{\int P(D|\vec{\theta})P(\vec{\theta})d\vec{\theta}} \quad (4.7)$$

<sup>1142</sup> Where  $P(\vec{\theta}_i, \vec{\theta}_n)$  encodes the prior knowledge about the uncertainty and correlations  
<sup>1143</sup> between the parameters of interest and the nuisance parameters. In practice, this  
<sup>1144</sup> is simply taking the one or two-dimensional projection of the multi-dimensional  
<sup>1145</sup> probability distribution.

Whilst in principle an easy solution to a complex problem, correlations between the interesting and nuisance parameters can bias the marginalised results. A similar effect is found when the parameters being marginalised over have non-Gaussian probability distributions. For example, Figure 4.5 highlights the marginalisation bias in the probability distribution found for a parameter when requiring a correlated parameter to have a positive parameter value. Due to the complex nature of this oscillation parameter fit presented in this thesis, there are correlations occurring between the oscillation parameters of interest and the other nuisance parameters included in the fit.

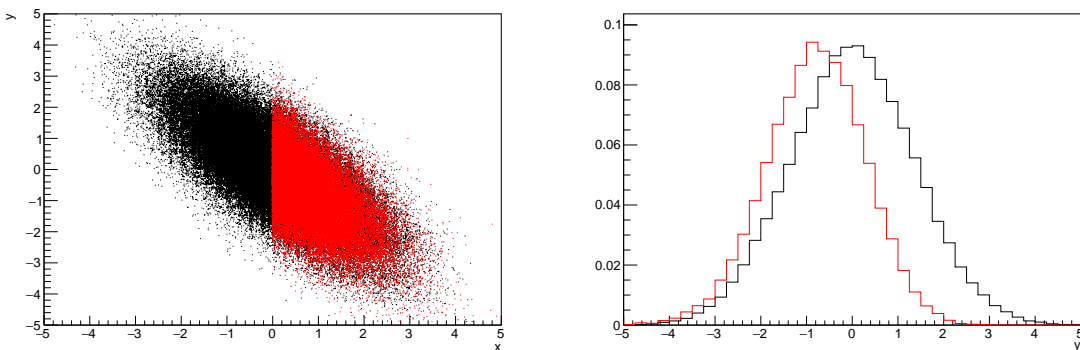


**Figure 4.5:** Left: The two dimensional probability distribution for two correlated parameters  $x$  and  $y$ . The red distribution shows the two dimensional probability distribution when  $0 \leq x \leq 5$ . Right: The marginalised probability distribution for the  $y$  parameter found when requiring the  $x$  to be bound between  $-5 \leq x \leq 5$  and  $0 \leq x \leq 5$  for the black and red distribution, respectively.

### 4.3.2 Parameter Estimation and Credible Intervals

The purpose of this analysis is to determine the best fit values for the oscillation parameters that the beam and atmospheric samples are sensitive to:  $\sin^2(\theta_{23})$ ,  $\sin^2(\theta_{13})$ ,  $\Delta m_{23}^2$ , and  $\delta_{CP}$ . Typically, the results presented take the form of one or two-dimension marginalised probability distributions for the appearance ( $\sin^2(\theta_{13})$  and  $\delta_{CP}$ ) and disappearance ( $\sin^2(\theta_{23})$  and  $\Delta m_{23}^2$ ) parameters. The posterior probability density

<sub>1161</sub> taken from the output MCMC chain is binned in these parameters. The parameter  
<sub>1162</sub> best-fit point is then taken to be the value that has the highest posterior probability.  
<sub>1163</sub> This is performed in both one and two-dimensional projections.

<sub>1164</sub> However, the single best-fit point in a given parameter is not of much use on its  
<sub>1165</sub> own. We would also like to determine the uncertainty, or credible interval, on that  
<sub>1166</sub> best-fit point. The definition of the  $1\sigma$  credible interval is that we have 68% belief that  
<sub>1167</sub> the parameter is within those bounds. For a more generalised definition, the credible  
<sub>1168</sub> interval is the region,  $R$ , of the posterior distribution that contains a specific fraction of  
<sub>1169</sub> the total probability, such that

$$\int_R P(\theta|D)d\theta = \alpha \quad (4.8)$$

<sub>1170</sub> Where  $\theta$  is the parameter on which we calculate the credible interval. This technique  
<sub>1171</sub> then calculates the  $\alpha \times 100\%$  credible interval.

<sub>1172</sub> In practice, this analysis uses the highest posterior density (HPD) credible intervals  
<sub>1173</sub> which are calculated through the following method. First, the probability distribution  
<sub>1174</sub> is area-normalised such that it has an integrated area equal to 1.0. The bins of proba-  
<sub>1175</sub> bility are then summed from the highest to lowest until the sum exceeds the  $1\sigma$  level  
<sub>1176</sub> (0.68 in this example). This process is repeated for a range of credible intervals, notably  
<sub>1177</sub> the  $1\sigma$ ,  $2\sigma$  and  $3\sigma$  along with other levels where the critical values for each level can  
<sub>1178</sub> be found in [139]. This process can be repeated for the two-dimensional probability  
<sub>1179</sub> distributions by creating two-dimensional contours of credible intervals rather than a  
<sub>1180</sub> one-dimensional result.

---

### <sup>1181</sup> 4.3.3 Bayesian Model Comparisons

<sup>1182</sup> Due to the matter resonance, this analysis has some sensitivity to the mass hierarchy  
<sup>1183</sup> of neutrino states (whether  $\Delta m_{23}^2$  is positive or negative) and the octant of  $\sin^2(\theta_{23})$   
<sup>1184</sup> . The Bayesian approach utilised within this analysis gives an intuitive method of  
<sup>1185</sup> model comparison by determining which hypothesis is most favourable. Taking the  
<sup>1186</sup> ratio of Equation 4.3 for the two hypotheses of normal hierarchy,  $NH$ , and inverted  
<sup>1187</sup> hierarchy,  $IH$ , gives

$$\frac{P(\vec{\theta}_{NH}|D)}{P(\vec{\theta}_{IH}|D)} = \frac{P(D|\vec{\theta}_{NH})}{P(D|\vec{\theta}_{IH})} \times \frac{P(\vec{\theta}_{NH})}{P(\vec{\theta}_{IH})}. \quad (4.9)$$

<sup>1188</sup> The middle term defines the Bayes factor which is a data-driven interpretation of  
<sup>1189</sup> how strong the data prefers one hierarchy to the other. For this analysis, equal priors  
<sup>1190</sup> on both mass hierarchy hypotheses are chosen ( $P(\vec{\theta}_{NH}) = P(\vec{\theta}_{IH}) = 0.5$ ). In practice,  
<sup>1191</sup> the MCMC chain proposes a value of  $|\Delta m_{23}^2|$  and then applies a 50% probability  
<sup>1192</sup> that the value is sign flipped. Consequently, the Bayes factor can be calculated from  
<sup>1193</sup> the ratio of the probability density in either hypothesis. This equates to counting the  
<sup>1194</sup> number of steps taken in the normal and inverted hierarchies and taking the ratio. The  
<sup>1195</sup> same approach can be taken to compare the upper octant (UO) compared to the lower  
<sup>1196</sup> octant (LO) hypothesis of  $\sin^2(\theta_{23})$ .

<sup>1197</sup> Whilst the value of the Bayes factor should always be shown, the Jeffreys scale [140]  
<sup>1198</sup> (highlighted in Table 4.1) gives an indication of the strength of preference for one model  
<sup>1199</sup> compared to the other. Other interpretations of the strength of preference of a model  
<sup>1200</sup> exist, e.g. the Kass and Raferty Scale [141].

$\log_{10}(B_{AB})$	$B_{AB}$	Strength of Preference
< 0.0	< 1	No preference for hypothesis A (Supports hypothesis B)
0.0 – 0.5	1.0 – 3.16	Preference for hypothesis A is weak
0.5 – 1.0	3.16 – 10.0	Preference for hypothesis A is substantial
1.0 – 1.5	10.0 – 31.6	Preference for hypothesis A is strong
1.5 – 2.0	31.6 – 100.0	Preference for hypothesis A is very strong
> 2.0	> 100.0	Decisive preference for hypothesis A

**Table 4.1:** Jeffreys scale for strength of preference for two models  $A$  and  $B$  as a function of the calculated Bayes factor ( $B_{AB} = B(A/B)$ ) between the two models [140]. The original scale is given in terms of  $\log_{10}(B(A/B))$  but converted to linear scale for easy comparison throughout this thesis.

#### 1201 4.3.4 Comparison of MCMC Output to Expectation

1202 To ensure the fit is performing well, a best-fit spectrum is produced using the pos-  
 1203 terior probability distribution and compared with the data, allowing easy by-eye  
 1204 comparisons to be made. A simple method of doing this is to perform a comparison  
 1205 in the fitting parameters (For instance, the reconstructed neutrino energy and lepton  
 1206 direction for T2K far detector beam samples) of the spectra generated by the MCMC  
 1207 chain to ‘data’. This ‘data’ could be true data or some variation of Monte Carlo predic-  
 1208 tion. This allows easy comparison of the MCMC probability distribution to the data.  
 1209 To perform this,  $N$  steps from the post burn-in MCMC chain are randomly selected  
 1210 (Where for all plots of this style in this thesis,  $N = 3000$ ). From these, the Monte Carlo  
 1211 prediction at each step is generated by reweighting the model parameters to the values  
 1212 specified at that step. Due to the probability density being directly correlated with  
 1213 the density of steps in a certain region, parameter values close to the best fit value are  
 1214 most likely to be selected.

1215 In practice, for each bin of the fitting parameters has a probability distribution  
 1216 of event rates, with one entry per sampled MCMC step. This distribution is binned  
 1217 where the bin with the highest probability is selected as the mean and an error on

1218 the width of this probability distribution is calculated using the approach highlighted  
1219 in subsection 4.3.2. Consequently, the best fit distribution in the fit parameter is not  
1220 necessarily that which would be attained by reweighting the Monte Carlo prediction  
1221 to the most probable parameter values.

1222 A similar study can be performed to illustrate the freedom of the model parameter  
1223 space prior to the fit. This can be done by throwing parameter values from the prior  
1224 uncertainty of each parameter. This becomes troublesome for parameters with no  
1225 prior uncertainty as the range is technically infinite. Where applicable solutions to  
1226 remove these have been addressed.

<sub>1227</sub> **Chapter 5**

<sub>1228</sub> **Simulation, Reconstruction, and Event  
Reduction**

<sub>1230</sub> As a crucial part of the oscillation analysis, an accurate prediction of the expected  
<sub>1231</sub> neutrino spectrum at the far detector is required. This includes modeling the flux  
<sub>1232</sub> generation, neutrino interactions, and detector effects. All of the simulation packages  
<sub>1233</sub> required to do this are briefly described in section 5.1. The reconstruction of neutrino  
<sub>1234</sub> events inside the far detector, including the `fitQun` algorithm, is documented in  
<sub>1235</sub> section 5.2. This also includes data quality checks of the SK-V data which the author  
<sub>1236</sub> performed for the T2K oscillation analysis presented at Neutrino 2020 [80]. Finally,  
<sub>1237</sub> section 5.3 describes the steps taken in the SK detector to trigger on events of interest  
<sub>1238</sub> whilst removing the comparatively large rate of cosmic ray muon events.

<sub>1239</sub> **5.1 Simulation**

<sub>1240</sub> In order to generate a Monte Carlo prediction of the expected event rate at the far  
<sub>1241</sub> detector, all the processes in the beam and atmospheric flux, neutrino interaction, and  
<sub>1242</sub> detector need to be modeled. Each of these parts is individually modeled and each of  
<sub>1243</sub> them is detailed below.

<sub>1244</sub> The beamline simulation consists of three distinct parts: the initial hadron inter-  
<sub>1245</sub> action modeled by FLUKA [142], the target station geometry and particle tracking

performed by JNUBEAM, [143, 144] and any hadronic re-interactions simulated by GCALOR [145]. The primary hadronic interactions are  $O(10)\text{GeV}$ , where FLUKA matches external cross-section data better than GCALOR [146]. However, FLUKA is not very adaptable so a small simulation is built to model the interactions in the target and the output is then passed to JNUBEAM and GCALOR for propagation. The hadronic interactions are tuned to data from the NA61/SHINE [147–149] and HARP [150] experiments. The tuning is done by reweighting the FLUKA and GCALOR predictions to match the external data multiplicity and cross-section measurements, based on final state particle kinematics [146]. The culmination of this simulation package generates the predicted flux for neutrino and antineutrino beam modes which are illustrated in Figure 3.7.

The atmospheric neutrino flux **predictions are is** simulated by the HKKM model [43, 45]. The primary cosmic ray flux is tuned to AMS [151] and BESS [152] data assuming the US-standard atmosphere '76 [153] density profile and includes geomagnetic field effects. The primary cosmic rays interact to generate pions and muons. The interaction of these secondary particles to generate neutrinos is handled by DPMJET-III [154] for energies above 32GeV and JAM [45, 155] for energies below that value **DB: Question for Giles: Why different generators for above/below 32GeV?**. These hadronic interactions are tuned to BESS and L3 data [156, 157] using the same methodology as the tuning of the beamline simulation. The energy and cosine zenith predictions of  $\nu_e, \bar{\nu}_e, \nu_\mu, \bar{\nu}_\mu$  flux are given in Figure 2.3 and Figure 2.5, respectively. The flux is approximately symmetrical and peaked around the horizon ( $\cos(\theta_Z) = 0.0$ ). This is because horizontally-going pions and kaons can travel further than their vertically-going counterparts resulting in a larger probability of decaying to neutrinos. The symmetry is broken in low-energy neutrinos due to geomagnetic effects, which modify the track of the primary cosmic rays. Updates to the HKKM model are currently ongoing [158].

Once a flux prediction has been made for all three detectors, NEUT 5.4.0 [159, 160] models the interactions of the neutrinos in the detectors. For the purposes of this analysis, quasi-elastic (QE), meson exchange (MEC), single meson production (PROD), coherent pion production (COH), and deep inelastic scattering (DIS) interactions are simulated. These interaction categories can be further broken down by whether they were propagated via a  $W^\pm$  boson in Charged Current (CC) interactions or via a  $Z^0$  boson in Neutral Current (NC) interactions. CC interactions have a charged lepton in the final state, which can be flavour-tagged in reconstruction to determine the flavour of the neutrino. In contrast, NC interactions have a neutrino in the final state so no flavour information can be determined from the observables left in the detector after an interaction. **This is the reason why NC events** **This is the reason why neutrinos which interact through NC modes** are assumed to not oscillate within this analysis. Both CC and NC interactions are modeled for all the above interaction categories, other than MEC interactions which are only modeled for CC events. The SK detector is only sensitive to charged particles, so all charged current interactions are simulated whilst only neutral current processes that produce charged mesons (NCDIS, NCCOH, and NCPROD) are modeled. NC MEC interactions can only produce charged particles through secondary re-interactions which is a low cross-section process.

As illustrated in Figure 5.1, CC QE interactions dominate the low-energy cross-section of neutrino interactions. The NEUT implementation adopts the Llewellyn Smith [161] model for neutrino-nucleus interactions, where the nuclear ground state of any bound nucleons (neutrino-oxygen interactions) is approximated by a spectral-function [162] model that simulates the effects of Fermi momentum and Pauli blocking. The cross-section of QE interactions are controlled by vector and axial-vector form factors parameterised by the BBBA05 [163] model and a dipole form factor with  $M_A^{QE} = 1.21\text{GeV}$  fit to external data [164], respectively. NEUT implements the Valencia

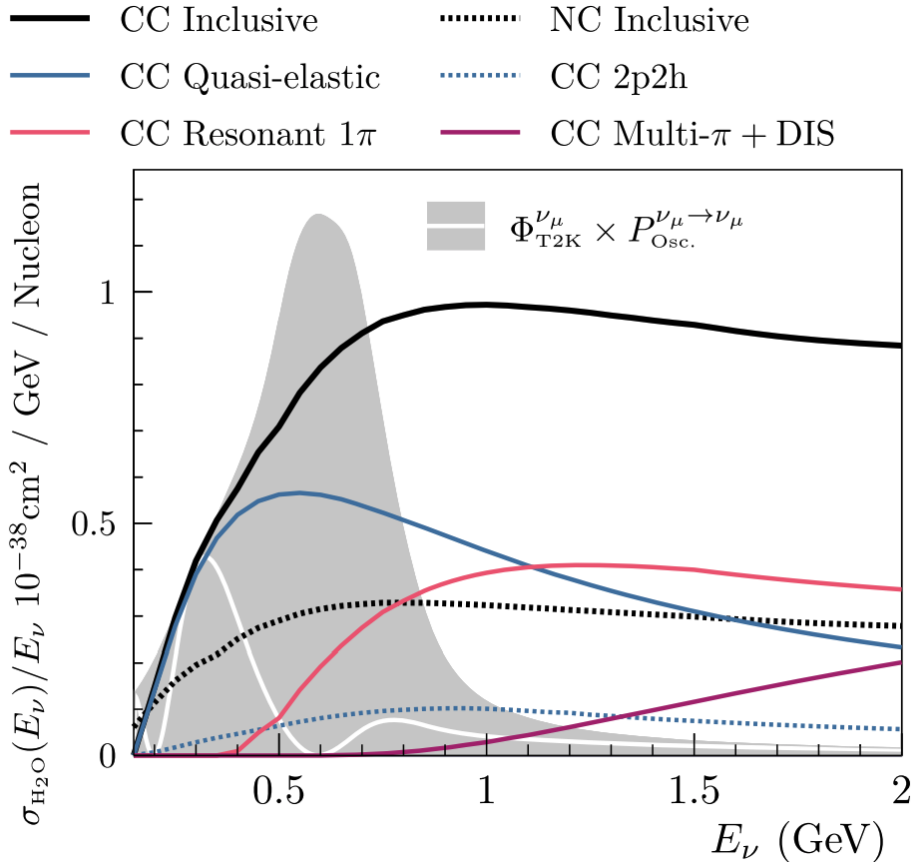


**Figure 5.1:** The NEUT prediction of the  $\nu_\mu$ -H<sub>2</sub>O cross-section overlaid on the T2K  $\nu_\mu$  flux. The charged current (black, solid) and neutral current (black, dashed) inclusive, charged current quasi-elastic (blue, solid), charged current 2p2h (blue, dashed), charged current single pion production (pink), and charged current multi- $\pi$  and DIS (Purple) cross-sections are illustrated. Figure taken from [159].

[1298] model to simulate MEC events, where two nucleons and two holes in the nuclear  
 [1299] target are produced (Often called 2p2h interactions).

[1300] For neutrinos of energy  $O(1)\text{GeV}$ , PROD interactions become dominant. These  
 [1301] predominantly produce charged and neutral pions although  $\gamma$ , kaon, and  $\eta$  production  
 [1302] is also considered. To simulate these interactions, the Berger-Sehgal [166] model is  
 [1303] implemented within NEUT. It simulates the excitation of a nucleon from a neutrino  
 [1304] interaction, production of an intermediate baryon, and the consequential decay to a  
 [1305] single meson or  $\gamma$ . Pions can also be produced through COH interactions, which occur  
 [1306] when the incoming neutrino interacts with the entire oxygen nuclei target leaving a

1307 single pion outside of the nucleus. NEUT utilises the Berger-Sehgal [167] model to  
1308 simulate these COH interactions.

1309 DIS and multi- $\pi$  producing interactions become the most dominant for energies  
1310  $> O(5)\text{GeV}$ . PYTHIA [168] is used to simulate any interaction with invariant mass,  
1311  $W > 2\text{GeV}/c^2$ , which produces at least one meson. For any interaction which produces  
1312 at least two mesons but has  $W < 2\text{GeV}/c^2$ , the Bronner model is invoked [169].  
1313 Both of these models use Parton distribution functions based on the Bodek-Yang  
1314 model [170–172].

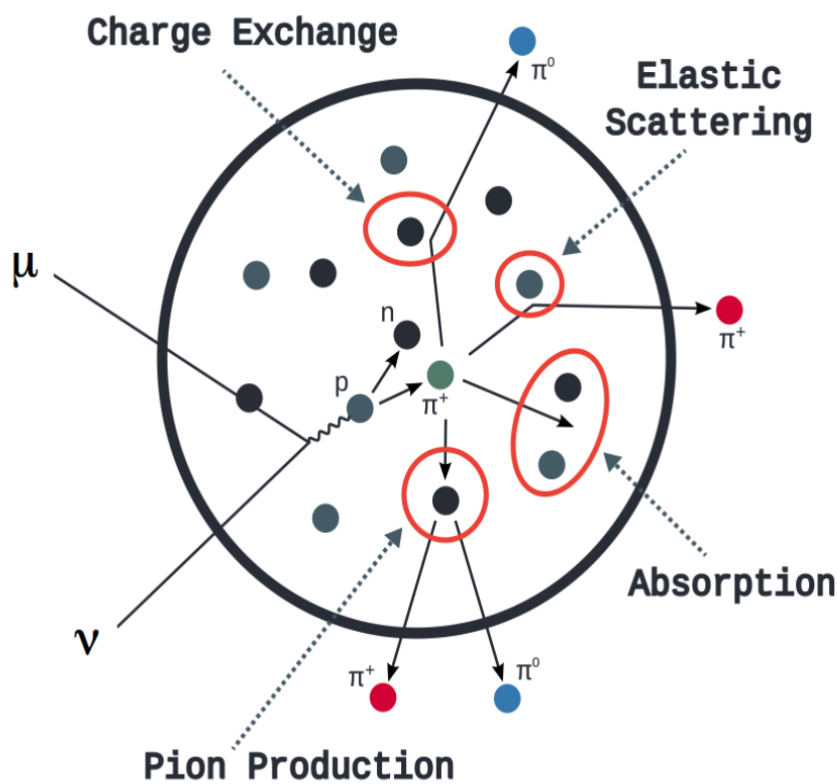


**Figure 5.2:** Illustration of the various processes which a pion can undergo before exiting the nucleus. Taken from [173].

1315 Any pion which is produced within the nucleus can re-interact through final state  
1316 interactions before it exits, as illustrated by the scattering, absorption, production, and  
1317 exchange interactions in Figure 5.2. These re-interactions alter the observable particles

1318 within the detector. For instance, if the charged pion from a CC PROD interaction is  
1319 absorbed, the observables would mimic a CC QE interaction. To simulate these effects,  
1320 NEUT uses a semi-classical intranuclear cascade model [159]. This cascade functions by  
1321 stepping the pion through the nucleus in fixed-length steps equivalent to  $dx = R_N/100$ ,  
1322 where  $R_N$  is the radius of the nucleus. At each step, the simulation allows the pion  
1323 to interact through scattering, charged exchange, absorption, or production with an  
1324 interaction-dependent probability calculated from a fit to external data [174]. This  
1325 cascade continues until the pion is absorbed or exits the nucleus.

1326 Once the final state particle kinematics have been determined from NEUT, they  
1327 are passed into the detector simulation. The near detectors, ND280 and INGRID, are  
1328 simulated using a GEANT4 package [118,175] to simulate the detector geometry, particle  
1329 tracking, and energy deposition. The response of the detectors is simulated using  
1330 the elecSim package [118]. The far detector simulation is based upon the original  
1331 Kamiokande experiment software which uses the GEANT3-based SKDETSIM [118,176]  
1332 package. This controls the interactions of particles in the water as well as Cherenkov  
1333 light production. The water quality and PMT calibration measurements detailed in  
1334 subsection 3.1.2 are also used within this simulation to make accurate predictions of  
1335 the detector response.

## 1336 5.2 Event Reconstruction at SK

1337 Any above Cherenkov threshold event which occurs in SK will be recorded by the  
1338 PMT array, where each PMT records the time and accumulated charge. This recorded  
1339 information is shown in event displays similar to those illustrated in Figure 5.3. To  
1340 be useful for physics analyses, this series of PMT hit information needs to be recon-  
1341 structed to determine the particle's identity and kinematics (or track parameters):

1342 four-vertex, direction, and momenta. This is because the charge and timing distribu-  
 1343 tion of photons generated by a particular particle in an event is dependent upon its  
 1344 initial kinematics. The concept of distinguishing electron and muon events is from the  
 1345 “fuzziness” of the ring. Muons are heavier and less affected by scattering or showering  
 1346 meaning they typically produce “crisp” rings. Electrons are more likely to interact  
 1347 via electromagnetic showering or scattering which results in larger variations of their  
 1348 direction from the initial direction. Consequently, electrons typically produce “fuzzier”  
 1349 rings compared to muons.

1350 For the purposes of this analysis, the `fitQun` reconstruction algorithm is utilised.  
 1351 Its core function is to compare a prediction of the accumulated charge and timing  
 1352 distribution from each PMT, generated for a particular particle identity and track  
 1353 parameters, to that observed in the neutrino event. It determines the preferred values  
 1354 by minimising a likelihood function which includes information from PMTs which  
 1355 were hit and those that were not hit. The `fitQun` algorithm improves upon the APFit  
 1356 reconstruction algorithm which has been used for many previous SK analyses. APFit  
 1357 fits the vertex from timing information and then fits the momentum and direction  
 1358 of the particle from PMT hits within a 43 deg Cherenkov cone (which assumes an  
 1359 ultra-relativistic particle). It then fits the particle identity once the track parameters  
 1360 have been fit. Conversely, `fitQun` performs a simultaneous fit of particle kinematics  
 1361 and identity, improving both the accuracy of the fit parameters and the rejection of  
 1362 neutral current  $\pi^0$  events [177,178]. The `fitQun` algorithm is based on the key concepts  
 1363 of the MiniBooNE reconstruction algorithm [179] and is described in [180] which is  
 1364 summarised below.

1365 An event in SK can consist of multiple particles. For example, a charge current  
 1366 muon neutrino interaction can generate two particles that have the potential of gen-  
 1367 erating Cherenkov photons: the primary muon, and the secondary decay-electron

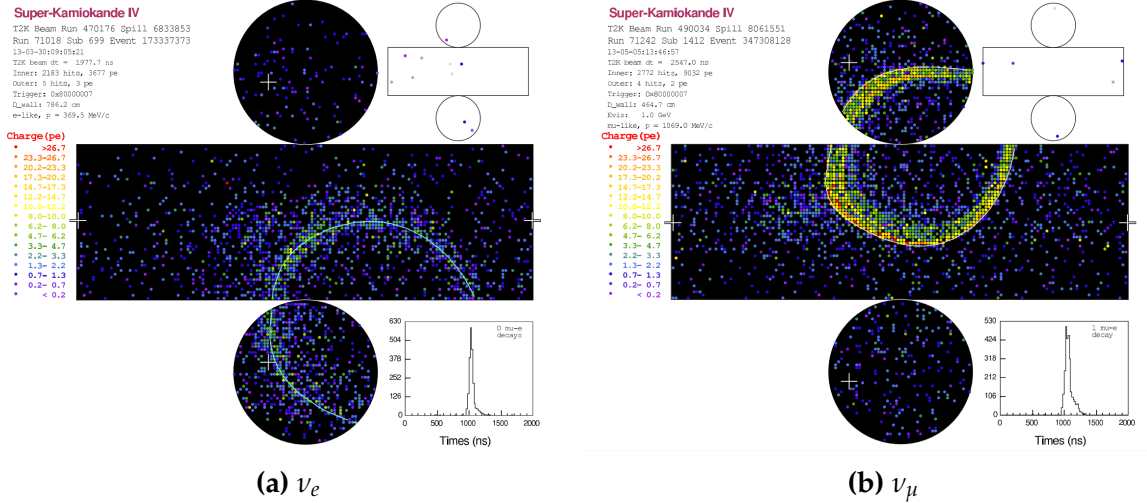


**Figure 5.3:** Event displays from Super Kamiokande illustrating the “crisp” ring from a muon and the typically “fuzzy” electron ring. Each pixel represents a PMT and the color scheme denotes the accumulated charge deposited on that PMT. Figures taken from [181].

from the muon. To ensure both subevents are reconstructed separately, each event is divided into time clusters which are called “subevents”. The number of subevents is equal to the number of decay electrons minus one (the primary event). To find all the subevents in an event, a vertex goodness metric is calculated for some vertex position  $\vec{x}$  and time  $t$ ,

$$G(\vec{x}, t) = \sum_i^{\text{hit PMTs}} \exp \left( -\frac{1}{2} \left( \frac{T_{Res}^i(\vec{x}, t)}{\sigma} \right)^2 \right) \quad (5.1)$$

where

$$T_{Res}^i(\vec{x}, t) = t^i - t - |R_{PMT}^i - \vec{x}| / c_n \quad (5.2)$$

1374        is the residual hit time. It is the difference in time between the PMT hit time,  $t^i$ ,  
 1375        of the  $i^{th}$  PMT and the expected time of the PMT hit if the photon was emitted at  
 1376        the start of the vertex.  $R_{PMT}^i$  is the position of the  $i^{th}$  PMT,  $c_n$  is the speed of light in  
 1377        water and  $\sigma = 4\text{ns}$  which is comparable to the time resolution of the PMT. When the  
 1378        proposed fit values of time and vertex are close to the true values,  $T_{Res}^i(\vec{x}, t)$  tends to  
 1379        zero resulting in subevents appearing as spikes in the goodness metric. The proposed  
 1380        fit vertex and time are grid-scanned, and the values which maximise the goodness  
 1381        metric are selected as the “pre-fit vertex”. Whilst this predicts a vertex for use in  
 1382        the clustering algorithm, the final vertex is fit using the higher-precision maximum  
 1383        likelihood method described below.

1384        Once the pre-fit vertex has been determined, the goodness metric is scanned as  
 1385        a function of  $t$  to determine the number of subevents. A peak-finding algorithm is  
 1386        then used on the goodness metric, requiring the goodness metric to exceed some  
 1387        threshold and drop below a reduced threshold before any subsequent additional  
 1388        peaks are considered. The thresholds are set such that the rate of false peak finding  
 1389        is minimised while still attaining good data to Monte Carlo agreement. To improve  
 1390        performance, the pre-fit vertex for each delayed subevent is re-calculated after PMT  
 1391        hits from the previous subevent are masked. This improves the decay-electron tagging  
 1392        performance. Once all subevents have been determined, the time window around  
 1393        each subevent is then defined by the earliest and latest time which satisfies  $-180 <$   
 1394         $T_{Res}^i < 800\text{ns}$ . The subevents and associated time windows are then used as seeds for  
 1395        further reconstruction.

1396        For a given subevent, the `fitQun` algorithm constructs a likelihood based on the  
 1397        accumulated charge  $q_i$  and time information  $t_i$  from the  $i^{th}$  PMT,

$$L(\Gamma, \vec{\theta}) = \prod_j^{\text{unhit}} P_j(\text{unhit}|\Gamma, \vec{\theta}) \prod_i^{\text{hit}} \{1 - P_i(\text{unhit}|\Gamma, \vec{\theta})\} f_q(q_i|\Gamma, \vec{\theta}) f_t(t_i|\Gamma, \vec{\theta}), \quad (5.3)$$

1398 where  $\vec{\theta}$  defines the track parameters; vertex position, direction vector and mo-  
 1399 ments, and  $\Gamma$  represents the particle hypothesis.  $P_i(\text{unhit}|\Gamma, \vec{\theta})$  defines the probability  
 1400 of the  $i^{\text{th}}$  tube to not register a hit given the track parameters and particle hypothesis.  
 1401 The charge likelihood,  $f_q(q_i|\Gamma, \vec{\theta})$ , and time likelihood,  $f_t(t_i|\Gamma, \vec{\theta})$ , represent the prob-  
 1402 ability density function of observing charge  $q_i$  and time  $t_i$  on the  $i^{\text{th}}$  PMT given the  
 1403 specified track parameters and particle hypothesis.

1404 As the generation and propagation of the optical photons are independent of the  
 1405 PMT and electronics response, it is natural to split the calculation into two. Firstly,  
 1406 the expected number of photoelectrons (or predicted charge),  $\mu_i = \mu_i(\vec{\theta}, \Gamma)$ , at the  $i^{\text{th}}$   
 1407 PMT is calculated. This value is then substituted into the likelihood function. This  
 1408 allows the charge likelihood density  $f_q(q_i|\mu_i)$  and unhit probability  $P_i(\text{unhit}|\mu_i)$  to be  
 1409 expressed via quantities that are only dependent on the response of the PMT.

1410 The predicted charge is calculated based on contributions from both the direct  
 1411 light and the scattered light. The direct light contribution is determined based on the  
 1412 integration of the Cherenkov photon profile along the track. PMT angular acceptance,  
 1413 water quality, and calibration measurements discussed in subsection 3.1.2 are included  
 1414 to accurately predict the charge probability density at each PMT. The scattered light  
 1415 is calculated in a similar way, although it includes a scattering function that depends  
 1416 on the vertex of the particle and the position of the PMT. The charge likelihood is  
 1417 calculated by comparing the prediction to the observed charge in the PMT.

1418 The time likelihood is approximated to depend on the vertex  $\vec{x}$ , direction  $\vec{d}$ , and  
 1419 time  $t$  of the track parameters as well as the particle hypothesis. The expected time

<sup>1420</sup> for PMT hits is calculated by assuming unscattered photons being emitted from the  
<sup>1421</sup> midpoint of the track,  $S_{mid}$ ,

$$t_{exp}^i = t + S_{mid}/c + |R_{PMT}^i - \vec{x} - S_{mid}\vec{d}|/c_n, \quad (5.4)$$

<sup>1422</sup> where  $c$  is the speed of light in a vacuum. The time likelihood is then expressed in  
<sup>1423</sup> terms of the residual difference between the PMT hit time and the expected hit time,  
<sup>1424</sup>  $t_{Res}^i = t^i - t_{exp}^i$ . The particle hypothesis and momentum also affect the Cherenkov  
<sup>1425</sup> photon distribution. These parameters modify the shape of the time likelihood density  
<sup>1426</sup> since in reality not all photons are emitted at the midpoint of the track. As with the  
<sup>1427</sup> charge likelihood, the contributions from both the direct and scattered light to the time  
<sup>1428</sup> likelihood density are calculated separately, which are both calculated from particle  
<sup>1429</sup> gun studies.

<sup>1430</sup> The track parameters and particle identity which maximise  $L(\Gamma, \vec{\theta})$  are defined as  
<sup>1431</sup> the best-fit parameters. In practice MINUIT [182] is used to minimise the value of  
<sup>1432</sup>  $-\ln L(\Gamma, \vec{\theta})$ . The `fitQun` algorithm considers an electron-like, muon-like, and charged  
<sup>1433</sup> pion-like hypothesis for events with a single final state particle, denoted “single-ring  
<sup>1434</sup> events”. The particle’s identity is determined by taking the ratio of the likelihood  
<sup>1435</sup> of each of the hypotheses. For instance, electrons and muons are distinguished by  
<sup>1436</sup> considering the value of  $\ln(L(e, \vec{\theta}_e)/L(\mu, \vec{\theta}_\mu))$  in comparison to the reconstructed  
<sup>1437</sup> momentum of the electron hypothesis [180]. This distance from this criteria is termed  
<sup>1438</sup> the PID parameter and is illustrated in Figure 5.4.

<sup>1439</sup> **DB: Mention Pi0 rejection and mu/pip separation cuts**

<sup>1440</sup> The `fitQun` algorithm also considers a  $\pi^0$  hypothesis. To do this, it performs a  
<sup>1441</sup> fit looking for two standard electron-hypothesis tracks which point to the same four-

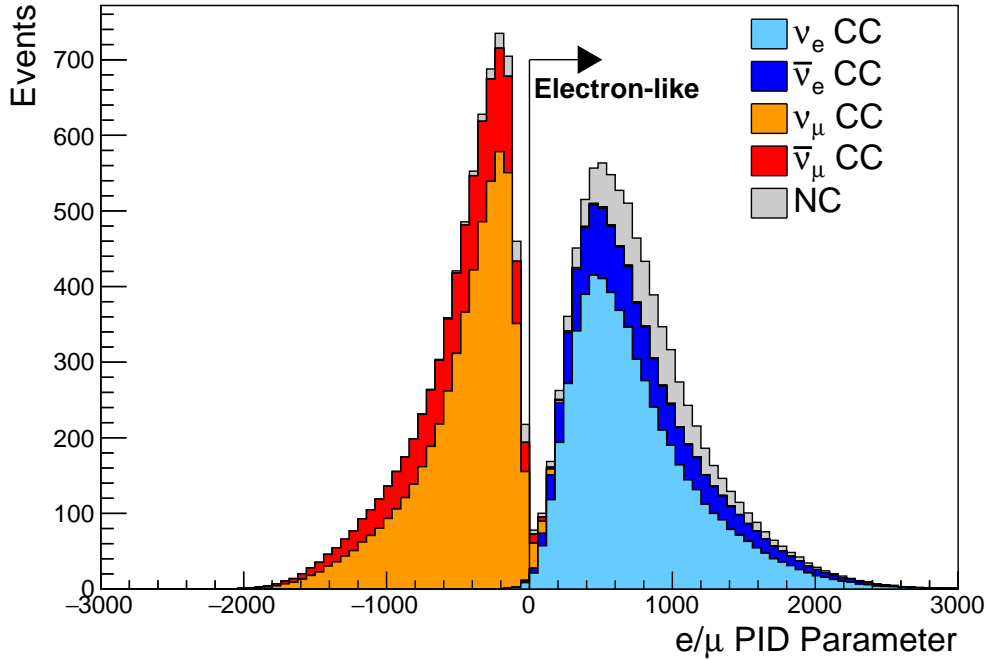


**Figure 5.4:** The electron/muon PID separation parameter for all sub-GeV single-ring events in SK-IV. The charged current (CC) component is broken down in four flavours of neutrino ( $\nu_\mu$ ,  $\bar{\nu}_\mu$ ,  $\nu_e$  and  $\bar{\nu}_e$ ). Events with positive values of the parameter are determined to be electron-like.

1442 vertex. This assumes the electron tracks are generated from photon-conversion so the  
 1443 electron tracks actually appear offset from the proposed  $\pi^0$  vertex. For these fits, the  
 1444 conversion length, direction, and momenta of each photon are also considered as track  
 1445 parameters which are then fit in the same methodology as the standard single-ring  
 1446 hypotheses.

1447 Whilst low energy events are predominately single-ring events, higher energy  
 1448 neutrino events can generate final states with multiple particles which generate  
 1449 Cherenkov photons. These “multi-ring” hypotheses are also considered in the `fitQun`  
 1450 algorithm. When calculating the charge likelihood density, the predicted charge  
 1451 associated with each ring is calculated separately and then merged to calculate the  
 1452 total accumulated charge on each PMT. Similarly, the time likelihood for the multi-ring  
 1453 hypothesis is calculated assuming each ring is independent. Each track is time-ordered

1454 based on the time of flight from the center of the track to the PMT and the direct light  
1455 from any ring incident on the PMT is assumed to arrive before any scattered light. To  
1456 reduce computational resources, the multi-ring fits only consider electron-like and  
1457 charged pion-like rings as the pion fit can be used as a proxy for a muon fit due to  
1458 their similar mass.

1459 Multi-ring fits proceed by proposing another ring to the previous fit and then  
1460 fitting the parameters in the method described above. Typically, multi-ring fits have  
1461 the largest likelihood because of the additional degrees of freedom introduced. Conse-  
1462 quently, the additional ring is only added if the ratio of likelihoods passes a criterion,  
1463 which is determined by Monte Carlo studies.

1464 As an example of how the reconstruction depends on the detector conditions, the  
1465 author of this thesis assessed the quality of event reconstruction for SK-V data. The  
1466 detector systematics invoked within the T2K-only oscillation analysis are determined  
1467 using data to Monte Carlo comparisons using the SK-IV data [183]. Due to tank-open  
1468 maintenance occurring between SK-IV and SK-V, the dark rate of each PMT was  
1469 observed to increase in SK-V due to light exposure for a significant time during the  
1470 repairs. This increase can be seen in Figure 5.5. Run-10 of the T2K experiment was  
1471 conducted in the SK-V period, so the consistency of SK-IV and SK-V data needs to  
1472 be studied to determine whether the SK-IV-defined systematics can be applied to the  
1473 run-10 data. This comparison study was performed using the stopping muon data set  
1474 for both the SK-IV and SK-V periods. This data sample is used due to the high rate of  
1475 interactions ( $O(200)$  events per hour) as well as having similar energies to muons from  
1476 CCQE  $\nu_\mu$  interactions from beam interactions. The rate of cosmic muons does depend  
1477 on the solar activity cycle [184] but has been neglected in this comparison study. This  
1478 is because the shape of the distributions is most important for the purposes of being

<sup>1479</sup> compared to the detector systematics. The SK-IV and SK-V data samples consist of  
<sup>1480</sup> 2398.42 and 626.719 hours of data which equates to 686k and 192k events respectively.

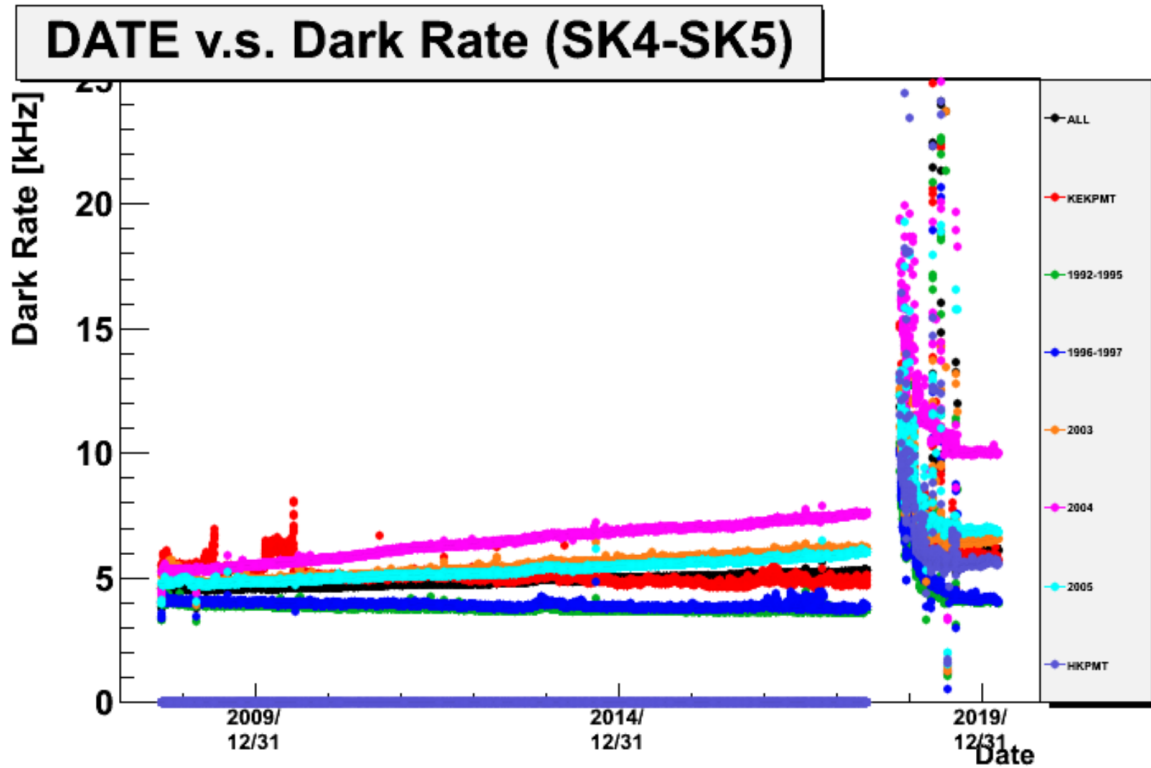


**Figure 5.5:** The variation of the measured dark rate as a function of date, broken down by PMT type. The SK-IV and SK-V periods span September 2008 to May 2018 and January 2019 to July 2020, respectively. The break in measurement in 2018 corresponds to the period of tank repair and refurbishment. Figure adapted from [183].

<sup>1481</sup> The predicted charge calculated in the `f1TQun` charge likelihood prediction includes  
<sup>1482</sup> a contribution from the photoelectron emission due to dark noise. Therefore, the  
<sup>1483</sup> increase in the SK-V dark rate needs to be accounted for. In practice, the average dark  
<sup>1484</sup> rate in each SK period is calculated and used as an input in the reconstruction. This  
<sup>1485</sup> is calculated by averaging the dark rate per run for each period separately, using the  
<sup>1486</sup> calibration measurements detailed in subsection 3.1.2. The average dark rate from  
<sup>1487</sup> SK-IV and SK-V were found to be 4.57kHz and 6.30kHz, respectively. The associated  
<sup>1488</sup> charge with the muon and decay electron subevents are illustrated in Figure 5.6. The

photoelectron emission from dark noise will be more noticeable for events that have lower energy. This is because this contribution becomes more comparable to the number of photoelectrons emitted from incident photons in low-energy events. This behaviour is observed in the data, where the charge deposited by the muon subevent is mostly unaffected by the increase in dark rate, whilst the charge associated with the decay-electron is clearly affected.

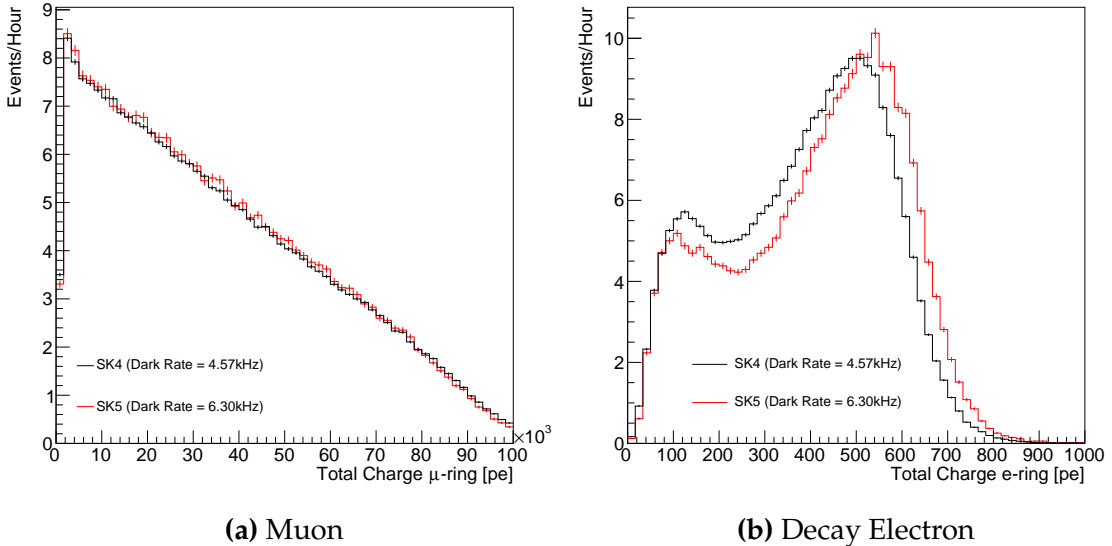


**Figure 5.6:** Comparison of the measured raw charge deposited per event from the stopping muon data samples between SK-IV (Blue) and SK-V (Red), split by the primary muon subevent and the associated decay electron subevent.

The energy scale systematic for the SK-IV period was determined to be 2.1% [185]. It is defined to be equal to the difference between data and Monte Carlo prediction in the stopping muon data sample. To determine the consistency of the SK-IV and SK-V with respect to the energy scale systematic, the muon momentum distribution is compared between the two SK periods. As the total number of Cherenkov photons is integrated across the track length, the reconstructed momentum divided by track length (or range) is compared between SK-IV and SK-V as illustrated in Figure 5.7.

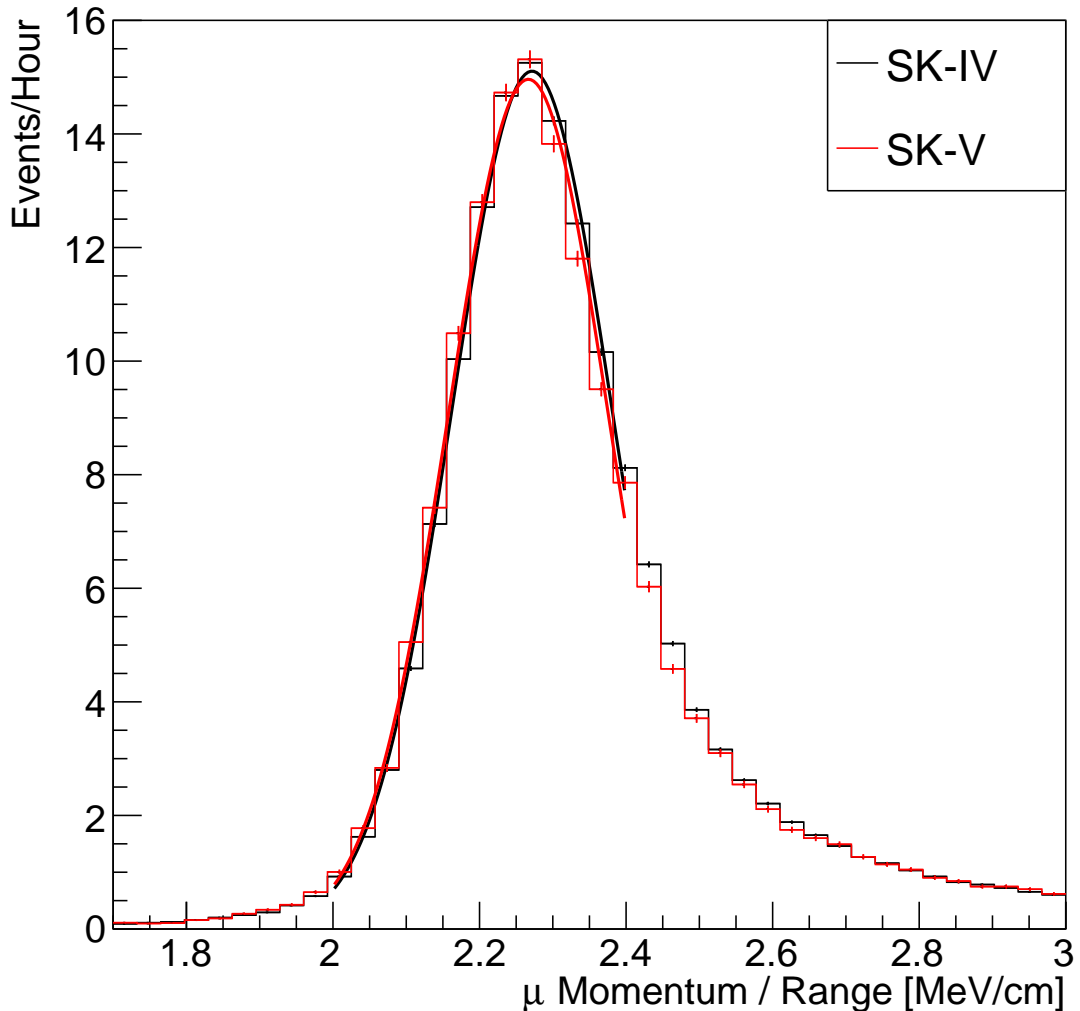


**Figure 5.7:** The distribution of the reconstructed momentum from the muon ring divided by the distance between the reconstructed muon and decay electron vertices as found in the stopping muon data sets of SK-IV (Black) and SK-IV (Red). Only events with one tagged decay electron are considered. A Gaussian fit is considered in the range [2.0, 2.4] MeV/cm and illustrated as the solid curve.

1502        The consistency between these distributions has been computed in two ways.  
 1503        Firstly, a Gaussian is fit to each distribution separately. The mean of which is found to  
 1504        be  $(2.272 \pm 0.003)$  MeV/cm and  $(2.267 \pm 0.006)$  MeV/cm for SK-IV and SK-V respec-  
 1505        tively. The ratio of these is equal to  $1.002 \pm 0.003$ . The mean of the Gaussian fits are  
 1506        consistent with the expected stopping power of a minimum ionising muon for a target  
 1507        material (water) with  $Z/A \sim 0.5$  [186]. The second consistency check is performed by

1508 introducing a nuisance parameter,  $\alpha$ , which modifies the SK-V distribution. The value  
 1509 of  $\alpha$  which minimises the  $\chi^2$  value between the SK-IV and SK-V is determined by  
 1510 scanning across a range of values. This is repeated by applying the nuisance parameter  
 1511 as both a multiplicative factor and an additive shift. The  $\chi^2$  distributions for different  
 1512 values of  $\alpha$  is illustrated in Figure 5.8. The values which minimise the  $\chi^2$  are found to  
 1513 be 0.0052 and 1.0024 for the additive and multiplicative implementations, respectively.  
 1514 No evidence of shifts larger than the 2.1% uncertainty on the energy scale systematic  
 1515 has been found in the reconstructed momentum distribution of SK-IV and SK-V.

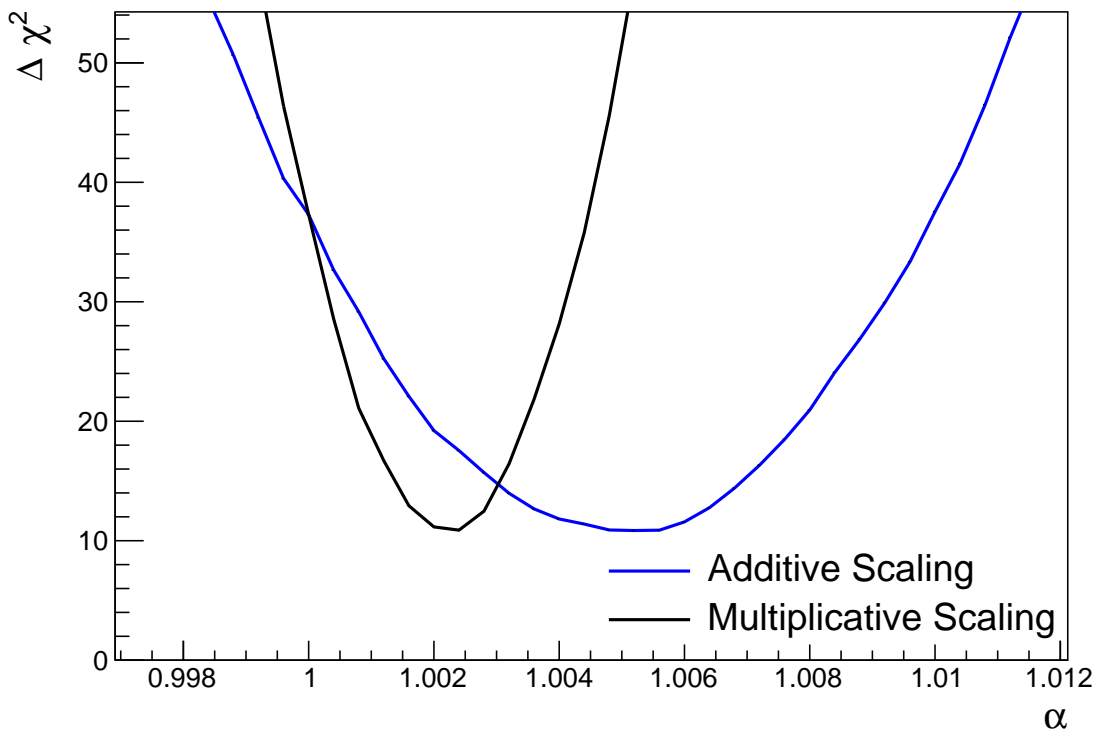


**Figure 5.8:** The  $\chi^2$  difference between the SK-IV and SK-V reconstructed muon momentum divided by range when the SK-V is modified by the scaling parameter  $\alpha$ . Both additive (Blue) and multiplicative (Black) scaling factors have been considered. In practice, the additive scaling factor actually uses the value of  $(\alpha - 1.0)$  but is illustrated like this so the results can be shown on the same axis range.

## 1516 5.3 Event Reduction at SK

1517 Atmospheric neutrino events observed in the SK detector are categorised into three  
1518 different types of samples: fully contained (FC), partially contained (PC) and up-  
1519 going muon (Up- $\mu$ ), using PMT hit signatures in the inner and outer detector (ID  
1520 and OD, respectively). To identify FC neutrino events, it is required that the neutrino  
1521 interacts inside the fiducial volume of the ID such that no significant OD activity is  
1522 observed. For this analysis, an event is defined to be in the fiducial volume providing  
1523 the event vertex is at least 0.5m away from the ID walls. PC events have the same  
1524 ID requirements but can have a larger signal present inside the OD. Typically these  
1525 events are higher energy muon interactions that penetrate the ID walls. The Up- $\mu$   
1526 sample contains events where muons are created from neutrino interactions in the  
1527 OD water or rock below the tank. They then propagate upwards through the detector.  
1528 The reason downward-going muons generated from neutrino interactions above the  
1529 tank are neglected is due to the difficulty in separating their signature from the cosmic  
1530 muon shower background. The sample categories are visually depicted in Figure 5.9.

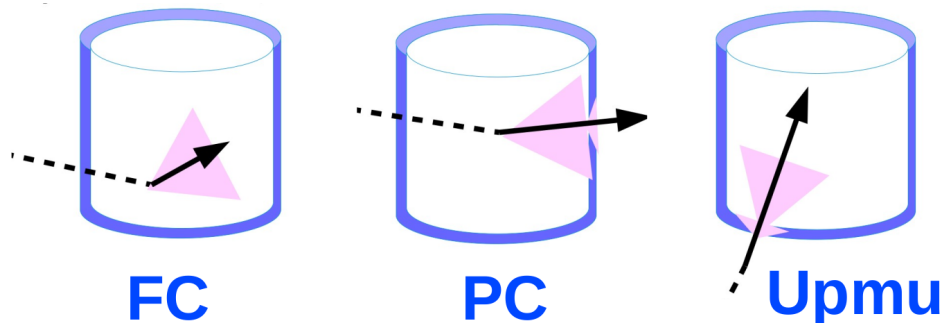


**Figure 5.9:** A depiction of the topology patterns for fully-contained (FC), partially-contained (PC) and up-going muon (Up- $\mu$ ) samples included in this analysis.

1531 Based on the event characteristics, as defined by the `fitQun` event reconstruction  
1532 software, the FC events are categorised by

- **Visible Energy:** equal to the sum of the reconstructed kinetic energy above the Cerenkov threshold for all rings present in the event. The purpose is to separate events into sub-GeV and multi-GeV categories.
- **Number of observed Cerenkov rings.** The purpose is to separate single-ring and multi-ring events, where single-ring events predominantly consist of quasi-elastic interactions and multi-ring events are typically resonant pion production or deep inelastic scattering events.
- **Particle identification parameter of the most energetic ring:** A value determined from the maximum likelihood value based on fiTQun's electron, muon, or pion hypothesis. The purpose is to separate electron-like and muon-like events.
- **Number of decay electrons:** The purpose is to separate quasi-elastic events (which have one decay electron emitted from the muon decay) and resonant pion production events (which have two decay electrons emitted from the muon and pion).

The PC and Up- $\mu$  categories are broken down into “through-going” and “stopping” samples depending on whether the muon left the detector. This is because the stopping events deposit the entire energy of the interaction into the detector, resulting in better reconstruction. The energy of events that exit the detector has to be estimated which introduces much larger systematic uncertainties. Through-going Up- $\mu$  samples are further broken down by whether any hadronic showering was observed in the event which typically indicates DIS interactions. The expected neutrino energy for the different categories is given in Figure 5.10. FC sub-GeV and multi-GeV events peak around 0.7GeV and 3GeV respectively, with slightly different peak energies for  $\nu_x \rightarrow \nu_e$  and  $\nu_x \rightarrow \nu_\mu$  oscillation channels. PC and Up- $\mu$  are almost entirely comprised of  $\nu_x \rightarrow \nu_\mu$  events and peak around 7GeV and 100GeV, respectively.

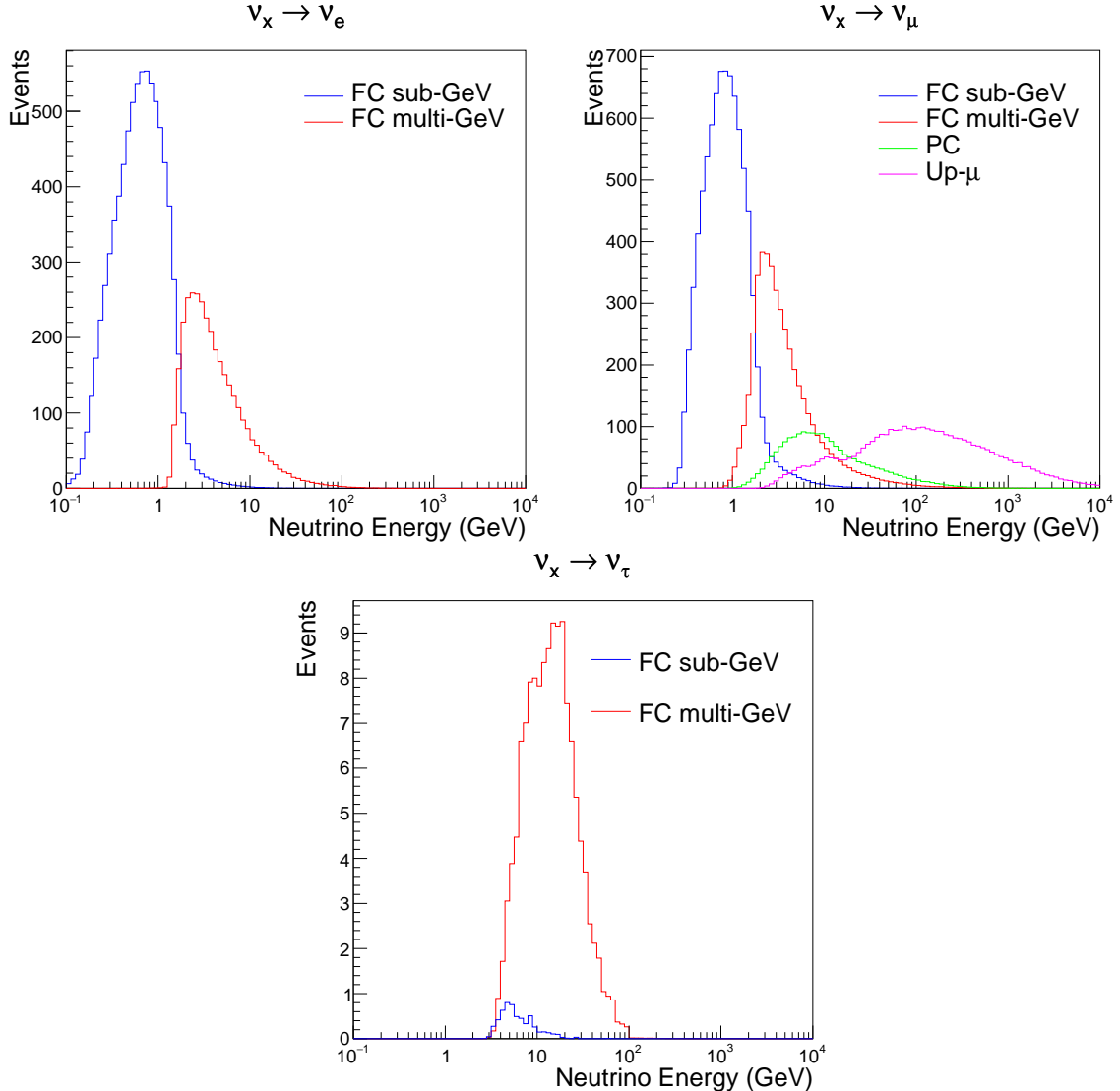


**Figure 5.10:** The predicted neutrino flux of the fully contained (FC) sub-GeV and multi-GeV, partially contained (PC), and upward-going muon (Up- $\mu$ ) events. The prediction is broken down by the  $\nu_x \rightarrow \nu_e$  prediction (top left),  $\nu_x \rightarrow \nu_\mu$  prediction (top right) and  $\nu_x \rightarrow \nu_\tau$  prediction (bottom). All systematic dials are set to their nominal values and the Asimov A oscillation parameters are assumed.

1558     In normal data-taking operations, the SK detector observes many background  
 1559     events alongside the beam and atmospheric neutrino signal events of physics interest.  
 1560     Cosmic ray muons and flasher events, which are the spontaneous discharge of a given  
 1561     PMT, contribute the largest amount of background events in the energy range relevant  
 1562     to any analysis searching for neutrino events. Lower energy analyses like DSNB  
 1563     searches are also subject to radioactive backgrounds [187]. Therefore the data recorded

1564 is reduced with the aim of removing these background events. The reduction process  
1565 is detailed in [47, 89] and briefly summarised below.

1566 The first two steps in the FC reconstruction remove the majority of cosmic ray  
1567 muons by requiring a significant amount of ID activity compared to that measured in  
1568 the OD. Events that pass this cut are typically very high momentum muons or events  
1569 that leave very little activity in the OD. Consequently, a third reduction step is then  
1570 applied to select cosmic-ray muons that pass the initial reduction step. A purpose-built  
1571 cosmic muon fitter is used to determine the entrance (or exit) position of the muon and  
1572 a cut is applied to OD activity contained within 8m of this position. Flasher events are  
1573 removed in the fourth reduction step which is based on the close proximity of PMT  
1574 hits surrounding the PMT producing the flash. Events that pass all these reduction  
1575 steps are reconstructed with the APFit algorithm. The fifth step of the reduction uses  
1576 information from the more precise fitter to repeat the previous two steps with tighter  
1577 cuts. Muons below the Cherenkov threshold can not generate optical photons in the  
1578 ID but the associated decay electron can due to its lower mass. These are the types of  
1579 events targeted in the fifth reduction step. The final cuts require the event vertex to be  
1580 within the fiducial volume (0.5m from the wall although the nominal distance is 2.0m),  
1581 visible energy  $E_{vis} > 30\text{MeV}$  and fewer than 16 hits within the higher energy OD  
1582 cluster. The culmination of the fully contained reduction results in 8.09 events/day in  
1583 the nominal fiducial volume [188]. The uncertainty in the reconstruction is calculated  
1584 by comparing Monte Carlo prediction to data. The largest discrepancy is found to be  
1585 1.3% in the fourth reduction step.

1586 The PC and Up- $\mu$  events are processed through their own reduction processes  
1587 detailed in [47]. Both of these samples are reconstructed with the APFit algorithm  
1588 rather than fitQun. This is because the efficiency of reconstructing events that leave

1589 the detector has not been sufficiently studied for reliable systematic uncertainties. The  
 1590 PC and Up- $\mu$  samples attain events at approximately 0.66 and 1.44 events/day.

1591 Events due to beam neutrinos undergo the same reduction steps as FC events and  
 1592 are then subject to further cuts [189]. The GPS system which links the timing between  
 1593 the beam facility and SK needs to be operating correctly and there should be no activity  
 1594 within the detector in the previous  $100\mu\text{s}$  before the trigger. The events then need to  
 1595 triggered between  $-2\mu\text{s}$  and  $10\mu\text{s}$  of the expected spill timing.

1596 Due to the lower energy beam neutrinos, the T2K samples are not dependent  
 1597 upon the visible energy neutrino as the range of neutrino energies are smaller than  
 1598 that found in atmospheric neutrinos. Furthermore, the 2020 T2K-only oscillation  
 1599 analysis only considers events which contain a single ring. Similar to atmospheric  
 1600 event selection, the number of decay electrons is used as a proxy for distinguishing  
 1601 CCQE and CCRES events. The expected neutrino energy, broken down by number of  
 1602 decay electrons, is given in Figure 5.11.

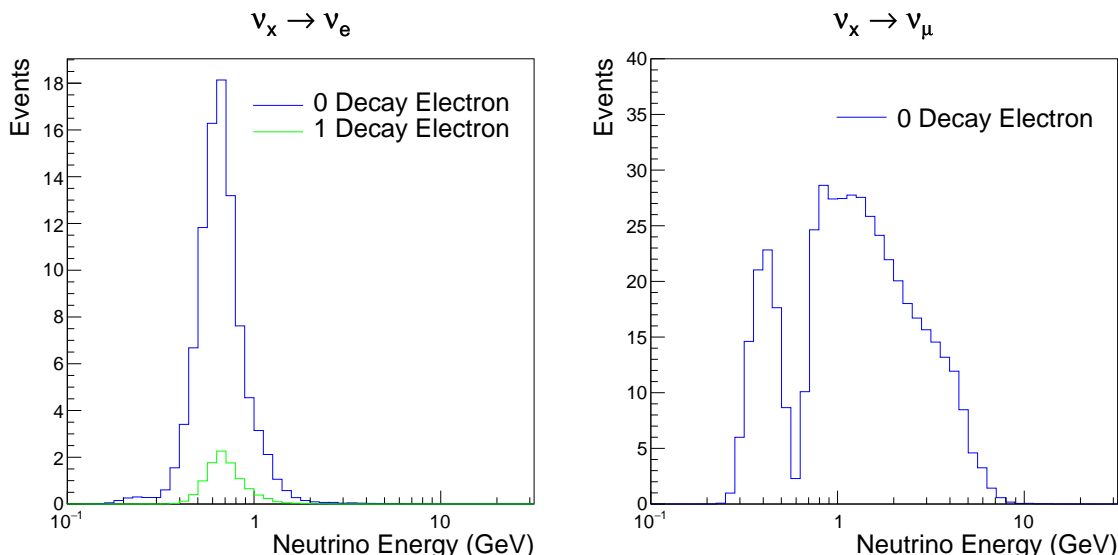


**Figure 5.11:** The predicted neutrino flux of the beam neutrinos, illustrated as a function of neutrino energy. The predictions are broken down by the number of decay electrons associated with the particular events. All systematic dials are set to their nominal values and the Asimov A oscillation parameters are assumed.

<sub>1603</sub> **Chapter 6**

<sub>1604</sub> **Sample Selections and Systematics**

<sub>1605</sub> The oscillation analysis presented within this thesis is built upon a simultaneous  
<sub>1606</sub> fit to atmospheric data at SK, neutrino beam data in the near detector, and beam  
<sub>1607</sub> data measured at SK. The definitions of these samples are documented in section 6.1,  
<sub>1608</sub> section 6.2, and section 6.3, respectively. The data collected and used within this  
<sub>1609</sub> analysis is detailed in Table 6.1. The near and far detector data corresponds to T2K  
<sub>1610</sub> runs 2-9 and runs 1-10, respectively. The accumulated POT and beam power for runs  
<sub>1611</sub> 1 – 10 are illustrated in Figure 6.1.

Data Type	Total
Near Detector FHC	$1.15 \times 10^{21}$ POT
Near Detector RHC	$8.34 \times 10^{20}$ POT
Far Detector FHC	$1.97 \times 10^{21}$ POT
Far Detector RHC	$1.63 \times 10^{21}$ POT
Atmospheric SK-IV	3244.4 days

**Table 6.1:** The amount of data collected in each detector used within this analysis. The data collected at the near and far detector, for both neutrino beam (FHC) and antineutrino beam (RHC), is measured as the number of protons on target (POT).

<sub>1612</sub> The difference in POT recorded at the near and far detector is due to the difference  
<sub>1613</sub> in downtime of the respective detector. The SK detector is very stable with almost 100%  
<sub>1614</sub> of data recorded during beam operation. Due to various technical and operational  
<sub>1615</sub> issues, the downtime of the near detector is significantly higher due to its more  
<sub>1616</sub> complex design and operating requirements.

1617 The systematic parameters invoked within the flux, detector, and interaction models  
 1618 used within this analysis are documented in section 6.4. The standard configuration of  
 1619 the joint beam and atmospheric data fit utilises far detector systematics provided in  
 1620 the official inputs from the two experiments. Additionally, a correlated detector model  
 1621 which fits the parameters used in sample selections to data has been developed and  
 1622 documented in subsection 6.4.5.

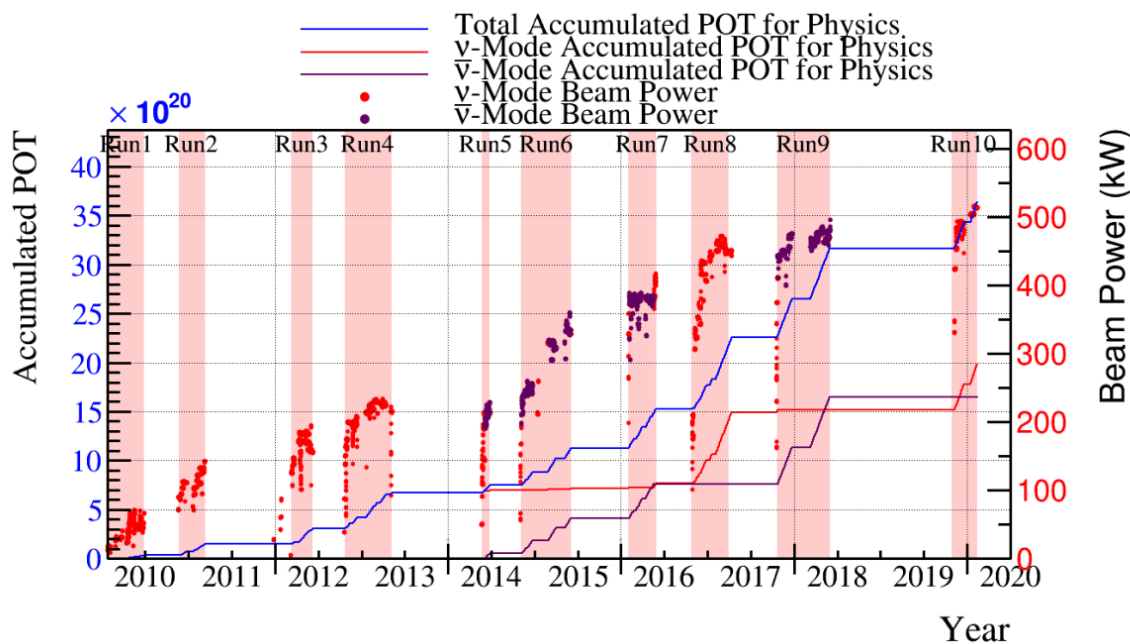


**Figure 6.1:** The accumulated beam data, measured as the number of protons on target (POT). The total data (blue) is given which comprises of the neutrino beam (red) and antineutrino (purple) components. The beam power for neutrino and antineutrino beams is given as the markers using the same colour scheme. The timescale runs from Run 1 which started in January 2010 until Run 10 which ended in February 2020. The ratio of accumulated data in neutrino and antineutrino beam is 54.7% : 45.3%.

## <sup>1623</sup> 6.1 Atmospheric Samples

<sup>1624</sup> The atmospheric event selection follows the official SK-IV analysis presented in [89]  
<sup>1625</sup> and is documented below. The Monte Carlo prediction used within this analysis  
<sup>1626</sup> corresponds to 500 years worth of neutrino events, which is scaled down to match the  
<sup>1627</sup> SK-IV livetime of 3244.4 days.

<sup>1628</sup> The fully contained (FC), partially contained (PC), and upward going muon events  
<sup>1629</sup> ( $\text{up-}\mu$ ) which pass the reduction cuts discussed in section 5.3 are further broken down  
<sup>1630</sup> into different samples based on reconstruction information. This section details the  
<sup>1631</sup> samples used within this oscillation analysis, alongside the chosen binning, used  
<sup>1632</sup> within the fit.

<sup>1633</sup> FC events are first separated by the visible energy deposited within the detector.  
<sup>1634</sup> This is calculated as the sum of the reconstructed kinetic energy above the Cherenkov  
<sup>1635</sup> threshold for all rings present in the event. Events are separated by whether they were  
<sup>1636</sup> above or below  $E_{\text{vis}} = 1.33\text{GeV}$ . This separates “subGeV” and “multiGeV” events.  
<sup>1637</sup> Typically, lower energy events consist of charge current quasi-elastic (CCQE) inter-  
<sup>1638</sup> actions which are better understood and simpler to reconstruct resulting in smaller  
<sup>1639</sup> systematic uncertainties. Events are further separated by the number of rings as-  
<sup>1640</sup> sociated with the event due to similar reasoning. As the oscillation probability is  
<sup>1641</sup> dependent upon the flavour of neutrino, electron and muon events are separated  
<sup>1642</sup> using a similar likelihood method to that discussed in section 5.2. To reduce computa-  
<sup>1643</sup> tional resources required for the reconstruction, only electron and pion hypotheses are  
<sup>1644</sup> considered so this separation cut depends on the ratio of the electron to pion likeli-  
<sup>1645</sup> hoods,  $\log(L_e/L_\pi)$ . Finally, the number of decay electrons is used to classify events.  
<sup>1646</sup> Charged current resonant pion production (CCRES) interactions generate a final-state  
<sup>1647</sup> pion. This can decay, mostly likely through a muon, into a decay electron. Therefore

- <sub>1648</sub> any electron-like event with one decay electron or muon-like event with two decay  
<sub>1649</sub> electrons was most likely produced by a CCRES interaction. Consequently, the number  
<sub>1650</sub> of decay electrons can be used to distinguish CCQE and CCRES interaction modes.  
<sub>1651</sub> Ultimately, FC subGeV events are separated into the samples listed in Table 6.2.

Sample Name	Description
SubGeV-e-like-0dcy	Single ring $e$ -like events with zero decay electrons
SubGeV-e-like-1dcy	Single ring $e$ -like events with one or more decay electrons
SubGeV-mulike-0dcy	Single ring $\mu$ -like events with zero decay electrons
SubGeV-mulike-1dcy	Single ring $\mu$ -like events with one decay electrons
SubGeV-mulike-2dcy	Single ring $\mu$ -like events with two or more decay electrons
SubGeV-pi0like	Two $e$ -like ring events with zero decay electrons and reconstructed $\pi^0$ mass $85 \leq m_{\pi^0} < 215\text{MeV}$

**Table 6.2:** The fully contained subGeV samples, defined as events with visible energy  $E_{vis} < 1.33\text{GeV}$ , used within this oscillation analysis.

- <sub>1652</sub> In addition to the cuts discussed above, multiGeV samples also have additional cuts  
<sub>1653</sub> to separate samples which target neutrino and antineutrino separation. As discussed  
<sub>1654</sub> in section 7.1, the matter resonance only occurs for neutrinos in normal hierarchy  
<sub>1655</sub> and antineutrinos in an inverted mass hierarchy. Therefore, having flavour-enriched  
<sub>1656</sub> samples aids in the determination of the mass hierarchy. For a CCRES interaction,

$$\begin{aligned}
 \bar{\nu}_e + N &\rightarrow e^+ + N' + \pi^-, \\
 \nu_e + N &\rightarrow e^- + N' + \pi^+ \\
 &\quad \downarrow \mu^+ + \nu_\mu \\
 &\quad \downarrow e^+ + \nu_e + \bar{\nu}_\mu.
 \end{aligned} \tag{6.1}$$

- <sub>1657</sub> The  $\pi^-$  emitted from a  $\bar{\nu}_e$  interaction is more likely to be absorbed within the  
<sub>1658</sub> oxygen nucleus compared to the  $\pi^+$  from  $\nu_e$  interactions [190]. These pions then

1659 decay, mostly through muons, to electrons. Therefore the number of tagged decay  
 1660 electrons associated with an event gives an indication of whether the interaction  
 1661 was due to a neutrino or antineutrino: zero for  $\bar{\nu}_e$  events, and one for  $\nu_e$  events.  
 1662 The ability to separate neutrino from antineutrino events is illustrated in Table 6.4,  
 1663 where the MultiGeV-*e*like-nue has 78% purity of neutrino interactions with only 7%  
 1664 antineutrino background in that sample and the rest of the sample comprising of  
 1665 neutral current backgrounds.

1666 This relatively simple discriminator works reasonably well for single-ring events.  
 1667 However, this is not the case for multi-ring events. A multiGeV multiring separation  
 1668 (MME) likelihood cut which specifically targets multiGeV multiRing electron-like  
 1669 events was introduced in [191, 192]. This is a two-stage likelihood selection cut. Four  
 1670 observables are used within the first likelihood cut to distinguish CC $\nu_e$  and CC $\bar{\nu}_e$   
 1671 events from background:

- 1672 • The number of decay electrons
- 1673 • The maximum distance between the vertex of the neutrino and the decay electrons
- 1674 • The energy deposited by the leading energy ring
- 1675 • The reconstructed particle identification of that highest energy ring

1676 Background events consist of CC $\nu_\mu$  and NC interactions. Typically these produce  
 1677 events where the majority of the energy is carried by the hadronic system. Additionally,  
 1678 muons tend to travel further than the pions from CC $\nu_e$  before decaying. Consequently,  
 1679 the parameters used within the likelihood cut target the typical background interaction  
 1680 kinematics.

1681 Neutrino and antineutrino events are then separated by a second likelihood method  
 1682 ( $\nu/\bar{\nu}$  separation) detailed in [52]. This uses the number of decay electrons, the number  
 1683 of reconstructed rings, and the event's transverse momentum. The last two parameters

Sample Name	Description
MultiGeV- <i>e</i> -like-nue	Single ring <i>e</i> -like events with zero decay electrons
MultiGeV- <i>e</i> -like-nuebar	Single ring <i>e</i> -like events with one or more decay electrons
MultiGeV- <i>μ</i> -like	Single ring <i>μ</i> -like events
MultiRing- <i>e</i> -like-nue	Two or more ring events with leading energy <i>e</i> -like ring and passed both MME and $\nu/\bar{\nu}$ separation cuts
MultiRing- <i>e</i> -like-nuebar	Two or more ring events with leading energy <i>e</i> -like ring and passed MME and failed $\nu/\bar{\nu}$ separation cuts
MultiRing- <i>μ</i> -like	Two or more ring events with leading energy <i>μ</i> -like ring and only requires $E_{vis} > 0.6\text{GeV}$ <b>DB: Why is this not }1.33\text{GeV? N</b>
MultiRing-Other1	Two or more ring events with leading energy <i>e</i> -like ring and failed the MME likelihood cut

**Table 6.3:** The fully contained multiGeV samples used within this oscillation analysis. Both the sample name and description are given.

1684 are used because higher-energy samples tend to have more pions produced above  
1685 the Cherenkov threshold which results in more rings compared to an antineutrino  
1686 interaction. Furthermore, the angular distribution also tends to be more forward  
1687 peaked in antineutrino interactions as compared to neutrino interactions [89]. These  
1688 FC multiGeV sample definitions are detailed in Table 6.3.

1689 The PC and up- $\mu$  events are split by the amount of energy deposited within the  
1690 outer detector, into “stopping” and “through-going” samples. This is because the  
1691 momentum of events leaving the detector has to be approximated, which increases the  
1692 systematic uncertainty. This estimate is particularly poor for very high-energy events.  
1693 This is why up- $\mu$  through-going events are not binned in reconstructed momentum.  
1694 If an event leaves the detector, the energy it takes with it has to be estimated which  
1695 increases the systematic uncertainty compared to events entirely contained within the  
1696 inner detector. The through-going up- $\mu$  are further separated by the presence of any  
1697 electromagnetic showering in the event, as the assumption of non-showering muon

<sub>1698</sub> does not give reliable reconstruction for these types of events [47]. In total, 13 FC, 2  
<sub>1699</sub> PC, and 3 up- $\mu$  atmospheric samples are included within this analysis.

Sample	CC $\nu_e$	CC $\bar{\nu}_e$	CC( $\nu_\mu + \bar{\nu}_\mu$ )	CC( $\nu_\tau + \bar{\nu}_\tau$ )	NC
SubGeV-elike-0dcy	72.17	23.3	0.724	0.033	3.77
SubGeV-elike-1dcy	86.81	1.773	7.002	0.062	4.351
SubGeV-mulike-0dcy	1.003	0.380	90.07	0.036	8.511
SubGeV-mulike-1dcy	0.023	0.	98.46	0.029	1.484
SubGeV-mulike-2dcy	0.012	0.	99.25	0.030	0.711
SubGeV-pi0like	6.923	2.368	0.928	0.011	89.77
MultiGeV-elike-nue	78.18	7.041	3.439	1.886	9.451
MultiGeV-elike-nuebar	56.68	37.81	0.174	0.614	4.718
MultiGeV-mulike	0.024	0.005	99.67	0.245	0.058
MultiRing-elike-nue	59.32	12.39	4.906	3.385	20
MultiRing-elike-nuebar	52.39	31.03	1.854	1.585	13.14
MultiRing-mulike	0.673	0.080	97.33	0.342	1.578
MultiRingOther-1	27.98	2.366	34.93	4.946	29.78
PCStop	8.216	3.118	84.45	0.	4.214
PCThrus	0.564	0.207	98.65	0.	0.576
UpStop-mu	0.829	0.370	98.51	0.	0.289
UpThruNonShower-mu	0.206	0.073	99.62	0.	0.103
UpThruShower-mu	0.128	0.054	99.69	0.	0.132

**Table 6.4:** The purity of each atmospheric sample used within this analysis, broken down by charged current (CC) and neutral current (NC) interactions and which neutrino flavour interacted within the detector. Asimov A oscillation parameter sets are assumed (given in Table 2.2). Electron neutrino and antineutrino events are separated to illustrate the ability of the separation likelihood cuts used within the multiGeV and multiring sample selections.

<sub>1700</sub> The atmospheric samples are binned in direct observables: reconstructed lepton  
<sub>1701</sub> momentum and direction, as given by Table 6.5. The distribution of the reconstructed  
<sub>1702</sub> lepton momentum (for samples that only have one bin reconstructed zenith angle)  
<sub>1703</sub> and reconstructed direction for each atmospheric sample used within this analysis is  
<sub>1704</sub> illustrated in Figure 6.2.

Sample	$\cos(\theta_Z)$ Bins	Momentum Bin Edges ( $\log_{10}(P)$ MeV)
SubGeV- <i>e</i> like-0dcy	10	2.0, 2.4, 2.6, 2.8, 3.0, 3.2
SubGeV- <i>e</i> like-1dcy	1	2.0, 2.4, 2.6, 2.8, 3.0, 3.2
SubGeV- <i>m</i> ulike-0dcy	10	2.0, 2.4, 2.6, 2.8, 3.0, 3.2
SubGeV- <i>m</i> ulike-1dcy	10	2.0, 2.4, 2.6, 2.8, 3.0, 3.2
SubGeV- <i>m</i> ulike-2dcy	1	2.0, 2.4, 2.6, 2.8, 3.0, 3.2
SubGeV- <i>p</i> i0like	1	2.0, 2.2, 2.4, 2.6, 2.8, 3.2
MultiGeV- <i>e</i> like-nue	10	3.0, 3.4, 3.7, 4.0, 5.0
MultiGeV- <i>e</i> like-nuebar	10	3.0, 3.4, 3.7, 4.0, 5.0
MultiGeV- <i>m</i> ulike	10	3.0, 3.4, 5.0
MultiRing- <i>e</i> like-nue	10	3.0, 3.4, 3.7, 5.0
MultiRing- <i>e</i> like-nuebar	10	3.0, 3.4, 3.7, 5.0
MultiRing- <i>m</i> ulike	10	2.0, 3.124, 3.4, 3.7, 5.0
MultiRing- <i>O</i> ther1	10	3.0, 3.4, 3.7, 4.0, 5.0
PC-Stop	10	2.0, 3.4, 5.0
PC-Through	10	2.0, 3.124, 3.4, 3.7, 5.0
Upmu-Stop	10	3.2, 3.4, 3.7, 8.0
Upmu-Through-Showering	10	2.0, 8.0
Upmu-Through-NonShowering	10	2.0, 8.0

**Table 6.5:** The reconstructed cosine zenith and lepton momentum binning assigned to the atmospheric samples. The “ $\cos(\theta_Z)$  Bins” column illustrates the number of bins uniformly distributed over the  $-1.0 \leq \cos(\theta_Z) \leq 1.0$  region for fully and partially contained samples and  $-1.0 \leq \cos(\theta_Z) \leq 0.0$  region for up- $\mu$  samples. **DB: Does this belong in the appendix?**

1705

**DB: By-mode spectra of each sample needed?**

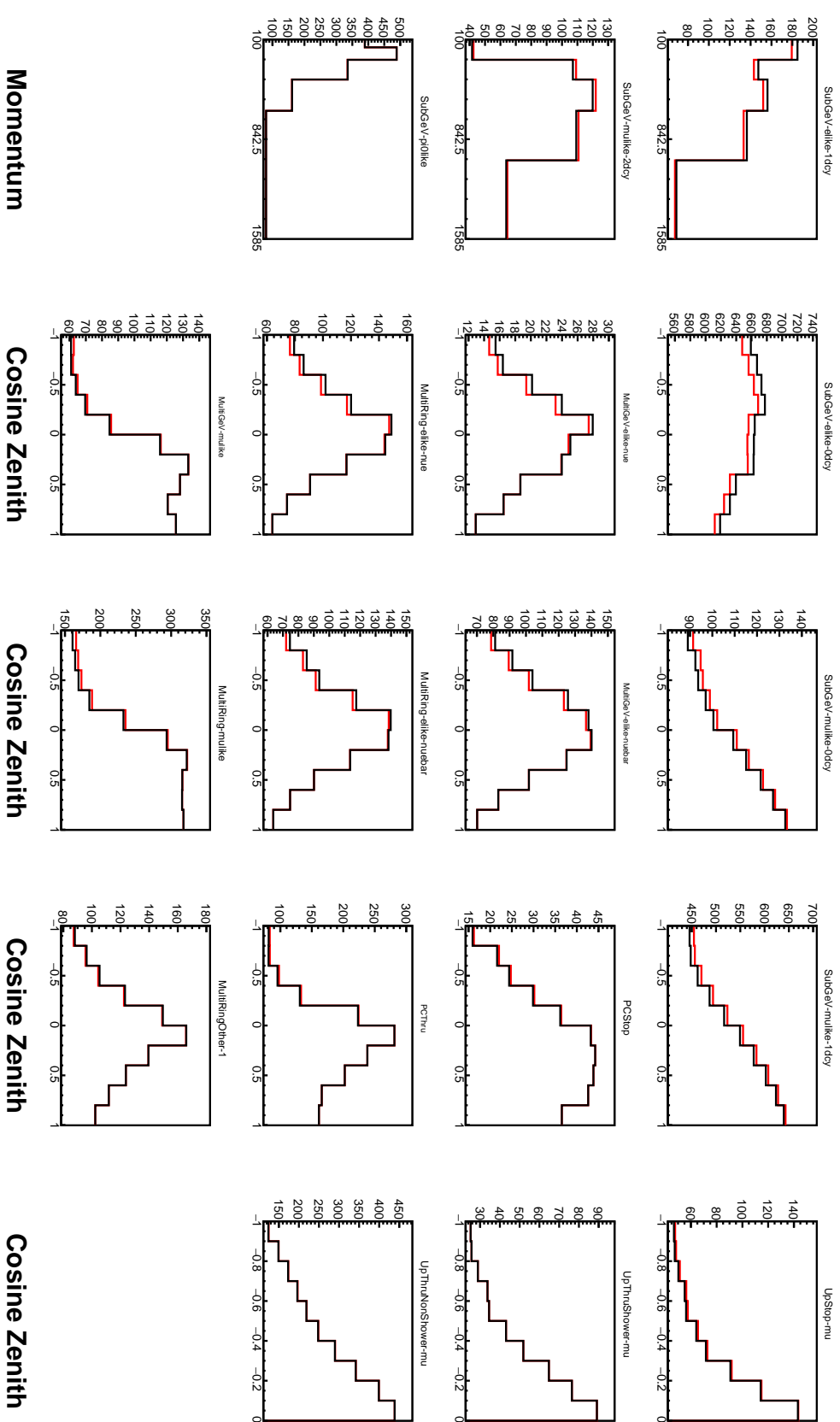


**Figure 6.2:** Comparison of the SK-IV atmospheric samples between predictions made with the CP-violating Asimov A (Black) and CP-conserving Asimov B (Red) oscillation parameter sets (given in Table 2.2). The subGeV samples CCRES and  $\pi^0$ -like samples are given in their reconstructed lepton momentum. All other samples are presented in their reconstructed zenith angle projection.

## 1706 6.2 Near Detector Beam Samples

1707 The near detector sample selections are documented in detail within [193] and sum-  
1708 marised below. Samples are selected based upon the particular FGD in which the  
1709 vertex of the neutrino interaction is in as well as the operating mode of the beam:  
1710 FHC or RHC. For additional constraints on model parameters, wrong-sign neutrino  
1711 samples are also considered when the beam is operating in RHC mode. Samples  
1712 from the wrong-sign component of the FHC beam mode are not included as they are  
1713 statistically insignificant compared to those samples already listed.

1714 Before being assigned a sample, all events must undergo CC-inclusive cuts, as  
1715 defined in [194]:

- 1716 • Event Timing: The DAQ must be operational and the event must occur within  
1717 the expected beam time window
- 1718 • TPC Requirement: The track path must intercept one or more TPCs
- 1719 • Fiducial volume: The event must originate from within the fiducial volume. The  
1720 fiducial volumes are defined as a region within each sub-detector [195].
- 1721 • Upstream Background: Remove events that have muons tracks that originate  
1722 upstream of the FGDs by requiring no high-momentum tracks within 150mm  
1723 upstream of the candidate vertex. Additionally, events that occur within the  
1724 downstream FGD are vetoed if a secondary track starts within the upstream FGD
- 1725 • Broken track removal: All candidates where the muon candidate is broken in two  
1726 are removed
- 1727 • Muon PID: Measurements of  $dE/dx$  in a TPC are used to distinguish muon-like  
1728 events using a likelihood cut

<sub>1729</sub> In addition to these cuts, RHC neutrino events also have to undergo the following  
<sub>1730</sub> cuts to aid in the separation of neutrino and antineutrino [196]:

- <sub>1731</sub> • TPC Requirement: The track path must intercept TPC2
- <sub>1732</sub> • Positive Track: The highest momentum track must be positive
- <sub>1733</sub> • TPC1 Veto: Remove any events originating upstream of TPC1

<sub>1734</sub> Once all CC-inclusive events have been determined, they are further segregated  
<sub>1735</sub> into sub-samples that target the constraints on interaction modes most relevant at  
<sub>1736</sub> the far detector. They are split by pion multiplicity: CC0 $\pi$ , CC1 $\pi$ , and CCOther.  
<sub>1737</sub> These target specific interaction modes CCQE, CCRES, and other CC background  
<sub>1738</sub> interactions, respectively. Pions in the TPCs and FGDs are selected by requiring a  
<sub>1739</sub> second track to be observed, which is separate from the muon track and is in the same  
<sub>1740</sub> beam spill window and sub-detector. If the pion originated within a FGD, it must also  
<sub>1741</sub> pass through the sequential downstream TPC (TPC2 for FGD1, TPC3 for FGD2).

<sub>1742</sub> CC0 $\pi$ , CC1 $\pi$ , and CCOther samples are defined with the following cuts:

- <sub>1743</sub> •  $\nu_\mu$ CC0 $\pi$  Selection: No electrons in TPC and no charged pions or decay electrons  
<sub>1744</sub> within the TPC or FGD
- <sub>1745</sub> •  $\nu_\mu$ CC1 $\pi$  Selection: Exactly one charged pion in either the TPC or FGD, where  
<sub>1746</sub> the number of charged pions in the FGD is equal to the number of decay electrons
- <sub>1747</sub> •  $\nu_\mu$ CCOther Selection: All events which are not classified into the above two  
<sub>1748</sub> selections.

<sub>1749</sub> Counting the three selections for each FGD in FHC and RHC running, including  
<sub>1750</sub> the wrong-sign background in RHC, 18 near detector samples are used within this  
<sub>1751</sub> analysis. These samples are binned in reconstructed lepton momentum (illustrated in  
<sub>1752</sub> Figure 6.3) and direction with respect to the beam. The binning is chosen such that

each event has at least 20 Monte Carlo events in each bin [195]. This is to ensure that the bins are coarse enough to ensure the reduction of statistical errors, whilst also being fine enough to sample the high-resolution peak regions. The exact binning is detailed in [195].

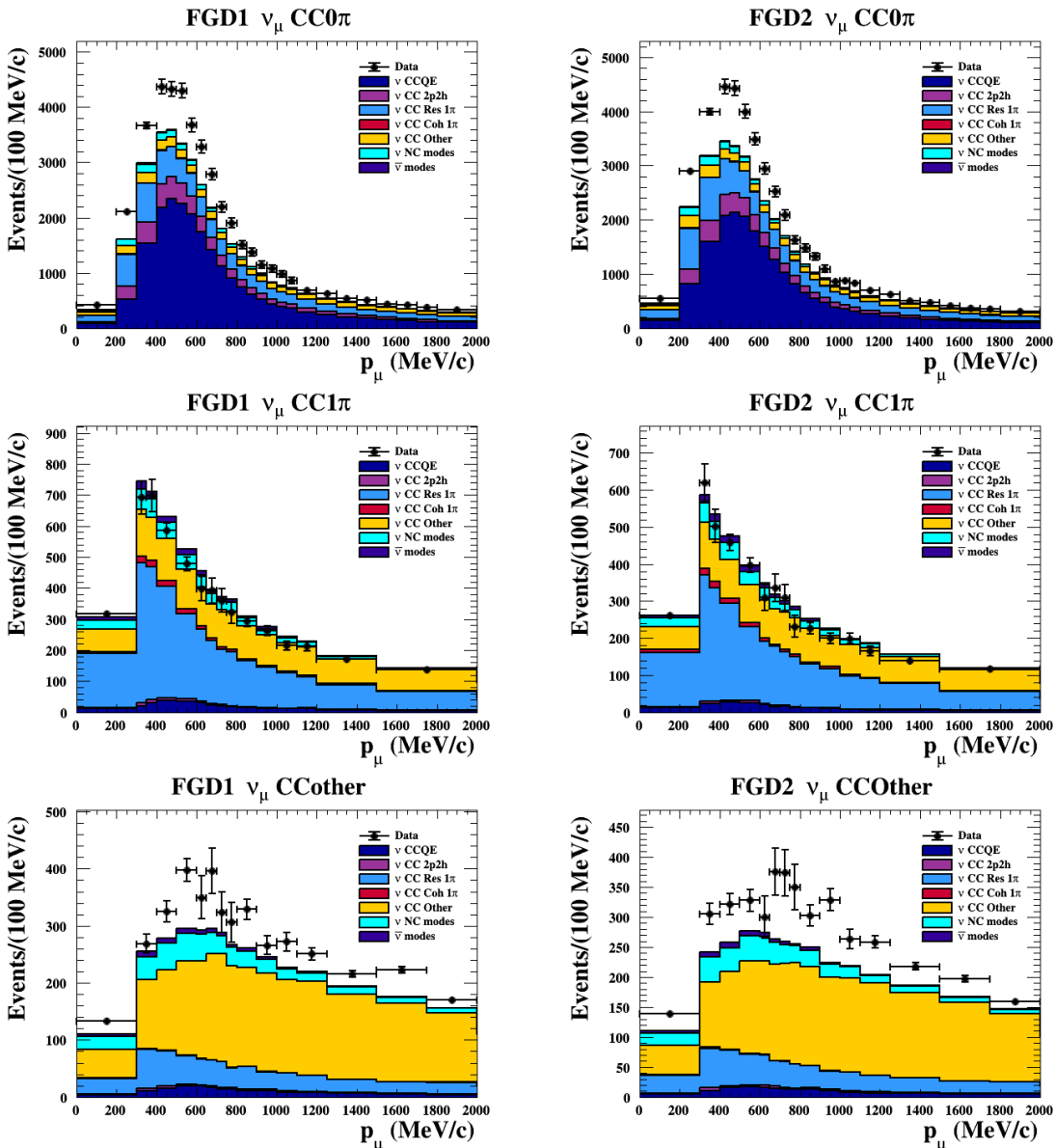


**Figure 6.3:** The nominal Monte Carlo predictions for the FGD1 and FGD2 samples in neutrino beam mode, broken down into the  $\text{CC}\nu_\mu 0\pi$ ,  $\text{CC}\nu_\mu 1\pi$  and  $\text{CC}\nu_\mu$  Other categories. Figures taken from [193].

## <sup>1757</sup> 6.3 Far Detector Beam Samples

<sup>1758</sup> The beam neutrino events which occur at the SK detector, which pass the reduction cuts  
<sup>1759</sup> detailed in section 5.3, are separated depending on whether the beam was operating  
<sup>1760</sup> in FH or RHC mode. The events are then separated into three samples: electron-like  
<sup>1761</sup> ( $1Re$ ), muon-like ( $1R\mu$ ), and CC $1\pi^+$ -like ( $1Re1de$ ) which are observed as electron-like  
<sup>1762</sup> events with an associated decay electron [183]. As discussed in section 6.1, positively  
<sup>1763</sup> charged pions emitted from neutrino interactions are more likely to produce decay  
<sup>1764</sup> electrons than negatively charged pions. Consequently, the CC $1\pi^+$ -like sample is only  
<sup>1765</sup> selected when the beam is operating in FHC mode. Therefore, five beam samples  
<sup>1766</sup> measured at SK are used in this analysis.

<sup>1767</sup> The fiducial volume definition for beam samples is slightly different from that used  
<sup>1768</sup> within the atmospheric samples. It uses both the distance to the closest wall ( $d_{Wall}$ )  
<sup>1769</sup> and the distance to the wall along the trajectory of the particle ( $to_{Wall}$ ). This allows  
<sup>1770</sup> events that originate close to the wall but are facing into the tank to be included within  
<sup>1771</sup> the analysis, which would have otherwise been removed. These additional events are  
<sup>1772</sup> beneficial for a statistics-limited experiment. The exact cut values for both  $d_{Wall}$  and  
<sup>1773</sup>  $to_{Wall}$  are different for each of the three types of sample and are optimised based on  
<sup>1774</sup> T2K sensitivity to  $\delta_{CP}$  [197,198]. They are:

<sup>1775</sup> DB: Diagram of  $d_{Wall}$  and  $to_{Wall}$  needed?

<sup>1776</sup> **1Re event selection** For an event to be classified as a  $1Re$ -like, the event must follow:

- <sup>1777</sup> • Fully-contained and within  $d_{Wall} > 80\text{cm}$  and  $to_{Wall} > 170\text{cm}$
- <sup>1778</sup> • Total of one ring which is reconstructed as electron-like with reconstructed mo-  
<sup>1779</sup> mentum  $P_e > 100\text{MeV}$

- 1780     • Zero decay electrons are associated with the event  
1781     • Passes  $\pi^0$  rejection cut discussed in section 5.2

1782     The zero decay electron cut specifically targets CCQE interactions. Whereas, the  $\pi^0$   
1783     rejection cut is designed to remove neutral current  $\pi^0$  background events which can  
1784     be easily reconstructed as 1Re-like events.

1785     **CC1 $\pi^+$  event selection** This event selection is very similar to that of the 1Re sample.  
1786     The only difference is that the dWall and toWall criteria are changed to  $> 50\text{cm}$  and  
1787      $> 270\text{cm}$ , respectively. Furthermore, exactly one decay electron is required from the  
1788      $\pi^+$  decay.

1789     **1R $\mu$  event selection** A 1R $\mu$ -like event is determined by the following cuts:

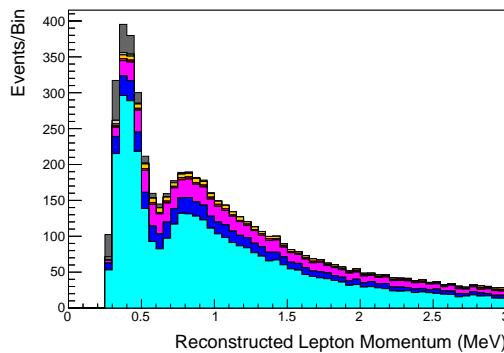
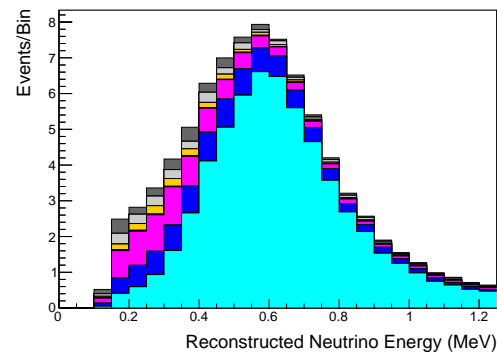
- 1790     • Fully-contained and within  $\text{dWall} > 50\text{cm}$  and  $\text{toWall} > 250\text{cm}$   
1791     • Total of one ring which is reconstructed as muon-like with reconstructed momen-  
1792       tum  $P_\mu > 200\text{MeV}$   
1793     • Fewer than two decay electrons are associated with the event  
1794     • Passes  $\pi^+$  rejection cut discussed in section 5.2

1795     As pions and muons have similar masses, the Cherenkov rings they generate have  
1796     similar opening angles. To enhance the purity, the events have to pass the  $\pi^+$  rejection  
1797     cut which is specifically optimised to separate the two types of events.

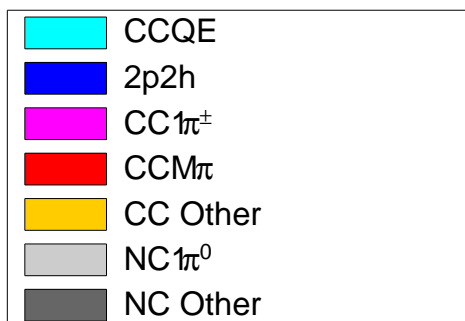
1798     All of these samples are binned in reconstructed neutrino energy. This is possible  
1799     as the direction from the source is known extremely well. This value is calculated for  
1800     the 1Re-like and 1R $\mu$ -like samples assuming CCQE interactions,

$$E_\nu^{rec} = \frac{(M_N - V_{nuc})E_l - m_l^2/2 + M_N V_{nuc} - V_{nuc}^2/2 + (M_P^2 + M_N^2)/2}{M_N - V_{nuc} - E_l + P_l \cos(\theta_{beam})} \quad (6.2)$$

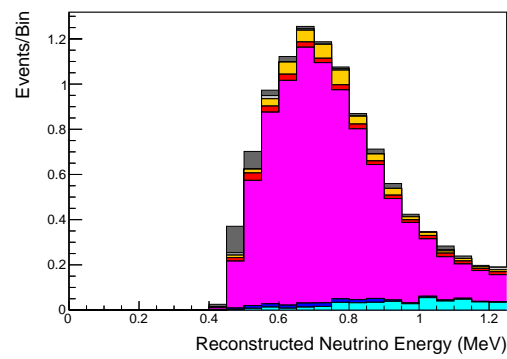
Where  $M_N$ ,  $M_P$  and  $m_l$  are the masses of the neutron, proton and outgoing lepton, respectively.  $V_{nuc} = 27\text{MeV}$  is the binding energy of the oxygen nuclei [183],  $\theta_{beam}$  is the angle between the beam and the direction of the outgoing lepton, and  $E_l$  and  $P_l$  are the energy and momentum of that outgoing lepton.

(a) FHC 1R $\mu$ 

(b) FHC 1Re



(c)

(d) FHC CC1 $\pi^+$ 

**Figure 6.4:** The reconstructed neutrino energy, as defined by Equation 6.2 and Equation 6.3, for the 1R $\mu$ -like, 1Re-like and CC1 $\pi^+$ -like samples. Asimov A oscillation parameter sets are assumed (given in Table 2.2). These samples are the FHC mode samples. For ease of viewing, the 1R $\mu$  sample only shows the  $0. \leq E_\nu^{rec} < 3.0\text{GeV}$  but the binning extends to 30.0GeV.

1805 The reconstructed neutrino energy of the CC1 $\pi^+$ -like events is modified to include  
1806 the delta resonance produced within the interaction,

$$E_\nu^{rec} = \frac{2M_N E_l + M_{\Delta^{++}}^2 - M_N^2 - m_l^2}{2(M_N - E_l + P_l \cos(\theta_{beam}))} \quad (6.3)$$

1807 Where  $M_{\Delta^{++}}$  is the mass of the delta baryon. Binding energy effects are not  
1808 considered as a two-body process with the delta baryon is assumed. This follows  
1809 the T2K oscillation analysis presented in [80], although recent developments of the  
1810 interaction model in the latest T2K oscillation analysis do include effects from binding  
1811 energy in this calculation [199].

1812 The reconstructed neutrino energy for the FHC samples is illustrated in Figure 6.4.  
1813 As expected, the 1R $\mu$ -like and 1Re-like samples are heavily dominated by CCQE in-  
1814 teractions, with smaller contributions from 2p2h meson exchange and resonant pion  
1815 production interactions. The CC1 $\pi^+$ -like sample predominantly consists of charged  
1816 current resonant pion production interactions. The 1Re-like and CC1 $\pi^+$ -like samples  
1817 are also binned by the angle between the neutrino beam and the reconstructed lepton  
1818 momentum. This is to aid in charged current and neutral current separation, as indi-  
1819 cated in Figure 6.5. This is because the neutral current backgrounds are predominantly  
1820 due to  $\pi^0$ -decays, where the opening angle of the two gammas alongside the different  
1821 final state kinematics produces a slightly broader angular distribution compared to  
1822 the final state particles originating from charged current  $\nu_e$  interactions.

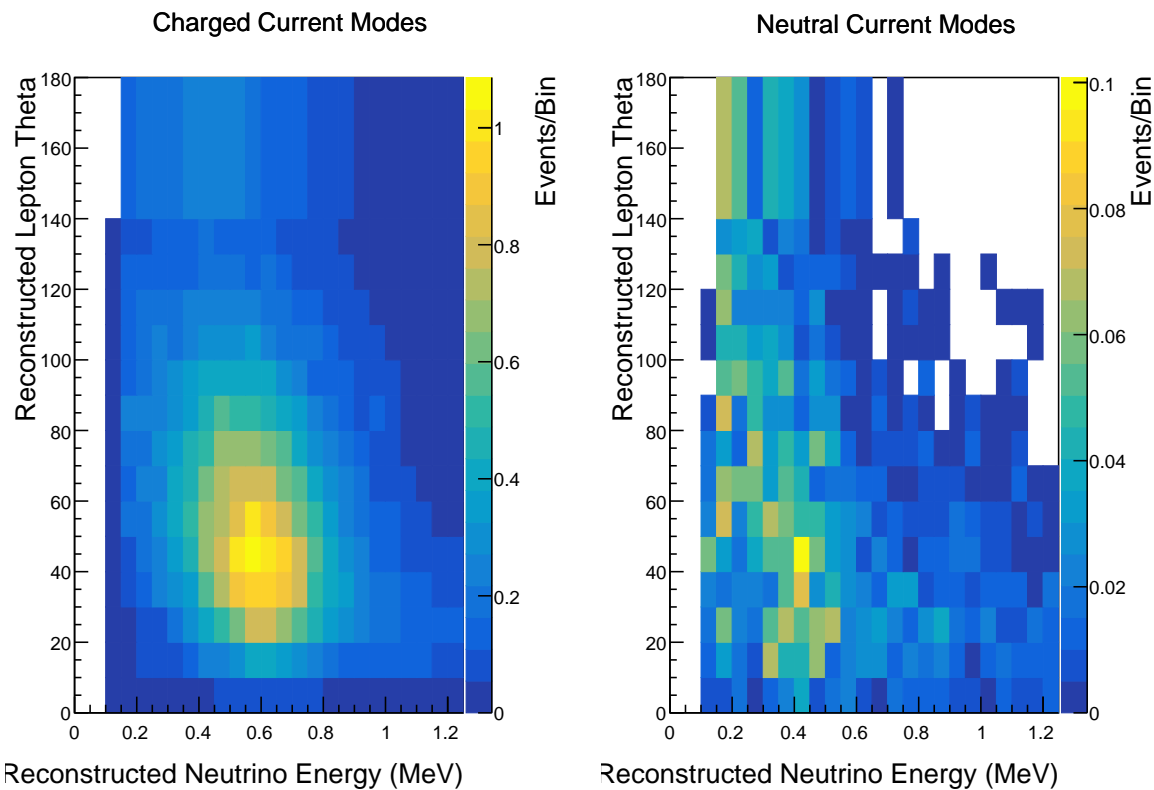


**Figure 6.5:** The distribution of the angle between the neutrino beam direction and the reconstructed final state lepton, for the FHC 1Re-like sample. The distribution is broken down by neutrino interaction mode into charged current (left) and neutral current (right) components. Asimov A oscillation parameter sets are assumed (given in Table 2.2). DB: Is this needed or will it just bring up more questions?

## <sup>1823</sup> 6.4 Systematic Uncertainties

<sup>1824</sup> The systematic model parameters for this analysis are split into groups, or blocks,  
<sup>1825</sup> depending on their purpose. They consist of flux uncertainties, neutrino-matter  
<sup>1826</sup> interaction systematics, and detector efficiencies. There are also uncertainties on the  
<sup>1827</sup> oscillation parameters which this analysis will not be sensitive to,  $\Delta m_{12}^2$  and  $\sin^2(\theta_{12})$ .  
<sup>1828</sup> These uncertainties are taken from the 2018 PDG measurements [81]. As described in  
<sup>1829</sup> chapter 4, each model parameter used within this analysis requires a prior uncertainty.  
<sup>1830</sup> This is provided via separate covariance matrices for each block. The covariance  
<sup>1831</sup> matrices can include prior correlations between parameters within a single block, but  
<sup>1832</sup> the separate treatment means prior uncertainties can not be included for parameters  
<sup>1833</sup> in different groups. Some parameters in these models have no reasonably motivated  
<sup>1834</sup> uncertainties and are assigned flat priors which do not modify the likelihood penalty.  
<sup>1835</sup> The flux, neutrino interaction, and detector modeling simulations have already been  
<sup>1836</sup> discussed in section 5.1 and section 5.2. The uncertainties invoked within each of these  
<sup>1837</sup> models are described below.

### <sup>1838</sup> 6.4.1 Beam Flux

<sup>1839</sup> The neutrino beam flux systematics is based upon the uncertainty in the modeling of  
<sup>1840</sup> the components of the beam. This includes the hadron production model and their re-  
<sup>1841</sup> interactions, the shape, intensity, and alignment of the beam with respect to the target,  
<sup>1842</sup> and the uniformity of the magnetic field produced by the horn, alongside other effects.  
<sup>1843</sup> The uncertainty, as a function of neutrino energy, is illustrated in Figure 6.6 which  
<sup>1844</sup> includes a depiction of the total uncertainty as well as the contribution from individual  
<sup>1845</sup> components. The uncertainty around the peak of the energy distribution ( $E_\nu \sim 0.6\text{GeV}$ )

<sup>1846</sup> is dominated by the measurements of the beam profile and alignment. Outside of this  
<sup>1847</sup> region, the uncertainties within hadron production dominate the uncertainty.

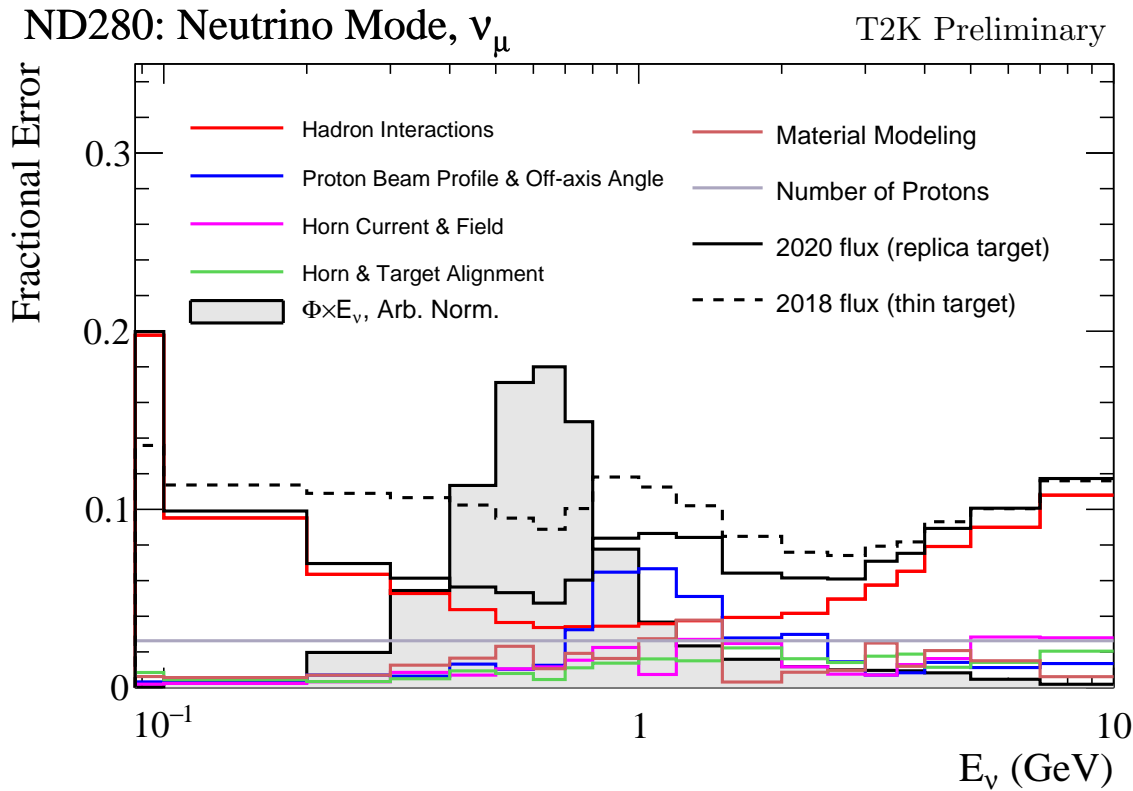


**Figure 6.6:** The total uncertainty evaluated on the near detector  $\nu_\mu$  flux prediction constrained by the replica-target data, illustrated as a function of neutrino energy. The solid(dashed) line indicates the uncertainty used within this analysis(the T2K 2018 analysis [200]). The solid histogram indicates the neutrino flux as a function of energy. Figure taken from [201].

<sup>1848</sup> The beam flux uncertainties are described by one hundred parameters. They are  
<sup>1849</sup> split between the ND280 and SK detectors and binned by neutrino flavour:  $\nu_\mu$ ,  $\bar{\nu}_\mu$ ,  $\nu_e$   
<sup>1850</sup> and  $\bar{\nu}_e$ . The response is then broken down as a function of neutrino energy. The bin  
<sup>1851</sup> density in the neutrino energy is the same for the  $\nu_\mu$  in FHC and  $\bar{\nu}_\mu$  in RHC beams,  
<sup>1852</sup> and narrows for neutrino energies close to the oscillation maxima of  $E_\nu = 0.6\text{GeV}$ .  
<sup>1853</sup> This binning is specified in Table 6.6. All of these systematic uncertainties are applied  
<sup>1854</sup> as normalisation parameters with Gaussian priors centered at 1.0 and error specified  
<sup>1855</sup> from a covariance matrix provided by the T2K beam group [201].

Neutrino Flavour	Sign	Neutrino Energy Bin Edges (GeV)
$\mu$	Right	0., 0.4, 0.5, 0.6, 0.7, 1., 1.5, 2.5, 3.5, 5., 7., 30.
$\mu$	Wrong	0., 0.7, 1., 1.5, 2.5, 30.
$e$	Right	0., 0.5, 0.7, 0.8, 1.5, 2.5, 4., 30.
$e$	Wrong	0., 2.5, 30.

**Table 6.6:** The neutrino energy binning for the different neutrino flavours. “Right” sign indicates neutrinos in the FHC beam and antineutrinos in the RHC beam. “Wrong” sign indicates antineutrinos in the FHC beam and neutrinos in the RHC beam. The binning of the detector response is identical for the FHC and RHC modes as well as at ND280 and SK.

#### 1856 6.4.2 Atmospheric Flux

1857 The atmospheric neutrino flux is modeled by the HKKM model [43]. 16 systematic  
 1858 uncertainties are applied to control the normalisation of each neutrino flavour, energy,  
 1859 and direction. All of the parameters are given Gaussian priors centered at 0 and width  
 1860 equal to one. They are summarised below:

- 1861 • **Absolute Normalisation:** The overall normalisation of each neutrino flavour is  
 1862 controlled by two independent systematic uncertainties, for  $E_\nu < 1\text{GeV}$  and  $E_\nu >$   
 1863  $1\text{GeV}$ , respectively. This is driven mostly by hadronic interaction uncertainties for  
 1864 the production of pions and kaons [43]. The strength of the response is dependent  
 1865 upon the neutrino energy.
- 1866 • **Relative Normalisation:** Uncertainties on the ratio of  $(\nu_\mu + \bar{\nu}_\mu) / (\nu_e + \bar{\nu}_e)$  are  
 1867 controlled by the difference between the HKKM model [43], FLUKA [46] and  
 1868 Bartol models [42]. Three independent parameters are applied in the energy  
 1869 ranges:  $E_\nu < 1\text{GeV}$ ,  $1\text{GeV} < E_\nu < 10\text{GeV}$ , and  $E_\nu > 10\text{GeV}$ .
- 1870 •  **$\nu/\bar{\nu}$  Normalisation:** The uncertainties in the  $\pi^+/\pi^-$  (and kaon equivalent) pro-  
 1871 duction uncertainties in the flux of  $\nu/\bar{\nu}$ . The response is applied using the same  
 1872 methodology as the relative normalisation parameters.

1873 • **Up/Down and Vertical/Horizontal Ratio:** Similar to the above two systematics,  
1874 the difference between the HKKM, FLUKA, and Bartol model predictions, as a  
1875 function of  $\cos(\theta_Z)$ , is used to control the normalisation of events as a function of  
1876 zenith angle.

1877 •  **$K/\pi$  Ratio:** Higher energy neutrinos ( $E_\nu > 10\text{GeV}$ ) become dependent upon  
1878 kaon decay as the dominant source of neutrinos. Measurements of the ratio of  
1879  $K/\pi$  [202] are used to control the systematic uncertainty of the expected ratio of  
1880 pion and kaon production.

1881 • **Solar Activity:** As the 11-year solar cycle can affect the Earth's magnetic field,  
1882 the flux of primary cosmic rays varies across the same period. The uncertainty is  
1883 calculated by taking a  $\pm 1$  year variation, equating to a 10% uncertainty for the  
1884 SK-IV period.

1885 • **Atmospheric Density:** The height of the interaction of the primary cosmic rays is  
1886 dependent upon the atmospheric density. The HKKM assumes the US standard  
1887 1976 [153] profile. This systematic controls the uncertainty in that model.

1888 Updates to the HKKM and Bartol models are underway [158] to use a similar  
1889 tuning technique to that used in the beam flux predictions. After those updates, it may  
1890 be possible to include correlations in the hadron production uncertainty systematics  
1891 for beam and atmospheric flux predictions.

#### 1892 6.4.3 Neutrino Interaction

1893 The neutrino interactions which occur within all the detectors are modeled by NEUT.  
1894 The two independent oscillation analyses, T2K-only [203] and the SK-only [52], have  
1895 developed separate interaction models. To leverage the most sensitivity out of this  
1896 simultaneous beam and atmospheric analysis, a correlated interaction model has been

1897 defined. Where applicable, correlations allow the systematic uncertainties applied to  
1898 the atmospheric samples to be constrained by measurements of the near detector in  
1899 the beam experiment. This can lead to stronger sensitivity to oscillation parameters as  
1900 compared to an uncorrelated model.

1901 The low energy T2K systematic model has a more sophisticated treatment of CCQE,  
1902 CCMEC, and CCRES uncertainties which is due to the purpose-made cross-section  
1903 measurements made by the near detector. Furthermore, extensive comparisons of this  
1904 model have been performed to external data [203]. However, the model is not designed  
1905 for high-energy atmospheric events, like those illustrated in Figure 5.10. Therefore  
1906 the high energy systematic model from the SK-only analysis is implemented for the  
1907 relevant multiGeV, PC, and up- $\mu$  samples. The CCQE systematic parameters invoked  
1908 within the SK high energy model are actually contained within T2K's CCQE model.  
1909 Consequently, the more sophisticated CCQE and CCMEC T2K model parameters  
1910 have been incorporated into the high energy model but are uncorrelated from the low  
1911 energy counterparts.

1912 The high energy systematic model includes parameters developed from com-  
1913 parisons of Nieves and Rein-Seghal models which affect resonant pion producing  
1914 interactions, comparisons of the GRV98 and CKMT models which control DIS interac-  
1915 tions, and hadron multiplicity measurements which modulate the normalisation of  
1916 multi-pion producing events. The uncertainty of the  $\nu_\tau$  cross-section is particularly  
1917 large and is controlled by a 25% normalisation uncertainty. These parameters are  
1918 applied via normalisation or shape parameters. The former linearly scales the weight  
1919 of all affected Monte-Carlo events, whereas the latter can increase or decrease a partic-  
1920 ular event's weight depending on its neutrino energy and mode of interaction. The  
1921 response of the shape parameters is defined by third-order polynomial splines which  
1922 return a weight for a particular neutrino energy. To reduce computational resources

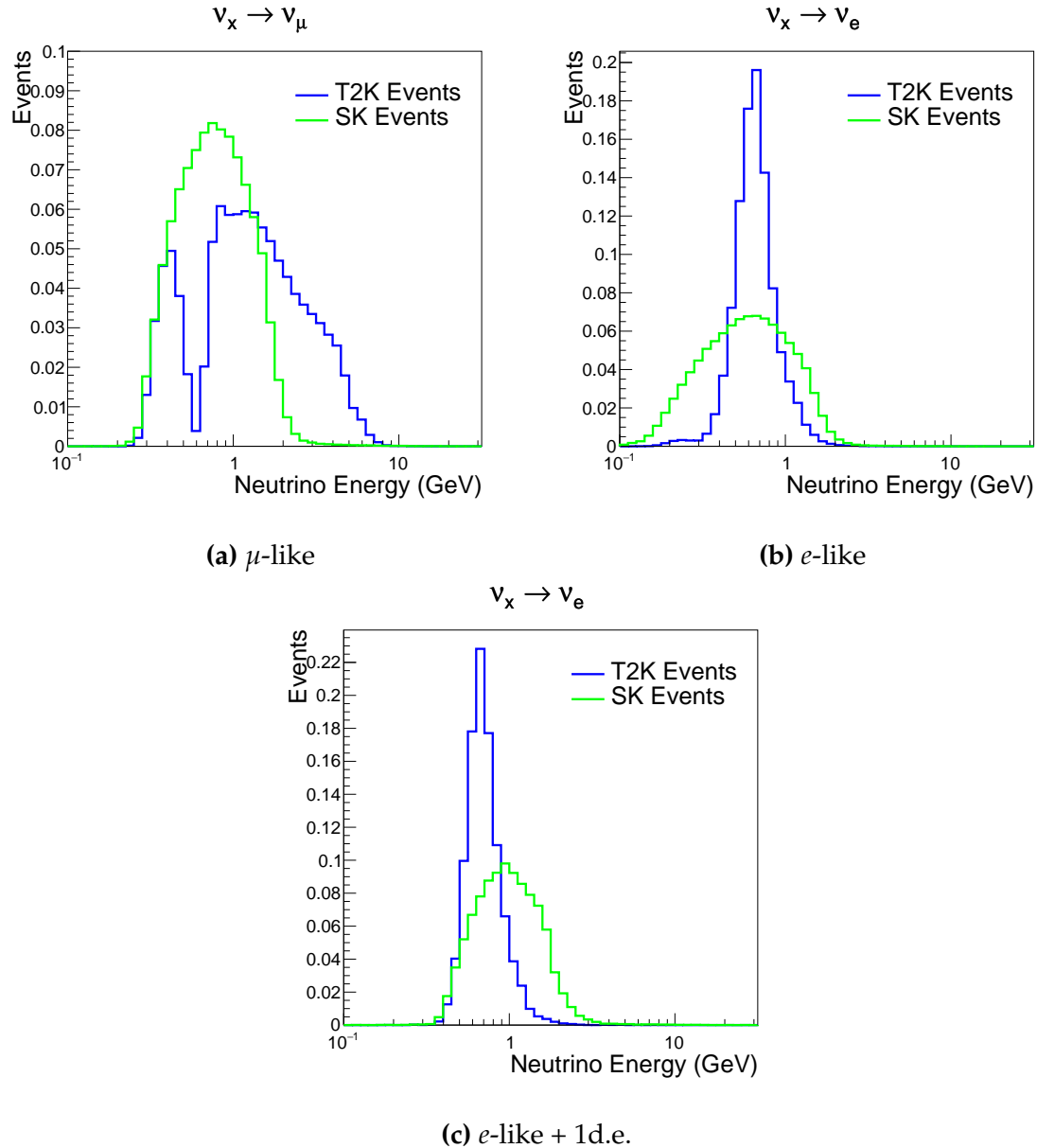
for the far detector fit, the response is binned by neutrino energy and sample binning: lepton momentum and cosine zenith binning for atmospheric splined responses and reconstructed neutrino energy and direction binning for beam samples. In total, 17 normalisation and 15 shape parameters are included in the high-energy model within this analysis.

Figure 6.7 indicates the predicted neutrino energy distribution for both beam and subGeV atmospheric samples. There is clearly significant overlap in neutrino energy between the subGeV atmospheric and beam samples, allowing similar kinematics in the final state particles. Figure 6.8 illustrates the fractional contribution of the different interaction modes per sample.

Comparing beam and atmospheric samples which target CCQE interactions (S.G. e-like 0de, S.G.  $\mu$ -like [0,1]de, [FHC,RHC] 1R  $\mu$ -like and [FHC,RHC] 1R e-like samples), there is a very similar contribution of CCQE, CC 2p2h, and CC1 $\pi^\pm$  interactions. The samples which target CC1 $\pi^\pm$  interactions, (S.G. e-like 0de, S.G.  $\mu$ -like 2de and FHC 1R+1d.e e-like) also consist of very similar mode interactions.

As a consequence of the similarity in energy and mode contributions, correlating the systematic model between the beam and subGeV atmospheric samples ensures that this analysis attains the largest sensitivity to oscillation parameters while still ensuring neutrino interaction systematics are correctly accounted for. Due to its more sophisticated CCQE and 2p2h model, the T2K systematic model was chosen as the basis of the correlated model.

The T2K systematic model [203] is applied in a similar methodology to the SK model parameters. It consists of 19 shape parameters and 24 normalisation parameters. Four additional parameters, which model the uncertainty in the binding energy, are applied in a way to shift the momentum of the lepton emitted from a nucleus. This controls the uncertainty specified on the 27MeV binding energy assumed within Equation 6.2.



**Figure 6.7:** The predicted neutrino energy distribution for subGeV atmospheric and beam samples. FHC and RHC beam samples are summed together Asimov A oscillation parameters are assumed (given in Table 2.2). Beam and atmospheric samples with similar cuts are compared against one another.

1949 The majority of these parameters are assigned a Gaussian prior uncertainty. Those  
 1950 that have no reasonably motivated uncertainty, or those which have not been fit to  
 1951 external data, are assigned a flat prior which does not affect the penalty term.

1952 There are three particular tunes of the T2K flux and low energy cross section model  
 1953 typically considered. Firstly, the “generated” tune which is the set of dial values with

	CC QE	CC 2p2h	CC $1\pi^\pm$	CC $M\pi$	CC Other	NC $\pi^0$	NC $1\pi^\pm$	NC $M\pi$	NC Coh.	NC Other
FHC 1R+1d.e. e-like	<b>0.04</b>	<b>0.02</b>	<b>0.83</b>	<b>0.03</b>	<b>0.04</b>	<b>0.01</b>	<b>0.01</b>	<b>0.01</b>	<b>0.00</b>	<b>0.01</b>
RHC 1R e-like	<b>0.62</b>	<b>0.12</b>	<b>0.11</b>	<b>0.01</b>	<b>0.02</b>	<b>0.06</b>	<b>0.01</b>	<b>0.01</b>	<b>0.01</b>	<b>0.04</b>
FHC 1R e-like	<b>0.68</b>	<b>0.12</b>	<b>0.10</b>	<b>0.00</b>	<b>0.02</b>	<b>0.04</b>	<b>0.01</b>	<b>0.00</b>	<b>0.00</b>	<b>0.02</b>
RHC 1R $\mu$ -like	<b>0.62</b>	<b>0.13</b>	<b>0.17</b>	<b>0.02</b>	<b>0.03</b>	<b>0.00</b>	<b>0.02</b>	<b>0.00</b>	<b>0.00</b>	<b>0.00</b>
FHC 1R $\mu$ -like	<b>0.62</b>	<b>0.12</b>	<b>0.16</b>	<b>0.02</b>	<b>0.03</b>	<b>0.00</b>	<b>0.03</b>	<b>0.00</b>	<b>0.00</b>	<b>0.00</b>
S.G. $\pi^0$ -like	<b>0.05</b>	<b>0.01</b>	<b>0.02</b>	<b>0.00</b>	<b>0.01</b>	<b>0.68</b>	<b>0.06</b>	<b>0.07</b>	<b>0.06</b>	<b>0.04</b>
S.G. $\mu$ -like 2de	<b>0.04</b>	<b>0.01</b>	<b>0.80</b>	<b>0.10</b>	<b>0.04</b>	<b>0.00</b>	<b>0.00</b>	<b>0.00</b>	<b>0.00</b>	<b>0.00</b>
S.G. $\mu$ -like 1de	<b>0.72</b>	<b>0.11</b>	<b>0.12</b>	<b>0.01</b>	<b>0.02</b>	<b>0.00</b>	<b>0.01</b>	<b>0.00</b>	<b>0.00</b>	<b>0.00</b>
S.G. $\mu$ -like 0de	<b>0.68</b>	<b>0.11</b>	<b>0.10</b>	<b>0.01</b>	<b>0.02</b>	<b>0.01</b>	<b>0.05</b>	<b>0.01</b>	<b>0.00</b>	<b>0.02</b>
S.G. e-like 1de	<b>0.05</b>	<b>0.01</b>	<b>0.75</b>	<b>0.10</b>	<b>0.05</b>	<b>0.00</b>	<b>0.01</b>	<b>0.02</b>	<b>0.00</b>	<b>0.01</b>
S.G. e-like 0de	<b>0.73</b>	<b>0.11</b>	<b>0.10</b>	<b>0.01</b>	<b>0.02</b>	<b>0.02</b>	<b>0.00</b>	<b>0.00</b>	<b>0.00</b>	<b>0.00</b>

**Figure 6.8:** The interaction mode contribution of each sample given as a fraction of the total event rate in that sample. Asimov A oscillation parameters are assumed (given in Table 2.2). The Charged Current (CC) modes are broken into quasi-elastic (QE), 2p2h, resonant charged pion production ( $1\pi^\pm$ ), multi-pion production ( $M\pi$ ), and other interaction categories. Neutral Current (NC) interaction modes are given in interaction mode categories:  $\pi^0$  production, resonant charged pion production, multi-pion production, and others.

which the Monte Carlo was generated. Secondly, the set of dial values which are taken from external data measurements and used as inputs. These are the “pre-fit” dial values. The reason these two sets of dial values are different is that the external data measurements are continually updated but it is very computationally intensive to regenerate a Monte Carlo prediction after each update. The final tune is the “post-fit”, “post-ND fit” or “post-BANFF” dial values. These are the values taken from a fit to the beam near detector data. This fit is performed by two independent fitting frameworks, MaCh3 and BANFF, which ensures reliable measurements. The output of each fitter is converted into a covariance matrix to describe the error and correlations between all the flux and cross-section parameters. This is then propagated to the far-detector

1964 oscillation analysis group for use in the P-Theta fitting framework. As MaCh3 can  
1965 perform a near detector fit, it is included within the simultaneous fit of the far-detector  
1966 beam and atmospheric oscillation analysis. This is because this technique does not  
1967 require any assumption of Gaussian posterior distributions which is required in the  
1968 covariance matrix methodology.

1969 On top of the combination of the SK and T2K interaction models, several other  
1970 parameters have been specifically developed for the joint oscillation analysis. The  
1971 majority of the atmospheric samples'  $\delta_{CP}$  sensitivity comes from the normalisation  
1972 of subGeV electron-like events. These are modeled using a spectral function model  
1973 to approximate the nuclear ground state. However, the near detector is not able to  
1974 constrain the model. Therefore, an additional systematic is introduced which models  
1975 an alternative Continous Random Phase Approximation (CRPA) nuclear ground  
1976 state. The reasoning is documented in [204]. As the near detector can not sufficiently  
1977 constrain the model, this dial approximates the event weights if a CRPA model had  
1978 been assumed rather than a spectral function. This dial only effects  $\nu_e$  and  $\bar{\nu}_e$  and is  
1979 applied as a shape parameter.

1980 Further additions to the model have been introduced due to the inclusion of the  
1981 subGeV  $\pi^0$  atmospheric sample. This particularly targets charged current and neutral  
1982 current  $\pi^0$  producing interactions to help constrain the systematic uncertainties. There  
1983 is no analogous sample in the T2K beam-only analysis so no significant effort has  
1984 been placed into building a sufficient uncertainty model. Therefore, an uncertainty  
1985 that affects neutral current resonant  $\pi^0$  production is incorporated into this analysis.  
1986 Comparisons of NEUT's NC resonant pion production predictions have been made to  
1987 MiniBooNE [205] data and a consistent 16% to 21% underprediction is observed [204].  
1988 Consequently, a conservative 30% normalisation parameter is invoked.

1989 Down-going events are mostly insensitive to oscillation parameters and can act  
 1990 similar to the near detector within an accelerator experiment (Details will be dis-  
 1991 cussed in chapter 7). This region of phase space can act as a sideband and allows the  
 1992 cross-section model and near detector constraint to be studied. The distribution of  
 1993 events in this region is calculated using the technique outlined in subsection 4.3.4. For  
 1994 CCQE-targeting samples, the application of the near detector constraint is well within  
 1995 the statistical fluctuation of the down-going data such that no significant tension is  
 1996 observed between the data and the Monte Carlo prediction after the near detector  
 1997 constraint is applied. This is not the case for samples with target CCRES interac-  
 1998 tions. The electron-like data is consistent with the constrained prediction at high  
 1999 reconstructed momenta but diverges at lower momentum, whereas the muon-like  
 2000 sample is under-predicted throughout the range of momenta. To combat this disagree-  
 2001 ment, an additional cross-section systematic dial, specifically designed to inflate the  
 2002 low pion momentum systematics was developed in [204]. This is a shape parameter  
 2003 implemented through a splined response.

#### 2004 6.4.4 Near Detector

2005 The systematics applied due to uncertainties arising from the response of the near  
 2006 detector is documented in [133]. The response is described by 574 normalisation param-  
 2007 eters binned in the selected sample as well as momentum and angle,  $P_\mu$  and  $\cos(\theta_\mu)$ ,  
 2008 of the final-state muon. These are applied via a covariance matrix with each parameter  
 2009 being assigned a Gaussian prior from that covariance matrix. These normalisation  
 2010 parameters are built from underlying systematics, e.g. pion secondary interaction  
 2011 systematics, which are randomly thrown and the variation in each  $P_\mu \times \cos(\theta_\mu)$  bin is  
 2012 determined. Two thousand throws are evaluated and a covariance matrix response is  
 2013 created. This allows significant correlations between FGD1 and FGD2 samples, as well

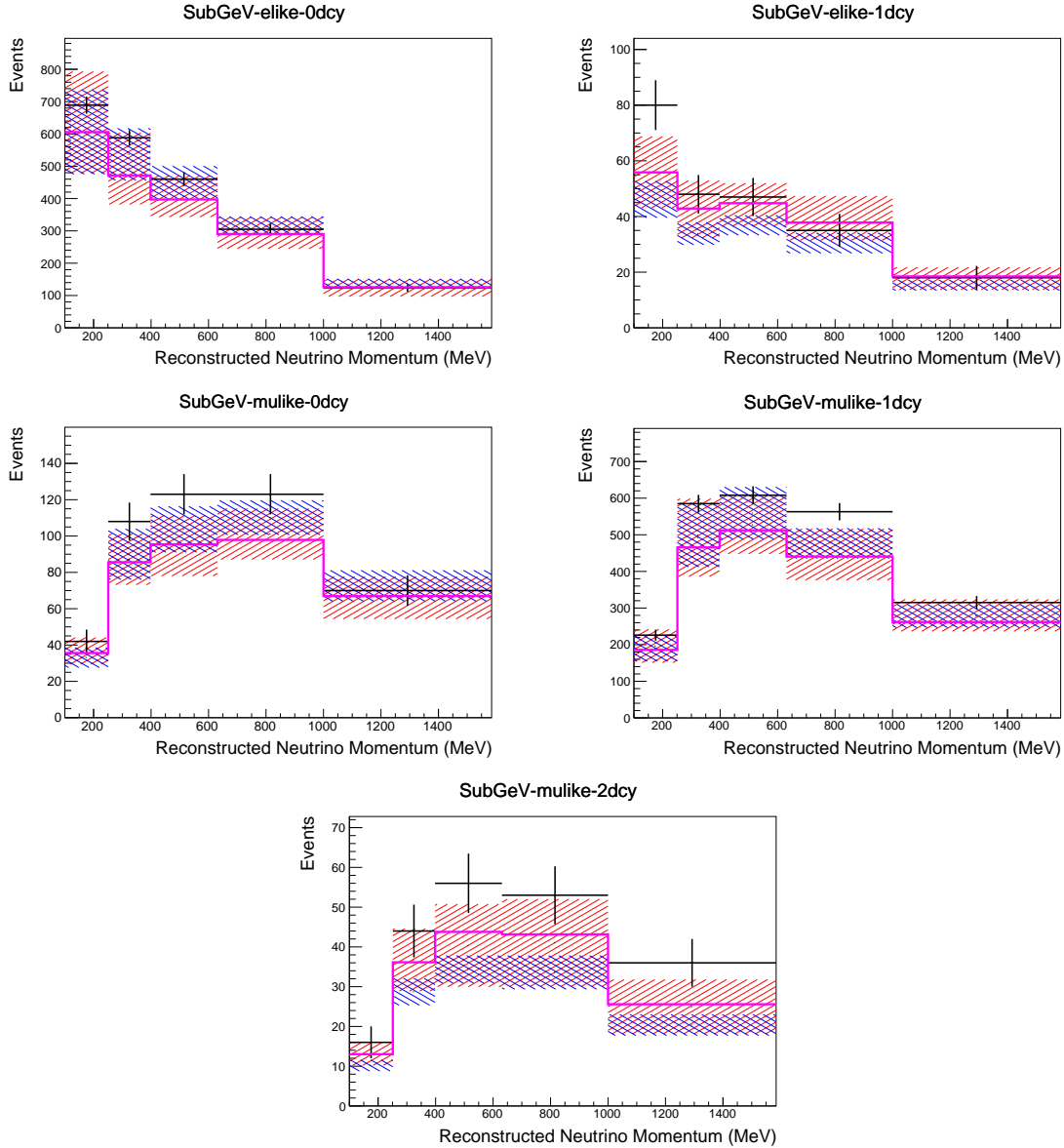


**Figure 6.9:** Down-going atmospheric subGeV single-ring samples comparing the mean and error of the pre-fit and post-fit Monte Carlo predictions in red and blue, respectively. The magenta histogram illustrates the Monte Carlo prediction using the generated dial values. The black points illustrate the down-going data with statistical errors given. The mean and errors of the Monte Carlo predictions are calculated by the techniques documented in subsection 4.3.4. The pre-fit spectrum is calculated by throwing the cross-section and atmospheric flux dial values from the pre-fit covariance matrix. The post-fit spectrum is calculated by sampling the cross-section dial values from an ND fit MCMC chain, whilst still throwing the atmospheric flux dials from the pre-fit covariance.

<sup>2014</sup> as adjacent  $P_\mu \times \cos(\theta_\mu)$  bins. Statistical uncertainties are accounted for by including

<sup>2015</sup> fluctuations of each event's weight from a Poisson distribution.

2016      Similar to the cross-section systematics, MaCh3 and BANFF are used to constrain  
2017    the uncertainty of these systematics through independent validations. Each fitter  
2018    generates a post-fit covariance matrix which is compared and passed to the far-detector  
2019    oscillation analysis working group. As the analysis presented within this thesis uses  
2020    the MaCh3 framework, a joint oscillation analysis fit of all three sets of samples and  
2021    their respective systematics is performed.

2022    **6.4.5 Far Detector**

2023    Two configurations of the far detector systematic model implementation have been  
2024    considered. Firstly, the far detector systematic uncertainties for beam and atmospheric  
2025    samples are taken from their respective analysis inputs, denoted “official inputs” anal-  
2026    ysis. Consequently, no correlations are assumed between the beam and atmospheric  
2027    samples. The generation of the beam- and atmospheric-specific inputs are documented  
2028    in subsubsection 6.4.5.1 and subsubsection 6.4.5.2. Secondly, a correlated detector  
2029    model has been developed. Here, the distribution of parameters used for applying  
2030    event cuts (e.g. electron-muon PID separation) is modified within the fit. It follows  
2031    a similar methodology to the beam far detector systematics implementation but per-  
2032    forms a joint fit of the beam and atmospheric data. This alternative implementation is  
2033    detailed in subsubsection 6.4.5.3.

2034    **6.4.5.1 Beam Samples**

2035    There are 45 systematics which describe the response of the far detector to beam  
2036    events [183], split into 44 normalisation parameters and one energy scale systematic.  
2037    The energy scale systematic is applied as a multiplicative scaling of the reconstructed  
2038    neutrino energy. It is described by a Gaussian, centered at one with equal to the

2039 difference in Monte Carlo to data comparisons performed in [185]. The normalisation  
 2040 parameters are assigned a Gaussian error centralised at one with width taken from a  
 2041 covariance matrix. A detailed breakdown of the generation of the covariance matrix  
 2042 is found in [197]. To build the covariance matrix, a fit is performed on atmospheric  
 2043 data which has been selected using beam sample selection cuts. These cuts use the  
 2044 variables,  $L^i$ , where the index  $i$  is detailed in Table 6.7. Each  $L^i$  is a smear,  $\alpha$ , and shift,  
 2045  $\beta$  parameter such that,

$$L_j^i \rightarrow \bar{L}_j^i = \alpha_j^i L + \beta_j^i \quad (6.4)$$

2046 Where  $L_j^i$  ( $\bar{L}_j^i$ ) correspond to nominal(varied) PID cut parameters given in Table 6.7.  
 2047 The shift and smear parameters are binned by final-state topology,  $j$ , where the binning  
 2048 is given in Table 6.8. The final-state topology binning is because the detector will  
 2049 respond differently to events that have one or multiple rings. For example, the detector  
 2050 will be able to distinguish single-ring events better than two overlapping ring events,  
 2051 resulting in smaller systematic uncertainty for one-ring events compared to two-ring  
 2052 events. This approach is used to allow the cut parameter distributions to be modified  
 2053 within the fit, allowing for better data to Monte Carlo agreement. Only the shape  
 2054 of each of the cut variables is used within this fit, such that physics effects are not  
 2055 considered.

Cut Variable	Parameter Name
0	<code>fitQun e/mu PID</code>
1	<code>fitQun e/pi0 PID</code>
2	<code>fitQun mu/pi PID</code>
3	<code>fitQun Ring-Counting Parameter</code>

**Table 6.7:** List of cut variables that are included within the shift/smear fit documented in [197].

Category	Description
$1e$	Only one electron above Cherenkov threshold in the final state
$1\mu$	Only one muon above Cherenkov threshold in the final state
$1e+other$	One electron and one or more other charged particles above Cherenkov threshold in the final state
$1\mu+other$	One muon and one or more other charged particles above Cherenkov threshold in the final state
$1\pi^0$	Only one $\pi^0$ in the final state
$1\pi^\pm$ or $1p$	Only one hadron (typically charged pion or proton) in the final state
Other	Any other final state

**Table 6.8:** Reconstructed event topology categories on which the SK detector systematics [197] are based.

2056      Beyond the uncertainty on the PID cut criteria, the mis-modeling of  $\pi^0$  events  
 2057    is also considered. If one of the two rings from a  $\pi^0$  event is missed, this will be  
 2058    reconstructed as a  $CC\nu_e$ -like event. This is one of the largest systematics hindering the  
 2059    electron neutrino appearance analyses. Consequently, additional systematics has been  
 2060    introduced to constrain the mis-modeling of  $\pi^0$  events in SK, binned by reconstructed  
 2061    neutrino energy. To evaluate this systematic uncertainty, a set of “hybrid- $\pi^0$ ” samples  
 2062    is constructed. These events are built by overlaying one electron-like ring from the  
 2063    SK atmospheric neutrino samples or decay electron ring from a stopping cosmic ray  
 2064    muon with one simulated photon ring. Both rings are chosen so that momenta and  
 2065    opening angle follow the decay kinematics of NC  $\pi^0$  events from the T2K-MC. Hybrid-  
 2066     $\pi^0$  Monte Carlo samples with both rings from the SK Monte Carlo are produced  
 2067    to compare with the hybrid- $\pi^0$  data samples and the difference in the fraction of  
 2068    events that pass the  $\nu_e$  selection criteria is used to assign the systematic errors. In  
 2069    order to investigate any data to Monte Carlo differences that may originate from  
 2070    either the higher energy ring or lower energy ring, two samples are built; a sample  
 2071    in which the electron constitutes the higher energy ring from the  $\pi^0$  decay called the  
 2072    primary sample and another one in which it constitutes the lower energy ring called

2073 the secondary sample. The standard T2K  $\nu_e$  fiTQun event selection criteria are used to  
2074 select events.

2075 Final contributions to the covariance matrix are determined by supplementary  
2076 uncertainties attained by comparing stopping muon data to Monte Carlo prediction,  
2077 as first introduced in section 5.2. The efficiency of tagging decay electrons is estimated  
2078 by the stopping muon data to Monte Carlo differences by comparing the number  
2079 of one decay electron events to the number of events with one or fewer decay elec-  
2080 trons. Similarly, the rate at which fake decay electrons are reconstructed by fiTQun  
2081 is estimated by comparing the number of two decay electron events to the number  
2082 of events with one or two reconstructed decay electrons. The two sources of sys-  
2083 tematics are added in quadrature weighted by the number of events with one true  
2084 decay electron yielding a 0.2% systematic uncertainty. A fiducial volume systematic of  
2085  $\pm 2.5\text{cm}$  which corresponds to a 0.5% shift in the normalisation of events. Additional  
2086 normalisation uncertainties based on neutrino flavour and interaction mode are also  
2087 defined in [183,206,207].

2088 Two additional sources of uncertainty are included: secondary and photo-nuclear  
2089 interactions. These are estimated by varying the underlying parameters are building a  
2090 distribution of sample event rates. These contributions are then added in quadrature  
2091 to the above covariance matrix.

#### 2092 6.4.5.2 Atmospheric Samples

2093 The systematic parameters which control the detector systematics for atmospheric  
2094 samples, documented in [89], are split into two sub-groups. Those which are related  
2095 to particle identification and ring counting systematics and those which are related to  
2096 calibration, separation, and reduction uncertainties.

2097     The particle identification systematics consist of five parameters. The ring separation systematic enforces an anti-correlated response between the single-ring and  
 2098 multi-ring samples. This is implemented as a fractional increase/decrease in the  
 2099 overall normalisation of each sample, depending on the distance to the nearest wall  
 2100 from an event's vertex. The coefficients of the normalisation are estimated prior to the  
 2101 fit and depend on the particular atmospheric sample. The single-ring and multi-ring  
 2102 PID systematics encode the detector's ability to separate electron-like and muon-like  
 2103 events and are implemented in a similar way to the ring separation systematic.  
 2104

2105     The multi-ring electron-like separation likelihood, discussed in section 6.1, encodes  
 2106 the ability of the detector to separate neutrino from anti-neutrino events. As an impor-  
 2107 tant systematic in the mass hierarchy determination, systematic uncertainties control  
 2108 the relative normalisations of the  $\nu_e$  and  $\bar{\nu}_e$  enriched samples. Two normalisation  
 2109 parameters are implemented which vary the event rate of each multi-ring sample,  
 2110 whilst ensuring the total event rate is conserved.

2111     There are 22 systematics related to calibration measurements, including effects  
 2112 from backgrounds, reduction, and showering effects. They are documented in [89] and  
 2113 briefly summarised in Table 6.9. They are applied via normalisation parameters, with  
 2114 the separation systematics requiring the conservation of event rate across all samples.

2115     **6.4.5.3 Correlated Detector Model**

2116     A complete uncertainty model of the SK detector would be able to determine the  
 2117 systematic shift on the sample spectra for a variation of the underlying parameters,  
 2118 e.g. PMT angular acceptance. However, this is computationally intensive, requiring  
 2119 Monte Carlo predictions to be made for each plausible variation. Consequently, an  
 2120 effective parameter model has been utilised for a correlated detector model following  
 2121 from the T2K-only model implementation documented in subsubsection 6.4.5.1. The

**Table 6.9:** Sources of systematic errors specified within the grouped into the “calibration” systematics model.

Index	Description
0	Partially contained reduction
1	Fully contained reduction
2	Separation of fully contained and partially contained events
3	Separation of stopping and through-going partially contained events in top of detector
4	Separation of stopping and through-going partially contained events in barrel of detector
5	Separation of stopping and through-going partially contained events in bottom of detector
6	Background due to cosmic rays
7	Background due to flasher events
8	Vertex systematic moving events into and out of fiducial volume
9	Upward going muon event reduction
10	Separation of stopping and through-going in upward going muon events
11	Energy systematic in upward going muon events
12	Reconstruction of the path length of upward going muon events
13	Separation of showering and non-showering upward going muon events
14	Background of stopping upward going muon events
15	Background of non-showering through-going upward going muon events
16	Background of showering through-going upward going muon events
17	Efficiency of tagging two rings from $\pi^0$ decay
18	Efficiency of decay electron tagging
19	Background from downgoing cosmic muons
20	Asymmetry of energy deposition in tank
21	Energy scale deposition

<sup>2122</sup> implementation performs a simultaneous fit of detector and oscillation parameters,  
<sup>2123</sup> for the detector parameters given in Table 6.7.

<sup>2124</sup> The correlated detector model utilises the same smear and shift parameters docu-  
<sup>2125</sup> mented in subsubsection 6.4.5.1, split by final state topology. Beyond this, the shift  
<sup>2126</sup> and smear parameters are split by visible energy deposited within the detector, with

2127 binning specified in Table 6.10. This is because atmospheric events are categorised  
2128 by subGeV and multiGeV events based on visible energy, so this splitting is required  
2129 when correlating the systematic model for beam and atmospheric events. Alongside  
2130 the technical requirement, higher energy events will be better reconstructed due to  
2131 fractionally less noise within the detector. This implementation correlates the detector  
2132 systematics between the far-detector beam and subGeV atmospheric samples due  
2133 to their similar energies and interaction types. As a result of the inclusion of visible  
2134 energy binning, Equation 6.4 becomes

$$L_{jk}^i \rightarrow \bar{L}_{jk}^i = \alpha_{jk}^i L + \beta_{jk}^i, \quad (6.5)$$

2135 where  $k$  is the visible energy bin. As there are no equivalent beam samples, the  
2136 multiGeV, multiring, PC, and Up- $\mu$  samples will be subject to the ATMPD particle  
2137 identification systematics implementation as described in subsubsection 6.4.5.2 rather  
2138 than using this correlated detector model. The calibration systematics also described  
2139 in the aforementioned chapter still apply to all atmospheric samples.

Index	Range (MeV)
0	$30 \geq x > 300$
1	$300 \geq x > 700$
2	$700 \geq x > 1330$
3	$1330 \geq x$

**Table 6.10:** Visible energy binning for which the correlated SK detector systematics are based

2140 The implementation of this systematic model takes the events reconstructed values  
2141 of the cut parameters, modifies them by the particular shift and smear parameter for  
2142 that event, and then re-applies event selection. This invokes event migration, which is

2143 a new feature incorporated into the MaCh3 framework which is only achievable due  
2144 to the event-by-event reweighting scheme.

2145 Particular care has to be taken when varying the ring counting parameter. This  
2146 is because the number of rings is a finite value (one-ring, two-rings, etc.) which can  
2147 not be continuously varied through this shift and smear technique. Consequently a  
2148 ring counting parameter,  $RC_i$ , is calculated for the  $i^{th}$  event, following the definition  
2149 in [208]. The likelihood from all considered one-ring ( $L_{1R}$ ) and two-ring ( $L_{2R}$ ) fits  
2150 are compared to determine the preferred hypothesis. The difference is computed as  
2151  $\Delta_{LLH} = \log(L_{1R}) - \log(L_{2R})$ . The ring counting parameter is then defined as,

$$RC_i = \text{sgn}(\Delta_{LLH}) \times \sqrt{|\Delta_{LLH}|}, \quad (6.6)$$

2152 where  $\text{sgn}(x) = x/|x|$ . This ring counting parameter corresponds to an intermedi-  
2153 ate likelihood value used within the `fitQun` algorithm to decide the number of rings  
2154 associated with a particular event. However, fake-ring merging algorithms are applied  
2155 after this likelihood value is used. Consequently, this ring counting parameter does  
2156 not always exactly correspond to the number of reconstructed rings. This can be seen  
2157 in Figure 6.10.

2158 As the `fitQun` algorithm does not provide a likelihood value after the fake-ring  
2159 algorithms have been applied, the ring counting parameter distribution is correlated to  
2160 the final number of reconstructed rings through “maps”. These are two-dimensional  
2161 distributions of the ring counting parameter and the final number of reconstructed  
2162 rings. An example is illustrated in Figure 6.11. In principle, the `fitQun` reconstruction  
2163 algorithm should be re-run after the variation in the ring counting parameter. However,

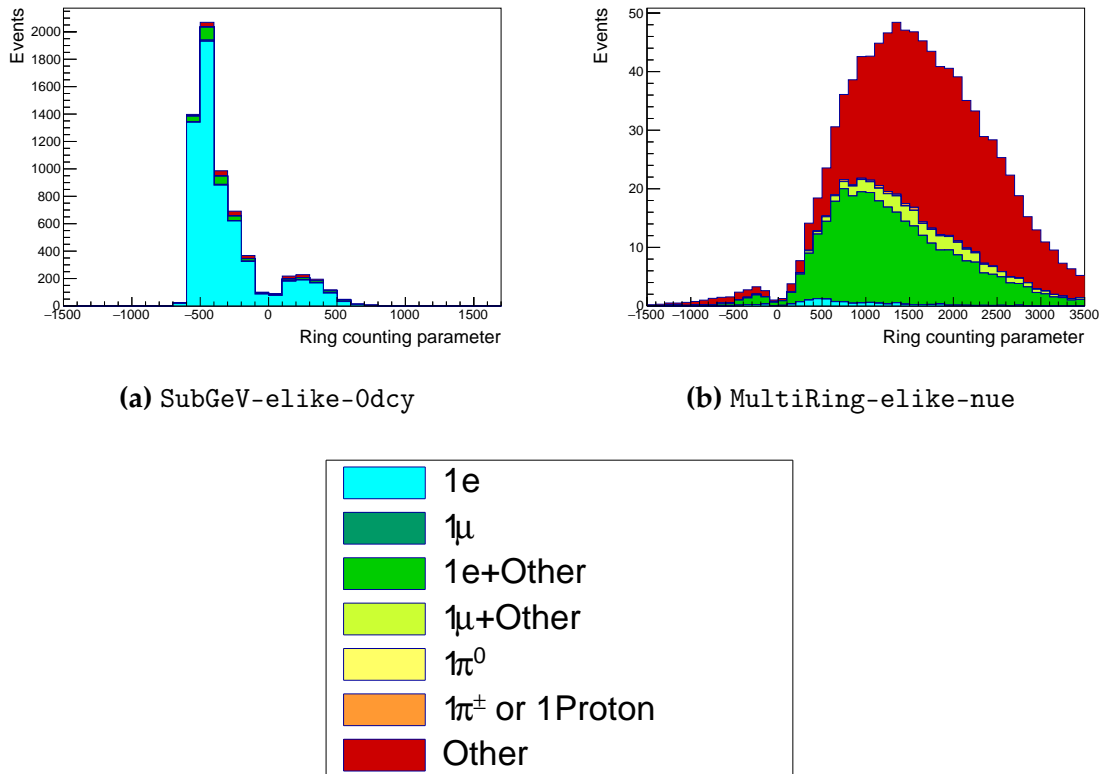


**Figure 6.10:** The ring counting parameter as defined in Equation 6.6 for the SubGeV-*elike*-0dcy and MultiRing-*elike*-*nue* samples.

<sup>2164</sup> this is not computationally viable. Therefore the “maps” are used as a reweighting  
<sup>2165</sup> template.

The maps are split by final state topology and true neutrino flavour and all fitQun-reconstructed Monte Carlo events are used to fill them. The maps are row-normalised to represent the probability of X number of rings for a given  $RC_i$  value. Prior to the fit, an event's nominal weight is calculated as  $W^i(N_{Rings}^i, L_{jk}^i)$ , where  $N_{Rings}^i$  is the reconstructed number of rings for the  $i^{th}$  event and  $W^i(x, y)$  is the bin content in map associated with the  $i^{th}$  event, where  $x$  number of rings and  $y$  is ring counting parameter. Then during the fit, the value of  $R = W^i(N_{Rings}^i, \bar{L}_{jk}^i) / W^i(N_{Rings}^i, L_{jk}^i)$  is calculated as the event weight for the  $i^{th}$  event. This is the only cut variable that uses a reweighting scheme rather than event migration.

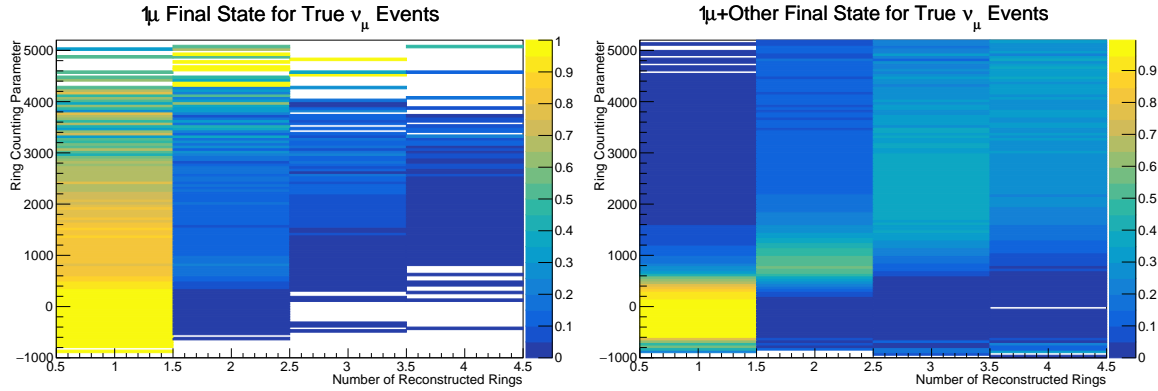


**Figure 6.11:** The ring counting parameter, defined in Equation 6.6, as a function of the number of reconstructed rings as found by the `fitQun` reconstruction algorithm. Left: true  $\nu_\mu$  events with only one muon above the Cherenkov threshold in the final state. Right: true  $\nu_\mu$  events with one muon and at least one other charged particle above the Cherenkov threshold in the final state.

2175     The  $\pi^0$  systematics introduced in subsection 6.4.4 are applied via a covariance  
 2176     matrix. This is not possible in the alternative model as no covariance matrix is used.  
 2177     Thus, the implementation of the  $\pi^0$  systematics has been modified. The inputs from  
 2178     the hybrid  $\pi^0$  sample is included via the use of “ $\chi^2$  maps”, which are two-dimensional  
 2179     histograms in  $\alpha_{jk}^i$  and  $\beta_{jk}^i$  parameters over some range. Illustrative examples of the  $\chi^2$   
 2180     maps are given in Figure 6.12. Due to their nature, the shift and smear parameters are  
 2181     typically very correlated. A map is produced for each cut parameter given in Table 6.7  
 2182     and for each visible energy bin given in Table 6.10.

2183     The maps are filled through the  $\chi^2$  comparison of the hybrid  $\pi^0$  Monte Carlo and  
 2184     data in the particle identification parameters documented in Table 6.7. The Monte  
 2185     Carlo distribution is modified by the  $\alpha_{jk}^i$  and  $\beta_{jk}^i$  scaling, whilst cross-section and flux  
 2186     nuisance parameters are thrown from their prior uncertainties. The  $\chi^2$  between the  
 2187     scaled Monte Carlo and data is calculated and the relevant point in the  $\chi^2$  map is filled.

2188     The implementation within this alternative detector model is to add the bin contents  
 2189     of the maps, for the relevant values of the  $\alpha_{jk}^i$  and  $\beta_{jk}^i$  parameters, to the likelihood  
 2190     penalty. Only  $1\pi^0$  final state topology shift and smear parameters use this prior  
 2191     uncertainty.

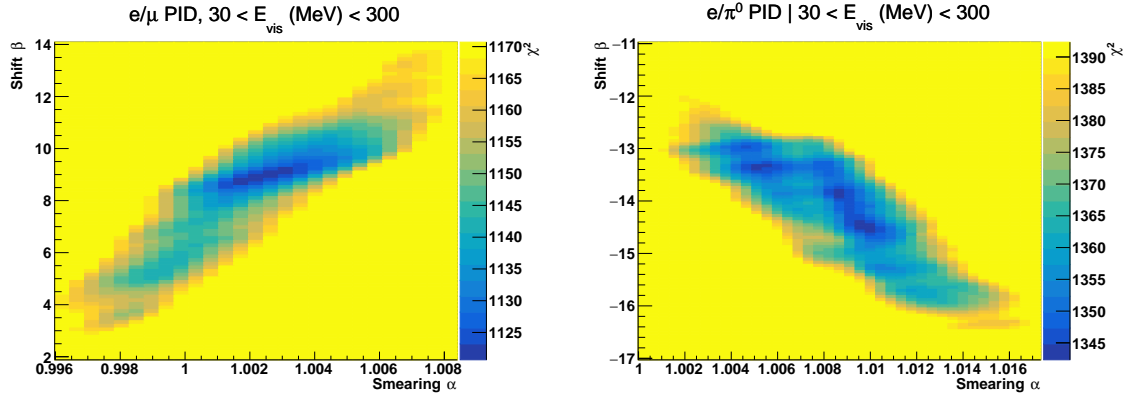


**Figure 6.12:** The  $\chi^2$  between the hybrid- $\pi^0$  Monte Carlo and data samples, as a function of smear ( $\alpha$ ) and shift ( $\beta$ ) parameters, for events which have  $1\pi^0$  final state topology. Left: Electron-muon separation PID parameter for events with  $30 \geq E_{vis}(\text{MeV}) < 300$ . Right: Electron- $\pi^0$  separation PID parameter for events with  $30 \geq E_{vis}(\text{MeV}) < 300$ .

Similarly, the implementation of the supplementary systematics documented in subsubsection 6.4.5.1 needs to be modified. A new framework [209] was built in tandem with the T2K-SK working group [183] so the additional parameters can be incorporated into the MaCh3 framework. These are applied as normalisation parameters, depending on the particular interaction mode, number of tagged decay electrons, and whether the primary particle generated Cherenkov light. They are assigned Gaussian uncertainties with widths described by a covariance matrix. Furthermore, the secondary interaction and photo-nuclear effects need to be accounted for in this detector model using a different implementation than that in subsubsection 6.4.5.1. This was done by including a shape parameter for each of the secondary interactions and the photo-nuclear systematic parameters.

There are a total of 224  $\alpha_{jk}^i$  and  $\beta_{jk}^i$  parameters, of which 32 have prior constraints from the hybrid  $\pi^0$  samples.

One final complexity of this correlated detector model is that the two sets of samples, beam and subGeV atmospheric, use slightly different parameters to distinguish electron and muon-like events. The T2K samples use the value of  $\log(L_e/L_\mu)$  whereas the atmospheric samples use the value of  $\log(L_e/L_\pi)$ , where  $L_X$  is the likelihood for

2209 hypothesis X. This is because the T2K fits use single-ring `fitQun` fitting techniques,  
 2210 whereas multi-ring fits are applied to the atmospheric samples where only the electron  
 2211 and pion hypothesis are considered. The correlation between the two likelihood ratios  
 2212 is illustrated in Figure 6.13. As discussed in section 5.2, the pion hypothesis is a very  
 2213 good approximation of the muon hypothesis due to their similar mass. Consequently,  
 2214 using the same shift and smear parameters correlated between the beam and subGeV  
 2215 atmospheric samples is deemed a good approximation.

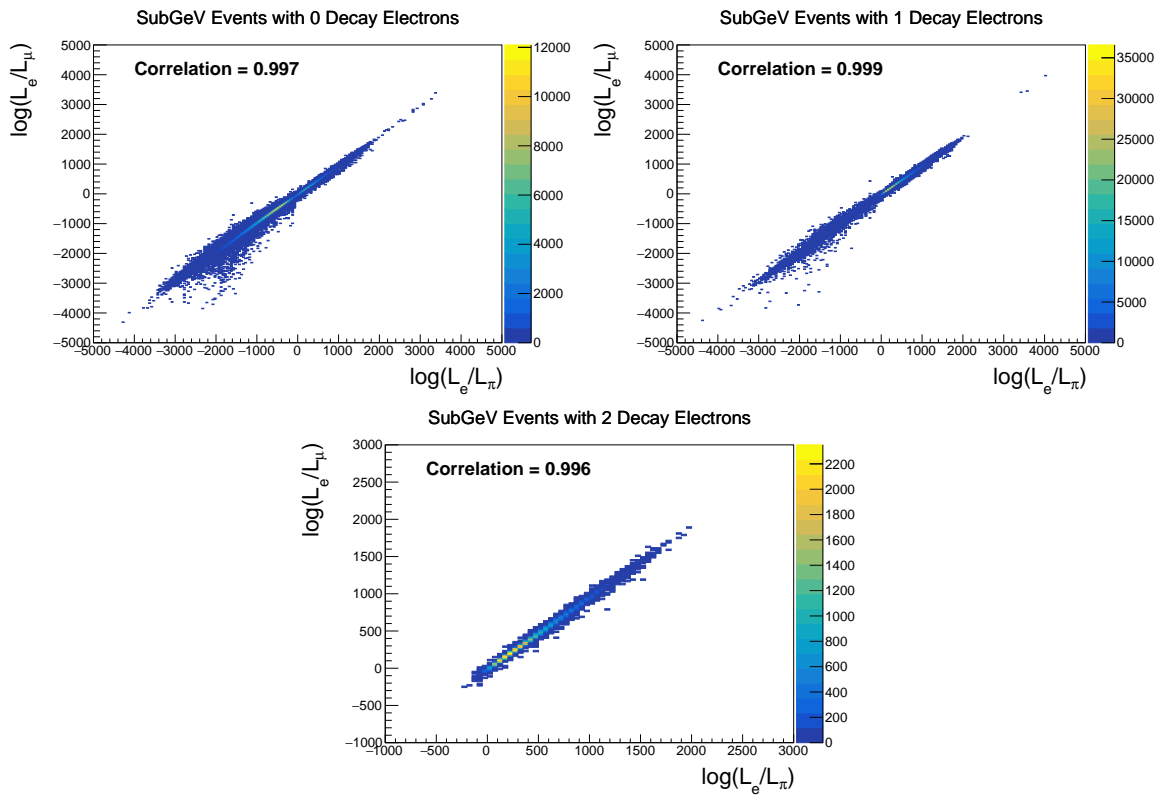


**Figure 6.13:** The distribution of  $\log(L_e/L_\mu)$  compared to  $\log(L_e/L_\pi)$  for subGeV events with zero (top left), one (top right) or two (bottom) decay electrons. The correlation in the distribution is calculated as 0.997, 0.999 and 0.996, respectively.

2216

# Chapter 7

2217

## Oscillation Probability Calculation

2218 It is important to understand how and where the sensitivity to the oscillation pa-  
2219 rameters comes from for both atmospheric and beam samples. An overview of how  
2220 these samples observe changes in  $\delta_{CP}$ ,  $\Delta m_{23}^2$ , and  $\sin^2(\theta_{23})$  is given in section 7.1. It  
2221 also explains the additional complexities involved when performing an atmospheric  
2222 neutrino analysis as compared to a beam-only analysis.

2223 Without additional techniques, atmospheric sub-GeV upward-going neutrinos  
2224 ( $E_\nu < 1.33\text{GeV}, \cos(\theta_Z) < 0.$ ) can artificially inflate the sensitivity to  $\delta_{CP}$  due to the  
2225 quickly varying oscillation probability in this region. Therefore, a “sub-sampling”  
2226 approach has been developed to reduce these biases ensuring accurate and reliable  
2227 sensitivity measurements. This technique ensures that small-scale unresolvable fea-  
2228 tures of the oscillation probability have been averaged over whilst the large-scale  
2229 features in the oscillation probability are unaffected. The documentation and valida-  
2230 tion of this technique are found in section 7.2. The oscillation probability calculation is  
2231 computationally intensive due to the large number of matrix multiplications needed.  
2232 Consequently, the CUDAProb3 implementation choice made within the fitting frame-  
2233 work, as detailed in section 7.3, ensures that the analysis can be done in a timely  
2234 manner.

2235 Whilst the beam neutrinos are assumed to propagate through a constant density  
2236 slab of material, the density variations through the Earth result in more complex  
2237 oscillation patterns. Furthermore, the uncertainty in the electron density can modify  
2238 the oscillation probability for the denser core layers of the Earth. The model of the

2239 Earth used within this analysis is detailed in section 7.4. This includes information  
2240 about the official SK-only methodology as well as improvements that can be made  
2241 to remove some of the approximations made in that analysis. Another complexity of  
2242 atmospheric neutrinos oscillation studies is that the height of production in the atmo-  
2243 sphere is not known on an event-by-event basis. An analytical averaging technique  
2244 that approximates the uncertainty of the oscillation probability has been followed,  
2245 with the author of this thesis being responsible for the implementation and validation.  
2246 This implementation of an external technique is illustrated in section 7.5.

## 2247 7.1 Overview

2248 DB: Should this be moved into an earlier chapter? The selections chapter references  
2249 the matter resonance which has not yet been explained at that point

2250 The analysis presented within this thesis focuses on the determination of oscillation  
2251 parameters from atmospheric and beam neutrinos. Whilst subject to the same oscil-  
2252 lation formalism, the way in which the two samples have sensitivity to the different  
2253 oscillation parameters differs quite significantly.

2254 Atmospheric neutrinos have a varying baseline, or “path length”,  $L$ , such that  
2255 the distance each neutrino travels before interacting is dependent upon the zenith  
2256 angle,  $\theta_Z$ . As primary cosmic rays can interact anywhere between the Earth’s surface  
2257 and  $\sim 50\text{km}$  above that, the height,  $h$ , in the atmosphere at which the neutrino was  
2258 generated also affects the path length,

$$L = \sqrt{(R_E + h)^2 - R_E^2 (1 - \cos^2(\theta_Z))} - R_E \cos(\theta_Z). \quad (7.1)$$

2259 Where  $R_E = 6,371\text{km}$  is the Earth's radius. Consequently, the oscillation probabil-  
2260 ity is dependent upon two parameters,  $\cos(\theta_Z)$  and  $E_\nu$ .

2261 The oscillation probability used within this analysis is based on [21]. The neutrino  
2262 wavefunction in the vacuum Hamiltonian evolves in each layer of constant matter  
2263 density via

$$i \frac{d\psi_j(t)}{dt} = \frac{m_j^2}{2E_\nu} \psi_j(t) - \sum_k \sqrt{2} G_F N_e U_{ej} U_{ke}^\dagger \psi_k(t), \quad (7.2)$$

2264 where  $m_j^2$  is the square of the  $j^{th}$  vacuum eigenstate mass,  $E_\nu$  is the neutrino  
2265 energy,  $G_F$  is Fermi's constant,  $N_e$  is the electron number density and  $U$  is the PMNS  
2266 matrix. The transformation  $N_e \rightarrow -N_e$  and  $\delta_{CP} \rightarrow -\delta_{CP}$  is applied for antineutrino  
2267 propagation. Thus, a model of the Earth's density is required for atmospheric neutrino  
2268 propagation. Following the official SK-only methodology [210], this analysis uses the  
2269 Preliminary Reference Earth Model (PREM) [211]. This model provides piecewise cubic  
2270 polynomials as a function of the Earth's radius which results in the density profile  
2271 illustrated in Figure 7.1. As discussed, the propagator requires layers of constant  
2272 density. The SK methodology approximates the PREM model by using four layers of  
2273 constant density [210]. The details of these layers are detailed in Table 7.1.

Layer	Outer Radius [km]	Density [ $\text{g}/\text{cm}^3$ ]	Chemical composition (Z/A)
Inner Core	1220	13	$0.468 \pm 0.029$
Outer Core	3480	11.3	$0.468 \pm 0.029$
Lower Mantle	5701	5.0	0.496
Transition Zone	6371	3.3	0.496

**Table 7.1:** Description of the four layers of the Earth invoked within the constant density approximation of the PREM model [211].

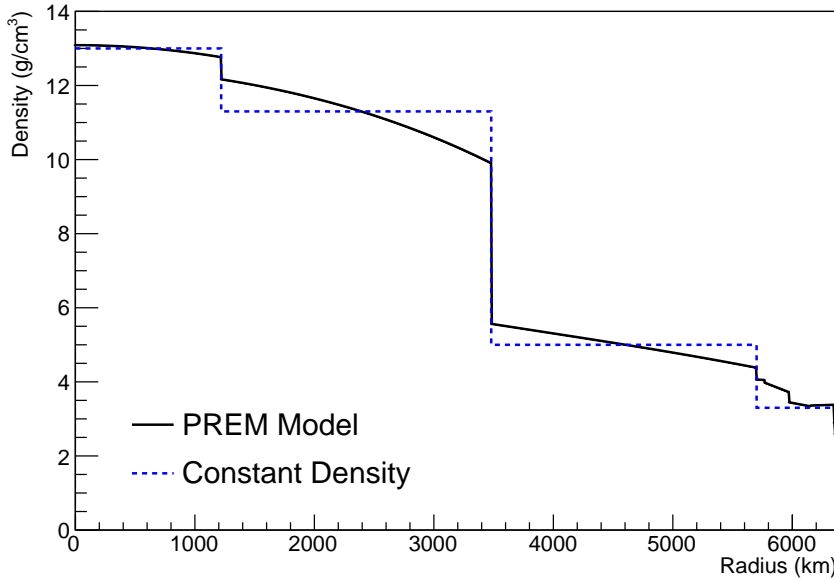


**Figure 7.1:** The density of the Earth given as a function of the radius, as given by the PREM model (Black), and the constant density four-layer approximation (Blue), as used in the official SK-only analysis.

2274     The atmospheric neutrino oscillation probabilities can be presented as two dimen-  
 2275     sional “oscillograms” as illustrated in Figure 7.2. The distinct discontinuities, as a  
 2276     function of  $\cos(\theta_Z)$ , are due to the discrete change in density invoked within the PREM  
 2277     model.

2278     Atmospheric neutrinos do have sensitivity to  $\delta_{CP}$  through a normalisation term.  
 2279     Figure 7.3 illustrates the difference in oscillation probability between CP-conserving  
 2280     ( $\delta_{CP} = 0$ ) and a CP-violating ( $\delta_{CP} = -1.601$ ) value taken from Asimov A oscillation  
 2281     parameter set (Table 2.2). The result is a complicated oscillation pattern in the appear-  
 2282     ance probability for sub-GeV upgoing neutrinos. The detector does not have sufficient  
 2283     resolution to resolve these individual patterns so the sensitivity to  $\delta_{CP}$  for atmospheric  
 2284     neutrinos comes via the overall normalisation of these events.

2285     The presence of matter means that the effect  $\delta_{CP}$  has on the oscillation probability  
 2286     is not equal between neutrinos and antineutrinos, which would be expected when  
 2287     propagating through a vacuum. This is further extenuated by the fact that SK can

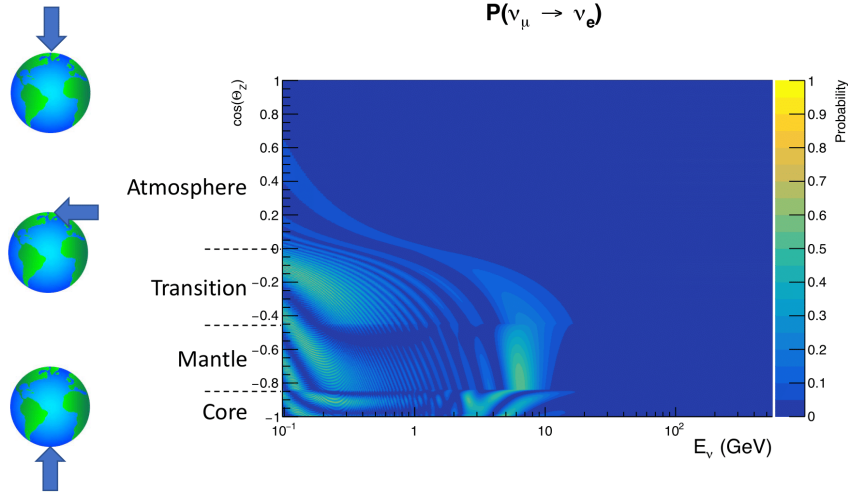


**Figure 7.2:** An “oscillogram” that depicts the  $P(\nu_\mu \rightarrow \nu_e)$  oscillation probability as a function of neutrino energy and cosine of the zenith angle. The zenith angle is defined such that  $\cos(\theta_Z) = 1.0$  represents neutrinos that travel from directly above the detector. The four-layer constant density PREM model approximation is used and Asimov A oscillation parameters are assumed (Table 2.2).

not distinguish neutrinos and antineutrinos well and that the cross-section neutrino interaction is larger than that for antineutrinos. Finally, sample selections (discussed in section 6.1) targeting different neutrino interaction modes result in an imbalance in the percentage of neutrinos to anti-neutrinos. This is because negatively charged pions from antineutrino interactions are more likely to be captured by a nucleus compared to a positively charged pion. All of these effects lead to a difference in the number of neutrinos detected compared to antineutrinos. This changes how the  $\delta_{CP}$  normalisation term is observed, resulting in a very complex sensitivity to  $\delta_{CP}$ .

Atmospheric neutrinos are subject to matter effects as they travel through the dense matter in the Earth. The vacuum and matter oscillation probabilities for  $P(\nu_e \rightarrow \nu_e)$  and  $P(\bar{\nu}_e \rightarrow \bar{\nu}_e)$  are presented in Figure 7.4, where the PREM model has been assumed. The oscillation probability for both neutrinos and antineutrinos is affected in the presence of matter. However, the resonance effects around  $O(5)\text{GeV}$  only occur for neutrinos in normal mass hierarchy and antineutrinos in inverse mass hierarchy. The

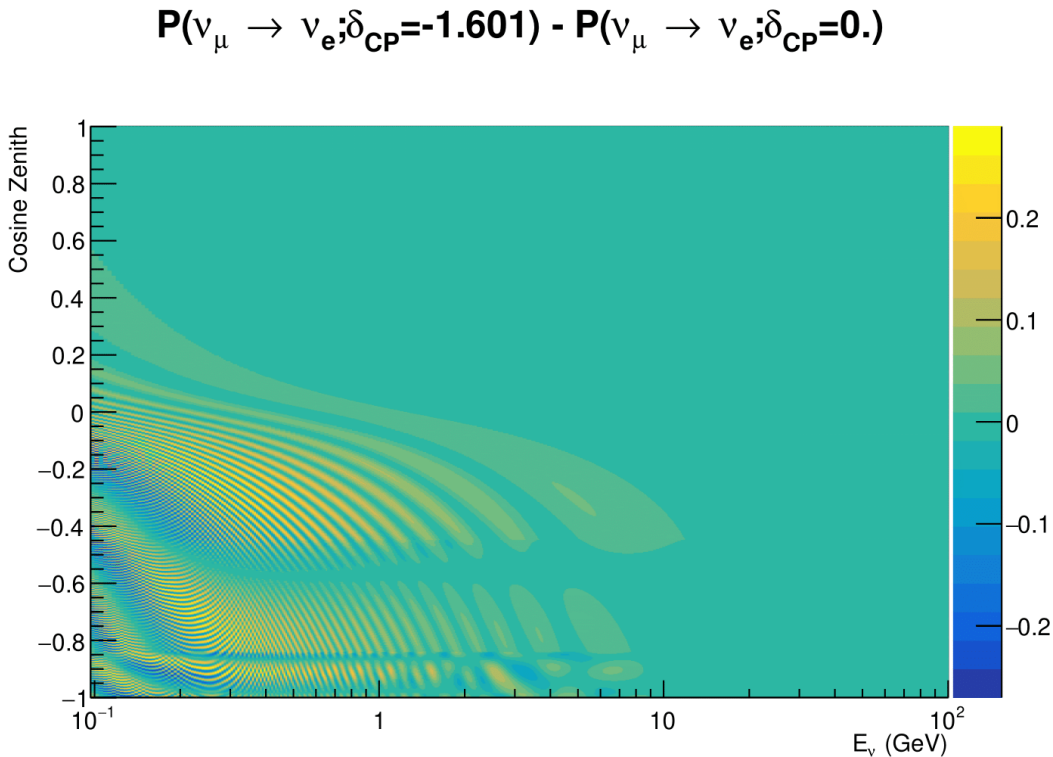


**Figure 7.3:** The effect of  $\delta_{CP}$  for atmospheric neutrinos given in terms of the neutrino energy and zenith angle. This oscillogram compares the  $P(\nu_\mu \rightarrow \nu_e)$  oscillation probability for a CP conserving ( $\delta_{CP} = 0.0$ ) and a CP violating ( $\delta_{CP} = -1.601$ ) value taken from the Asimov A parameter set. The other oscillation parameters assume the Asimov A oscillation parameter set given in Table 2.2.

exact position and amplitude of the resonance depend on  $\sin^2(\theta_{23})$  meaning that the atmospheric neutrinos have sensitivity to  $\sin^2(\theta_{23})$ .

As the T2K beam flux is centered at the first oscillation maximum ( $E_\nu = 0.6\text{GeV}$ ), the sensitivity to  $\delta_{CP}$  is predominantly observed as a change in the event-rate of e-like samples in  $\nu/\bar{\nu}$  modes. Figure 7.5 illustrates the  $P(\nu_\mu \rightarrow \nu_e)$  oscillation probability for a range of  $\delta_{CP}$  values. A circular modulation of the first oscillation peak (in both magnitude and position) is observed when varying throughout the allowable values of  $\delta_{CP}$ . The CP-conserving values of  $\delta_{CP} = 0, \pi$  have a lower(higher) oscillation maximum than the CP-violating values of  $\delta_{CP} = -\pi/2(\delta_{CP} = \pi/2)$ . A sub-dominant

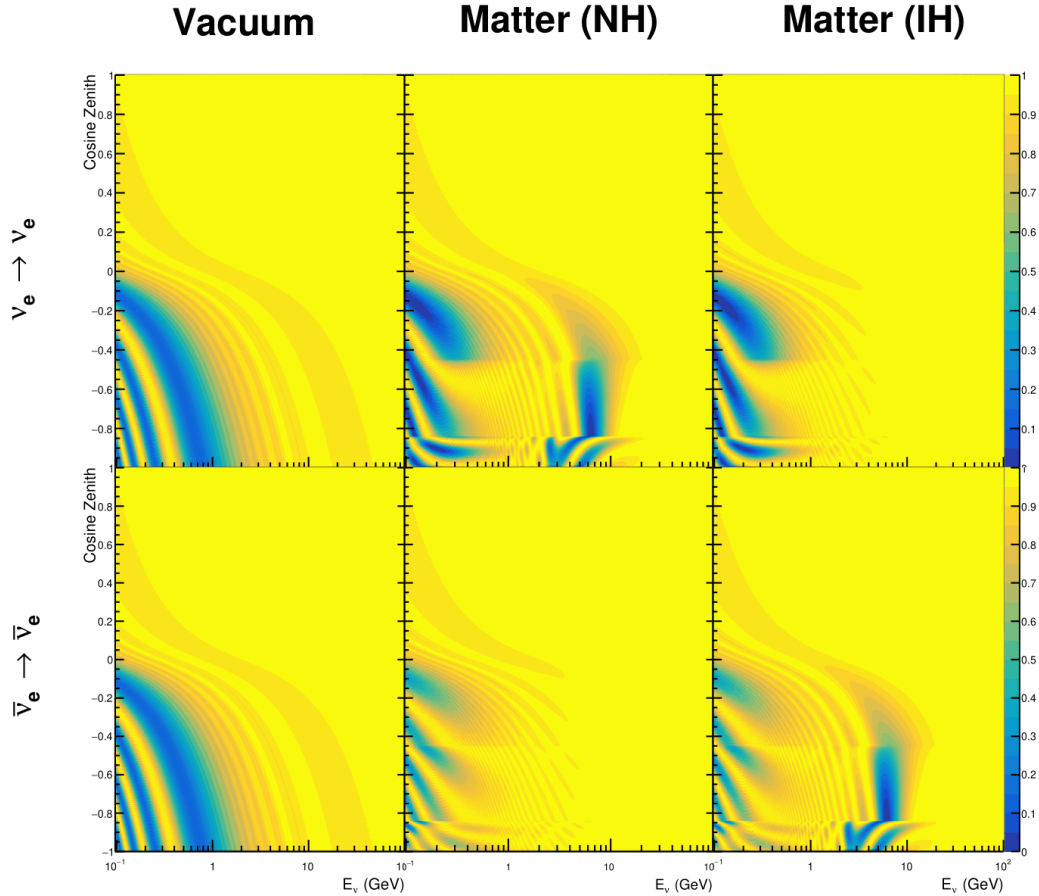


**Figure 7.4:** An illustration of the matter-induced effects on the oscillation probability, given as a function of neutrino energy and zenith angle. The top row of panels gives the  $P(\nu_e \rightarrow \nu_e)$  oscillation probability and the bottom row illustrates the  $P(\bar{\nu}_e \rightarrow \bar{\nu}_e)$  oscillation probability. The left column highlights the oscillation probability in a vacuum, whereas the middle and right column represents the oscillation probabilities when the four-layer fixed density PREM model is assumed. All oscillation probabilities assume the “Asimov A” set given in Table 2.2, but importantly, the right column sets an inverted mass hierarchy. The “matter resonance” effects at  $E_\nu \sim 5\text{GeV}$  can be seen in the  $P(\nu_e \rightarrow \nu_e)$  for normal mass hierarchy and  $P(\bar{\nu}_e \rightarrow \bar{\nu}_e)$  for inverted hierarchy.

shift in the energy of the oscillation peak is also present to aid in separating the two

CP-conserving values of  $\delta_{CP}$ .

T2K’s sensitivity to the  $\sin^2(\theta_{23})$  and  $\Delta m_{23}^2$  is observed as a shape-based variation

of the muon-like samples, as illustrated in Figure 7.5. The value of  $\Delta m_{32}^2$  laterally shifts

the position of the oscillation dip (around  $E_\nu \sim 0.6\text{GeV}$ ) in the  $P(\nu_\mu \rightarrow \nu_\mu)$  oscillation

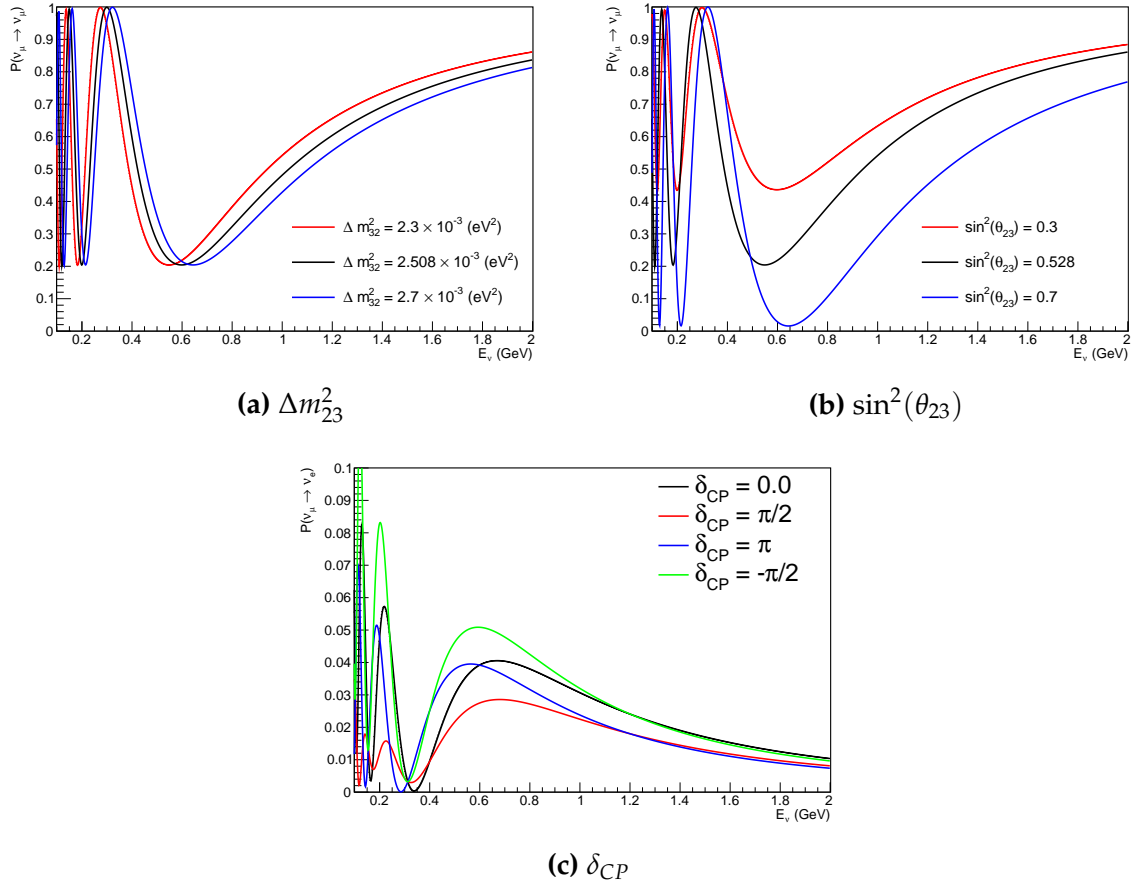


**Figure 7.5:** The oscillation probability for beam neutrino events given as a function of neutrino energy. All oscillation parameters assume the “Asimov A” set given in Table 2.2 unless otherwise stated. Each panel represents a change in one of the oscillation parameters whilst keeping the remaining parameters fixed.

probability. A variation of  $\sin^2(\theta_{23})$  is predominantly observed as a vertical shift of the oscillation dip with second-order horizontal shifts being due to matter effects. The beam neutrinos have limited sensitivity to matter effects due to the relatively shorter baseline as well as the Earth’s mantle being a relatively low-density material (as compared to the Earth’s core). For some values of  $\delta_{CP}$ , the degeneracy in the number of e-like events allows the mass hierarchy to be resolved. This leads to a  $\delta_{CP}$ -dependent mass hierarchy sensitivity which can be seen in Figure 7.6.

Whilst all oscillation channels should be included for completeness, the computational resources required to run a fit are limited and any reasonable approximations

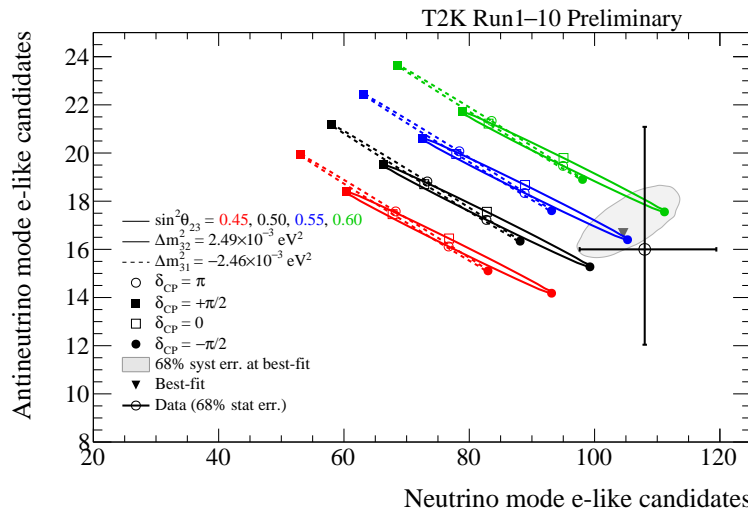


**Figure 7.6:** The number of electron-like events in the FHC and RHC operating mode of the beam, as a function of the oscillation probabilities. Both normal hierarchy (Solid) and inverse hierarchy (Dashed) values of  $\Delta m_{23}^2$  are given.

which reduce the number of oscillation probability calculations that need to be made  
 should be applied. The  $\nu_e \rightarrow \nu_{e,\mu,\tau}$  (and antineutrino equivalent) oscillations can be  
 ignored for beam neutrinos as the  $\nu_e/\bar{\nu}_e$  fluxes are approximately two orders of magni-  
 tude smaller than the corresponding  $\nu_\mu/\bar{\nu}_\mu$  flux. Furthermore, as the peak neutrino  
 energy of the beam is well below the threshold for charged current tau production  
 ( $E_\nu = 3.5 \text{ GeV}$  [51], only a small proportion of the neutrinos produced in the beam have  
 the required energy. For the few neutrinos that have sufficient energy, the oscillation  
 probability is very small due to the short baseline. Whilst these approximations can  
 be made for the beam neutrinos, the atmospheric flux of  $\nu_e$  is of the same order of  
 magnitude as the  $\nu_\mu$  flux and the energy distribution of atmospheric neutrinos extends  
 well above the tau production threshold.

## 2336 7.2 Treatment of Fast Oscillations

2337 As shown in Figure 7.7, atmospheric neutrino oscillations have a significantly more  
2338 complex structure for upgoing neutrinos with energy below 1GeV. This is because the  
2339  $L/E$  dependence of the oscillation probability in this region induces rapid variations  
2340 for small changes in  $L$  or  $E$ . As discussed in section 7.1, this is also the region in which  
2341 atmospheric neutrinos have sensitivity to  $\delta_{CP}$ . In practice, the direction of the neutrino  
2342 is inferred from the direction of the final state particles traveling in the detector, which  
2343 can be poor for low-energy neutrino interactions. This creates a distinct difference  
2344 from the beam neutrinos where the position of the source is very precisely known.

2345 As a consequence of the unresolvable structure, an average oscillation probability  
2346 is observed in the subGeV upgoing region. This creates a computational problem; A  
2347 significantly large amount of Monte Carlo statistics would be required to accurately  
2348 predict the number of events if Monte Carlo averaging was the only technique used.  
2349 This section describes the ‘sub-sampling’ approach developed for this analysis and  
2350 compares it to the methodology used within the SK-only analysis.

2351 The official SK-only analysis uses the osc3++ oscillation parameter fitter [210].  
2352 To perform the fast oscillation averaging, it uses a ‘nearest-neighbour’ technique.  
2353 For a given neutrino event, the nearest twenty neighbours in reconstructed lepton  
2354 momentum and zenith angle are found and a distribution of their neutrino energies is  
2355 built. The RMS,  $\sigma$ , of this distribution is then used to compute an average oscillation  
2356 probability for the given neutrino Monte Carlo event.

2357 For the  $i^{th}$  event, the oscillation weight is calculated as

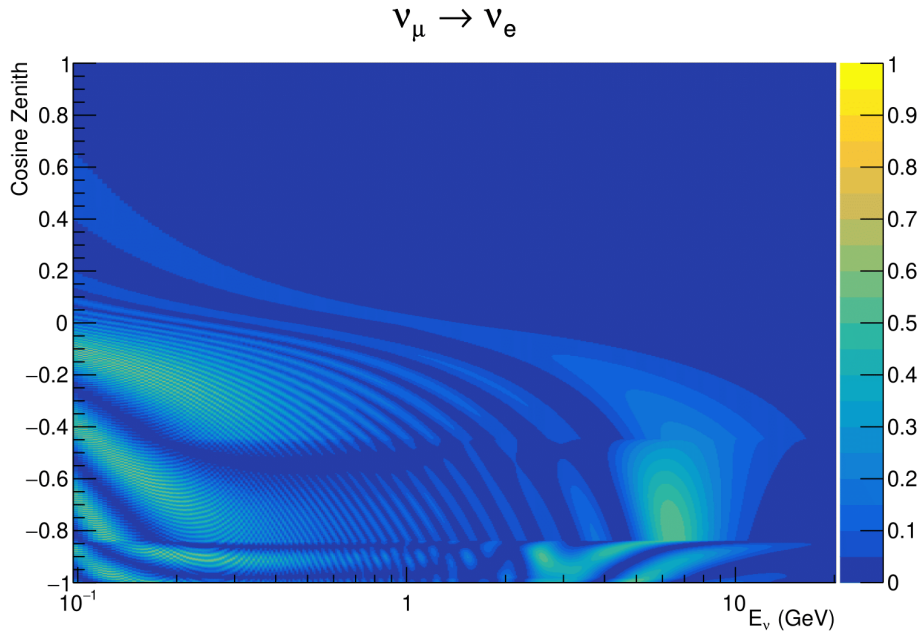


**Figure 7.7:** The oscillation probability  $P(\nu_\mu \rightarrow \nu_e)$ , given as a function of neutrino energy and zenith angle, which highlights an example of the “fast” oscillations in the sub-GeV upgoing region.

$$W_i = \frac{1}{5}P(E_i, \bar{L}_i) + \frac{1}{5} \sum_{\beta=-1,-0.5,0.5,1} P(E_i + \beta\sigma_i, L_\beta), \quad (7.3)$$

where  $P(E, L)$  is the oscillation probability calculation for neutrino energy  $E$  and path length  $L$  and the two path lengths,  $\bar{L}_i$  and  $L_\beta$  are discussed below. All of the oscillation probability calculations are performed with a fixed zenith angle such that the same density profile is used.

The uncertainty in the production height is controlled by using an “average” production height,  $\bar{L}_i$ , which represents the average path length computed using twenty production heights taken from the Honda flux model’s prediction [45]. For a given event, the production heights are sampled in steps of 5% of their cumulative distribution function.  $L_\beta$  values are similarly calculated but instead use different combinations of four production heights,

$$\begin{aligned}
 L_{-1.0} &= \frac{1}{4}L(45, 50, 55, 60), \\
 L_{-0.5} &= \frac{1}{4}L(35, 40, 65, 70), \\
 L_{+0.5} &= \frac{1}{4}L(25, 30, 75, 68), \\
 L_{+1.0} &= \frac{1}{4}L(15, 20, 85, 89).
 \end{aligned} \tag{7.4}$$

2368 This averaging technique works because of the inference between the zenith angle  
 2369 and the reconstructed direction of final state particles in the detector. For low-energy  
 2370 neutrinos, where the resolution of the true neutrino direction is poor,  $\sigma_i$  will be large,  
 2371 resulting in significant averaging effects. Contrary to this, the inferred direction of  
 2372 high-energy neutrinos will be much closer to the true value, meaning that  $\sigma_i$  will be  
 2373 smaller, culminating in small averaging effects.

2374 In practice, this technique is performed before the fit in order to deal with the  
 2375 computational cost. This is possible as the Osc3++ framework uses binned oscillation  
 2376 parameters rather than continuous so the oscillation parameters used in the fit are  
 2377 known prior to run-time. The framework used in this analysis uses continuous  
 2378 oscillation parameters, and due to the MCMC fitting technique, there is no way to  
 2379 know which oscillation parameter values will be selected *a priori*. Therefore, the  
 2380 oscillation parameter calculation has to be performed at run-time. Computing five  
 2381 oscillation probabilities per event would require far too many computational resources  
 2382 to be viable. Therefore SK technique can not be used within this analysis. However,  
 2383 the concept of the averaging technique can be taken from it.

2384 To perform a similar averaging as the SK analysis, a sub-sampling approach using  
 2385 binned oscillograms has been devised. The technique can be explained by considering  
 2386 a “fine” and “coarse” oscillogram. The fine oscillograms are used to define the array of

2387  $\cos(\theta_Z)$  and  $E_\nu$  used in the oscillation engine. The coarse oscillograms cover the same  
2388 phase-space but have fewer bins, where the value of a particular coarse bin is taken  
2389 as the linear average (flat prior in  $E_\nu$  and  $\cos(\theta_Z)$ ) of all fine bins which falls into it.  
2390 The coarse oscillogram is then used for determining the oscillation weight for a given  
2391 event. The binning which is used to calculate the oscillation probabilities, known as  
2392 the ‘fine’ binning, has  $N \times N$  subdivisions per coarse bin. Figure 7.8 illustrates the  
2393  $N = 2$  example where the assigned value to a coarse bin is the average of the four fine  
2394 bins which fall in that coarse bin. Whilst the coarse bin edges do not have to be linear  
2395 on either axis, the sub-division of the fine bins is linear over the range of a coarse bin.

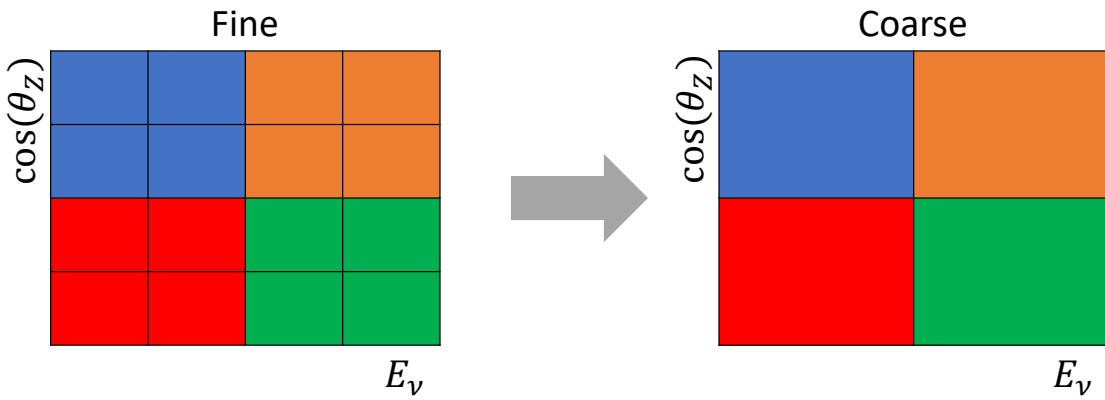


**Figure 7.8:** Illustration of the averaging procedure for  $N = 2$ . The oscillation probabilities calculated on the finer left binning are averaged to obtain the oscillation probabilities in the coarser right binning. These averaged oscillation probabilities with the coarser binning are then applied to each event during the fit.

2396 The coarse binning is defined with  $67 \times 52$  bins in true neutrino energy  $\times$  cosine  
2397 zenith. It is picked to be identical to that provided in [212]. In general, the binning is  
2398 logarithmically spaced in neutrino energy but has some hand-picked bin edges. Firstly,  
2399 the bin density around the matter resonance is smoothly increased around the matter  
2400 resonance region. This is to avoid smearing this region which can be well sampled by  
2401 the Monte Carlo. Secondly, bin edges are selected to hit  $0.4, 0.6, 1, 10, 30, 50, 100\text{GeV}$ .  
2402 This is to ensure that the Coulomb correction systematic and the atmospheric flux  
2403 systematics definitions in neutrino energy can be hit. The cosine zenith binning is

2404 approximately linearly spaced across the allowable range but the values of layer  
2405 transitions are hit precisely:  $-0.8376$  (core-mantle) and  $-0.4464$  (mantle/transition  
2406 zone). Bins are spread further apart for downgoing events as this is a region unaffected  
2407 by the fast oscillation wavelengths and reduces the total number of calculations  
2408 required to perform the calculation.

2409 The choice of  $N$  is justified based on two studies. Firstly, the variation of event rates  
2410 of each sample is studied as a function of  $N$ . For a given set of oscillation parameters  
2411 thrown from the PDG prior constraints (detailed in Table 2.1), the oscillation probabili-  
2412 ties are calculated using a given value of  $N$ . Each sample is re-weighted and the event  
2413 rate is stored. The value of  $N$  is scanned from 1, which corresponds to no averaging, to  
2414 24, which corresponds to the largest computationally viable subdivision binning. The  
2415 event rate of each sample at large  $N$  is expected to converge to a stationary value due  
2416 to the fine binning fully sampling the small-scale structure. Figure 7.9 illustrates this  
2417 behaviour for the SubGeV\_elike\_0dcy sample for 30 different throws of the oscillation  
2418 parameters.

2419 Denoting the event rate for one sample for a given throw  $t$  at each  $N$  by  $\lambda_t^N$ , the  
2420 average over all considered  $N$  values ( $\bar{\lambda}_t = \frac{1}{24} \sum_{N=1}^{24} \lambda_t^N$ ) is computed. The variance in  
2421 the event rate at each  $N$  is then calculated as

$$\text{Var}[\lambda^N] = \frac{1}{N_{\text{throws}}} \sum_{t=1}^{N_{\text{throws}}} (\lambda_t^N - \bar{\lambda}_t)^2 - \left[ \frac{1}{N_{\text{throws}}} \sum_{t=1}^{N_{\text{throws}}} (\lambda_t^N - \bar{\lambda}_t) \right]^2. \quad (7.5)$$

2422 The aim of the study is to find the lowest value of  $N$  such that this variance is  
2423 below 0.001. This is the typical threshold used by T2K fitters to validate systematic  
2424 implementation so has been set as the same criteria. The results of this study for  
2425 each atmospheric sample used within this thesis are illustrated in Figure 7.10 for

### SubGeV-elike-0dcy

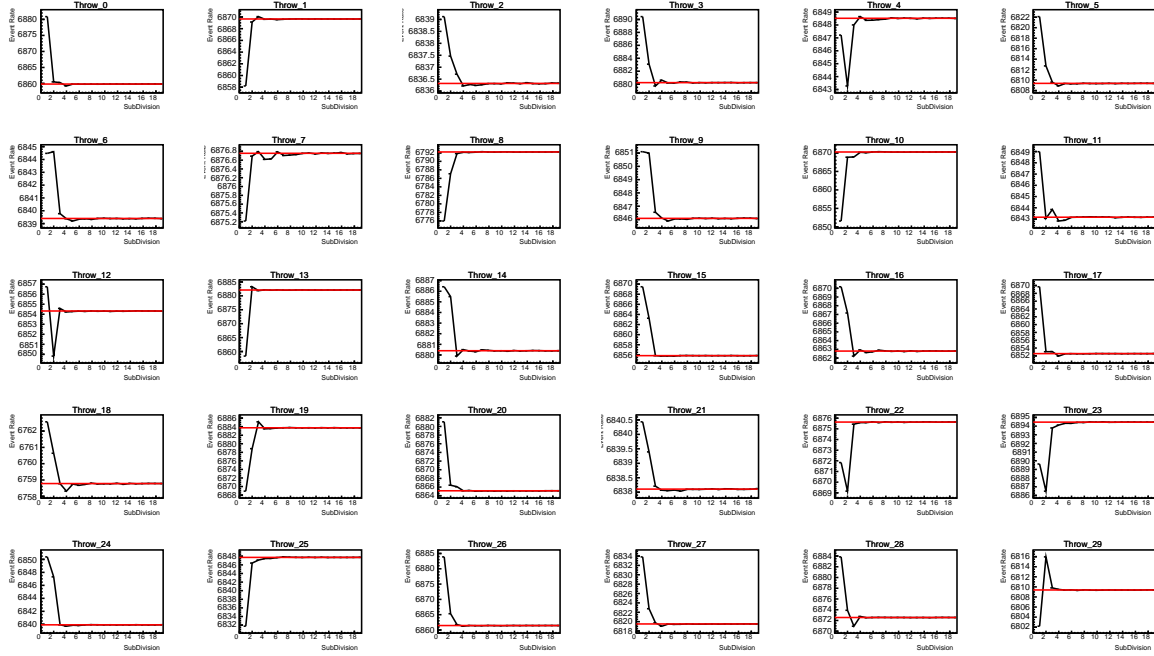


**Figure 7.9:** Event rate of the SubGeV\_elike\_0dcy sample as a function of the number of subdivisions per coarse bin. Each subplot represents the event rate of the sample at a different oscillation parameter set thrown from the PDG priors detailed in Table 2.1. The red line in each subplot represents the mean of the event rate over the different values of sub-divisions for that particular oscillation parameter throw.

2426 2000 throws of the oscillation parameters. As can be seen, the variance is below  
 2427 the threshold at  $N = 10$ , and is driven primarily by the SubGeV\_mulike\_1dcy and  
 2428 SubGeV\_elike\_0dcy samples.

2429 The second study to determine the value of  $N$  is as follows. The likelihood for each  
 2430 sample is computed against an Asimov data set created with Asimov A oscillation  
 2431 parameters (Table 2.2). Following Equation 7.5, the variance of the log-likelihood over  
 2432 all considered  $N$  is computed. The results are shown in Figure 7.11.

2433 A choice of  $N = 10$  sub-divisions per coarse bin has a variance in both event rate  
 2434 and log-likelihood residuals less than the required threshold of 0.001. The largest  
 2435 value of the likelihood variance is of order  $10^{-7}$ , corresponding to an error on the log-

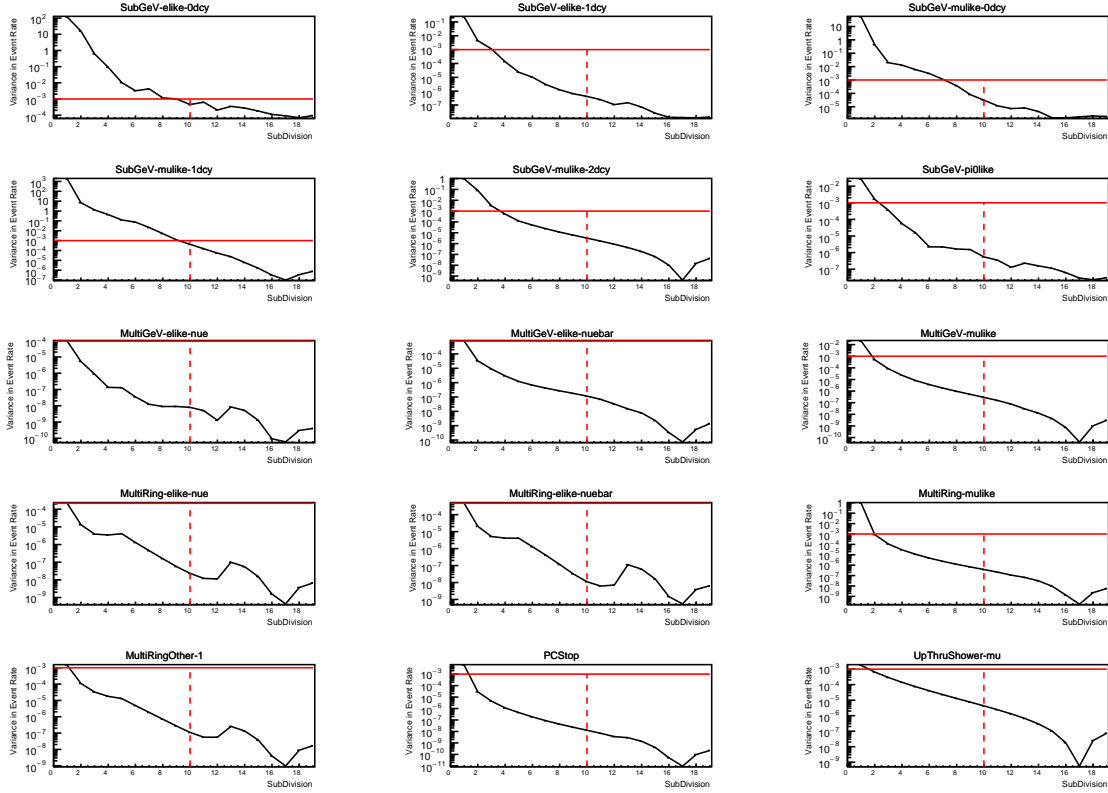


**Figure 7.10:** Variance of event rate for each atmospheric sample as a function of the number of sub-divisions per coarse bin. The solid red line indicates the 0.1% threshold and the dashed red line indicates the variance at a sub-division  $N = 10$ .

2436 likelihood of about  $3 \times 10^{-4}$  which is small enough to be negligible for the oscillation  
 2437 analysis.

2438 Figure 7.12 illustrates the effect of the smearing using  $N = 10$ . The fast oscillations  
 2439 in the sub-GeV upgoing region have been replaced with a normalisation effect whilst  
 2440 the large matter resonance structure remains.

### 2441 7.3 Calculation Engine

2442 As previously discussed in section 7.2, the calculation of oscillation probabilities is per-  
 2443 formed at run-time due to utilising continuous oscillation parameters. Consequently,  
 2444 the time per calculation is crucial for fit performance. The initial fitting framework

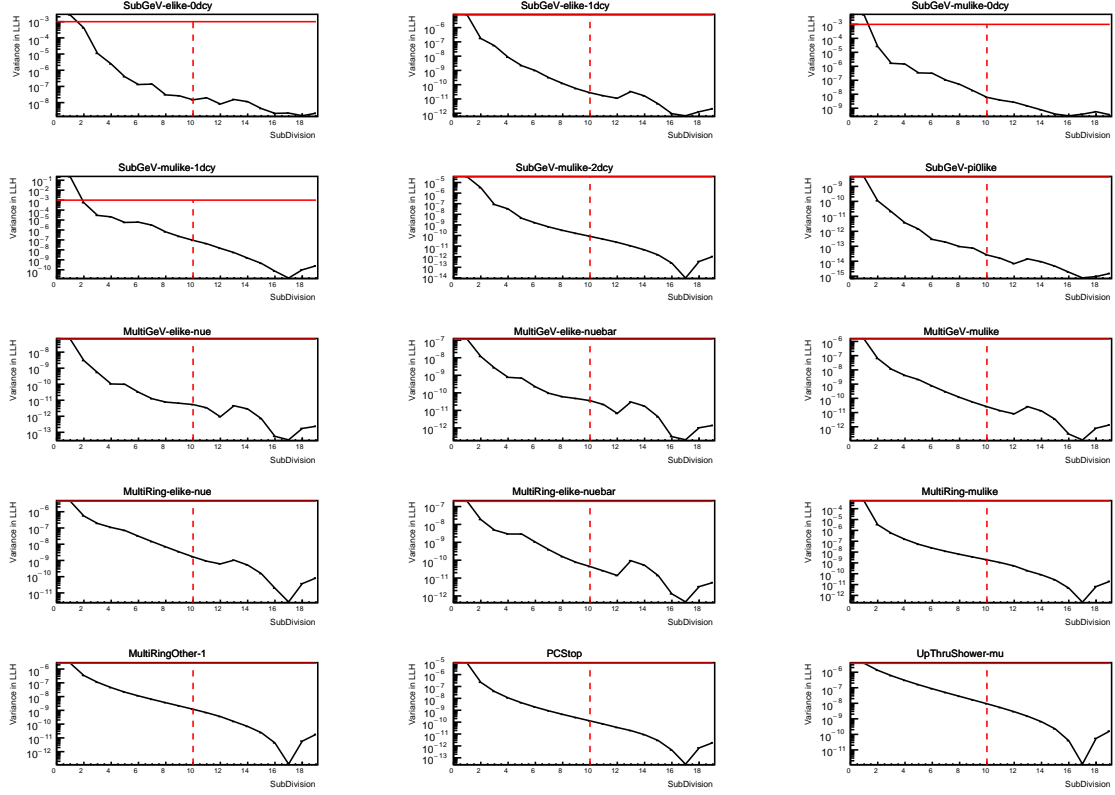


**Figure 7.11:** Variance of sample likelihood, when compared to ‘Asimov data’ set at Asimov A, for each atmospheric sample as a function of the number of sub-divisions per coarse bin. The solid red line indicates the 0.1% threshold and the dashed red line is a graphical indication of the variance at a sub-division  $N = 10$ .

used for this analysis was developed with ProbGPU [213]. This is a GPU-only implementation of the prob3 engine [214]. It is primarily designed for neutrino propagation in a beam experiment (single layer of constant density) with the atmospheric propagation code not being used prior to the analysis in this thesis.

Another engine, CUDAProb3 [215], has been implemented within the fitting framework used in this analysis. It has been specifically optimised for atmospheric neutrino oscillation calculation so does not contain the code to replace the beam oscillation calculation. The engine utilises object-orientated techniques as compared to the functional implementation of ProbGPU. This allows the energy and cosine zenith arrays to be kept on GPU memory, rather than having to load these arrays onto GPU memory for each calculation. General memory interfacing is one of the slowest tasks which

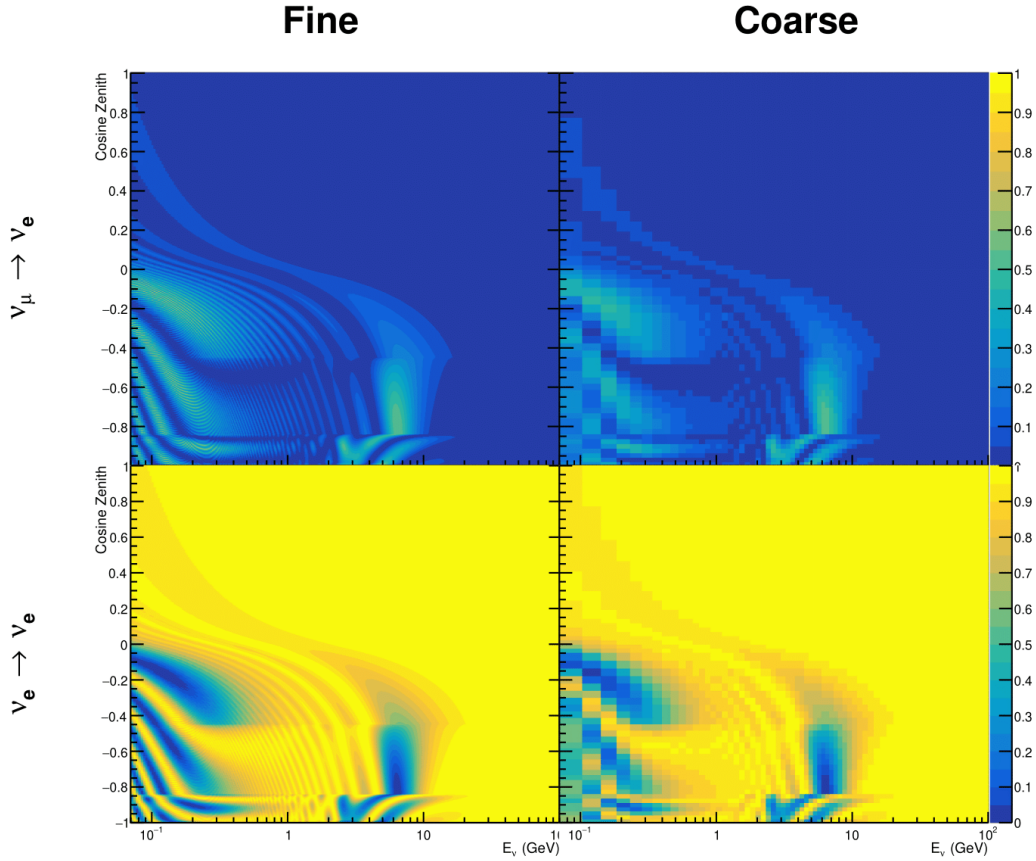


**Figure 7.12:** The oscillation probability,  $P(\nu_\mu \rightarrow \nu_e)$  (top row) and  $P(\nu_e \rightarrow \nu_\mu)$  (bottom row), given as a function of neutrino energy and zenith angle. The left column gives the “fine” binning used to calculate the oscillation probabilities and the right column illustrates the “coarse” binning used to reweight the Monte Carlo events. The fine binning choice is given with  $N = 10$ , which was determined to be below the threshold from Figure 7.10 and Figure 7.11.

2456    GPUs can do, so being able to eliminate this significantly reduces the time required  
 2457    for calculation. This can be seen in Figure 7.13, where the GPU implementation of  
 2458    CUDAProb3 is approximately three times faster than the ProbGPU engine.

2459       Another significant advantage of CUDAProb3 is that it contains a CPU multithreaded  
 2460    implementation which is not possible with the ProbGPU or prob3 engines. This elimi-  
 2461    nates the requirement for GPU resources when submitting jobs to batch systems. As  
 2462    illustrated in Figure 7.13, the calculation speed depends on the number of available

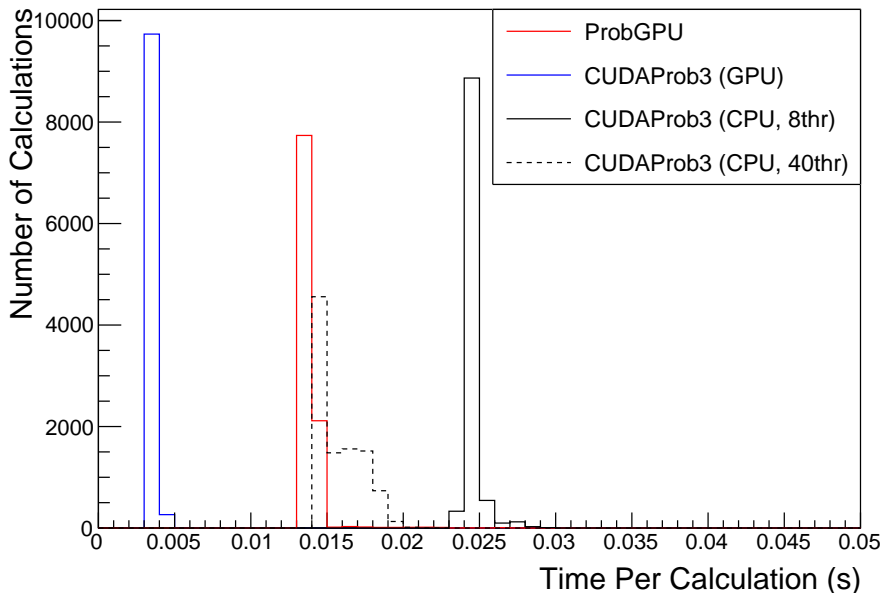


**Figure 7.13:** The calculation time taken to both calculate the oscillation probabilities and fill the “coarse” oscillograms, following the technique given in section 7.2, for the CUDAProb3 and ProbGPU (Red) calculation engines. CUDAProb3 has both a GPU (Blue) and CPU (Black) implementation, where the CPU implementation is multithreaded. Therefore, 8-threads (solid) and 40-threads (dashed) configurations have been tested. Prob3, which is a CPU single-thread implementation has a mean step time of 1.142s.

2463 threads. Using 8 threads (which is typical of the batch systems being used) is ap-  
 2464 proximately twice as slow as the ProbGPU engine implementation, but would allow  
 2465 the fitting framework to be run on many more resources. This fact is utilised for any  
 2466 SK-only fits but GPU resources are required for any fits which include beam samples  
 2467 due to the ProbGPU requirement. Based on the benefits shown by the implementation  
 2468 in this section, efforts are being placed into including linear propagation for beam  
 2469 neutrino propagation into the engine [216].

## 2470 7.4 Matter Density Profile

2471 For an experiment observing atmospheric neutrinos propagating through the Earth, a  
 2472 model of the Earth’s density profile is required. The model used within this analysis is

2473 the Preliminary Reference Earth Model (PREM) [211], as illustrated in Figure 7.1. As  
2474 discussed in section 7.1, the propagator used within the calculation engine requires  
2475 constant density layers. To follow the official SK-only analysis [210], the average  
2476 density of each layer has been taken from the PREM model. Table 7.1 documents  
2477 the density and radii of the layers used within this approximation. The density  
2478 measurements provided in the PREM model are provided in terms of mass density,  
2479 whereas neutrino oscillations are sensitive to the electron number density. This value  
2480 can be computed as the product of the chemical composition, or the  $Z/A$  value, and  
2481 the mass density of each layer. Currently, the only way to calculate the chemical  
2482 composition value for layers close to the Earth’s core is through neutrino oscillations.  
2483 The chemical composition of the upper layers of the Earth’s Mantle and the Transition  
2484 zone is well known due to it being predominantly pyrolite which has a chemical  
2485 composition value of 0.496 [217]. The components of the Earth’s core region are less  
2486 well known. Consequently, the chemical composition dial for the core layers is set to a  
2487 value of 0.468, as calculated in [218]. This value is assigned a Gaussian error with a  
2488 standard deviation equivalent to the difference in chemical composition in core and  
2489 mantle layers. Figure 7.14 illustrates the effect of moving from the  $Z/A = 0.5$  method  
2490 which is used in the official SK-only analysis [210] to these more precise values.

2491 The beam oscillation probability in this thesis uses a baseline of 295km, density  
2492  $2.6\text{g/cm}^3$ , and chemical composition 0.5 as is done by the official T2K-only analysis  
2493 [219].

2494 Whilst the propagator requires a fixed density layer model of the Earth, the density  
2495 only has to be fixed for a specific  $E_\nu \times \cos(\theta_Z)$  bin in a given layer. As the density is a  
2496 function of radius, which is a function of the direction in which a neutrino propagates,  
2497 a better approximation of the PREM model can be made if a  $\cos(\theta_Z)$ -specific density is  
2498 calculated.

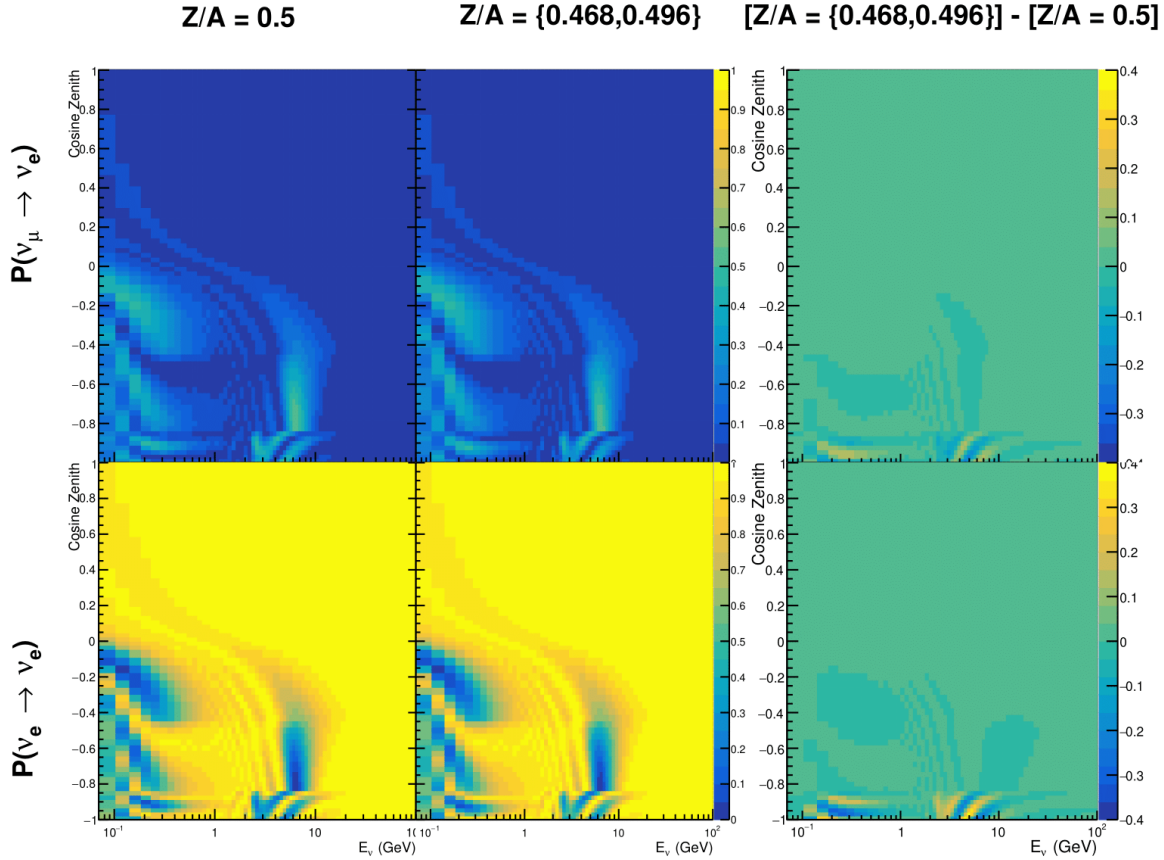


**Figure 7.14:** The oscillation probability,  $P(\nu_\mu \rightarrow \nu_e)$  (top row) and  $P(\nu_e \rightarrow \nu_e)$  (bottom row), given as a function of neutrino energy and zenith angle. The left column gives probabilities where the constant  $Z/A = 0.5$  approximation which is used in the official SK-only analysis. The middle column gives the probabilities where  $Z/A = [0.468, 0.498]$  values are used, as given in Table 7.1. The right column illustrates the difference in oscillation probability between the two different techniques.

2499 To achieve this, the average density,  $\langle \rho \rangle_i$ , in the  $i^{th}$  layer, is calculated as the density,  
 2500  $\rho(t)$ , integrated over the track a given  $\cos(\theta_Z)$ ,

$$\langle \rho \rangle_i = \frac{1}{t_{i+1} - t_i} \int_{t_i}^{t_{i+1}} \rho(t) dt \quad (7.6)$$

2501 where  $t_i$  are the intersection points between each layer and  $t$  is the path length of  
 2502 the trajectory across the layer.

2503 The oscillation probability calculation speed is approximately linear in the number  
 2504 of layers invoked within the Earth model. Therefore a four-layer model is still utilized  
 2505 with the only difference to the official SK-only analysis being that the four-layer model  
 2506 used for each value of  $\cos(\theta_Z)$  is different. Following the method outlined in [220],  
 2507 a four-layer piecewise quadratic polynomial is fit to the PREM model for the four  
 2508 layers defined in Table 7.1. This fit was not performed by the author of the thesis  
 2509 and is documented in [212]. The coefficients of the quadratic fit to each layer are  
 2510 given in Table 7.2 with the final distribution illustrated in Figure 7.15. The quadratic  
 2511 approximation is clearly much closer to the PREM model as compared to the constant  
 2512 density approximation.

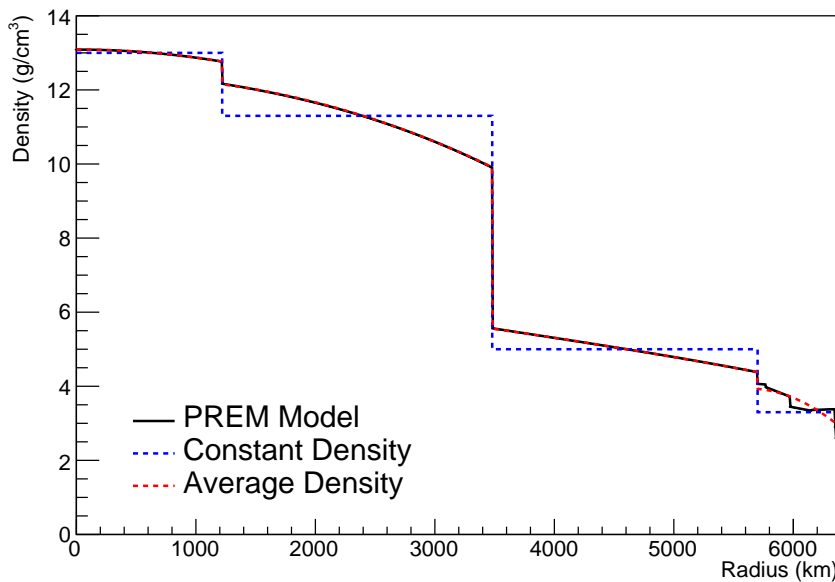


**Figure 7.15:** The density of the Earth given as a function of the radius, as given by the PREM model (Black), the constant density four-layer approximation (Blue), as used in the official SK-only analysis, and the quadratic approximation of the PREM model (Red).

Layer	Outer Radius [km]	Density [g/cm <sup>3</sup> ]
Inner Core	1220	$13.09 - 8.84x^2$
Outer Core	3480	$12.31 + 1.09x - 10.02x^2$
Lower Mantle	5701	$6.78 - 1.56x - 1.25x^2$
Transition Zone	6371	$-50.42 + 123.33x - 69.95x^2$

**Table 7.2:** The quadratic polynomial fits to the PREM model for four assumed layers of the PREM model. The fit to calculate the coefficients is given in [212], where  $x = R/R_{Earth}$ .

2513     The effect of using the quadratic density per  $\cos(\theta_Z)$  model is highlighted in  
 2514     Figure 7.16. The slight discontinuity in the oscillation probability around  $\cos(\theta_Z) \sim -$   
 2515     0.45 in the fixed density model, which is due to the transition to mantle layer boundary,  
 2516     has been reduced. This is expected as the difference in the density across this boundary  
 2517     is significantly smaller in the quadratic density model as compared to the constant  
 2518     density model. Whilst the difference in density across the other layer transitions  
 2519     is reduced, there is still a significant difference. This means the discontinuities in  
 2520     the oscillation probabilities remain but are significantly reduced. However, as the  
 2521     quadratic density approximation matches the PREM model well in this region, these  
 2522     discontinuities are due to the Earth model rather than an artifact of the oscillation  
 2523     calculation.

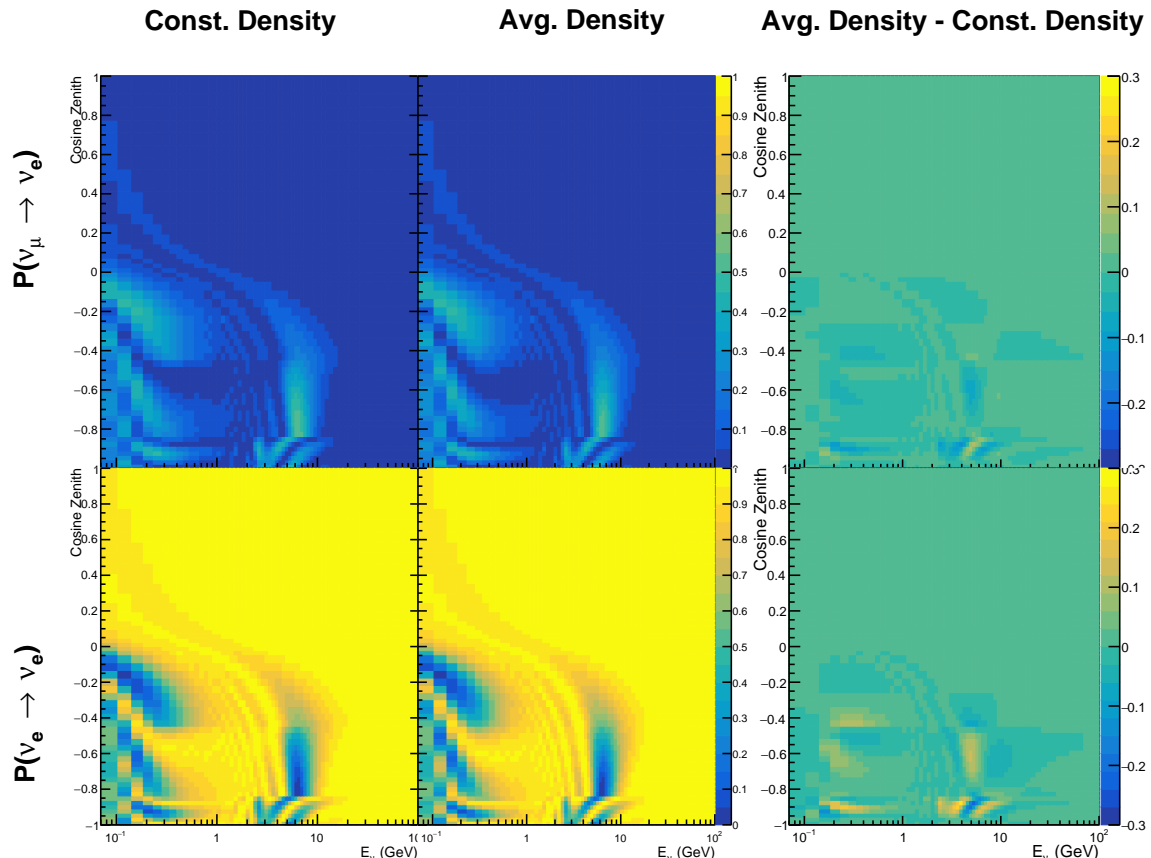


**Figure 7.16:** The oscillation probability,  $P(\nu_\mu \rightarrow \nu_e)$  (top row) and  $P(\nu_e \rightarrow \nu_\mu)$  (bottom row), given as a function of neutrino energy and zenith angle. The left column gives probabilities where the four-layer constant density approximation is used. The middle column gives the probabilities where the density is integrated over the trajectory, using the quadratic PREM approximation, for each  $\cos(\theta_Z)$  is used. The right column illustrates the difference in oscillation probability between the two different techniques.

## <sup>2524</sup> 7.5 Production Height Averaging

<sup>2525</sup> As discussed in section 7.1, the height at which the cosmic ray flux interacts in the  
<sup>2526</sup> atmosphere is not known on an event-by-event basis. The production height can vary  
<sup>2527</sup> from the Earth’s surface to  $\sim 50\text{km}$  above that. The SK-only analysis methodology  
<sup>2528</sup> (described in section 7.2) for including the uncertainty on the production height is  
<sup>2529</sup> to include variations from the Honda model when pre-calculating the oscillation  
<sup>2530</sup> probabilities prior to the fit. This technique is not possible for this analysis which  
<sup>2531</sup> uses continuous oscillation parameters that can not be known prior to the fit. Conse-  
<sup>2532</sup> quently, an analytical averaging technique was developed in [212]. The author of this  
<sup>2533</sup> thesis was not responsible for the derivation of the technique but has performed the  
<sup>2534</sup> implementation and validation of the technique for this analysis alone.

<sup>2535</sup> Using the 20 production heights per Monte Carlo neutrino event, provided as 5%  
<sup>2536</sup> percentiles from the Honda flux model, a production height distribution  $p_j(h|E_\nu, \cos\theta_Z)$   
<sup>2537</sup> is built for each neutrino flavour  $j = \nu_e, \bar{\nu}_e, \nu_\mu, \bar{\nu}_\mu$ . In practice, a histogram is filled with  
<sup>2538</sup> 20 evenly spaced bins in production height  $h$  between 0 and 50km. The neutrino energy  
<sup>2539</sup> and cosine zenith binning of the histogram is the same as that provided in section 7.2.  
<sup>2540</sup> The average production height,  $\bar{h} = \int dh \frac{1}{4} \sum_j p_j(h|E_\nu, \cos(\theta_Z))$ , is calculated. The  
<sup>2541</sup> production height binning of this histogram is then translated into  $\delta t(h) = t(\bar{h}) - t(h)$ ,  
<sup>2542</sup> where  $t(h)$  is the distance travelled along the trajectory.

<sup>2543</sup> For the  $i^{\text{th}}$  traversed layer, the transition amplitude,  $D_i(t_{i+1}, t_i)$ , is computed. The  
<sup>2544</sup> time-ordered product of these is then used as the overall transition amplitude via

$$A(t_{n+1}, t_0) = D_n(t_{n+1}, t_n) \dots D_1(t_2, t_1) D_0(t_1, t_0), \quad (7.7)$$

2545

where,

$$\begin{aligned} D_n(t_{n+1}, t_n) &= \exp[-iH_n(t_{n+1} - t_n)] \\ &= \sum_{k=1}^3 C_k \exp[ia_k(t_{n+1} - t_n)] \end{aligned} \quad (7.8)$$

2546

is expressed as a diagonalised time-dependent solution to the Schrodinger equation.

2547

The  $0^{th}$  layer is the propagation through the atmosphere and is the only term that depends on the production height. Using the substitution  $t_0 = t(\bar{h}) - \delta t(h)$ , it can be shown that

2549

$$D_0(t_1, t_0) = D_0(t_1, \bar{h})D_0(\delta t). \quad (7.9)$$

2550

Thus Equation 7.7 becomes

$$\begin{aligned} A(t_{n+1}, t_0) &= D_n(t_{n+1}, t_n) \dots D_1(t_2, t_1) D_0(t_1, \bar{h}) D(\delta t) \\ &= A(t_{n+1}, \bar{h}) \sum_{k=1}^3 C_k \exp[ia_k \delta t], \\ &= \sum_{k=1}^3 B_k \exp[ia_k \delta t]. \end{aligned} \quad (7.10)$$

2551

The oscillation probability averaged over production height is then calculated as

$$\begin{aligned}
 \bar{P}(\nu_j \rightarrow \nu_i) &= \int d(\delta t) p_j(\delta t | E_\nu, \cos \theta_Z) P(\nu_j \rightarrow \nu_i) \\
 &= \int d(\delta t) p_j(\delta t | E_\nu, \cos \theta_Z) A(t_{n+1}, t_0) A^*(t_{n+1}, t_0) \\
 &= \sum_{km} (B_k)_{ij} (B_m)_{ij}^* \int d(\delta t) p_j(\delta t | E_\nu, \cos \theta_Z) \exp[i(a_k - a_m)\delta t]
 \end{aligned} \tag{7.11}$$

2552 In practice, implementation in CUDAProb3 [215] is relatively straightforward as  
 2553 the majority of these terms are already calculated in the standard oscillation calculation.  
 2554 Figure 7.17 illustrates the results of the production height averaging. As expected,  
 2555 the main effect is observed in the low-energy downward-going and horizontal-going  
 2556 events. Upward-going events have to travel the radius of the Earth,  $R_E = 6371\text{km}$ ,  
 2557 where the production height uncertainty is a small fraction of the total path length.

2558

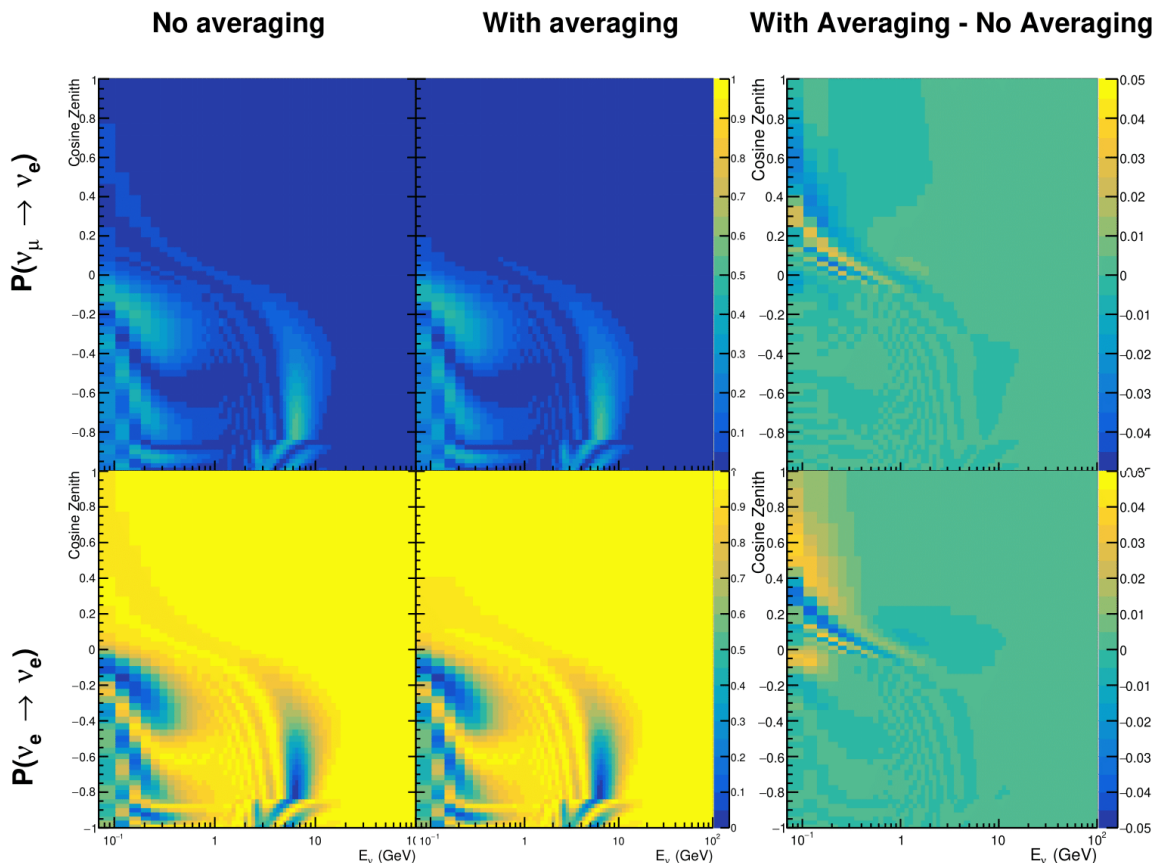


**Figure 7.17:** The oscillation probability,  $P(\nu_\mu \rightarrow \nu_e)$  (top row) and  $P(\nu_e \rightarrow \nu_\mu)$  (bottom row), given as a function of neutrino energy and zenith angle. The left column gives probabilities where a fixed production height of 25km is used. The middle column gives the probabilities where the production height is analytically averaged. The right column illustrates the difference in oscillation probability between the two different techniques.

<sub>2559</sub> **Bibliography**

- <sub>2560</sub> [1] J. Chadwick, Verhandl. Dtsc. Phys. Ges. **16**, 383 (1914).
- <sub>2561</sub> [2] C. D. Ellis and W. A. Wooster, Proc. R. Soc. Lond. A Math. Phys. Sci. **117**, 109  
<sub>2562</sub> (1927).
- <sub>2563</sub> [3] W. Pauli, Phys. Today **31N9**, 27 (1978).
- <sub>2564</sub> [4] E. Fermi, Z. Phys. **88**, 161 (1934).
- <sub>2565</sub> [5] F. Reines and C. L. Cowan, Phys. Rev. **92**, 830 (1953).
- <sub>2566</sub> [6] C. L. Cowan, F. Reines, F. B. Harrison, H. W. Kruse, and A. D. McGuire, Science  
<sub>2567</sub> **124**, 103 (1956), <http://science.sciencemag.org/content/124/3212/103.full.pdf>.
- <sub>2568</sub> [7] G. Danby *et al.*, Phys. Rev. Lett. **9**, 36 (1962).
- <sub>2569</sub> [8] K. Kodama *et al.*, Physics Letters B **504**, 218 (2001).
- <sub>2570</sub> [9] LSND, A. Aguilar-Arevalo *et al.*, Phys. Rev. **D64**, 112007 (2001), hep-ex/0104049.
- <sub>2571</sub> [10] MiniBooNE Collaboration, A. A. Aguilar-Arevalo *et al.*, Phys. Rev. Lett. **110**,  
<sub>2572</sub> 161801 (2013).
- <sub>2573</sub> [11] Planck Collaboration *et al.*, aap **641** (2020).
- <sub>2574</sub> [12] The ALEPH Collaboration, The Delphi Collaboration, The L3 Collaboration, The  
<sub>2575</sub> SLD Collaboration, The LEP Electroweak Working Group, The SLD Electroweak  
<sub>2576</sub> and Heavy Flavour Groups, J. A. Bagger *et al.*, Physics Reports **427**, 257 (2006).
- <sub>2577</sub> [13] B. Pontecorvo, Sov. Phys. JETP **26**, 984 (1968), [Zh. Eksp. Teor. Fiz. 53, 1717 (1967)].
- <sub>2578</sub> [14] B. Pontecorvo, Sov. Phys. JETP **7**, 172 (1958), [Zh. Eksp. Teor. Fiz. 34, 247 (1957)].
- <sub>2579</sub> [15] M. Kobayashi and T. Maskawa, Progress of Theoretical Physics **49**, 652 (1973).
- <sub>2580</sub> [16] N. Cabibbo, Phys. Rev. Lett. **10**, 531 (1963).
- <sub>2581</sub> [17] A. M. and, Journal of Physics: Conference Series **587**, 012030 (2015).
- <sub>2582</sub> [18] A. Y. Smirnov, (2003).
- <sub>2583</sub> [19] S. Mikheyev and A. Smirnov, Soviet Journal of Nuclear Physics **42**, 913 (1985).

- 2584 [20] L. Wolfenstein, Phys. Rev. D **17**, 2369 (1978).
- 2585 [21] V. D. Barger, K. Whisnant, S. Pakvasa, and R. J. N. Phillips, Phys. Rev. D **22**, 2718  
2586 (1980).
- 2587 [22] The Super-Kamiokande Collaboration, Y. Ashie *et al.*, Phys. Rev. Lett. **93**, 101801  
2588 (2004).
- 2589 [23] SNO Collaboration, Q. R. Ahmad *et al.*, Phys. Rev. Lett. **89**, 011301 (2002).
- 2590 [24] 2015 Nobel prize in Physics as listed by Nobelprize.org, [https://www.](https://www.nobelprize.org/nobel_prizes/physics/laureates/2015/)  
2591 [nobelprize.org/nobel\\_prizes/physics/laureates/2015/](https://www.nobelprize.org/nobel_prizes/physics/laureates/2015/), Accessed: 22-06-  
2592 2022.
- 2593 [25] J. A. Formaggio and G. P. Zeller, Rev. Mod. Phys. **84**, 1307 (2012), 1305.7513.
- 2594 [26] A. Bellerive, Int. J. Mod. Phys. A **19**, 1167 (2004).
- 2595 [27] R. Davis, D. S. Harmer, and K. C. Hoffman, Phys. Rev. Lett. **20**, 1205 (1968).
- 2596 [28] N. Vinyoles *et al.*, Astrophys. J. **835**, 202 (2017).
- 2597 [29] V. Gribov and B. Pontecorvo, Phys. Lett. B **28**, 493 (1969).
- 2598 [30] K. S. Hirata *et al.*, Phys. Rev. Lett. **63**, 16 (1989).
- 2599 [31] W. Hampel *et al.*, Phys. Lett. B **447**, 127 (1999).
- 2600 [32] SAGE Collaboration, J. N. Abdurashitov *et al.*, Phys. Rev. C **60**, 055801 (1999).
- 2601 [33] Q. R. Ahmad *et al.*, Phys. Rev. Lett. **89** (2002).
- 2602 [34] Borexino Collaboration, Nature **562**, 505 (2018).
- 2603 [35] B. Aharmim *et al.*, Astrophys. J. **653**, 1545 (2006).
- 2604 [36] M. Agostini *et al.*, (2020).
- 2605 [37] S. Andringa *et al.*, Adv. High Energy Phys. **2016**, 1 (2016).
- 2606 [38] J. F. Beacom *et al.*, Chin. phys. C **41**, 023002 (2017).
- 2607 [39] F. An *et al.*, J. Phys. G Nucl. Part. Phys. **43**, 030401 (2016).
- 2608 [40] J. Aalbers *et al.*, (2020), 2006.03114.
- 2609 [41] T. K. Gaisser and M. Honda, (2002).

- 2610 [42] G. D. Barr, T. K. Gaisser, P. Lipari, S. Robbins, and T. Stanev, Physical Review D  
2611 **70** (2004).
- 2612 [43] M. Honda, T. Kajita, K. Kasahara, S. Midorikawa, and T. Sanuki, Physical Review  
2613 D **75** (2007).
- 2614 [44] M. Honda, T. Kajita, K. Kasahara, and S. Midorikawa, Phys. Rev. D **70**, 043008  
2615 (2004).
- 2616 [45] M. Honda, T. Kajita, K. Kasahara, and S. Midorikawa, Phys. Rev. D **83**, 123001  
2617 (2011).
- 2618 [46] A. Fasso, A. Ferrari, P. R. Sala, and J. Ranft, (2001).
- 2619 [47] Y. Ashie *et al.*, Physical Review D **71** (2005).
- 2620 [48] F. Reines *et al.*, Phys. Rev. Lett. **15**, 429 (1965).
- 2621 [49] D. Casper *et al.*, Phys. Rev. Lett. **66**, 2561 (1991).
- 2622 [50] K. S. Hirata *et al.*, Phys. Lett. B **280**, 146 (1992).
- 2623 [51] Z. Li *et al.*, Physical Review D **98** (2018).
- 2624 [52] Kamiokande Collaboration *et al.*, (2017).
- 2625 [53] T2K Collaboration, Nature **580**, 339 (2020).
- 2626 [54] M. A. Acero *et al.*, Phys. Rev. Lett. **123**, 151803 (2019).
- 2627 [55] M. G. Aartsen *et al.*, Phys. Rev. Lett. **120** (2018).
- 2628 [56] P. Adamson *et al.*, Phys. Rev. Lett. **112** (2014).
- 2629 [57] M. S. Athar *et al.*, Progress in Particle and Nuclear Physics **124**, 103947 (2022).
- 2630 [58] G. Danby *et al.*, Phys. Rev. Lett. **9**, 36 (1962).
- 2631 [59] K. Abe *et al.*, Physical Review D **87** (2013).
- 2632 [60] MINOS Collaboration, D. G. Michael *et al.*, Phys. Rev. Lett. **97**, 191801 (2006).
- 2633 [61] G. Danby *et al.*, Phys. Rev. Lett. **9**, 36 (1962).
- 2634 [62] NOvA Collaboration, M. A. Acero *et al.*, Phys. Rev. Lett. **123**, 151803 (2019).
- 2635 [63] B. Abi, R. Acciarri, M. A. Acero, and G. e. a. Adamov, Eur. Phys. J. C Part. Fields

- 2636       **80** (2020).
- 2637 [64] Hyper-Kamiokande Proto-Collaboration *et al.*, Prog. Theor. Exp. Phys. **2015**,  
2638       53C02 (2015).
- 2639 [65] C. Blanco, D. Hooper, and P. Machado, Physical Review D **101** (2020).
- 2640 [66] MicroBooNE Collaboration *et al.*, Search for an Excess of Electron Neutrino  
2641       Interactions in MicroBooNE Using Multiple Final State Topologies, 2021.
- 2642 [67] KARMEN Collaboration, B. Armbruster *et al.*, Phys. Rev. D **65**, 112001 (2002).
- 2643 [68] S.-B. Kim, T. Lasserre, and Y. Wang, Adv. High Energy Phys. **2013**, 1 (2013).
- 2644 [69] M. Sajjad Athar *et al.*, Prog. Part. Nucl. Phys. **124**, 103947 (2022), 2111.07586.
- 2645 [70] K. Abe *et al.*, Nucl. Instrum. Methods Phys. Res. A **1027**, 166248 (2022).
- 2646 [71] F. P. An *et al.*, Phys. Rev. Lett. **108**, 171803 (2012).
- 2647 [72] RENO Collaboration, J. K. Ahn *et al.*, Phys. Rev. Lett. **108**, 191802 (2012).
- 2648 [73] Double Chooz Collaboration, Y. Abe *et al.*, Phys. Rev. Lett. **108**, 131801 (2012).
- 2649 [74] J. Collaboration *et al.*, TAO Conceptual Design Report: A Precision Measurement  
2650       of the Reactor Antineutrino Spectrum with Sub-percent Energy Resolution, 2020,  
2651       2005.08745.
- 2652 [75] for the RENO Collaboration, New results from RENO and the 5 MeV excess,  
2653       AIP Publishing LLC, 2015.
- 2654 [76] Y. Abe *et al.*, Journal of High Energy Physics **2014** (2014).
- 2655 [77] Daya Bay Collaboration, D. Adey *et al.*, Phys. Rev. Lett. **123**, 111801 (2019).
- 2656 [78] M. P. Decowski, Nucl. Phys. B. **908**, 52 (2016).
- 2657 [79] The KamLAND Collaboration, A. Gando *et al.*, Phys. Rev. D **83**, 052002 (2011).
- 2658 [80] P. Dunne, Latest Neutrino oscillation results from T2K, 2020.
- 2659 [81] M. Tanabashi *et al.*, Phys. Rev. D. **98** (2018).
- 2660 [82] Particle Data Group, R. L. Workman and Others, PTEP **2022**, 083C01 (2022).
- 2661 [83] T2K Collaboration, K. Abe *et al.*, Phys. Rev. Lett. **112**, 181801 (2014).

- [84] Y. Fukuda *et al.*, Phys. Rev. Lett. **81**, 1562 (1998).
- [85] Linyan Wan, (2022).
- [86] K. Abe *et al.*, Nuclear Instruments and Methods in Physics Research Section A: Accelerators, Spectrometers, Detectors and Associated Equipment **737**, 253 (2014).
- [87] S. Fukuda *et al.*, Nucl. Instrum. Methods Phys. Res. A **501**, 418 (2003).
- [88] Y. Itow *et al.*, (2001).
- [89] M. Jiang *et al.*, Prog. Theor. Exp. Phys. **2019** (2019).
- [90] S. Fukuda *et al.*, Nuclear Instruments and Methods in Physics Research Section A: Accelerators, Spectrometers, Detectors and Associated Equipment **501**, 418 (2003), <http://www.sciencedirect.com/science/article/pii/S016890020300425X>.
- [91] Y. Nakano *et al.*, Nucl. Instrum. Methods Phys. Res. A **977**, 164297 (2020).
- [92] Hamamatsu, Hamamatsu Photonics Photomultiplier Tubes Handbook.
- [93] K. Abe *et al.*, Nucl. Instrum. Methods Phys. Res. A **1027**, 166248 (2022).
- [94] J. F. Beacom and M. R. Vagins, Phys. Rev. Lett. **93**, 171101 (2004).
- [95] L. Marti *et al.*, Nucl. Instrum. Methods Phys. Res. A **959**, 163549 (2020).
- [96] L. Marti *et al.*, (2019).
- [97] M. Vagins, Solar/DSNB Neutrino\_SK-Gd, 2022.
- [98] J. Focht, PhD thesis, Massachusetts Institute of Technology, 2004.
- [99] T. Tanimori *et al.*, IEEE Transactions on Nuclear Science **36**, 497 (1989).
- [100] Super-Kamiokande Collaboration, J. Hosaka *et al.*, Phys. Rev. D **73**, 112001 (2006).
- [101] H. Nishino *et al.*, Nucl. Instrum. Methods Phys. Res. A **610**, 710 (2009).
- [102] S. Yamada *et al.*, IEEE Transactions on Nuclear Science **57**, 428 (2010).
- [103] S. Yamada, Y. Hayato, Y. Obayashi, and M. Shiozawa, New online system without hardware trigger for the Super-Kamiokande experiment, in *2007 IEEE Nuclear Science Symposium Conference Record*, IEEE, 2007.

- 2689 [104] G. Carminati, Phys. Procedia **61**, 666 (2015).
- 2690 [105] P. A. Čerenkov, Phys. Rev. **52**, 378 (1937).
- 2691 [106] I. Frank and I. Tamm, Coherent visible radiation of fast electrons passing  
2692 through matter, in *Selected Papers*, pp. 29–35, Springer Berlin Heidelberg, Berlin,  
2693 Heidelberg, 1991.
- 2694 [107] The T2K Collaboration, KEK Proposal (2001),  
2695 <http://neutrino.kek.jp/jhfnu/loi/loi.v2.030528.pdf>.
- 2696 [108] Y. Itow *et al.*, (2001), hep-ex/0106019.
- 2697 [109] The K2K Collaboration and S. H. Ahn, (2001), hep-ex/0103001.
- 2698 [110] The T2K Collaboration, KEK Proposal (2006), [http://j-parc.jp/researcher/Hadron/en/pac\\_0606/pdf/p11-Nishikawa.pdf](http://j-parc.jp/researcher/Hadron/en/pac_0606/pdf/p11-Nishikawa.pdf).
- 2700 [111] C. Bronner, Accelerator Neutrino I\_Recent results from T2K, 2022.
- 2701 [112] T2K Collaboration, K. Abe *et al.*, Phys. Rev. Lett. **112**, 061802 (2014),  
2702 <https://link.aps.org/doi/10.1103/PhysRevLett.112.061802>.
- 2703 [113] NINJA Collaboration, T. Fukuda *et al.*, Proposal for precise measurement of  
2704 neutrino-water cross-section in NINJA physics run, Proposal for J-PARC and  
2705 KEK, 2017.
- 2706 [114] T. Ovsiannikova *et al.*, Physics of Particles and Nuclei **48**, 1014 (2017),  
2707 <https://doi.org/10.1134/S1063779617060478>.
- 2708 [115] M. Antonova *et al.*, Journal of Instrumentation **12**, C07028 (2017),  
2709 <http://stacks.iop.org/1748-0221/12/i=07/a=C07028>.
- 2710 [116] The T2K Collaboration, K. Abe *et al.*, Phys. Rev. D **102**, 012007 (2020).
- 2711 [117] K. Abe *et al.*, Progress of Theoretical and Experimental Physics **2021** (2021).
- 2712 [118] The T2K Collaboration, K. Abe *et al.*, Nuclear Instruments  
2713 and Methods in Physics Research Section A: Accelerators, Spectrometers,  
2714 Detectors and Associated Equipment **659**, 106 (2011),  
2715 <http://www.sciencedirect.com/science/article/pii/S0168900211011910>.
- 2716 [119] K. Matsuoka *et al.*, Nuclear Instruments and Methods in Physics Research Section  
2717 A: Accelerators, Spectrometers, Detectors and Associated Equipment **624**, 591

- 2718 (2010), <http://www.sciencedirect.com/science/article/pii/S016890021002098X>.
- 2719 [120] K. Abe *et al.*, Phys. Rev. D. **103** (2021).
- 2720 [121] T. Vladisavljevic, *Predicting the T2K neutrino flux and measuring oscillation parameters* Springer theses, 1 ed. (Springer Nature, Cham, Switzerland, 2020).
- 2722 [122] D. Beavis, A. Carroll, and I. Chiang, (1995).
- 2723 [123] P.-A. Amaudruz *et al.*, Nuclear Instruments and Methods in Physics Research  
2724 Section A: Accelerators, Spectrometers, Detectors and Associated Equipment  
2725 **696**, 1 (2012).
- 2726 [124] N. Abgrall *et al.*, Nuclear Instruments and Methods in Physics Research Section  
2727 A: Accelerators, Spectrometers, Detectors and Associated Equipment **637**, 25  
2728 (2011).
- 2729 [125] S. Assylbekov *et al.*, Nuclear Instruments and Methods in Physics Research  
2730 Section A: Accelerators, Spectrometers, Detectors and Associated Equipment  
2731 **686**, 48 (2012).
- 2732 [126] D. Allan *et al.*, Journal of Instrumentation **8**, P10019 (2013).
- 2733 [127] F. Vannucci, Advances in High Energy Physics **2014**, 1 (2014).
- 2734 [128] UA1 magnet sets off for a second new life, 2022.
- 2735 [129] S. Aoki *et al.*, Nuclear Instruments and Methods in Physics Research Section  
2736 A: Accelerators, Spectrometers, Detectors and Associated Equipment **698**, 135  
2737 (2013).
- 2738 [130] K. Suzuki *et al.*, Progress of Theoretical and Experimental Physics **2015**, 53C01  
2739 (2015).
- 2740 [131] S. Brooks, A. Gelman, G. L. Jones, and X.-L. Meng, *Handbook of Markov Chain  
2741 Monte Carlo* (CRC Press, 2011).
- 2742 [132] W. R. Gilks, S. Richardson, and D. J. Spiegelhalter, *Markov Chain Monte Carlo in  
2743 Practice* (Chapman & Hall/CRC Interdisciplinary Statistics, 1995).
- 2744 [133] C. Wret, *Minimising systematic uncertainties in the T2K experiment using near-  
2745 detector and external data*, PhD thesis, Imperial College London, 2018.
- 2746 [134] K. E. Duffy, *Measurement of the Neutrino Oscillation Parameters  $\sin^2 \theta_{23}$ ,  $\Delta m_{32}^2$ ,*

- 2747         $\sin^2 \theta_{13}$ , and  $\delta_{CP}$  in Neutrino and Antineutrino Oscillation at T2K, PhD thesis, Oriel  
2748        College, University of Oxford, 2016.
- 2749 [135] T. Bayes, Rev. Phil. Trans. Roy. Soc. Lond. **53**, 370 (1764).
- 2750 [136] N. Metropolis, A. W. Rosenbluth, M. N. Rosenbluth, A. H. Teller, and E. Teller,  
2751        Journal of Chemical Physics **21** (1970).
- 2752 [137] W. K. Hastings, Biometrika **57** (1970).
- 2753 [138] J. Dunkley, M. Bucher, P. G. Ferreira, K. Moodley, and C. Skordis, Mon. Not. R.  
2754        Astron. Soc. **356**, 925 (2005).
- 2755 [139] Particle Data Group *et al.*, Prog. Theor. Exp. Phys. **2020** (2020).
- 2756 [140] H. Jeffreys, *The Theory of Probability* Oxford Classic Texts in the Physical Sciences  
2757        (, 1939).
- 2758 [141] R. E. Kass and A. E. Raftery, J. Am. Stat. Assoc. **90**, 773 (1995).
- 2759 [142] T. Böhlen *et al.*, Nuclear Data Sheets **120**, 211 (2014),  
2760        <http://www.sciencedirect.com/science/article/pii/S0090375214005018>.
- 2761 [143] R. Brun *et al.*, GEANT: Detector Description and Simulation Tool; Oct 1994 CERN  
2762        Program Library (CERN, Geneva, 1993), <http://cds.cern.ch/record/1082634>,  
2763        Long Writeup W5013.
- 2764 [144] T2K Collaboration, K. Abe *et al.*, Phys. Rev. D **87**, 012001 (2013).
- 2765 [145] C. Zeitnitz and T. Gabriel, Nuclear Instruments and Methods in Physics Research Section A: Accelerators, Spectrometers, Detectors and Associated Equipment **349**, 106 (1994),  
2766        <http://www.sciencedirect.com/science/article/pii/0168900294906130>.
- 2769 [146] A. Fiorentini *et al.*, T2K Technical Note **217** (2017).
- 2770 [147] N. Abgrall *et al.*, Physical Review C **84** (2011).
- 2771 [148] N. Abgrall *et al.*, Physical Review C **85** (2012).
- 2772 [149] N. Abgrall *et al.*, Nuclear Instruments and Methods in Physics Research Section  
2773        A: Accelerators, Spectrometers, Detectors and Associated Equipment **701**, 99  
2774        (2013), <http://www.sciencedirect.com/science/article/pii/S016890021201234X>.

- 2775 [150] HARP Collaboration, M. Apollonio *et al.*, Phys. Rev. C **80**, 035208 (2009),  
2776 <https://link.aps.org/doi/10.1103/PhysRevC.80.035208>.
- 2777 [151] B. Blau *et al.*, Nuclear Physics B - Proceedings Supplements **113**, 125 (2002).
- 2778 [152] S. Haino *et al.*, Physics Letters B **594**, 35 (2004).
- 2779 [153] NASA, U.S. Standard Atmosphere, 1976, 1976.
- 2780 [154] S. Roesler, R. Engel, and J. Ranft, The Monte Carlo Event Generator DPMJET-III,  
2781 in *Advanced Monte Carlo for Radiation Physics, Particle Transport Simulation and*  
2782 *Applications*, pp. 1033–1038, Springer Berlin Heidelberg, 2001.
- 2783 [155] K. Niita *et al.*, Radiation Measurements **41**, 1080 (2006).
- 2784 [156] T. Sanuki *et al.*, Physics Letters B **541**, 234 (2002).
- 2785 [157] P. Achard *et al.*, Physics Letters B **598**, 15 (2004).
- 2786 [158] K. Sato, Atmospheric Neutrino\_Reviews on neutrino fluxes (low E atm nu),  
2787 2022.
- 2788 [159] Y. Hayato and L. Pickering, The European Physical Journal Special Topics **230**,  
2789 4469 (2021).
- 2790 [160] Y. Hayato, Acta Physica Polonica B **40** (2009).
- 2791 [161] C. L. Smith, Physics Reports **3**, 261 (1972),  
2792 <http://www.sciencedirect.com/science/article/pii/0370157372900105>.
- 2793 [162] O. Benhar, A. Fabrocini, and S. Fantoni, Nuclear Physics A **497**, 423 (1989).
- 2794 [163] R. Bradford, A. Bodek, H. Budd, and J. Arrington, Nuclear Physics B - Proceedings Supplements **159**, 127 (2006),  
2795 <http://www.sciencedirect.com/science/article/pii/S0920563206005184>,  
2796 Proceedings of the 4th International Workshop on Neutrino-Nucleus Interac-  
2797 tions in the Few-GeV Region.
- 2798 [164] A. A. Aguilar-Arevalo *et al.*, Physical Review D **81** (2010).
- 2800 [165] R. Gran, J. Nieves, F. Sanchez, and M. J. V. Vacas, Phys. Rev. D **88**, 113007 (2013),  
2801 <https://link.aps.org/doi/10.1103/PhysRevD.88.113007>.
- 2802 [166] C. Berger and L. M. Sehgal, Phys. Rev. D **76**, 113004 (2007).

- 2803 [167] C. Berger and L. M. Sehgal, Phys. Rev. D **79**, 053003 (2009),  
2804 <https://link.aps.org/doi/10.1103/PhysRevD.79.053003>.
- 2805 [168] T. Sjöstrand, Computer Physics Communications **82**, 74 (1994).
- 2806 [169] C. Bronner and M. Hartz, Tuning of the Charged Hadrons Multiplicities for Deep  
2807 Inelastic Interactions in NEUT, in *Proceedings of the 10th International Workshop on*  
2808 *Neutrino-Nucleus Interactions in Few-GeV Region (NuInt15)*, Journal of the Physical  
2809 Society of Japan, 2016.
- 2810 [170] M. Glück, E. Reya, and A. Vogt, The European Physical Journal C **5**, 461 (1998).
- 2811 [171] A. Bodek and U.-k. Yang, Axial and Vector Structure Functions for Electron- and  
2812 Neutrino- Nucleon Scattering Cross Sections at all  $Q^2$  using Effective Leading  
2813 order Parton Distribution Functions, 2010.
- 2814 [172] A. Bodek and U.-K. Yang, (2010).
- 2815 [173] S. Gollapinni, (2016).
- 2816 [174] E. S. P. Guerra *et al.*, Phys. Rev. D **99**, 052007 (2019).
- 2817 [175] GEANT4, S. Agostinelli *et al.*, Nucl. Instrum. Meth. **A506**, 250 (2003).
- 2818 [176] R. Brun, F. Bruyant, M. Maire, A. C. McPherson, and P. Zanarini, (1987).
- 2819 [177] K. Abe *et al.*, Physical Review Letters **121** (2018).
- 2820 [178] K. Abe *et al.*, Physical Review D **91** (2015).
- 2821 [179] R. Patterson *et al.*, Nuclear Instruments and Methods in Physics Research Section  
2822 A: Accelerators, Spectrometers, Detectors and Associated Equipment **608**, 206  
2823 (2009).
- 2824 [180] e. a. S. Berkman, T2K Technical Note **146** (2013).
- 2825 [181] e. a. A. Himmel, T2K Technical Note **219** (2015).
- 2826 [182] F. a. James, (1998), CERN Program Library Long Writeups.
- 2827 [183] e. a. D. Barrow, T2K Technical Note **399** (2020).
- 2828 [184] A. Maghrabi, A. Aldosari, and M. Almutairi, Advances in Space Research **68**,  
2829 2941 (2021).

- 2830 [185] Super-Kamiokande Collaboration, K. Abe *et al.*, Phys. Rev. D **97**, 072001 (2018),  
2831 <https://link.aps.org/doi/10.1103/PhysRevD.97.072001>.
- 2832 [186] Particle Data Group, J. Beringer *et al.*, Phys. Rev. D **86**, 010001 (2012).
- 2833 [187] Y. N. and, Journal of Physics: Conference Series **888**, 012191 (2017).
- 2834 [188] M. Jiang, *Study of the neutrino mass hierarchy with the atmospheric neutrino data*  
2835 *collected in Super-Kamiokande IV*, PhD thesis, Kyoto University, 2019.
- 2836 [189] S. N. K. Iyogi and Y. Obayashi., T2K Technical Note **027** (2011).
- 2837 [190] LeeKaPik, *Study of the neutrino mass hierarchy with the atmospheric neutrino data*  
2838 *observed in Super-Kamiokande*, PhD thesis, Tokyo University, 2012.
- 2839 [191] The Super-Kamiokande Collaboration, R. Wendell *et al.*, Phys. Rev. D **81**, 092004  
2840 (2010).
- 2841 [192] Super-Kamiokande Collaboration, J. Hosaka *et al.*, Phys. Rev. D **74**, 032002  
2842 (2006).
- 2843 [193] L. M. et al, T2K Technical Note **395** (2020).
- 2844 [194] P. B. et al., T2K Technical Note **212** (2015).
- 2845 [195] W. Parker, *Constraining Systematic Uncertainties at T2K using Near Detector Data*,  
2846 PhD thesis, Royal Holloway University of London, 2020.
- 2847 [196] V. B. et al., T2K Technical Note **246** (2015).
- 2848 [197] J. Misset, T2K Technical Note **318** (2017).
- 2849 [198] X. Li and M. Wilking, T2K Technical Note **319** (2017).
- 2850 [199] e. a. J. Chakrani, T2K Technical Note **414** (2022).
- 2851 [200] T2K Collaboration, M. Wascko, T2K Status, Results, and Plans, Neutrino 2018,  
2852 2018.
- 2853 [201] e. a. Tomislav Vladisavljevic, T2K Technical Note **354** (2020).
- 2854 [202] G. Ambrosini *et al.*, Phys. Lett. B **420**, 225 (1998).
- 2855 [203] e. a. Edward Atkin, T2K Technical Note **344** (2019).
- 2856 [204] e. a. D. Barrow, T2K Technical Note **422** (2022).

- 2857 [205] The MiniBooNE Collaboration, A. A. Aguilar-Arevalo *et al.*, Phys. Rev. D **81**,  
2858 013005 (2010), <https://link.aps.org/doi/10.1103/PhysRevD.81.013005>.
- 2859 [206] P. de Perio and J. Imber, T2K Technical Note **186** (2014).
- 2860 [207] P. de Perio and J. Imber, T2K Technical Note **107** (2012).
- 2861 [208] S. Tobayama, *An Analysis of the Oscillation of Atmospheric Neutrinos*, PhD thesis,  
2862 British Columbia U., 2016.
- 2863 [209] C. V. Daniel Barrow, T2K-SK Detector Matrix Uncertainties - MaCh3 In-  
2864 tegration, <https://git.t2k.org/t2k-sk/t2ksk-detcovmat/-/tree/feature/MaCh3Integration>, Accessed: 22-06-2022.
- 2866 [210] R. Wendell, *Three Flavor Oscillation Analysis of Atmospheric Neutrinos in Super-*  
2867 *Kamiokande*, PhD thesis, University of North Carolina, 2008.
- 2868 [211] A. M. Dziewonski and D. L. Anderson, Phys. Earth Planet. Inter. **25**, 297 (1981).
- 2869 [212] e. a. D. Barrow, T2K Technical Note **425** (2022).
- 2870 [213] R. G. Calland, A. C. Kaboth, and D. Payne, **9**, P04016 (2014).
- 2871 [214] R. Wendell, <http://www.phy.duke.edu/raw22/public/Prob3++/>.
- 2872 [215] F. Kallenborn, C. Hundt, S. Böser, and B. Schmidt, Computer Physics Communi-  
2873 cations **234**, 235 (2019).
- 2874 [216] L. Warsame, MaCh3 Analysis Progress.
- 2875 [217] S. Bourret, J. A. B. Coelho, and V. V. E. and, Journal of Physics: Conference Series  
2876 **888**, 012114 (2017).
- 2877 [218] C. Rott, A. Taketa, and D. Bose, Scientific Reports **5** (2015).
- 2878 [219] K. Hagiwara, N. Okamura, and K. ichi Senda, Journal of High Energy Physics  
2879 **2011** (2011).
- 2880 [220] D. Typinski, Earth Gravity, <http://www.typnet.net/Essays/EarthGravGraphics/EarthGrav.pdf>, Accessed: 24-06-2022.

# 2882 List of Figures

<small>2883</small>	2.1	The cross-section of neutrinos from various natural and man-made sources as a function of neutrino energy. Taken from [25] . . . . .	<small>2884</small>	10				
<small>2885</small>	2.2	The solar neutrino flux as a function of neutrino energy for various fusion reactions and decay chains as predicted by the Standard Solar Model. Taken from [26]. . . . .	<small>2886</small>	<small>2887</small>	11			
<small>2888</small>	2.3	Left panel: The atmospheric neutrino flux for different neutrino flavours as a function of neutrino energy as predicted by the 2007 Honda model (“This work”) [43], the 2004 Honda model (“HKKM04”) [44], the Bartol model [42] and the FLUKA model [46]. Right panel: The ratio of the muon to electron neutrino flux as predicted by all the quoted models. Both figures taken from [43]. . . . .	<small>2889</small>	<small>2890</small>	<small>2891</small>	<small>2892</small>	<small>2893</small>	14
<small>2894</small>	2.4	A diagram illustrating the definition of zenith angle as used in the Super Kamiokande experiment [47]. . . . .	<small>2895</small>	14				
<small>2896</small>	2.5	Prediction of $\nu_e, \bar{\nu}_e, \nu_\mu, \bar{\nu}_\mu$ fluxes as a function of zenith angle as calculated by the HKKM model [45]. The left, middle and right panels represent three values of neutrino energy, 0.32GeV, 1.0GeV and 3.2GeV respectively. Predictions for other models including Bartol [42], Honda [43] and FLUKA [46] are given in [47]. . . . .	<small>2897</small>	<small>2898</small>	<small>2899</small>	<small>2900</small>	15	
<small>2901</small>	2.6	Constraints on the atmospheric oscillation parameters, $\sin^2(\theta_{23})$ and $\Delta m_{23}^2$ , from atmospheric and long baseline experiments: SK [52], T2K [53], NO $\nu$ A [54], IceCube [55] and MINOS [56]. Figure taken from [57].	<small>2902</small>	<small>2903</small>	16			
<small>2904</small>	2.7	Reactor electron antineutrino fluxes for $^{235}\text{U}$ (Black), $^{238}\text{U}$ (Green), $^{239}\text{Pu}$ (Purple), and $^{241}\text{Pu}$ (Orange) isotopes. The inverse $\beta$ -decay cross-section (Blue) and corresponding measurable neutrino spectrum (Red) are also given. Top panel: Schematic of Inverse $\beta$ -decay interaction including the eventual capture of the emitted neutron. This capture emits a $\gamma$ -ray which provides a second signal of the event. Taken from [69]. . . . .	<small>2905</small>	<small>2906</small>	<small>2907</small>	<small>2908</small>	<small>2909</small>	19
<small>2910</small>	3.1	A schematic diagram of the Super-Kamiokande Detector. Taken from [88].	25					

2911	3.2	The location of “standard PMTs” (red) inside the SK detector. Taken from [86]. . . . .	29
2912			
2913	3.3	Schematic view of the data flow through the data acquisition and online system. Taken from [102]. . . . .	32
2914			
2915	3.4	The cross-section view of the Tokai to Kamioka experiment illustrating the beam generation facility at J-PARC, the near detector situated at a baseline of 280m and the Super Kamiokande far detector situated 295km from the beam target. . . . .	35
2916			
2917			
2918			
2919	3.5	The near detector suite for the T2K experiment showing the ND280 and INGRID detectors. The distance between the detectors and the beam target is 280m. . . . .	36
2920			
2921			
2922	3.6	Top panel: Bird’s eye view of the most relevant part of primary and secondary beamline used within the T2K experiment. The primary beamline is the main-ring proton synchrotron, kicker magnet, and graphite target. The secondary beamline consists of the three focusing horns, decay volume, and beam dump. Figure taken from [118]. Bottom panel: The side-view of the secondary beamline including the focusing horns, beam dump and neutrino detectors. Figure taken from [119]. . . . .	38
2923			
2924			
2925			
2926			
2927			
2928			
2929	3.7	The Monte Carlo prediction of the energy spectrum for each flavour of neutrino ( $\nu_e$ , $\bar{\nu}_e$ , $\nu_\mu$ and $\bar{\nu}_\mu$ ) in the neutrino dominated beam FHC mode (Left) and antineutrino dominated beam RHC mode (Right) expected at SK. Taken from [120]. . . . .	39
2930			
2931			
2932			
2933	3.8	Top panel: T2K muon neutrino disappearance probability as a function of neutrino energy. Middle panel: T2K electron neutrino appearance probability as a function of neutrino energy. Bottom panel: The neutrino flux distribution for three different off-axis angles (Arbitrary units) as a function of neutrino energy. . . . .	41
2934			
2935			
2936			
2937			
2938	3.9	The components of the ND280 detector. The neutrino beam travels from left to right. Taken from [118]. . . . .	42
2939			
2940	3.10	Comparison of data to Monte Carlo prediction of integrated deposited energy as a function of track length for particles that stopped in FGD1. Taken from [123]. . . . .	44
2941			
2942			

2943	3.11 Schematic design of a Time Projection Chamber detector. Taken from [124].	45
2944	3.12 The distribution of energy loss as a function of reconstructed momentum for charged particles passing through the TPC, comparing data to Monte Carlo prediction. Taken from [124].	45
2945		
2946		
2947	3.13 A schematic of the P0D side-view. Taken from [125].	47
2948	3.14 Left panel: The Interactive Neutrino GRID on-axis Detector. 14 modules are arranged in a cross-shape configuration, with the center modules being directly aligned with the on-axis beam. Right panel: The layout of a single module of the INGRID detector. Both figures are recreated from [118].	49
2949		
2950		
2951		
2952		
2953	4.1 Example of using Monte Carlo techniques to find the area under the blue line. The gradient and intercept of the line are 0.4 and 1.0 respectively. The area found to be under the curve using one thousand samples is 29.9 units.	54
2954		
2955		
2956		
2957	4.2 The area under a line of gradient 0.4 and intercept 1.0 for the range $0 \leq x \leq 10$ as calculated using Monte Carlo techniques as a function of the number of samples used in each repetition. The analytical solution to the area is 30 units as given by the red line.	54
2958		
2959		
2960		
2961	4.3 Three MCMC chains, each with a stationary distribution equal to a Gaussian centered at 0 and width 1 (As indicated by the black dotted lines). All of the chains use a Gaussian proposal function but have different widths (or 'step size $\sigma$ '). The top panel has $\sigma = 0.1$ , middle panel has $\sigma = 0.5$ and the bottom panel has $\sigma = 5.0$ .	60
2962		
2963		
2964		
2965		
2966	4.4 The log-likelihood from the fit detailed in <a href="#">DB: Link to AsimovA Sensitivity Section</a> as a function of the number of steps accumulated in each fit. Many independent MCMC chains were run in parallel and overlaid on this plot. The red line indicates the $1 \times 10^5$ step burn-in period after which the log-likelihood becomes stable.	61
2967		
2968		
2969		
2970		

2971	4.5 Left: The two dimensional probability distribution for two correlated parameters $x$ and $y$ . The red distribution shows the two dimensional probability distribution when $0 \leq x \leq 5$ . Right: The marginalised probability distribution for the $y$ parameter found when requiring the $x$ to be bound between $-5 \leq x \leq 5$ and $0 \leq x \leq 5$ for the black and red distribution, respectively. . . . .	63
2977	5.1 The NEUT prediction of the $\nu_\mu$ -H <sub>2</sub> O cross-section overlaid on the T2K $\nu_\mu$ flux. The charged current (black, solid) and neutral current (black, dashed) inclusive, charged current quasi-elastic (blue, solid), charged current 2p2h (blue, dashed), charged current single pion production (pink), and charged current multi- $\pi$ and DIS (Purple) cross-sections are illustrated. Figure taken from [159]. . . . .	71
2983	5.2 Illustration of the various processes which a pion can undergo before exiting the nucleus. Taken from [173]. . . . .	72
2985	5.3 Event displays from Super Kamiokande illustrating the “crisp” ring from a muon and the typically “fuzzier” electron ring. Each pixel represents a PMT and the color scheme denotes the accumulated charge deposited on that PMT. Figures taken from [181]. . . . .	75
2989	5.4 The electron/muon PID separation parameter for all sub-GeV single-ring events in SK-IV. The charged current (CC) component is broken down in four flavours of neutrino ( $\nu_\mu$ , $\bar{\nu}_\mu$ , $\nu_e$ and $\bar{\nu}_e$ ). Events with positive values of the parameter are determined to be electron-like. . .	79
2993	5.5 The variation of the measured dark rate as a function of date, broken down by PMT type. The SK-IV and SK-V periods span September 2008 to May 2018 and January 2019 to July 2020, respectively. The break in measurement in 2018 corresponds to the period of tank repair and refurbishment. Figure adapted from [183]. . . . .	81
2998	5.6 Comparison of the measured raw charge deposited per event from the stopping muon data samples between SK-IV (Blue) and SK-V (Red), split by the primary muon subevent and the associated decay electron subevent. . . . .	82

3002	5.7 The distribution of the reconstructed momentum from the muon ring divided by the distance between the reconstructed muon and decay electron vertices as found in the stopping muon data sets of SK-IV (Black) and SK-IV (Red). Only events with one tagged decay electron are considered. A Gaussian fit is considered in the range [2.0, 2.4] MeV/cm and illustrated as the solid curve. . . . .	83
3003		
3004		
3005		
3006		
3007		
3008	5.8 The $\chi^2$ difference between the SK-IV and SK-V reconstructed muon momentum divided by range when the SK-V is modified by the scaling parameter $\alpha$ . Both additive (Blue) and multiplicative (Black) scaling factors have been considered. In practice, the additive scaling factor actually uses the value of $(\alpha - 1.0)$ but is illustrated like this so the results can be shown on the same axis range. . . . .	84
3009		
3010		
3011		
3012		
3013		
3014	5.9 A depiction of the topology patterns for fully-contained (FC), partially-contained (PC) and up-going muon (Up- $\mu$ ) samples included in this analysis. . . . .	85
3015		
3016		
3017	5.10 The predicted neutrino flux of the fully contained (FC) sub-GeV and multi-GeV, partially contained (PC), and upward-going muon (Up- $\mu$ ) events. The prediction is broken down by the $\nu_x \rightarrow \nu_e$ prediction (top left), $\nu_x \rightarrow \nu_\mu$ prediction (top right) and $\nu_x \rightarrow \nu_\tau$ prediction (bottom). All systematic dials are set to their nominal values and the Asimov A oscillation parameters are assumed. . . . .	87
3018		
3019		
3020		
3021		
3022		
3023	5.11 The predicted neutrino flux of the beam neutrinos, illustrated as a function of neutrino energy. The predictions are broken down by the number of decay electrons associated with the particular events. All systematic dials are set to their nominal values and the Asimov A oscillation parameters are assumed. . . . .	89
3024		
3025		
3026		
3027		

3028      6.1	The accumulated beam data, measured as the number of protons on target (POT). The total data (blue) is given which comprises of the neutrino beam (red) and antineutrino (purple) components. The beam power for neutrino and antineutrino beams is given as the markers using the same colour scheme. The timescale runs from Run 1 which started in January 2010 until Run 10 which ended in February 2020. The ratio of accumulated data in neutrino and antineutrino beam is 54.7% : 45.3%. . . . .	91
3036      6.2	Comparison of the SK-IV atmospheric samples between predictions made with the CP-violating Asimov A (Black) and CP-conserving Asimov B (Red) oscillation parameter sets (given in Table 2.2). The subGeV samples CCRES and $\pi^0$ -like samples are given in their reconstructed lepton momentum. All other samples are presented in their reconstructed zenith angle projection. . . . .	98
3042      6.3	The nominal Monte Carlo predictions for the FGD1 and FGD2 samples in neutrino beam mode, broken down into the $CC\nu_\mu 0\pi$ , $CC\nu_\mu 1\pi$ and $CC\nu_\mu$ Other categories. Figures taken from [193]. . . . .	101
3045      6.4	The reconstructed neutrino energy, as defined by Equation 6.2 and Equation 6.3, for the $1R\mu$ -like, $1Re$ -like and $CC1\pi^+$ -like samples. Asimov A oscillation parameter sets are assumed (given in Table 2.2). These samples are the FHC mode samples. For ease of viewing, the $1R\mu$ sample only shows the $0. \leq E_\nu^{rec} < 3.0\text{GeV}$ but the binning extends to $30.0\text{GeV}$ . . . . .	104
3050      6.5	The distribution of the angle between the neutrino beam direction and the reconstructed final state lepton, for the FHC $1Re$ -like sample. The distribution is broken down by neutrino interaction mode into charged current (left) and neutral current (right) components. Asimov A oscillation parameter sets are assumed (given in Table 2.2). <b>DB: Is this needed or will it just bring up more questions?</b> . . . . .	106
3056      6.6	The total uncertainty evaluated on the near detector $\nu_\mu$ flux prediction constrained by the replica-target data, illustrated as a function of neutrino energy. The solid(dashed) line indicates the uncertainty used within this analysis(the T2K 2018 analysis [200]). The solid histogram indicates the neutrino flux as a function of energy. Figure taken from [201]. . . . .	108

3061	6.7	The predicted neutrino energy distribution for subGeV atmospheric and beam samples. FHC and RHC beam samples are summed together Asimov A oscillation parameters are assumed (given in Table 2.2). Beam and atmospheric samples with similar cuts are compared against one another. . . . .	113
3066	6.8	The interaction mode contribution of each sample given as a fraction of the total event rate in that sample. Asimov A oscillation parameters are assumed (given in Table 2.2). The Charged Current (CC) modes are broken into quasi-elastic (QE), 2p2h, resonant charged pion production ( $1\pi^\pm$ ), multi-pion production ( $M\pi$ ), and other interaction categories. Neutral Current (NC) interaction modes are given in interaction mode categories: $\pi^0$ production, resonant charged pion production, multi- pion production, and others. . . . .	114
3074	6.9	Down-going atmospheric subGeV single-ring samples comparing the mean and error of the pre-fit and post-fit Monte Carlo predictions in red and blue, respectively. The magenta histogram illustrates the Monte Carlo prediction using the generated dial values. The black points illustrate the down-going data with statistical errors given. The mean and errors of the Monte Carlo predictions are calculated by the techniques documented in subsection 4.3.4. The pre-fit spectrum is calculated by throwing the cross-section and atmospheric flux dial values from the pre-fit covariance matrix. The post-fit spectrum is calculated by sampling the cross-section dial values from an ND fit MCMC chain, whilst still throwing the atmospheric flux dials from the pre-fit covariance. . . . .	117
3086	6.10	The ring counting parameter as defined in Equation 6.6 for the SubGeV-elike-0dcy and MultiRing-elike-nue samples. . . . .	126
3088	6.11	The ring counting parameter, defined in Equation 6.6, as a function of the number of reconstructed rings as found by the <code>fitQun</code> recon- struction algorithm. Left: true $\nu_\mu$ events with only one muon above the Cherenkov threshold in the final state. Right: true $\nu_\mu$ events with one muon and at least one other charged particle above the Cherenkov threshold in the final state. . . . .	127

3094	6.12 The $\chi^2$ between the hybrid- $\pi^0$ Monte Carlo and data samples, as a function of smear ( $\alpha$ ) and shift ( $\beta$ ) parameters, for events which have $1\pi^0$ final state topology. Left: Electron-muon separation PID parameter for events with $30 \geq E_{vis}(MeV) < 300$ . Right: Electron- $\pi^0$ separation PID parameter for events with $30 \geq E_{vis}(MeV) < 300$ . . . . .	128
3101		
3102		
3103	6.13 The distribution of $\log(L_e/L_\mu)$ compared to $\log(L_e/L_\pi)$ for subGeV events with zero (top left), one (top right) or two (bottom) decay electrons. The correlation in the distribution is calculated as 0.997, 0.999 and 0.996, respectively. . . . .	129
3104		
3105		
3106	7.1 The density of the Earth given as a function of the radius, as given by the PREM model (Black), and the constant density four-layer approximation (Blue), as used in the official SK-only analysis. . . . .	133
3107		
3108		
3109		
3110		
3111		
3112	7.2 An “oscillogram” that depicts the $P(\nu_\mu \rightarrow \nu_e)$ oscillation probability as a function of neutrino energy and cosine of the zenith angle. The zenith angle is defined such that $\cos(\theta_Z) = 1.0$ represents neutrinos that travel from directly above the detector. The four-layer constant density PREM model approximation is used and Asimov A oscillation parameters are assumed (Table 2.2). . . . .	134
3113		
3114		
3115		
3116		
3117		
3118	7.3 The effect of $\delta_{CP}$ for atmospheric neutrinos given in terms of the neutrino energy and zenith angle. This oscillogram compares the $P(\nu_\mu \rightarrow \nu_e)$ oscillation probability for a CP conserving ( $\delta_{CP} = 0.0$ ) and a CP violating ( $\delta_{CP} = -1.601$ ) value taken from the Asimov A parameter set. The other oscillation parameters assume the Asimov A oscillation parameter set given in Table 2.2. . . . .	135
3119		

3118      7.4 An illustration of the matter-induced effects on the oscillation probability, given as a function of neutrino energy and zenith angle. The top row 3119 of panels gives the $P(\nu_e \rightarrow \nu_e)$ oscillation probability and the bottom 3120 row illustrates the $P(\bar{\nu}_e \rightarrow \bar{\nu}_e)$ oscillation probability. The left column 3121 highlights the oscillation probability in a vacuum, whereas the middle 3122 and right column represents the oscillation probabilities when the four- 3123 layer fixed density PREM model is assumed. All oscillation probabilities 3124 assume the “Asimov A” set given in Table 2.2, but importantly, the right 3125 column sets an inverted mass hierarchy. The “matter resonance” effects 3126 at $E_\nu \sim 5\text{GeV}$ can be seen in the $P(\nu_e \rightarrow \nu_e)$ for normal mass hierarchy 3127 and $P(\bar{\nu}_e \rightarrow \bar{\nu}_e)$ for inverted hierarchy. . . . .	136
3129      7.5 The oscillation probability for beam neutrino events given as a function 3130 of neutrino energy. All oscillation parameters assume the “Asimov A” 3131 set given in Table 2.2 unless otherwise stated. Each panel represents a 3132 change in one of the oscillation parameters whilst keeping the remaining 3133 parameters fixed. . . . .	137
3134      7.6 The number of electron-like events in the FHC and RHC operating 3135 mode of the beam, as a function of the oscillation probabilities. Both 3136 normal hierarchy (Solid) and inverse hierarchy (Dashed) values of 3137 $\Delta m_{23}^2$ are given. . . . .	138
3138      7.7 The oscillation probability $P(\nu_\mu \rightarrow \nu_e)$ , given as a function of neutrino 3139 energy and zenith angle, which highlights an example of the “fast” 3140 oscillations in the sub-GeV upgoing region. . . . .	140
3141      7.8 Illustration of the averaging procedure for $N = 2$ . The oscillation 3142 probabilities calculated on the finer left binning are averaged to obtain 3143 the oscillation probabilities in the coarser right binning. These averaged 3144 oscillation probabilities with the coarser binning are then applied to 3145 each event during the fit. . . . .	142
3146      7.9 Event rate of the SubGeV_elike_0dcy sample as a function of the num- 3147 ber of sub-divisions per coarse bin. Each subplot represents the event 3148 rate of the sample at a different oscillation parameter set thrown from 3149 the PDG priors detailed in Table 2.1. The red line in each subplot 3150 represents the mean of the event rate over the different values of sub- 3151 divisions for that particular oscillation parameter throw. . . . .	144

---

3152	7.10 Variance of event rate for each atmospheric sample as a function of the number of sub-divisions per coarse bin. The solid red line indicates the 0.1% threshold and the dashed red line indicates the variance at a sub-division $N = 10$ . . . . .	145
3156	7.11 Variance of sample likelihood, when compared to ‘Asimov data’ set at Asimov A, for each atmospheric sample as a function of the number of sub-divisions per coarse bin. The solid red line indicates the 0.1% threshold and the dashed red line is a graphical indication of the variance at a sub-division $N = 10$ . . . . .	146
3161	7.12 The oscillation probability, $P(\nu_\mu \rightarrow \nu_e)$ (top row) and $P(\nu_e \rightarrow \nu_e)$ (bottom row), given as a function of neutrino energy and zenith angle. The left column gives the “fine” binning used to calculate the oscillation probabilities and the right column illustrates the “coarse” binning used to reweight the Monte Carlo events. The fine binning choice is given with $N = 10$ , which was determined to be below the threshold from Figure 7.10 and Figure 7.11. . . . .	147
3168	7.13 The calculation time taken to both calculate the oscillation probabilities and fill the “coarse” oscillograms, following the technique given in section 7.2, for the CUDAProb3 and ProbGPU (Red) calculation engines. CUDAProb3 has both a GPU (Blue) and CPU (Black) implementation, where the CPU implementation is multithreaded. Therefore, 8-threads (solid) and 40-threads (dashed) configurations have been tested. Prob3, which is a CPU single-thread implementation has a mean step time of 1.142s. . . . .	148
3176	7.14 The oscillation probability, $P(\nu_\mu \rightarrow \nu_e)$ (top row) and $P(\nu_e \rightarrow \nu_e)$ (bottom row), given as a function of neutrino energy and zenith angle. The left column gives probabilities where the constant $Z/A = 0.5$ approximation which is used in the official SK-only analysis. The middle column gives the probabilities where $Z/A = [0.468, 0.498]$ values are used, as given in Table 7.1. The right column illustrates the difference in oscillation probability between the two different techniques. . . . .	150

- 3183     7.15 The density of the Earth given as a function of the radius, as given by  
3184       the PREM model (Black), the constant density four-layer approxima-  
3185       tion (Blue), as used in the official SK-only analysis, and the quadratic  
3186       approximation of the PREM model (Red). . . . . 151
- 3187     7.16 The oscillation probability,  $P(\nu_\mu \rightarrow \nu_e)$  (top row) and  $P(\nu_e \rightarrow \nu_e)$  (bot-  
3188       tom row), given as a function of neutrino energy and zenith angle. The  
3189       left column gives probabilities where the four-layer constant density ap-  
3190       proximation is used. The middle column gives the probabilities where  
3191       the density is integrated over the trajectory, using the quadratic PREM  
3192       approximation, for each  $\cos(\theta_Z)$  is used. The right column illustrates the  
3193       difference in oscillation probability between the two different techniques. 153
- 3194     7.17 The oscillation probability,  $P(\nu_\mu \rightarrow \nu_e)$  (top row) and  $P(\nu_e \rightarrow \nu_e)$  (bot-  
3195       tom row), given as a function of neutrino energy and zenith angle. The  
3196       left column gives probabilities where a fixed production height of 25km  
3197       is used. The middle column gives the probabilities where the produc-  
3198       tion height is analytically averaged. The right column illustrates the  
3199       difference in oscillation probability between the two different techniques. 157

# 3200 List of Tables

<small>3201</small>	2.1	The 2018 Particle Data Group constraints of the oscillation parameters taken from [81]. The value of $\Delta m_{23}^2$ is given for both normal hierarchy (N.H.) and inverted hierarchy (I.H.) and $\sin^2(\theta_{23})$ is broken down by whether its value is below (Q1) or above (Q2) 0.5. . . . .	<small>3202</small>	21
<small>3203</small>			<small>3204</small>	
<small>3205</small>	2.2	Reference values of the neutrino oscillation parameters for two different oscillation parameter sets. . . . .	<small>3206</small>	22
<small>3207</small>			<small>3208</small>	
<small>3209</small>	3.1	The various SK periods and respective live-time. The SK-VI live-time is calculated until 1 <sup>st</sup> April 2022. SK-VII started during the writing of this thesis. . . . .		24
<small>3210</small>			<small>3211</small>	
<small>3212</small>	3.2	The trigger thresholds and extended time windows saved around an event which were utilised throughout the SK-IV period. The exact thresholds can change and the values listed here represent the thresholds at the start and end of the SK-IV period. . . . .	<small>3213</small>	33
<small>3214</small>			<small>3215</small>	
<small>3216</small>	3.3	The threshold momentum and energy for a particle to generate Cherenkov light in ultrapure water, as calculated in Equation 3.2 in ultrapure water which has refractive index $n = 1.33$ . . . . .		34
<small>3217</small>			<small>3218</small>	
<small>3219</small>	4.1	Jeffreys scale for strength of preference for two models $A$ and $B$ as a function of the calculated Bayes factor ( $B_{AB} = B(A/B)$ ) between the two models [140]. The original scale is given in terms of $\log_{10}(B(A/B))$ but converted to linear scale for easy comparison throughout this thesis.	<small>3220</small>	66
<small>3221</small>			<small>3222</small>	
<small>3223</small>	6.1	The amount of data collected in each detector used within this analysis. The data collected at the near and far detector, for both neutrino beam (FHC) and antineutrino beam (RHC), is measured as the number of protons on target (POT). . . . .	<small>3224</small>	90
<small>3225</small>			<small>3226</small>	
6.2	The fully contained subGeV samples, defined as events with visible energy $E_{vis} < 1.33\text{GeV}$ , used within this oscillation analysis. . . . .			93

3227	6.3	The fully contained multiGeV samples used within this oscillation analysis. Both the sample name and description are given. . . . .	95
3228			
3229	6.4	The purity of each atmospheric sample used within this analysis, broken down by charged current (CC) and neutral current (NC) interactions and which neutrino flavour interacted within the detector. Asimov A oscillation parameter sets are assumed (given in Table 2.2). Electron neutrino and antineutrino events are separated to illustrate the ability of the separation likelihood cuts used within the multiGeV and multiring sample selections. . . . .	96
3230			
3231			
3232			
3233			
3234			
3235			
3236	6.5	The reconstructed cosine zenith and lepton momentum binning assigned to the atmospheric samples. The “ $\cos(\theta_Z)$ Bins” column illustrates the number of bins uniformly distributed over the $-1.0 \leq \cos(\theta_Z) \leq 1.0$ region for fully and partially contained samples and $-1.0 \leq \cos(\theta_Z) \leq 0.0$ region for up- $\mu$ samples. <b>DB: Does this belong in the appendix?</b> . . . . .	97
3237			
3238			
3239			
3240			
3241			
3242	6.6	The neutrino energy binning for the different neutrino flavours. “Right” sign indicates neutrinos in the FHC beam and antineutrinos in the RHC beam. “Wrong” sign indicates antineutrinos in the FHC beam and neutrinos in the RHC beam. The binning of the detector response is identical for the FHC and RHC modes as well as at ND280 and SK. . .	109
3243			
3244			
3245			
3246			
3247	6.7	List of cut variables that are included within the shift/smear fit documented in [197]. . . . .	119
3248			
3249	6.8	Reconstructed event topology categories on which the SK detector systematics [197] are based. . . . .	120
3250			
3251	6.9	Sources of systematic errors specified within the grouped into the “calibration” systematics model. . . . .	123
3252			
3253	6.10	Visible energy binning for which the correlated SK detector systematics are based . . . . .	124
3254			
3255	7.1	Description of the four layers of the Earth invoked within the constant density approximation of the PREM model [211]. . . . .	132
3256			

